Ab initio modeling of the electronic structure of d-metal systems and of resonant inelastic X-ray scattering responses

vorgelegt von

Lei Xu

geboren am 22.04.1987 in Shiyan, China

Gutachter:

1. Prof. Dr. Jeroen van den Brink

2. Prof. Dr. Jamal Berakdar

Eingereicht am 11 March 2019

Disputation am 31 July 2019

"Everything should be made as simple as possible, but not simpler."

Albert Einstein (1879−1955), Nobel laureate in Physics (1921)

"Physics is not the most important thing, love is."

Richard Phillips Feynman (1918−1988), Nobel laureate in Physics (1965)

Contents

List of Figures

List of Tables

List of Abbreviations

AF	Antiferromagnetic
CAS	Complete Active Space
CASCI	Complete Active Space Configuration Interaction
CASPT2	Complete Active Space Perturbation Theory 2nd order
CASSCF	Complete Active Space Self Consistent Field
CI	Configuration Interaction
CISD	Configuration Interaction Singles and Doubles
CSF	Configuration State Functions
CT	Charge Transfer
DC	Dirac-Coulomb
DCB	Dirac-Coulomb-Breit
DFT	Density Functional Theory
DM	Dzyaloshinskii-Moriya
DMFT	Dynamic Mean Field Theory
ECPs	Effective Core Potentials
FCI	Full Configuration Interaction
FM	Ferromagnetic
GGA	Generalized Gradient Approximation
GTO	Gaussian Type Orbitals

KD   Kramers Doublet

LCAO   Linear Combination of Atomic Orbitals

LDA   Local Density Approximation

MCSCF   Multi-Configurational Self-Consistent Field

MO   Molecular Orbital

MRCI   Multireference Configuration Interaction

NEVPT2 N-Electron Valence state Perturbation Theory

NN   Nearest Neighbor

NNN   Next Nearest Neighbor

PC   Point Charge

QC   Quantum Chemistry

RHF   Restricted Hartree-Fock

RIXS   Resonant Inelastic X-ray Scattering

ROHF   Restricted Open Hartree-Fock

SCF   Self-Consistent Field

SIA   Single-Ion Anisotropy

SOC   Spin-Orbit Coupling

TIPs   Total Ion Potentials

TM   Transition Metal

WF   Wave Function

XAS   X-ray Absorption Spectroscopy

ZFS   Zero-Field Splitting

Acknowledgement

Chapter 1

Introduction

1.1 The exciting physics of transition metal compounds

Transition metal (TM) compounds with partially filled d-shells form an unique class of materials which has attracted a huge amount of attention. For the TM ions in these systems, the d-electrons experience competing forces: Coulombic repulsion tends to localize individual electrons at the atomic lattice sites while hybridization with the ligand p orbitals tends to delocalize the d-electrons. The electron-electron interactions within the d-shells and the mutual interplay between spin, charge and orbital degrees of freedom give rise to a wealth of intriguing properties. These properties include the metal-insulator transition (MIT) [1] and colossal magnetoresistance [2] as well as various spin, charge and orbital ordering phenomena [3–5]. Another remarkable phenomenon TM compounds exhibit is superconductivity with high critical temperature in copper oxides [6, 7], which has triggered extensive research activity ever since its first discovery in the mid 1980's [6].

In the last several decades, the majority of studies on TM compounds have focused on $3d$ electron systems [1]. In insulating $3d$ TM compounds, the electronic states are reasonably well localized due to strong Coulomb interactions. The arrangement of the negatively charged ligands around the TM cation affects TM d orbitals differently, leading to a splitting of the five d energy levels which for a free ion have the same energy. An example is the splitting between triply degenerate t_{2g} (d_{xy}, d_{yz} and d_{xz}) and doubly degenerate e_g ($d_{x^2-y^2}$ and d_{z^2}) orbital states in octahedral environments. The degeneracy of such states (both t_{2g} and e_g) can be further lifted in symmetry lower than octahedral or by electron-phonon interactions (e.g., the Jahn-Teller effect). For lower symmetries, typically the scale of the energy splittings between d_{xy}, d_{yz} and d_{xz} ($d_{x^2-y^2}$ and d_{z^2}) levels is ~0.1 eV (~1 eV), which is much larger than that of the spin-orbit coupling (SOC) (~20 meV) [8]. Therefore, in $3d$ TM compounds, the orbital angular momentum is completely quenched and the magnetic ground state can often be reasonably well described in terms of a spin-only Hamiltonian. The simplest expression for such a Hamiltonian is the Heisenberg model

$$H_{Heis} = \sum_{i,j} J_{ij} \vec{S}_i \cdot \vec{S}_j, \tag{1.1}$$

where J_{ij} is the isotropic exchange interaction and $\vec{S}_i$, $\vec{S}_j$ are spins at lattice sites indexed by i and j. There are different kinds of magnetic interactions, such as ferromagnetic (FM), an-

tiferromagnetic (AFM) or combinations of these when there are inequivalent magnetic bonds or longer-range (beyond nearest-neighbour) interactions. The magnetic interaction depends on details of the crystal structure and the number of electrons in the d shell [9]. Materials of intensive investigations are certain low-dimensional TM systems in which the magnetic interaction is strong only in one or two directions. In such materials, spin-chain, spin-ladder and two-dimensional (2D) spin models can be realized. Prominent examples are layered compounds containing Cu^{2+} ($3d^9$, $S = 1/2$) ions, the parent compounds of the high-temperature superconductors [6]. Remarkable phenomena are also the nontrivial excited states in chain systems with the same Cu^{2+} sites, where the spin and charge degrees of freedom are separated [10] or when an orbiton separates itself from spinons with a substantial dispersion in energy over momentum [11]. Another example that has attracted considerable attention is the spin-chain system $TiPO_4$ ($3d^1$, $S = 1/2$), which was proposed to be a non-conventional spin-Peierls (SP) compound with two successive phase transitions (at $T_{c1} = 74$ K and $T_{c2} = 111$ K), having a SP distortion below 74 K with a dimerization of the Ti-O chains along the c axis [12].

$3d$ TM compounds have been studied for many decades. TM systems with $4d$ and $5d$ valence electrons have recently also attracted a lot of attention. When going to heavier TM elements, from $3d$ to $4d$ and $5d$, the d orbitals become more extended and the electronic repulsion U tends to be progressively weaker. Hence, a concomitant crossover to a weakly correlated electronic structure is expected. At the same time, the relativistic SOC increases dramatically when going to heavier elements. Therefore, in some $5d$ TM systems with strong SOC, the physics can be drastically different from systems in which SOC acts only as a minor perturbation.

In heavy TM compounds, such as iridates and osmates, the existence of several overlapping energy scales and competing interactions, including spin-orbit, Coulomb and exchange interactions, offers wide-ranging opportunities for the discovery of novel types of correlated ground states and novel properties. In particular, the strong SOC provides an interesting platform. In these systems, the spin ($\vec{S}$) and orbital angular momentum ($\vec{L}$) are entangled, producing an electronic state characterized by total angular momentum $\vec{J}=\vec{S}+\vec{L}$. The recent confirmation of spin-orbit $J_{eff}=1/2$ Mott states in iridates has stimulated extensive research on quantum phenomena [13, 14] in $5d$ TM materials. For instance, a theoretical study predicts that the $J_{eff}=1/2$ Mott states in the honeycomb iridates Na_2IrO_3 and Li_2IrO_3 lead to the low-energy quantum Hamiltonian of the Kitaev model, relevant for quantum computations [15]. Beyond that, SOC plays a crucial role in achieving topologically nontrivial electronic states. For example, it is suggested that the honeycomb lattice of Ir ions in Na_2IrO_3, with complex hopping amplitudes arising from strong SOC, may lead to a quantum spin-Hall insulator [16]. Close to Ir in the periodic table is Os. There is also extensive research focusing on osmates, which constitute another rich platform for the search of novel electronic phases. One of the most interesting cases for osmates is $NaOsO_3$ ($5d^3$, $S = 3/2$) [17], which experimentally displays a MIT driven by antiferromagnetic (AFM) ordering [18]. Another interesting examples are the Ba_2YMoO_6 and $Ba_2(Li, Na)OsO_6$ double-perovskite systems [19–30] containing d^1 metal ions, proposed to be possible candidates for spin liquid ground states.

It is instructive to consider a schematic phase diagram as shown in Fig.1.1 in terms of the
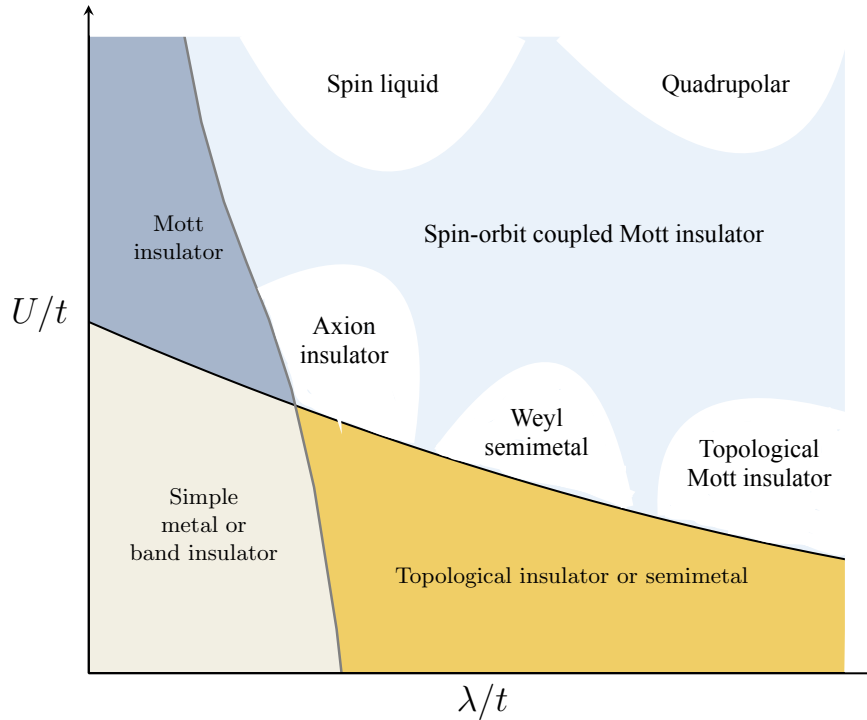
Figure 1.1: Schematic phase diagram of d-electron materials in terms of the effective electronic-structure parameters U/t and λ/t, where U is the on-site Coulomb repulsion, λ is the strength of SOC and t is a nearest-neighbor hopping amplitude. Adapted from Ref. [31].

relative strength of the effective parameters U/t and λ/t, where t is the hopping amplitude and λ is the strength of SOC entangling spin and angular momenta. In this phase diagram, two lines divide the whole space into four quadrants, which are the weak and strong correlation regions, the weak and strong SOC regimes. At the left side of the diagram are Mott insulators, band insulators and simple metals. In this region, where SOC is weak ($\lambda/t \ll 1$), the electronic behavior is dominated either by the interaction between electrons for the case of Mott insulators (large U/t) or by the interaction of electrons with the periodic lattice potential for band insulators and simple metals (small U/t). When U is comparable to t, an insulating gap is induced in the valence band structure by electron correlation effects (Coulomb interaction U) and in this case a conventional MIT occurs. For $5d$ TM compounds with strong SOC, when $U/t \ll 1$, a metallic or semiconducting state at small U may be converted to a topological insulator (TI) or to a semimetal. TIs are characterized by bulk insulating behavior but protected conducting states on their edge or surface, due to the combination of spin-orbit interactions and time-reversal symmetry (TRS). A significant amount of theoretical as well as experimental work has been performed on TIs over the past years [32–35]. For $5d$ TM compounds, when both U/t and λ/t are large, many kinds of exotic electronic and magnetic phases may emerge. Such examples include the axion insulator [36, 37], Weyl semimetals (WSM) [38–42], quantum spin liquid (QSL) phases [43–46] etc. The axion insulator, whose surface states are all gapped but the interior still obeys TRS, may exhibit an exotic quantized magnetoelectric effect [47–49] and is one of the most interesting quantum phases predicted for three-dimensional TIs [36]. A Weyl semimetal

is a three-dimensional analogue of graphene, in which the conduction and valence bands cross near the Fermi energy [50, 51]. A QSL phase is an exotic state for a system of strongly interacting magnetic units in which the magnetically ordered ground state is avoided owing to strong quantum fluctuations [52, 53]. In the middle of the phase diagram in Fig. 1.1, there is one region named spin-orbit coupled Mott insulator where the insulating behavior originates from a subtle interplay of SO interactions and electronic correlations. For example, in the iridate compound Sr_2IrO_4 [13, 54], without inclusion of SOC, the width of the Ir t_{2g} bands is so large that local density approximations with a reasonable correlation energy (U) can not account for the experimentally observed band gap. With inclusion of SOC, the t_{2g} manifold is split, into $j = 3/2$ and narrow half-filled $j = 1/2$ bands, and the application of a small U induces a finite Mott-like gap in the $j = 1/2$ levels. In such materials, λ and U tend to cooperate in generating insulating states.

1.2   *Ab initio* **quantum chemistry methods for solids**

The main purpose of *ab initio* simulations is to solve the many-body Schrödinger equation for getting the total energy and wave-function or the electron density of the system under study, which normally is the starting point for investigating material properties. There are many different *ab initio* approaches. In principle, *ab initio* approaches can be categorized as wave-function based methods, for example, quantum chemistry methods and quantum Monte Carlo, and density functional theory (DFT) based methods.

The most widely used approach for investigating the electronic structure of condensed matter systems is the DFT within the local density approximation (LDA) or generalized gradient approximation (GGA) [55]. In the DFT approach, the translational symmetry of the solid is exploited by means of periodic boundary conditions. The core idea of DFT is that all of the properties of the investigated system in its ground state can be accessed if the electron density is known. This drastically reduces the number of electronic variables in solving the Schrödinger equation, from three times the total number of electrons in a given system to only three, and therefore reduces the computational cost of DFT calculations as compared with other methods [56]. DFT has been proved to be very successful in describing a variety of compounds in condensed matter systems, especially in estimating properties like lattice parameters, elastic constants, dielectric functions and phonon frequencies of weakly correlated systems within a few percent of the experimental values [57]. However, the deficiencies of DFT are also well documented. One prominent example is that DFT meets problems in correctly describing systems which contain d or f elements where the electrons are strongly correlated [58–60]. Whereas the electronic structure of pure transition metals (e.g., iron and nickel), in which the $3d$ electrons are itinerant, can be described quite well within the GGA, the electronic structure of insulating TM oxide compounds, in which the $3d$ electrons undergo localization due to the strong onsite Coulomb repulsion, are often wrongly predicted to be metallic within the GGA. A well-known example is NiO: an insulator with the rock salt structure that the GGA predicts to be a metal. Although some of the limitations of DFT can be to some extent overcome by using various types

of refinements, such as DFT+dynamical-mean-field theory (DMFT) [59] or the DFT+U approach [61, 62], the use of parameters like the on-site Coulomb repulsion U restricts the predictive power.

By contrast, wave-function based quantum chemistry methods, which usually start from Hartree-Fock (HF) and next consider electron correlation in a systematic manner, provide an alternative. Such methods have been extensively applied for calculating molecular electronic structures in the theoretical chemistry community [63]. The difficulty with these wave-function approaches is that the treatment of large condensed-phase systems is extremely expensive computationally. Therefore, applying quantum chemistry to condensed matter is not straightforward, but it is something that is becoming increasingly popular. Over the last few decades, algorithms based on many-body second-order perturbation theory [64–70] and multireference configuration interaction formalisms [71, 72] have been developed to explicitly treat electron correlations in solids. A new method based on quantum Monte Carlo, full configuration interaction quantum Monte Carlo (FCIQMC), has been also proposed for solids recently [73].

In order to get a rigorous treatment of electron correlation in crystalline solids, the embedded cluster approach is a very attractive option. Its main idea is to treat explicitly only a small part of the solid with advanced many-body calculations while the rest of the system is dealt with at a more approximate level. Many different embedding schemes have been proposed over the past decades [74, 75]. One of the simplest embedding schemes is point-charge electrostatic embedding, where the cluster is placed inside a matrix of point charges that is fitted to reproduce the effective Madelung potential associated with the solid state environment. The localized character of valence electrons in TM oxides together with the localized nature of electron correlations [76] makes such an embedded-cluster approach widely applicable. This approach has been used to provide accurate estimates and predictions for different properties, such as d-d excitations [77–79], core level spectra [80, 81] and the strengths of magnetic interactions in many TM oxides with accuracy close to experimental results [82–86]. In more advanced embedding schemes, a more accurate representation of the extended solid-state surroundings can be achieved by building an effective potential that takes into account interactions beyond basic electrostatics [74, 75], via prior periodic HF [71, 87–89] or DFT calculations [88, 90–92].

1.3   RIXS spectroscopy

Spectroscopy studies material properties via the interaction between light and matter. By tuning the photon energy, various information can be extracted for the studied system. There are three spectral ranges of electromagnetic radiation that we are interested in: infrared (IR), optical till vacuum ultraviolet (VUV) and X-ray range. Photons with energy between approximately 1.24 meV and 1.7 eV are referred to as infrared radiation [93], which can probe the molecular vibrations, low energy electron transitions and collective magnon excitations. The energy region from optical till VUV is from 1.7 eV to 124 eV [93]. It allows to detect electron transitions from valence and inner valence shells. The X-ray domain includes photons with energy between 124 eV and 124 keV [93], which can be divided into soft (124 eV to 1 keV) and hard X-ray (1−10 keV).

These terms, "soft" and "hard", are used to quantitatively describe the penetrating ability of the photons. The X-ray radiation can be used to measure the excitation and ionization of electrons from core-shell orbitals.

X-ray spectroscopy comprises several well-established experimental techniques and has been growing with the continuous progress of technology, triggered also by large investments in this field. Among numerous X-ray techniques, resonant inelastic X-ray scattering (RIXS) is a powerful method for the investigation of the electronic properties of materials. With the advent of high resolution spectrometers, RIXS has been increasingly used in the soft X-ray regime for probing the low energy excitations of correlated materials. Here the word "resonant" simply means that the incident photon energy is tuned to a certain absorption edge, resulting in significant resonant enhancement of the electronic excitations. In addition, selection of the absorption edge and polarization can provide useful information on electronic states. For $3d$ TM compounds, one can either excite the $2s/2p$ electrons with photon energy in the range of $400-1000$ eV or the $1s$ electrons with energies of $4-10$ keV. In RIXS processes, when a system absorbs an incident X-ray photon, a core-electron is promoted to an unoccupied orbital, forming a core-excited state. This is a short-lived intermediate state on femtosecond time scale, which decays to an excited final state. The shape of RIXS spectra is very sensitive to the excitation energy, photon incident angle and polarization, which allows one to adjust the experiment to study different phenomena and properties of a given system. Chapter 8 of this thesis refers to theory development for calculating the RIXS double differential cross section, which can be directly compared with experimental RIXS spectra.

1.4   Overview of this thesis

To explore the exciting physics of TM compounds, it is essential to identify the ground state, to quantify the d-shell splittings of TM ions and the different coupling strengths and energy scales. The purpose of this thesis is to exploit the power of *ab initio* quantum chemistry methods in investigating the electronic structure and magnetic properties of crystalline $3d$ and $4d/5d$ TM compounds and for providing reliable estimates for relevant physical quantities. This thesis is organized as follows:

— In Chapter 2, the many-body quantum chemical methods employed for the study of strongly correlated systems in this work are outlined.

— In Chapter 3, we report results for the spin-Peierls compound $TiPO_4$ (Ti^{3+}, $3d^1$), including d-d splittings, nearest-neighbor (NN) and next nearest-neighbor (NNN) Heisenberg interactions. The d-d splittings and NN Heisenberg interactions are compared with those extracted from RIXS experiments.

— In Chapter 4, we explore the electronic structure and magnetic anisotropy of Fe^{1+} d^7 and Fe^{2+} d^6 species within the Li_3N lattice. Our results for the axial magnetic anisotropy are in excellent agreement with experiment. Moreover, our computational data suggest that the TM 2+ valence state dominates in the very dilute TM:Li_3N system, while TM 1+ plays a dominant

role for large concentrations of TM ions.

— In Chapter 5, the electronic structure and magnetic properties of $4d^1$ and $5d^1$ ions in molybdenum- and osmium-based double-perovskite systems [Ba_2YMoO_6, $Ba_2(Li, Na)OsO_6$] are discussed. We first provide reliable results for the d-level splittings, $t_{2g}-e_g$ and induced by SOC within the t_{2g}^1 manifold. We further analyse the role of TM $d-O$ p orbital mixing plus the strength of electron-lattice couplings. Our results demonstrate the subtle interplay of spin-orbit interactions, covalency and electron-lattice couplings as the major factor in deciding the nature of the magnetic ground states of $4d$ and $5d$ quantum materials.

— In Chapter 6, we present a study of the osmate compound $NaOsO_3$ (Os^{5+}, $5d^3$). We first discuss results for the d-level excitations. The calculated two-site magnetic spectrum is then mapped to an effective Hamiltonian with both isotropic Heisenberg interaction and antisymmetric Dzyaloshinskii-Moriya (DM) exchange.

— In Chapter 7, we map the magnetic spectrum obtained from quantum chemistry calculations for face-sharing [Ir_2O_9] and [Rh_2O_9] units onto an appropriate effective spin Hamiltonian, providing estimates for the strengths of the isotropic and anisotropic interactions in such iridate and rhodate compounds.

— In Chapter 8, we describe a computational scheme for obtaining absolute RIXS intensities. It is based on *ab initio* quantum chemistry methods and we apply it to the calculation of Cu^{2+} d^9 L_3-edge spectra in $KCuF_3$. A similar scheme is further used for the more complex Ni^{2+} d^8 L_3-edge excitations in La_2NiO_4.

— Finally, a short summary of the whole thesis and an outlook for future research directions is presented.

Chapter 2

Theory and Methods

Computational physics is a valuable tool that helps us understand fundamental physical problems by using computers and allows one to investigate the inner structure and properties of atoms, molecules and solids. One approach is the *ab initio* calculations, which means in Latin "from the beginning". A calculation is said to be *ab initio* if it relies on basic and established laws of nature without additional assumptions or special models. A wide range of *ab initio* methods are based on solving the Schrödinger equation for a given molecule. Once this equation is solved, a variety of chemical and physical properties can be determined directly from basic principles without using experimental data. Of course, such computations are far from trivial. Since the Schrödinger equation cannot be solved analytically for most systems, approximations have to be used.

In this chapter, we give a short overview of the quantum mechanical concepts and equations employed in this work. After comparing briefly the strategies of density functional theory (DFT) and quantum chemistry methods for investigating of electronic structure, we justify the use of quantum chemistry methods. The construction of many-electron wave-functions, starting from the Hartree-Fock (HF) level to multireference configuration interaction (MRCI) methods, is explained in some detail. A few representative equations for describing relativistic effects are then introduced. A detailed mathematical description of the various computational methods described in this chapter can be found in Ref. [63].

2.1 Introduction

The correct description of the electronic energy of a given system requires the wave-function or at least the electron density associated with a particular quantum state. Various methods have been developed throughout the years to find approximate solutions for the electronic Schrödinger equation. In principle, a quantum mechanical calculation classifies as wave-function-based (WFB) or electron-density-based (EDB) calculation. Computing exact wave-functions or electron densities is highly desirable, but it is limited in practice to only a small number of simple systems. Several models that allow the construction of approximate wave-functions and electron densities have been developed. The approximations used in these models have a hierarchical structure which permits the theory to be applied at levels of increasing sophistication and

accuracy. In practice, if we compare WFB methods and EDB theory, there is no better one than another for all purposes, and the successful application of a particular one strongly depends on the physics of the studied system.

In transition metal (TM) compounds the electron-electron interactions play an essential role. The calculations based on conventional DFT within the local density approximation (LDA) or generalized gradient approximation (GGA) have difficulties in predicting the correct insulating ground state (GS) of TM systems. The main reason for these difficulties is that these methods adopt a mean-field like approach, i.e., the Kohn-Sham scheme [94] to treat electron-electron interactions [60, 95]. This implies mapping a fully interacting system onto a non-interacting system whereby the electrons move within an effective, averaged potential. LDA+U [61, 96, 97] and LDA+DMFT (the LDA results are imported into constructing the lattice Green's function and the results are further used to solve the corresponding lattice model within dynamical mean field theory (DMFT)) [60, 98] are commonly used to account for correlation effects in insulating TM systems. The LDA+U method treats electronic correlation by adding an on-site Hubbard U term to the Kohn-Sham Hamiltonian. It is possible to estimate U using the constrained LDA [99, 100] or the constrained random-phase approximation (cRPA) method [101]. It is worth pointing out that in LDA+U and LDA+DMFT approaches double counting needs to be avoided. The double counting arises because LDA does not include all the interactions between strongly correlated d or f electrons, it captures some portion of them through the Hartree and exchange-correlation terms. The systematic way of expressing LDA contribution to exchange correlation energy in the DFT is not given explicitly. It is difficult to identify which part of interactions entering Hubbard correction (+U) or DMFT is already taken into account through LDA calculations. The expression for the double counting correction in LDA+U or LDA+DMFT is not rigorous defined. This leads to the problem that some contributions to the interactions are included twice in Hubbard correction or DMFT formalisms. Nevertheless, qualitative description can be obtained also with approximate parameters like Hubbard U and Hund's coupling J_H and properly accounting for the double counting [60, 102].

Wave-function-based methods provide an alternative route of dealing with electron-electron interactions. In most of these methods, the HF approximation is used as the starting point to construct the real space wave-function. The HF method approximates the N-electron wave-function as a product of N one-electron wave-functions. It is incapable of providing a robust description of behaviors in which electronic correlation has a major role. Nevertheless, the HF wave-function can be systematically improved to include electronic correlation effects using the post-HF quantum chemistry methods. Such an approach has been extensively used in the molecular chemistry community for several decades [63]. However, for solids, the key problem has been the development of treatments of electronic correlation having favourable scaling of the computational cost with the size of the system. It is only recently that algorithms have been developed to explicitly treat electronic correlations in solids using quantum chemistry methods [103, 104]. With nowaday computational facilities, computational schemes based on the MRCI approach and many-body second-order perturbation theory show the ability to describe electronic correlation also in solid-state systems [71, 77, 105].

In the remaining part of this chapter, our goal is to briefly explain the basic principles behind the quantum chemistry methods that we employ in our calculations. We first discuss the approximations used to construct the many-electron correlated wave-function, then introduce theoretical aspects on relativistic spin-orbit interactions. We further describe the point-charge (PC) embedding method for cluster calculations.

2.2 Approximations for many-electron correlated system

2.2.1 The Born-Oppenheimer approximation

One of central goals in electronic structure theory is to find an approximate solution to the many-particle Schrödinger equation. The Hamiltonian of a many-body solid-state system consisting of nuclei and electrons can be written as:

$$
\begin{aligned}
H_{tot} &= -\sum_{I} \frac{\hbar^2}{2M_I} \nabla_{\mathbf{R}_I}^2 - \sum_{i} \frac{\hbar^2}{2m_e} \nabla_{\mathbf{r}_i}^2 + \frac{1}{2} \sum_{I \neq J} \frac{1}{4\pi\epsilon_0} \frac{Z_I Z_J e^2}{|\mathbf{R}_I - \mathbf{R}_J|} \\
&\quad + \frac{1}{2} \sum_{i \neq j} \frac{1}{4\pi\epsilon_0} \frac{e^2}{|\mathbf{r}_i - \mathbf{r}_j|} - \sum_{I,i} \frac{1}{4\pi\epsilon_0} \frac{Z_I e^2}{|\mathbf{R}_I - \mathbf{r}_i|},
\end{aligned}
\tag{2.1}
$$

where the indexes I, J refer to nuclei, i, j refer to electrons, m_e is the electron mass, M_I is the mass of nucleus I, Z_I is the atomic number of nucleus I, R_I and r_i are positions of the nucleus and electron, respectively. In Eq.(2.1), the first term is the kinetic energy of the nuclei, the second term is the kinetic energy of the electrons, the third term is the potential energy coming from nucleus-nucleus Coulomb interactions, the fourth term is the potential energy concerning electron-electron Coulomb interactions and the last term is the potential energy concerning nucleus-electron Coulomb interactions. Everything about the system will be known if one can solve the above fundamental Schrödinger equation. However, since it is impossible to solve this equation analytically for most systems, approximations have to be used.

The first approximation to be made is to decouple the electronic and ionic degrees of freedom. According to the Born-Oppenheimer (BO) approximation [106, 107], introduced by Born and Oppenheimer in 1927, since the nuclei are much heavier and move much slower than the electrons, the movements of nuclei and electrons can be separated. In other words, it is often reasonable to consider the positions of the nuclei as fixed when we consider the movement of electrons. Therefore, the total wave-function can be written as:

$$
\Psi(\{\mathbf{R}_I\}, \{\mathbf{r}_i\}) = \Theta(\{\mathbf{R}_I\})\phi(\{\mathbf{r}_i\}, \{\mathbf{R}_I\}),
\tag{2.2}
$$

where $\Theta(\{\mathbf{R}_I\})$ stands for the wave-function of nuclei for which the positions are fixed and $\phi(\{\mathbf{r}_i\}, \{\mathbf{R}_I\})$ stands for the corresponding wave-function of the electrons with fixed nuclei positions.

Now we can consider that the electrons are moving in a static external potential V_{ext} formed by the nuclei. Thus the corresponding electronic Hamiltonian reads

$$
H = T_e + V_{ee} + V_{ext} + E_{nn},
\tag{2.3}
$$

where T_e is the kinetic energy of the electrons, V_{ee} is the electron-electron interaction, V_{ext} is the electron-nuclei interaction and the last term E_{nn} is the nuclei-nuclei Coulomb interaction which is a fixed energy in this frozen nuclei approximation (for electronic calculations, the internuclear distances are treated as constant parameters, and so this term can be omitted). By setting the fundamental constants $\hbar = m_e = |e| = 4\pi\epsilon_0 = 1$, the corresponding N-electron Schrödinger equation and the full electronic Hamiltonian read

$$\left\{ -\sum_{i=1}^{N} \frac{1}{2}\nabla_i^2 + \frac{1}{2}\sum_{i\neq j}^{N} \frac{1}{|\mathbf{r}_i - \mathbf{r}_j|} - \sum_{I,i} \frac{Z_I}{|\mathbf{R}_I - \mathbf{r}_i|} \right\} \Psi(\mathbf{r}_1,\ldots,\mathbf{r}_N) = E\Psi(\mathbf{r}_1,\ldots,\mathbf{r}_N), \tag{2.4}$$

$$H = -\sum_{i=1}^{N} \frac{1}{2}\nabla_i^2 + \frac{1}{2}\sum_{i\neq j}^{N} \frac{1}{|\mathbf{r}_i - \mathbf{r}_j|} + \sum_{I,i} \frac{Z_I}{|\mathbf{R}_I - \mathbf{r}_i|}. \tag{2.5}$$

The wave-function for N electrons in Eq.(2.4) is a function of $3N$ spatial coordinates (and N spin coordinates) and its solution is extremely complicated and demanding in case of large systems.

2.2.2 The Hartree-Fock approximation

As indicated in Eq.(2.4), electrons interact with each other by electrostatic repulsion, thus the wave-function is not strictly separable into parts related to single electrons. One approximation for getting N-electron wave-functions is given by the HF method [108]. The HF method consists of approximating the many-electron wave-function by appropriate products of single-electron wave-functions. The Pauli exclusion principle, which requires the many-electron wave-function to be antisymmetric with respect to the interchange of the coordinates of any two electrons, should be also fulfilled:

$$\Psi(\mathbf{x}_1,\ldots,\mathbf{x}_i,\ldots,\mathbf{x}_j,\ldots,\mathbf{x}_N) = -\Psi(\mathbf{x}_1,\ldots,\mathbf{x}_j,\ldots,\mathbf{x}_i,\ldots,\mathbf{x}_N). \tag{2.6}$$

Here, we use $\mathbf{x}_i$ to denote both the spin σ_i and position $\mathbf{r}_i$ coordinates. The way to construct such a product is to use the so called Slater determinant, which can be expressed in terms of a determinant of a matrix containing the single particle states:

$$\Psi(\mathbf{x}_1,\ldots,\mathbf{x}_N) = \frac{1}{\sqrt{N!}} \begin{vmatrix} \psi_1(\mathbf{x}_1) & \psi_2(\mathbf{x}_1) & \ldots & \psi_N(\mathbf{x}_1) \\ \psi_1(\mathbf{x}_2) & \psi_2(\mathbf{x}_2) & \ldots & \psi_N(\mathbf{x}_2) \\ \vdots & \vdots & \ddots & \vdots \\ \psi_1(\mathbf{x}_N) & \psi_2(\mathbf{x}_N) & \ldots & \psi_N(\mathbf{x}_N) \end{vmatrix}. \tag{2.7}$$

In Eq.(2.7), $1/\sqrt{N!}$ is a normalizing factor so that $\int |\Psi|^2 d\tau = 1$. It is easy to understand why the use of this determinant automatically takes into account the Pauli principle: if two electrons are in the same state, $\psi_i = \psi_j$, then two columns of the determinant would be equal and thus $\Psi=0$, in other words, $\psi_i = \psi_j$ is physically impossible. For the same reason, two electrons with the same spin can not occupy the same point in space. The antisymmetry property is also easy to see. If we interchange $\mathbf{x}_i$ and $\mathbf{x}_j$, then two rows of the determinant are interchanged, so that Ψ changes sign. All physical properties of the system in state Ψ depend only quadratically on Ψ,

so the physical properties are unaffected by the change of sign caused by the interchange of the two electrons. Using the Dirac notation, we can write the energy of a given system as

$$E = \langle \Psi | H | \Psi \rangle, \tag{2.8}$$

where H is give by Eq.(2.5), disregarding the nucleus-nucleus interactions. If the energy is evaluated in a state of the form (2.7), with orthonormal single electron wave-functions $\psi_1 \ldots \psi_N$, then the result is:

$$E = \sum_i^N \langle \psi_i(\mathbf{x}_i) | \hat{h} | \psi_i(\mathbf{x}_i) \rangle + \frac{1}{2} \sum_i^N \sum_j^N \langle \psi_i(\mathbf{x}_i) | \hat{J}_i - \hat{K}_i | \psi_i(\mathbf{x}_i) \rangle, \tag{2.9}$$

where the single-particle operator $\hat{h}$, Coulomb operator $\hat{J}_i$ and exchange operator $\hat{K}_i$ are defined as:

$$\hat{h}(\mathbf{x}_i) = -\frac{1}{2}\nabla_i^2 + \sum_I \frac{Z_I}{|\mathbf{X}_I - \mathbf{x}_i|} = -\frac{1}{2}\nabla_i^2 + V_{ext}(\mathbf{x}_i), \tag{2.10}$$

$$\hat{J}_i \left| \psi_j(\mathbf{x}_1) \right\rangle = \left\langle \psi_i(\mathbf{x}_2) \left| \frac{1}{|\mathbf{r}_1 - \mathbf{r}_2|} \right| \psi_i(\mathbf{x}_2) \right\rangle \left| \psi_j(\mathbf{x}_1) \right\rangle, \tag{2.11}$$

$$\hat{K}_i \left| \psi_j(\mathbf{x}_1) \right\rangle = \left\langle \psi_i(\mathbf{x}_2) \left| \frac{1}{|\mathbf{r}_1 - \mathbf{r}_2|} \right| \psi_j(\mathbf{x}_2) \right\rangle \left| \psi_i(\mathbf{x}_1) \right\rangle. \tag{2.12}$$

Then, a Fock operator $\hat{F}$ can be defined as:

$$\hat{F} = \hat{h} + \sum_{i=1}^N (\hat{J}_i - \hat{K}_i). \tag{2.13}$$

The single-particle operator $\hat{h}$ denotes the single-particle kinetic energy and the Coulomb interaction energy between the electrons and the nuclei. The Coulomb operator $\hat{J}$ takes into account the Coulombic repulsion between electrons and the exchange operator $\hat{K}$ represents the modification of this energy due to the effects of spin correlation.

We should find the wave-function that minimizes the energy E while ensuring that the spin-orbitals stay orthonormal. This amounts to a problem of optimization under constraints, which can be solved with the method of Lagrange [109] by defining the following function $\mathcal{L}$,

$$\mathcal{L} = E - \sum_{i,j} \lambda_{i,j} \left[\left\langle \psi_i | \psi_j \right\rangle - \delta_{i,j} \right], \tag{2.14}$$

where $\lambda_{i,j}$ are the Lagrange multipliers. Taking the derivative of the these equations to impose $\delta\mathcal{L} = 0$ leads to the HF equations:

$$\hat{F}\psi_i = \epsilon_i \psi_i. \tag{2.15}$$

Here ϵ_i is the energy of spin orbital ψ_i. Eq.(2.15) is for a single particle, not for all N particles, and the effects of all the other particles are included in the Fock operator $\hat{F}$.

The HF equations (2.15) appear as being simple but when inserting the precise form of the different operators, it becomes clear that they are complicated integro-differential equations that in most practical cases cannot be solved exactly. Therefore, simplified approaches are required.

To solve the resulting equations (2.15) numerically, we can express molecular orbitals (MOs) as a linear combinations of atomic orbitals (LCAO). In this procedure, a set of N basis functions $\{\chi(\mathbf{r})\}$, which are simple analytical one-electron Gaussian or Slater type functions, is introduced, and each spatial wave-function $\phi_k(\mathbf{r})$ is expressed as a linear combination of these basis functions,

$$\phi_k(\mathbf{r}) = \sum_{\mu=1}^{N} C_{\mu k}\, \chi_\mu(\mathbf{r}). \tag{2.16}$$

The solution of the HF equations now requires finding the values of the coefficients $\{C\}$ in order to obtain the best expression for the orbitals $\phi_k(\mathbf{r})$. Using matrix notation, the HF equation can be rewritten in terms of the coefficients $\{C\}$ as:

$$\mathcal{F}\mathcal{C} = \mathcal{S}\mathcal{C}\epsilon, \tag{2.17}$$

where $\mathcal{C}$ is the matrix of coefficients $\{C\}$, ϵ is the diagonal matrix of orbital energies, $\mathcal{S}$ is the overlap matrix between two basis functions and $\mathcal{F}$ is the Fock matrix, with elements

$$\mathcal{S}_{\mu'\mu} = \left\langle \chi_{\mu'}(\mathbf{r}) \middle| \chi_\mu(\mathbf{r}) \right\rangle, \qquad \mathcal{F}_{\mu'\mu} = \left\langle \chi_{\mu'}(\mathbf{r}) \middle| \hat{F} \middle| \chi_\mu(\mathbf{r}) \right\rangle. \tag{2.18}$$

This form of the HF equations is called the Roothan equation and can be solved by diagonalizing $\mathcal{F}$:

$$|\mathcal{F} - \mathcal{S}\epsilon| = 0. \tag{2.19}$$

Such an equation cannot be solved directly because the matrix elements $\mathcal{F}_{\mu'\mu}$ involve integrals over the Coulomb and exchange operators which themselves depend on the spatial wave-functions. This means that it can only be solved using a self-consistent procedure: starting from an initial guess for the orbitals, one generates the Fock matrix then a new set of coefficients $\{C\}$ is obtained by solving Eq. (2.17). These coefficients $\{C\}$ can be used in generating a new set of orbitals, with which a new Fock matrix is constructed and solved again for an updated $\{C\}$ matrix. This procedure is repeated until the orbitals and total energy no longer change within certain thresholds, at which point the orbitals fulfill the HF equations in Eq. (2.17).

2.2.3 Basis sets

The choice of an appropriate method is not the only factor that influences the accuracy of an *ab initio* calculation. As we have seen in Eq.(2.16), the molecular orbitals are generated as an expansion in a set of simple basis functions. However, a complete basis set means that an infinite number of functions must be used, which is impossible in actual calculations. The choice of basis functions is therefore important and the basis functions partly determine the quality of the wave-function. For instance, it may happen that a basis set with a small number of functions could give erroneous results regardless of the level of theory employed, whereas using a basis set with sufficient number of functions may yield qualitatively (or even quantitatively) correct results already at the multiconfiguration self-consistent field (MCSCF) level of theory. As a general rule of thumb, increasing the number of functions in the basis set allows a better description of the MOs and more accurate calculations. However, not all basis functions contribute equally

to the description of the MOs: a reasonably accurate description of MOs can be obtained if the functions included in the basis set are chosen properly.

There are two types of basis sets functions commonly used in electronic structure calculations: Slater-type orbitals (STO) [110], which are usually based on spherical harmonic functions and Gaussian-type orbitals (GTO) [111], which are composed of Gaussian functions or contracted Gaussian functions.

In this work, we use GTO basis functions. An GTO centered at an atomic nucleus has the form

$$\chi_p^l(r,\theta,\phi) = Y_{lm}(\theta,\phi)r^l e^{-\zeta r^2}, \tag{2.20}$$

where $Y_{lm}(\theta,\phi)$ are spherical harmonics for the angular momentum quantum number l, r is the distance from the nucleus and ζ are the exponents that are optimized separately for each element. The central advantage of GTOs is that the product of two Gaussian functions at different centres is equivalent to a single Gaussian function centred at a point between the two centres. Therefore, two-electron integrals on three and four different atomic centres can be reduced to integrals over two different centres. The latter are much easier to compute, leading to a significant computational speedup. To further speed up calculations, basis sets need to be contracted, i.e., the contracted GTOs (CGTOs) are composed of atomic orbitals that are expressed as combinations of Gaussian functions

$$\chi_o = \sum_i d_{oi}\chi_p, \tag{2.21}$$

with the contraction coefficients d_{oi} and the parameters of primitive Gaussian function χ_p held fixed during the actual calculation. There are two basic forms of contractions: segmented and general contraction. In a segmented contraction, a given set of primitive functions is partitioned into smaller sets of functions that are made into new contracted functions by determining suitable coefficients [112]. The Pople/Mc-Lean-Chandler basis sets [113, 114] and the Karlsruhe basis sets [115, 116] are some of the most popular segmented contracted GTOs. In a general contraction the primitive functions contribute to all contracted functions, with different contraction coefficients [112].

Modern contracted basis sets aimed at producing very accurate wave-functions often employ a general contraction scheme. The atomic natural orbitals (ANO) and correlation consistent basis sets are of the general contraction type. The idea in ANO type basis sets is to contract a large primitive GTO set to a fairly small number of contracted GTOs by using natural orbitals from a correlated calculation on the free atom, typically at the configuration interaction with singles and doubles (CISD) level [117]. The natural orbitals are those that diagonalize the density matrix.

We use the correlation-consistent basis sets optimized by Dunning *et al.* [118] in most of the calculations in this thesis. The name for these basis sets are commonly abbreviated as **aug-cc-pVmZ**:

— **aug**, meaning "augmented", denotes that the basis set contains diffuse functions, i.e.,

functions with components at large distances r, which increase the flexibility of the basis set.

— **cc-p**, standing for "correlation consistent polarized", means that they include increasingly larger shells of polarization functions (d,f,g,...) with increasing values of **m**.

— **V** indicates they are valence-only basis sets, while the core orbitals are each described by a single function.

— **m** is the number of functions per valence atomic orbital, corresponding to the number of contracted Gaussian type functions used to represent the particular GTOs. It is indicated as "D" (double zeta, m=2), "T" (triple zeta, m=3), "Q" (quadruple zeta, m=4), 5, 6, ...

One advantage of the Dunning basis sets is that they allow for complete basis set (CBS) extrapolation. The basis set used to describe a molecular system should contain a large number of functions to allow maximal flexibility in optimization and to therefore reach the lowest possible energy. Although this is impossible in practice, it is possible to estimate the result that would be obtained with an infinite basis set by performing calculations with cc-pVmZ (or aug-cc-pVmZ) bases of growing size, then extrapolating the results to $m = \infty$. This can be achieved by fitting the results for different values of m with an appropriate function, then extrapolating to $m = \infty$ [119, 120].

2.2.4   The electronic correlation energy

Through the single-configuration representation of the wave-function, HF theory makes the fundamental approximation that each electron moves in the average electric field created by all of the other electrons. It ignores the detailed, correlated motion of the electrons as induced by their instantaneous mutual repulsion. The latter is called dynamical correlation, which can be captured by the CI method. On the other hand, the non-dynamical correlation is important for systems where the ground state is well described with more than one configuration. In such cases the single-configuration HF wave-function is inadequate. This can be corrected by including additional configurations in the wave-function, which is referred to as the multi-configurational self-consistent field (MCSCF) method [63].

There is no clear distinction between dynamical correlation and non-dynamical correlation (or static correlation, in quantum chemical terminology) because both of them require a description beyond a single configuration. It is worth pointing out that in some sense a certain amount of electronic correlation is already considered within the HF approximation in the electron exchange term describing the correlation between electrons with parallel spin. This basic correlation effect prevents two parallel-spin electrons from being found at the same point in space. Since the single-configuration approximation does not take into account the correlation between the spatial position of electrons due to their Coulomb repulsion, it leads to a total electronic energy always above the exact solution of the non-relativistic Schrödinger equation within the BO approximation. The correlation energy is defined as the difference between the exact non-relativistic energy and the HF energy of the electronic system, both calculated in full basis set

[63, 121],

$$E_{corr} = E_{exact} - E_{HF}. \tag{2.22}$$

2.2.5 Configuration interaction

The HF method is often used as a first step to more refined approaches that aim at taking the electronic correlation into account. Solving the HF-Roothaan equations self-consistently will give us $N_b \geqslant N$ orthonormal single-electron orbitals. We occupy the N energetically lowest of those, which results in the HF ground-state wave-function:

$$\Psi_0 = \|\psi_a \psi_b \cdots \psi_l \psi_m \psi_N\|. \tag{2.23}$$

A singly excited determinant corresponds to a configuration for which a single electron in an occupied spin orbital ψ_m has been promoted to a virtual spin orbital ψ_p:

$$\Psi_m^p = \|\psi_a \psi_b \cdots \psi_l \psi_n \cdots \psi_p \cdots \psi_N\|. \tag{2.24}$$

A doubly excited determinant is one in which two electrons have been promoted, one from ψ_m to ψ_p and one from ψ_n to ψ_q:

$$\Psi_{mn}^{pq} = \|\psi_a \psi_b \cdots \psi_l \psi_o \cdots \psi_p \cdots \psi_q \cdots \psi_N\|. \tag{2.25}$$

In a similar manner, we can construct other multiply excited determinants. These determinants are eigenfunctions of the projected spin $\hat{S}_z$ but not of the total spin $\hat{S}^2$. However, a linear combination of the above determinants can be constructed so that they are also eigenfunctions of $\hat{S}^2$ [63]. Such a linear combination of Slater determinants having the same spin symmetry is called a configuration state function (CSF). The exact ground-state wave-function can be expressed as a linear combination of all possible N-electron Slater determinants with the same spin symmetry arising from a complete set of orbitals as

$$\Psi = c_0 \Psi_0 + \sum_{a,p} c_a^p \Psi_a^p + \sum_{ab,pq} c_{ab}^{pq} \Psi_{ab}^{pq} + \sum_{abc,pqr} c_{abc}^{pqr} \Psi_{abc}^{pqr} + \cdots, \tag{2.26}$$

where $\{c\}$ is the set of expansion coefficients. Equation 2.26 can be written in a simpler form as

$$\Psi = \sum_{J=1}^{L} C_J \Psi_J, \tag{2.27}$$

where the coefficients C_J are determined variationally by minimizing

$$E_C = \frac{\langle \Psi | H | \Psi \rangle}{\langle \Psi | \Psi \rangle}. \tag{2.28}$$

This minimization is equivalent to solving a set of secular equations

$$\sum_{J=1}^{L} (H_{IJ} - E S_{IJ}) C_J = 0 \tag{2.29}$$

and as usual

$$H_{IJ} = \langle \Psi_I | H | \Psi_J \rangle, \qquad S_{IJ} = \langle \Psi_I | \Psi_J \rangle. \tag{2.30}$$

The *ab initio* method in which the wave-function is expressed in the form of Eq. (2.26) is called configuration interaction (CI). A full CI approach takes into account every possible excitation of each electron in the total wave-function, and all the CSFs of the appropriate symmetry for a given finite basis set are used in constructing Ψ. In the case of large number of basis set functions and large electron systems, the full CI calculations require a prohibitive amount of resources, hence it is necessary to employ a truncation scheme to keep the computation to a manageable size. Since the two-electron operator $1/|\mathbf{r}_1 - \mathbf{r}_2|$ in Eq.(2.5) cannot affect more than two electrons, Hamiltonian matrix elements between the HF wave-function Ψ_0 and determinants Ψ_J that are more than doubly excited are zero. In addition, Hamiltonian matrix elements between Ψ_0 and all singly exited determinants also vanish[1]. Hence, a widely used approach is to limit the excited determinants to those that are single and doubly excited with respect to Ψ_0. Therefore this method is denoted as singles and doubles configuration interaction (SDCI):

$$\Psi_{SDCI} = c_0 \Psi_0 + \sum_{a,p} c_a^p \Psi_a^p + \sum_{ab,pq} c_{ab}^{pq} \Psi_{ab}^{pq}. \tag{2.31}$$

This is justified by the fact that the configurations corresponding to single and double excitations are those that contribute the most to the dynamical correlation energy, with triple excitations and beyond requiring more computational resources while only yielding diminishing corrections [122].

However, SDCI has a particularly unattractive feature, which is the lack of size-consistency. One of the most popular ways to overcome this problem is the Davidson correction [123], which estimates the CI energy up to quadruple excitations from the CI energy up to double excitations by

$$E_Q = (1 - c_0^2)(E_{SDCI} - E_{HF}), \tag{2.32}$$

where c_0 is the coefficient of Ψ_0 for the normalized truncated SDCI wave-function in Eq.(2.31), E_{SDCI} and E_{HF} are the SDCI and HF energies, respectively.

2.2.6 Multiconfiguration self-consistent field (MCSCF) and multireference CI (MRCI)

The CI method only takes into account excited variations of a single reference configuration, using the orbitals optimized for this configuration. However, many systems involving degenerate or nearly degenerate configurations cannot be accurately described by a single electronic configuration. Therefore, MCSCF methods are necessary.

The MCSCF method expresses the wave-function as a linear combination of a selected set of determinants and optimizes both the CI coefficients C_J in Eq.(2.27) and the LCAO expansion coefficients $C_{\mu k}$ in Eq.(2.16) simultaneously in order to minimize the energy. This simultaneous optimization of both sets of expansion coefficients makes MCSCF calculations computationally demanding. However, by optimizing $C_{\mu k}$, accurate results can be obtained with the inclusion of a small number of selected CSFs.

---

[1] Singly excited determinants do have a small effect on the ground state because they have non-zero matrix elements with doubly excited determinants, which themselves mix with Ψ_0.

The difficulty in setting up an MCSCF calculation is sometimes the selection of the configuration space. The latter can be achieved by the complete active-space self-consistent field (CASSCF) method [63]. In this approach, the molecular orbitals are divided into three classes:

1. The inactive orbitals, composed of the lowest energy orbitals which are doubly occupied in all considered configurations.

2. The virtual orbitals of very high energy which are unoccupied in all configurations.

3. The active orbitals, energetically intermediate between the inactive doubly occupied orbitals and excited virtual orbitals.

The CSFs included in the CASSCF calculations represent all possible ways of distributing the active electrons over the active orbitals.

In the multireference configuration interaction (MRCI) approximation, a MCSCF wave-function is chosen as a reference, from which excited determinants are considered in the subsequent CI calculation. Commonly, all single and double excitations from the reference configurations are included, which is referred to as multireference configuration interaction with singles and doubles (MRSDCI or MRCI(SD)). The wave-function can be written as

$$\Psi_{MRCISD} = \sum_I C^I \Phi_I + \sum_{Sa} C_a^s \Phi_s^a + \sum_{Pab} C_P^{ab} \Phi_P^{ab}, \tag{2.33}$$

where the sum I runs over all selected reference states, a and b denote external orbitals that are unoccupied in the reference configurations, and S and P stand for internal $N-1$ and $N-2$ hole states, respectively. Φ_I, Φ_s^a and Φ_P^{ab} are internal, singly external and doubly external excited electron configurations, respectively.

For systems which can be well described in MCSCF with one configuration (with weight much larger than the weights of all other configurations), the determinants defining the MCSCF expansion (i.e., a few singly and doubly excited determinants from the HF wave-function), combined with the single and double excitations in MRCI(SD) lead to the inclusion of most important determinants up to quadruple excitations. Therefore, the size-inconsistency problem commonly encountered in single-reference CISD is significantly reduced in MRCI(SD). For systems involving degenerate or nearly degenerate states, a MCSCF treatment is required even for obtaining a qualitatively correct description of the electronic structure. By carefully choosing the configurations that are included in the MCSCF expansion, a large fraction of the correlation energy can be recovered in the subsequent MRCI.

2.2.7   Perturbational methods

Normally, dynamical correlation is included through MRCI calculations. However, such an approach has limitations as concerns the size of the systems that can be treated, i.e., the number of electrons and the basis set dimension. Alternatively, electronic correlation can be captured by perturbation theory. In perturbative methods, the Hamiltonian operator consists of two parts,

a zeroth-order $H^{(0)}$ and a perturbation H'. The full Hamiltonian is H_{BO} given by Eq.2.5. The perturbation is formally defined as

$$H' = H_{BO} - H^{(0)} \tag{2.34}$$

and the second-order correction to the energy is

$$E^{(2)} = \sum_k \frac{\left\langle \Psi_k^{(1)} \middle| H' \middle| \Psi^{(0)} \right\rangle \left\langle \Psi^{(0)} \middle| H' \middle| \Psi_k^{(1)} \right\rangle}{E^{(0)} - E_k^0}, \tag{2.35}$$

where $\Psi_k^{(1)}$ is a multiply excited CSF with an expectation value $E_k^0 = \left\langle \Psi_k^{(1)} \middle| H^{(0)} \middle| \Psi_k^{(1)} \right\rangle$. The most widely used perturbational method is the complete active space second-order perturbational scheme (CASPT2) [124]. The zero-order Hamiltonian $H^{(0)}$ is constructed as the sum of one-electron Fock operators which reduces to the Møller-Plesset operator [125] in case of a single-configuration reference wave-function. The first order interacting space is spanned by an internally contracted expansion of all configurations related to single and double excitations from the reference CASSCF wave-function Ψ_0 [124]. Possible near-degeneracies are assumed to have been accounted for at the level of the CASSCF method.

A frequent difficulty with CASPT2 calculations is the so-called intruder-state problem. This happens if the difference between $E_k^{(0)}$ (in the configuration space of the first-order wave-function) and $E^{(0)}$ (in the configuration space of the reference wave-function) becomes very small, i.e. $E_k^{(0)} \approx E^{(0)}$. Then the CASPT2 will not converge or will even blow-up. This problem can be sometimes solved by applying a level shift to $E_k^{(0)}$ such that the near degeneracy is avoided [126, 127]. Another perturbational approach, N-electron valence second-order state perturbation theory (NEVPT2) devised by Angeli and co-workers has the advantage of displaying no intruder states [128, 129]. CASPT2 and NEVPT2 are both very efficient methods for the description of the electronic structure of insulating TM-based materials [130, 131].

2.3 Spin-orbit coupling

So far all of the discussion in this chapter has been based on the Schrödinger equation in a nonrelativistic quantum mechanical framework. Relativistic effects begin to play an important role in heavy atoms and their compounds. This is due to the fact that the relativistic effects on energies and on other physical quantities increase with the fourth power of the nuclear charge Z [132, 133].

Relativistic effects in atoms and molecules may be divided into kinematical effects and effects of spin-orbit coupling (SOC) [134]. Kinematical effects are caused by electrons moving with high velocity in the vicinity of a nucleus. Such effects lead to contracted orbitals and contracted electron density distribution. Connected with this contraction is a lowering of orbital energies and of the total energy if compared to the nonrelativistic calculations. These kinematical effects are important for s and p shells, since these shells have appreciable amplitude in the vicinity of the nucleus. Orbitals with higher angular momentum are hardly directly affected by kinematical relativistic effects. The modified shielding of the nuclear charge by the contracted core

orbitals mainly results in an expansion of the valence d and f orbitals. The relativistic SOC on the other hand gives rise to subshell splittings due to the interaction between orbital and spin. The field dealing with relativistic electronic structure theory of atoms and molecules is often called relativistic quantum chemistry. The latter has been developing rapidly in the last few decades, and more detailed discussion of relativistic effects can be found in Refs. [132, 134, 135].

Relativistic quantum chemistry calculations are much more expensive than the nonrelativistic analogue. This is due to the fact that in relativistic theory one has to consider for every particle also the degrees of freedom for its charge-conjugate particle (the positron in the case of the electrons of an atom or a molecule) on equal footing. The Dirac equation properly describes the motion of spin 1/2 particles using a four-component formulation [136, 137]. In the following, we first discuss briefly the Dirac equation and the Breit-Pauli Hamiltonian that treats electron-electron interactions and relativistic effects on the same footing, then outline the Foldy-Wouthuysen transformation, by which the four-component equation is reduced to a two-component equation for describing the electrons.

The Dirac equation

Work to introduce relativity in the Schrödinger equation has first been started by Klein and Gordon in 1926. Using the relativistic formulation of the kinetic energy, they have derived a relativistic Schrödinger-like equation that actually corresponds to the description of spinless particles [138, 139]. Hence, the Klein-Gordon equation does not include spin degrees of freedom and cannot be considered as a fully relativistic quantum theory. Dirac proposed the equation

$$H^{Dirac}\Psi = (c\boldsymbol{\alpha}\cdot\mathbf{p} + \boldsymbol{\beta}mc^2)\Psi, \tag{2.36}$$

where $\mathbf{p}$ is the momentum operator, $\boldsymbol{\alpha}$ and $\boldsymbol{\beta}$ are 4×4 matrices, $\boldsymbol{\alpha}$ is written in terms of the three Pauli 2×2 spin matrices $\boldsymbol{\sigma}$, and $\boldsymbol{\beta}$ in term of a 2×2 unit matrix $\mathbf{I}$,

$$\boldsymbol{\alpha}_{x,y,z} = \begin{pmatrix} 0 & \boldsymbol{\sigma}_{x,y,z} \\ \boldsymbol{\sigma}_{x,y,z} & 0 \end{pmatrix}, \qquad \boldsymbol{\beta} = \begin{pmatrix} \mathbf{I} & 0 \\ 0 & -\mathbf{I} \end{pmatrix}, \tag{2.37}$$

$$\boldsymbol{\sigma}_x = \begin{pmatrix} 0 & 1 \\ 1 & 0 \end{pmatrix}, \quad \boldsymbol{\sigma}_y = \begin{pmatrix} 0 & -i \\ i & 0 \end{pmatrix}, \quad \boldsymbol{\sigma}_z = \begin{pmatrix} 1 & 0 \\ 0 & -1 \end{pmatrix}, \quad \mathbf{I} = \begin{pmatrix} 1 & 0 \\ 0 & 1 \end{pmatrix}. \tag{2.38}$$

The Dirac equation is four-dimensional and the relativistic wave-function consequently contains four components. It is conventional to write the relativistic wave-function as:

$$\Psi = \begin{pmatrix} \Psi_{L\alpha} \\ \Psi_{L\beta} \\ \Psi_{S\alpha} \\ \Psi_{S\beta} \end{pmatrix}. \tag{2.39}$$

Here Ψ_L and Ψ_S are the large and small components of the wave-function respectively and α and β indicate the spin functions. For electrons, the large component reduces to the solutions of the Schrödinger equation and the small component disappears when $c \to \infty$ (the non-relativistic

limit). The small component of the electronic wave-function corresponds to a coupling with the positronic states.

The Breit-Pauli Hamiltonian

A fully relativistic treatment of more than one particle would have to incorporate many-body effects into the Dirac equation. The simplest way is to include the potential terms that describe the nuclear-electron and electron-electron Coulomb interactions. This leads to the Dirac-Coulomb (DC) Hamiltonian:

$$H^{DC} = \sum_i H_i^{Dirac} + \frac{1}{2} \sum_{i \neq j} \frac{1}{r_{ij}} + \sum_{i,K} \frac{1}{r_{iK}}, \tag{2.40}$$

where r_{ij} denotes the distance between electrons i, j and $r_{iK} = r_i - R_K$ is the position of the ith electron with respect to nucleus K. A Lorenz invariant[2] form of the DC Hamiltonian is the Bethe-Salpeter equation [140, 141], which is essentially a generalisation of the Dirac equation for two particles. The Bethe-Salpeter equation is an integro-differential equation and it features different time variables for the two particles. An approximate relativistic many-electron Hamiltonian can be constructed from the Dirac Hamiltonian by adding the Breit term [142]

$$H_{ij}^{Breit} = -\frac{1}{r_{ij}} \left[\alpha_i \cdot \alpha_j - \frac{(\alpha_i \cdot r_{ij})(\alpha_j \cdot r_{ij})}{2r_{ij}^2} \right], \tag{2.41}$$

that consists of the leading terms in the series obtained from the Bethe-Salpeter equation. This Breit Hamiltonian describes other pairwise additive interactions than the standard Coulomb interaction of electrons i and j, the first term being the magnetic Gaunt term and the second term representing retardation, i.e., the finite speed of interaction. Then, the Dirac-Coulomb-Breit Hamiltonian (DCB) including all relativistic effects on the kinetic energy as well as spin-orbit (SO) interaction is written as

$$H^{DCB} = \sum_i H_i^{Dirac} + \frac{1}{2} \sum_{i \neq j} \frac{1}{r_{ij}} + \sum_{i,K} \frac{1}{r_{iK}} + \frac{1}{2} \sum_{i \neq j} H_{ij}^{Breit}. \tag{2.42}$$

Since only positive energy solutions of the Dirac equation are relevant in electronic structure theory, it would be useful to decouple the positive and negative energy components of Eq.(2.39) to give a two-component equation for the positive energy solutions. Foldy and Wouthuysen [143] introduced a systematic procedure, the Foldy-Wouthuysen (FW) transformation, for decoupling the large and small components by finding a unitary transformation that block-diagonalizes the four-component Hamiltonian. The FW transformation gives rise to the Pauli Hamiltonian [144]

$$H^{Pauli} = V + \frac{p^2}{2} - \frac{1}{8c^2}(p^4 - \nabla^2 V) + \frac{1}{4c^2} \boldsymbol{\sigma} \cdot (\nabla V \times \boldsymbol{p}). \tag{2.43}$$

Here the first two terms correspond to the nonrelativistic Hamiltonian. The third and the fourth terms represent the mass-velocity and Darwin corrections, respectively, also referred to as scalar relativistic (SR) corrections. The last term is the spin-orbit coupling term. Then the Breit-Pauli (BP) Hamiltonian is obtained from the DCB Hamiltonian (2.42) for two-electron systems

---

[2]Lorentz invariance is required by Einstein's theory of special relativity.

through the FW transformation and a generalization of that to N electrons [145, 146]. The spin-orbit part of the Breit-Pauli Hamiltonian can be written as:

$$H_{SO}^{BP} = \sum_i h_i + \frac{1}{2} \sum_{i \neq j} h_{ij}, \tag{2.44}$$

where the one- and two-electron terms are

$$h_i = \frac{1}{4c^2} \sum_K \frac{Z_K}{r_{iK}^3} \boldsymbol{\sigma}_i \cdot (\boldsymbol{r}_{iK} \times \boldsymbol{p}_i), \tag{2.45}$$

$$h_{ij} = -\frac{1}{4c^2} \frac{\boldsymbol{\sigma}_i \cdot (\boldsymbol{r}_{ij} \times \boldsymbol{p}_i) - \boldsymbol{\sigma}_j \cdot (\boldsymbol{r}_{ij} \times \boldsymbol{p}_j)}{r_{ij}^3}$$
$$-\frac{1}{2c^2} \frac{\boldsymbol{\sigma}_i \cdot (\boldsymbol{r}_{ij} \times \boldsymbol{p}_j) - \boldsymbol{\sigma}_j \cdot (\boldsymbol{r}_{ij} \times \boldsymbol{p}_i)}{r_{ij}^3}. \tag{2.46}$$

The one-electron part (2.45) describes the interaction of an electron spin with the potential produced by the nuclei. The first term in the two-electron part (2.46) is the so called 'spin-same orbit' coupling that describes the interaction of the electron with its own orbital momentum and the second term is the 'spin-other orbit' coupling which describes the interaction of an electron spin with the orbital momenta of other electrons.

Dealing with the complicated two-electron part (2.46) in the H_{SO}^{BP} Hamiltonian is computationally quite demanding. In most quantum chemistry packages, e.g., MOLPRO, an efficient method for the calculation of BP spin-orbit matrix elements is to incorporate two-electron contributions of the spin-orbit operator by means of an effective one-electron Fock operator, instead of taking all two-electron contributions explicitly into account [147, 148]. For instance, in the spin-orbit treatment of MOLPRO, the full BP spin-orbit operator is used only for MCSCF wave-functions; for MRCI wave-functions, the full BP operator is used for computing the matrix elements between internal configurations (no electrons in external orbitals), while for contributions of external configurations a mean-field one-electron Fock operator is employed. It was shown that this approximation leads to errors of the order of only 1cm^{-1} [148].

For heavy elements, the effective core potential (ECP) approach is one of the most used approximate methods in relativistic wave-function based quantum chemistry calculations. ECPs have two main advantages. On the one hand, ECPs replace core electrons with properly parameterized potentials, consequently, reduce the number of electrons and basis functions to be treated and focus the computational effort on the valence electrons. Additionally, ECPs allow the inclusion of relativistic effects of core electrons without performing a relativistic treatment explicitly. For example, the ECPs used in this thesis were adjusted in two-component multiconfiguration calculations, using atomic valence-energy spectra from four-component multiconfiguration Dirac-Hartree-Fock calculations as reference data [149, 150].

2.4 Embedded cluster approach

A very simple picture of certain features of the electronic structure of many solid-state materials is given by the ionic model. The latter is based on the assumption that the crystal is constructed

from positive and negative ions which have strong attractive interactions. The cluster method naturally emerges from such an ionic model. Many properties of crystalline solids, for example, effects connected with the existence of isolated defects and impurities in a perfect infinite lattice, molecule–surface interactions, core level excitations, localized electronic states in TM and rare earth materials, etc., are well suited to be investigated by cluster methods. In cluster approaches, one considers that a system contains a target region of limited size but which is surrounded by a much larger "inactive" environment. This environment cannot be simply neglected as it interacts with the target region. Instead, the environment may be approximately described with less accurate but more affordable means, allowing computationally expensive theories to be focused on the target region of interest. In TM oxides, the short-range electronic correlations are important, either intra-atomic correlations, e.g., the so-called Hund's rule coupling, or correlations among electrons on neighboring sites [151]. With a cluster model the electronic structure of TM ions and such short-range correlations can be investigated by standard *ab initio* quantum chemistry methods.

Over the past decades, various embedding schemes based on both semi-empirical and quantum mechanical electronic-structure methods have been developed to ensure a proper connection of the cluster with the rest of the solid, see for example reviews [74] and [75]. In the following, we will first discuss in detail the point charge (PC) embedding scheme that is used in the present thesis, then briefly introduce the HF-based embedding method.

In the PC embedding approximation, the general strategy is to choose a finite atomic cluster and embed this cluster in a set of optimized point charges. The latter should reproduce the electrostatic field in the cluster region arising from ions around the cluster and the rest of the crystal. For the calculations in this work, we use the method proposed in Ref. [152]. The algorithm in this method computes the charge of the ions in the PC array so that the direct sum potential reproduces the Ewald potential. It can be summarized in the following steps [152, 153]:

1. An array of typically 1.0×10^4 PCs at their crystallographic positions and with formal charges is generated using $2M \times 2M \times 2M$ cells.

2. The array is divided into three zones, as shown in Fig.2.1. Zone 1 is defined by the atomic cluster of interest. Zone 2 consists of additional point charges that embed the atomic cluster spherically. Zone 3 is all other PCs.

3. The Ewald potentials are calculated for all sites in zone 1 and 2. These ions in zone 1 and 2 all have formal ionic charges.

4. A system of linear equations is solved to find the zone 3 charge values that make the zone 1 and zone 2 site potentials exactly equal to their Ewald values and the total charge and dipole moment equal zero.

5. The solution is checked at a large number of randomly chosen points within zone 1.

The direct sum potential V_{PC} generated at position $\vec{r}_i$ by PCs can be calculated as a sum over
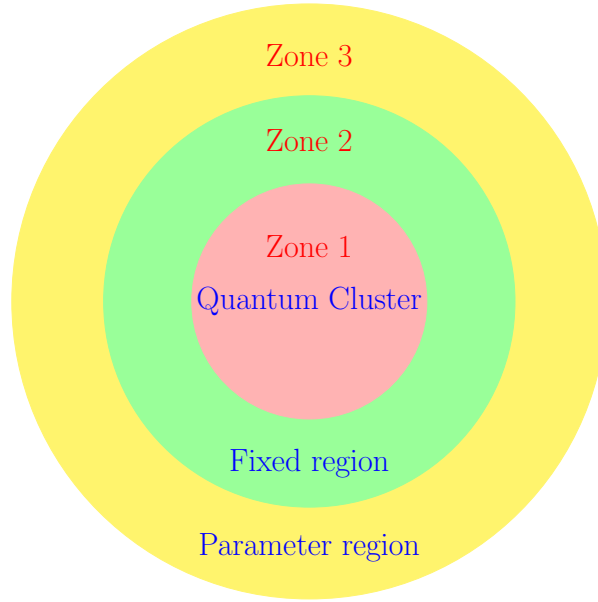
Figure 2.1: Schematic representation of the quantum cluster and the point charge array. Adapted from Ref. [154].

the lattice sites

$$V_{\text{PC}}(\vec{r}_i) = \sum_{j=1}^{N} \frac{q_j}{\left|\vec{r}_i - \vec{r}_j\right|}, \tag{2.47}$$

where N is the total number of atoms considered and q_j refers to the charge located at position $\vec{r}_j$. The Ewald potential V_{Ewald} is calculated according to the formulations given in Refs. [152, 155]. Zone 3 consists of PCs whose values are treated as parameters in the fitting procedure via a system of linear equations. In the latter, the variable is the change of charge (Δq), the ith equation is written as

$$\sum_{k}^{N} \frac{q_k + \Delta q_k}{\left|\vec{r}_i - \vec{r}_k\right|} - V_{\text{Ewald}}(\vec{r}_i) = 0, \tag{2.48}$$

$$N = N_1 + N_2 + N_3, \qquad \Delta q_k = 0, k \leqslant N_1 + N_2, \tag{2.49}$$

$$q_k = \begin{cases} \text{zone 1,} & 1 \leqslant k \leqslant N_1, \\ \text{zone 2,} & N_1 < k \leqslant N_2, \\ \text{zone 3,} & N_2 < k \leqslant N \end{cases} \tag{2.50}$$

and the four extra equations used to make conservation of charge and dipole moment are given by

$$\sum_{k}^{N} \Delta q_k = 0, \qquad \sum_{k}^{N} \Delta q_k \cdot \left|\vec{r}_{k,x}\right| = \sum_{k}^{N} \Delta q_k \cdot \left|\vec{r}_{k,y}\right| = \sum_{k}^{N} \Delta q_k \cdot \left|\vec{r}_{k,z}\right| = 0, \tag{2.51}$$

where N_1, N_2 and N_3 are number of atoms in Zone 1, Zone 2 and Zone 3, respectively.

Using 1000 randomly chosen points in the interior of the cluster the result is checked and the root-mean-square (rms) accuracy is computed

$$\Delta_{\text{rms}} = \left(\frac{\sum_{i}^{Nr} \left[V_{\text{Ewald}}(\vec{r}_i) - V_{\text{PC}}(\vec{r}_i) \right]^2}{Nr} \right)^{1/2}, \tag{2.52}$$

where Nr is the number of randomly chosen points in the cluster, $V_{\mathrm{Ewald}}(\vec{r}_i)$ and $V_{\mathrm{PC}}(\vec{r}_i)$ are the Ewald and direct sum potential at position $\vec{r}_i$, respectively. Δ_{rms} is usually $< 1\mu$V which is within the accuracy needed for quantum cluster calculations.

PC embeddings take into account the effect of the long-range electrostatic interactions of ions in the cluster with the remaining infinite solid. However, at the boundary between the QC cluster and the classical point-charge region, positive charges located next to the cluster cause an artificial polarization of electrons in the cluster due to the lack of short-range repulsion effects of quantum-mechanical nature. We can introduce a buffer region between the charges and the actual cluster in order to improve such deficiencies. This buffer is usually treated quantum-mechanically at the lowest level of approximation. One way is to increase the size of the QC cluster, perform a preliminary HF calculation for the extended cluster and freeze next orbitals centered at the buffer sites. The buffer sites can be also represented by large-core ECP's with no associated valence electrons (referred to as total-ion potentials).

By using prior periodic DFT or HF calculations, a more accurate description of the infinite surroundings including both short- and long-range interactions can be achieved. A detailed discussion of DFT-based frozen density embedding can be found in Refs [75, 156]. In the HF embedding scheme [71, 87, 88, 157, 158], the full system is partitioned into cluster and the embedding parts in real space. The orbital basis entering the post-HF correlation treatment is a set of projected Wannier functions: localized Wannier orbitals are first obtained from prior periodic HF calculations for the infinite crystal and subsequently projected onto the set of Gaussian basis functions associated with the atomic sites of the cluster. An effective embedding potential obtained from the Fock operator in the prior periodic HF calculations is generated for the chosen cluster and models the remaining part of the crystalline lattice. This embedding approach provides a frozen HF environment for the subsequent QC calculations.

In the present thesis, most of the calculations are performed on clusters containing one or two TMO_6 octahedra (as central active region, zone 1) plus all the NN TMO_6 octahedra (corresponding to zone 2) such that all atoms up to the fourth coordination shell of the central TM ion are included in the clusters. The inclusion of the NN octahedra is essential to account for short-range Pauli and exchange interactions of electrons in the central region with electrons distributed around the immediate NN sites. As we shall discuss in several chapters later on, our computational results obtained this way are in good to excellent agreement with available experimental data.

Chapter 3

Crystal-field and magnetic excitations in the spin-Peierls TiPO$_4$ compound

The on-site d-d excitations, the nearest-neighbor (NN) and the next nearest-neighbor (NNN) Heisenberg exchange couplings of the spin-Peierls (SP) TiPO$_4$ compound are discussed in this chapter. We start from analyzing the on-site d-level electron configuration by detailed quantum chemistry (QC) calculations. We find the ground state to be composed of an admixture of d_{z^2} and d_{xz} orbital character, highly unusual for six-fold coordinated d-metal ions. We further compute the NN and the NNN Heisenberg exchange interactions J and J_2, respectively, and study the bond-length dependence of J by changing the NN Ti-Ti distance. The computed d-d excitation energies and the value of J compare very well with resonant inelastic X-ray scattering (RIXS) experimental data.

3.1   Introduction

Understanding the complex interplay of spin, orbital and lattice degrees of freedom in strongly correlated electron systems is one of the most challenging tasks in modern solid state physics. Quasi one-dimensional magnetic systems are of special interest in this regard, displaying very intriguing effects that emerge from the reduced dimensionality, e.g., increased efficiency in solar cells where nanowires are functional centres [159], fractionalisation of an electron's degrees of freedom into several independent quasiparticles [11, 160, 161], large electron-phonon coupling due to poor electronic screening and instability towards Peierls-like dimerization [162].

One important manifestation of such an interplay of degrees of freedom is the SP transition, in which a progressive spin-lattice dimerization occurs in one-dimensional antiferromagnetic (AFM) Heisenberg chains below a critical temperature. Such dimerization induces a singlet ground state with a magnetic gap [163]. The first inorganic SP system CuGeO$_3$ was discovered by Hase *et al.* about two decades ago. In CuGeO$_3$, the magnetic susceptibility rapidly drops to a small, constant value with decreasing temperature below the phase-transition temperature near 14 K [164]. The ratio between the spin gap Δ and the SP transition temperature $2\Delta/T_{SP}$ corresponds to ∼ 3.5, which can be well described by a conventional SP mechanism based on a mean-field Barden-Cooper-Schrieffer (BCS) type relation [165]. Most of the prominent examples of low-dimensional quantum antiferromagnets with exotic magnetic ground states contain
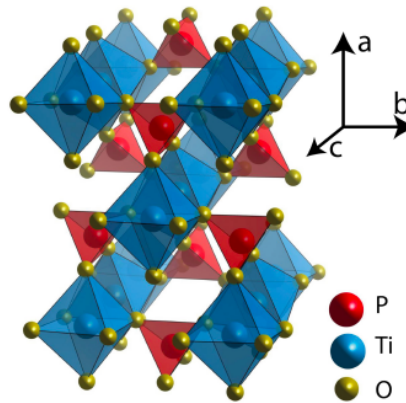
Figure 3.1: Crystal structure of TiPO$_4$, where the dark-blue and the red polyhedra represent TiO$_6$ octahedra and PO$_4$ tetrahedra, respectively. The chains of TiO$_6$ octahedra are along the c axis.

Cu^{2+} ($3d^9$, S =1/2) ions with one hole in the e_g orbitals and have been intensively investigated [166–168]. Compounds of early TM elements with one electron in the $3d$ shell received less attention in this context. If we consider a $3d$ electron in a high-symmetry or only slightly distorted octahedral environment, the partly filled t_{2g} orbitals may exhibit interesting phenomena due to the higher degeneracy (or near degeneracy) and the relative weakness of the Jahn-Teller (JT) coupling [169, 170]. Examples of low dimensional $3d^1$ systems that have attracted special attention are the compounds containing Ti^{3+} ions. TiOX (X=Cl, Br) [171–175], which crystallize in the FeOCl-type structure, have been found to be a more complex case of dimer formation [176, 177] due to the existence of an extended intermediate fluctuation regime for $T > T_{SP}$ with a ratio $2\Delta/T_{SP} \gg 3.5$.

Based on magnetic susceptibility, heat capacity and nuclear magnetic resonance (NMR) measurements, Law *et al.* reported an apparently similar SP scenario in Ti^{3+} $3d^1$ TiPO$_4$, with two successive phase transitions at T_{SP}=74 K and T^*= 111 K. TiPO$_4$ is a structurally one-dimensional compound which crystallizes in the CrVO$_4$ structure [178]. The Ti^{3+} ions, carrying S=1/2 spins, are located in axially compressed TiO$_6$ octahedra which share their edges to form corrugated TiO$_4$ ribbon chains along the c-axis. Each oxygen atom also belongs to a PO$_4$ tetrahedron (see Fig.3.1). Recent studies showed a SP transition with a large ratio $2\Delta/T_{SP} \sim 9$ [12, 179, 180]. Additionally, a very large difference was found between the magnetic exchange couplings J_c extracted from magnetic susceptibility and optical Raman scattering [179]. The large ratio $2\Delta/T_{SP}$ and the discrepancy for the magnetic exchange interactions were ascribed to the coupling of the spin degree of freedom to orbital excitations [179]. In particular, it has been suggested that the Ti orbital degrees of freedom heavily influence the SP transition. The unusual behavior was assigned to an orbital crossover scenario, supported by results from a crystal-field effective model [179] and DFT calculations [180], in which the symmetry of the ground state occupied orbital changes from $d_{z^2-x^2}$ to d_{xy} upon crossing the transition.

In this chapter, we discuss the electronic structure and magnetic interactions of TiPO$_4$ by means of state of the art QC calculations. In the next section, the computational approach we employed and other numerical details are described. The nature of the ground state along with

the calculated d-level excitation energies are presented in Sec.3.2. In Sec.3.3, we discuss the NN Heisenberg coupling J and its dependence on the Ti-Ti distance and we further compute the NNN Heisenberg coupling J_2. In Sec.3.2 and Sec.3.3, we also compare the results with available RIXS measurements. At the end of chapter, we give a brief summary of our findings.

3.2 Ti-ion ground-state configuration and d-level excitations

3.2.1 Computational method

To compute the on-site Ti $d-d$ excitations, an embedded cluster consisting of one central TiO_6 octahedron, the two NN TiO_6 octahedra and the nearby twelve P ions was considered (see Fig.3.2). The solid-state surroundings were modeled as a large array of point charges fitted [154] to reproduce the crystal Madelung field in the cluster region. All *ab initio* calculations were carried out with the QC package MOLPRO [181], using the $Cmcm$ crystallographic unit cell proposed for T = 2 K in Ref. [178].
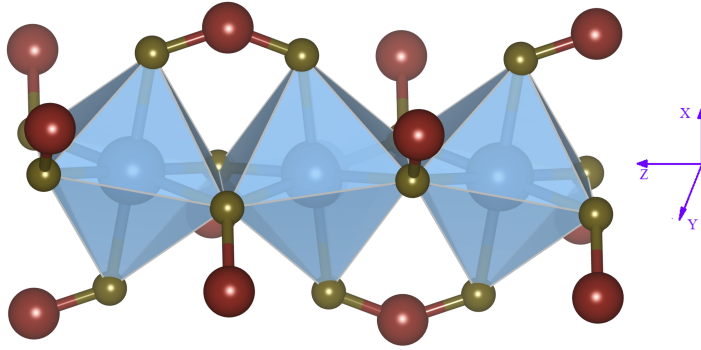
Figure 3.2: The cluster used for the QC calculations in computing the d-level excitations. It consists of a central TiO_6 octahedra and two other adjacent octahedra. Ti, O, P ions are shown in dark-blue, brown and red, respectively. The TiO_6 octahedra are shown in light-blue.

We used all-electron Douglas-Kroll (DK) basis sets of triple-zeta quality for the central Ti ion [182] and all-electron triple-zeta basis sets for the six adjacent O ligands [118], supplemented with polarization functions. For the Ti NN's, we employed effective core potentials (ECP's) [183] along with triple-zeta valence basis functions [184]; minimal atomic-natural-orbital basis sets [117] were applied for those O ions coordinating the NN Ti sites but not shared with the central octahedron. The P species were modeled with large-core ECP's supplemented with valence basis functions of double-zeta quality [185].

The step-by-step procedure followed for the calculation of the ground state electron configuration and of the on-site excitations is outlined below:

1. Firstly, a scalar-relativistic[1] closed-shell Hartree-Fock (HF) calculation was performed on the chosen cluster with the restriction that all the orbitals are doubly occupied. The cen-

---

[1]Scalar-relativistic effects are included by using DK basis sets and effective core potentials.

tral Ti and NN Ti ions were considered to have a closed-shell d^0 configuration in this preliminary HF calculation. The resulting HF orbitals can be separated into different groups by using the Pipek-Mezey localization module [186] implemented in MOLPRO.

2. Next, in a first MCSCF calculation, using the HF orbitals, an active space CAS[3,3] (one electron in one t_{2g} orbital of each Ti ion, i.e., the central Ti site and two NN Ti sites) was considered for a high-spin (S_{tot}= 3/2) configuration in order to get singly occupied t_{2g} orbitals for each Ti ion in the chosen cluster. All other orbitals were also optimized. The localized MCSCF orbitals can be visualized with the Jmol [187] plotting program and then reordered into frozen, inactive and active orbital groups for subsequent MCSCF and MRCI calculations. The $3d$ orbitals of the central Ti and NN Ti sites were considered as active, the O $2p$ orbitals of the central octahedron as inactive[2] orbitals. All other doubly occupied orbitals belonging to the TiO$_6$ octahedra and P sites were frozen in the subsequent CASSCF calculations.

3. In further multiconfiguration calculations, an active space CAS[3, 7] (3 electrons in seven $3d$ orbitals)[3] was considered, in which the NN ground state Ti t_{2g} orbitals were frozen in the active space.

4. In the subsequent MRCI(SD) calculations, used to capture dynamic correlation effects, the active orbitals are the central Ti $t_{2g} + e_g$ orbitals and the ground state t_{2g} orbital of each NN Ti site. The inactive space contains the O $2p$ orbitals of the central octahedron.

5. SOC gives rise to very tiny effects for the $3d$ Ti^{3+} ions we considered here.

3.2.2   Quantum chemistry results versus RIXS data on $d-d$ excitations

QC results and RIXS experimental data for the on-site $d-d$ excitations in TiPO$_4$ are summarized in Table 3.1. Given the C_{2h} point-group symmetry at the Ti site, with the y axis as C_2 symmetry element, the $d_{x^2-y^2}$, d_{xz} and d_{z^2} orbitals belong to the A_g irreducible representation, $\{d_{xy}, d_{yz}\}$ to B_g. The a and b labels in Table 3.1 are used to distinguish between states implying the same irreducible representation. In the scalar-relativistic calculations, at the CASSCF and MRCI levels, for the lower-energy part of the spectrum, the first excitation around 0.4 eV corresponds to the transition between aA_g and aB_g states, and the next excitation around 0.5 eV is identified as a transition between the aA_g and bA_g states. The two higher excited states are at ~1.7 eV and ~2.2 eV. Comparing the CASSCF and MRCI numbers, correlation effects brought by MRCI shift down the excitation energies of the aB_g and bB_g states by 0.06 eV and 0.17 eV, respectively, but shift up the excitation energies of the bA_g and cA_g states by 0.12 eV and 0.21 eV, respectively. The MRCI energy including Davidson corrections rises the relative energies of all excited states by $0.02-0.04$ eV as compared with the MRCI results. While in other TM oxides [77, 158] it is rather clear that the corrections brought by the CI treatment mainly imply ligand to TM charge transfer effects, a clear interpretation is not straightforward here.

---

[2]These orbitals are doubly occupied but still optimized in the subsequent CASSCF calculation.

[3]One electron for each Ti ion, five d orbitals for the central Ti ion and one t_{2g} orbital for each NN Ti site.

Table 3.1: Ti^{3+} $d-d$ excitation energies in TiPO$_4$ obtained from CASSCF and MRCI calculations as compared to RIXS experimental results [190]. The MRCI values including Davidson corrections [63, 123] are denoted as CISD(Q). Notations according to C_{2h} symmetry are used for denoting the states. The composition of the $3d^1$ wave-functions at the MCSCF level is also provided. The local coordinate system $\{x, y, z\}$ and the ground state wave-function are shown in Fig. 3.2 and Fig. 3.3, respectively.

$3d^1$ states	Relative energies (eV)				wave-function composition (normalised weights, %)
	CASSCF	MRCI	CISD(Q)	RIXS	
aA_g	0.00	0.00	0.00	0.00	$2\,\vert\,d_{x^2-y^2}\rangle + 42\,\vert\,d_{xz}\rangle + 56\,\vert\,d_{z^2}\rangle$
aB_g	0.44	0.38	0.42	0.420 ± 0.02	$91.5\,\vert\,d_{xy}\rangle + 8.5\,\vert\,d_{yz}\rangle$
bA_g	0.45	0.57	0.59	0.533 ± 0.10	$27\,\vert\,d_{x^2-y^2}\rangle + 48\,\vert\,d_{xz}\rangle + 25\,\vert\,d_{z^2}\rangle$
bB_g	1.87	1.70	1.72	1.75 ± 0.02	$8.5\,\vert\,d_{xy}\rangle + 91.5\,\vert\,d_{yz}\rangle$
cA_g	2.00	2.21	2.24	2.55 ± 0.03	$71\,\vert\,d_{x^2-y^2}\rangle + 10\,\vert\,d_{xz}\rangle + 19\,\vert\,d_{z^2}\rangle$

It is seen that the many-body QC calculations yield a ground-state wave-function of mainly d_{xz} and d_{z^2} character (see Table 3.1). Considering the C_{2h} point-group symmetry with the y axis as C_2 symmetry element at the Ti site, also $d_{x^2-y^2}$ can actually mix with d_{xz} and d_{z^2}, which is indeed found in the QC results (See Fig.3.3). The "stabilisation" of the d_{xz} and d_{z^2} levels as main "contributors" to the $3d^1$ ground state of TiPO$_4$ is likely related to the large positive ionic charge at P sites in the xz plane (defining the shortest Ti-P links) and of Ti nearest-neighbors along the z axis. Similar kind of electrostatics gives rise to an anomalous sequence of d-electron levels in $5d$ oxide compounds with high formal oxidation states [42, 188, 189]. The d_{xy} orbital, proposed to define the low-T ground state in ref. [179], shows up in our calculations only as an excited state.

The agreement between RIXS experimental data (see Table 3.1) and the QC calculations is excellent for the lower-energy part of the d-d excitation spectrum, which provides good support for the picture we propose here for the electronic structure and ground state of TiPO$_4$. Some deviations are found however for the higher-energy $d-d$ excitations, an aspect already reported for the case of Cu d^9 oxides [79].

3.3 Heisenberg interaction for nearest-neighbor Ti^{3+} sites

In order to compute the magnetic interactions between two NN Ti^{3+} sites, QC calculations were performed on embedded clusters that include two edge-sharing TiO$_6$ octahedra as magnetically active units. To accurately describe the charge distribution in the immediate neighborhood, the two adjacent TiO$_6$ octahedra and the closest fifteen P sites were also incorporated in the actual cluster (see Fig. 3.3), as for the smaller cluster designed to compute on-site d-d excitations. To make the analysis of the low-lying magnetic states tractable, the spin couplings with the adjacent $S = 1/2$ moments were cut off by replacing the open-shell Ti^{3+} NNs with closed-shell Sc^{3+} species. Such a procedure is very often followed in QC studies on TM systems [191–195]

and allows a straightforward mapping of the *ab initio* data onto an effective spin model. Another simple approach is to use effective total ion potentials (TIPs) for the NN Ti sites [196]. The surrounding solid-state matrix was described as a finite array of point charges fitted to reproduce the crystal Madelung field in the cluster region.

We used all-electron triple-zeta basis sets of Douglas-Kroll type for the two magnetically active Ti ions [182], all-electron basis sets of quintuple-zeta quality with polarization functions for the two bridging ligands, triple-zeta basis functions for the other central O's, and double-zeta basis functions for O ligands beyond the two reference octahedra [118]. We further employed two f polarization functions at each of the two central Ti sites [182]. The P species (P^{5+} ions) were modeled by large-core ECP's supplemented with valence basis functions of double-zeta quality [185].

Scalar-relativistic restricted HF calculations were first performed to obtain a set of suitable initial orbitals for the subsequent CASSCF calculations. An active space of two electrons and two t_{2g} orbitals at the two magnetically active Ti sites (CAS[2,2]) was considered. The self-consistent field optimization was carried out for an average of the one singlet and one triplet states arising from the $d_\alpha^1 - d_\alpha^1$ configuration (d_α denotes the orbital character of the ground state). To separate the orbitals corresponding to the reference fragment from those associated with the NN octahedra into different groups, the Pipek-Mezey orbital localization scheme [186] available in MOLPRO [181] was used. On top of the CASSCF reference, in the MRCI treatment, the O $2p$ and Ti $3d$ electrons within the central two-octahedra unit were correlated. Additionally, we constructed truncated CISD wave functions using the difference-dedicated configuration-interaction (DDCI) methodology [197, 198], with all double excitations from the inactive O $2p$ orbital space to the virtual set of orbitals excluded. The MRCI and DDCI were carried out for each spin multiplicity, singlet or triplet, as one-root calculations. It has been shown that the DDCI treatment predicts spin coupling parameters in very good agreement with the experimental data in both solid state ionic insulators [199, 200] and molecular complexes [201, 202].

Since the SOC effect is very tiny for TiPO$_4$, which is already seen for the case of the *d-d*
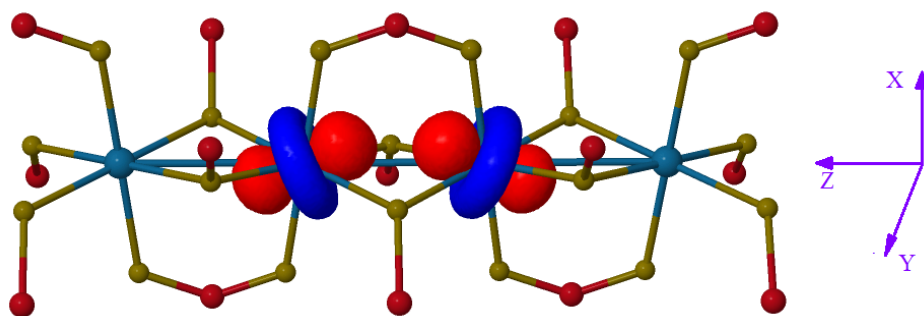
Figure 3.3: Ti $3d^1$ ground-state charge distribution as found by quantum chemistry MCSCF calculations. This sketch also shows the cluster used for the calculation of the NN magnetic interactions. It consists of a central [Ti$_2$O$_{10}$] fragment of two edge-sharing TiO$_6$ octahedra and two other adjacent octahedra, see text. Ti, O and P ions are shown in dark-blue, brown and red, respectively.

excitations, we did not include SOC in the calculations for the NN magnetic interaction. Without considering SOC, the NN exchange between a pair of ions i and j can be described by the Heisenberg Hamiltonian

$$\mathcal{H}_{ij} = J\tilde{\mathbf{S}}_i \cdot \tilde{\mathbf{S}}_j, \tag{3.1}$$

where J is the isotropic exchange interaction, $\tilde{\mathbf{S}}_i$ and $\tilde{\mathbf{S}}_j$ are spins at lattice sites indexed by i and j. If we consider a spin 1/2 at each site ($S_i = S_j = 1/2$), which is the case for Ti^{3+} ions in TiPO$_4$, the Heisenberg coupling parameter J is simply the energy splitting between the singlet and triplet states, i.e., $J = E_T - E_S$. The detailed derivation of this relation is given in ref.[203]. This relation implies that for $J < 0$, one has $E_T < E_S$ and ferromagnetic alignment with parallel spins ($\uparrow\uparrow$) in the ground state; whereas for $J > 0$, one has $E_T > E_S$ and antiferromagnetic alignment with antiparallel spins ($\uparrow\downarrow$) in the ground state.

Table 3.2: The Heisenberg coupling parameter J between NN Ti^{3+} sites in TiPO$_4$ at different levels of approximation (all values in meV).

	ROHF	CASSCF	MRCI	CISD(Q)	DDCI
J	-9.2	19.5	25.5	30.9	52.4

The Heisenberg coupling parameter J between NN Ti^{3+} sites in TiPO$_4$ at different levels of approximation [ROHF, CASSCF, MRCI, CISD(Q) and DDCI] is provided in Table 3.2. The ROHF approximation accounts for only direct exchange, since no intersite excitations are allowed. The value computed for J within the ROHF approximation, -9.2 meV, is comparable with that computed for square-lattice $3d^9$ Cu oxides [204]. In the CASSCF approximation, intersite $d_\alpha^0 - d_\alpha^2$ excitations are accounted for (d_α denotes the orbital character of the ground state). The CASSCF J, 19.5 meV, is much smaller than the CASSCF J's in layered $3d^9$ cuprates [204–207]. For the MRCI result, which includes as well additional TM t_{2g} to $\{t_{2g}, e_g\}$ and charge transfer O $2p$ to Ti $3d$ virtual states, J is 25.5 meV, about 31% larger as compared to the CASSCF value. With Davidson correction included on top of the MRCI(SD) treatment, J is enhanced up to 31 meV. For the DDCI treatment, which eliminates all the double excitations from the inactive O $2p$ orbitals to the virtual orbitals, J is 52.4 meV, about 70% larger than the CISD(Q) J.

The order of magnitude of the magnetic exchange interaction J is within a range of $30-60$ meV, based on the energy scale of the spin excitations measured by RIXS experiments [190]. The good agreement between DDCI and RIXS for the strength of the NN J gives strong support for the Ti d^1 ground state configuration (admixture of d_{xz} and d_{z^2} orbital character) that we propose for TiPO$_4$.

Having in mind possible charge redistribution effects and the modulation of the NN exchange couplings at the SP transition, we investigated by additional calculations the essential changes induced by moderately modifying the intersite Ti-Ti bond-length. The computations were carried out such that all atomic positions within the reference unit of two edge-sharing TiO$_6$ octahedra and within the surroundings solid-state embedding were kept as in the "homo-

Table 3.3: Dependence of the Heisenberg coupling parameter J on the Ti-Ti distance d(Ti-Ti) between NN Ti^{3+} sites in TiPO$_4$ at different levels of approximation (all values in meV).

d(Ti-Ti)(Å)	J				
	ROHF	CASSCF	MRCI	CISD(Q)	DDCI
3.060,−3%	−14.3	36.7	46.9	55.9	94.1
3.092,−2%	−12.5	30.0	39.1	47.2	84.2
3.123,−1%	−10.8	24.3	32.0	38.8	70.0
3.139,−0.5%	−10.0	21.8	28.8	35.1	63.7
3.155, 0% *	−9.2	19.5	25.5	30.9	52.4
3.171, 0.5%	−8.6	17.5	23.4	28.6	52.0
3.187, 1.0%	−8.0	15.6	21.0	25.8	47.7
3.218, 2.0%	−6.9	12.3	16.8	20.8	39.0
3.250, 3.0%	−5.9	9.7	13.4	16.7	31.8

* Corresponding to the data in Table 3.2.

geneous" $Cmcm$ crystal structure determined by Glaum et $al.$[178], except for the Ti ions of the reference two-octahedra block (see Fig. 3.3). The latter were shifted to achieve either shorter or longer Ti-Ti bonds. The dependence of the Heisenberg coupling parameter J on the Ti-Ti distance d(Ti-Ti) is listed in Table 3.3. The calculated DDCI difference $J' − J''$ between the Heisenberg coupling parameters corresponding to shorter (J') and elongated (J'') Ti-Ti links is ≈10 meV for bond-length alternation of ±0.5% and a 20 meV for ±1%, indicating a very strong sensitivity of the intersite exchange on this interatomic distance. However, even for bond-length alternation of ±3%, there is no significant charge redistribution among the Ti 3d orbitals (within 0.02 of an electronic charge). This shows that the scenario of an orbital crossover is unlikely, as the ground state found in our ab $initio$ computations is robust against SP-like modification of the Ti-Ti distances. The unusually strong dependence of the magnetic exchange coupling J on the Ti-Ti bond-length is related to having the Ti d_{z^2}–O p_y − Ti d_{z^2} path available for intersite superexchange, which maximizes the metal 3d–ligand 2p orbital overlap for edge-sharing octahedra (see Fig. 3.3 for a sketch of the ground-state Ti 3d charge distribution).

3.4 Heisenberg interaction for next nearest-neighbor Ti^{3+} sites

For better insight into the magnetic interactions in TiPO$_4$, we carried out a study of the NNN interaction between Ti^{3+} sites. In order to get access to the NNN magnetic interactions, three-center clusters are needed. The QC calculations were thus performed on embedded clusters including three edge-sharing TiO$_6$ octahedra as magnetically active units. The two adjacent TiO$_6$ octahdra and the closest eighteen P sites were also incorporated in the actual cluster, as shown in Fig.3.4. The Ti^{3+} ions of the two adjacent octahedra were modeled as closed-shell Sc^{3+}
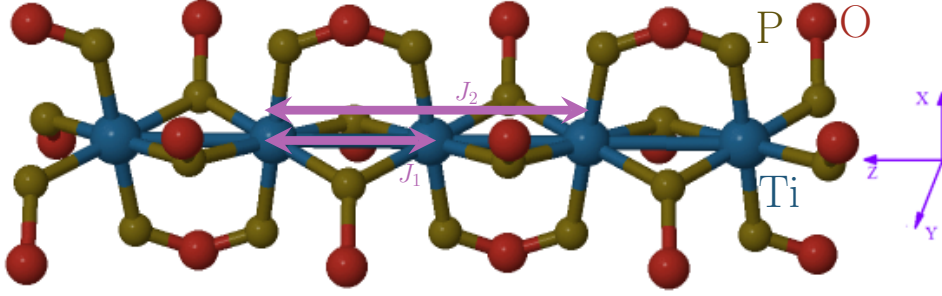
Figure 3.4: The cluster used in computing the NNN interaction between Ti^{3+} sites. It consists of a central $[Ti_3O_{14}]$ fragement of three edge-sharing TiO_6 octahedra and two other adjacent octahedra. Ti, O and P ions are shown in dark-blue, brown and red, respectively.

species. The solid-state surroundings were described as a finite array of point charges. The basis sets used in these calculations are similar to the calculations for the NN Heisenberg interaction. The finite set of Slater determinants was defined in the CASSCF treatment in terms of three electrons and three Ti t_{2g} orbitals for the three reference TiO_6 octahedra. The self-consistent field optimization was performed for an average of two doublet and one quartet states arising from the $d_\alpha^1 - d_\alpha^1 - d_\alpha^1$ configuration (d_α denotes the orbital character of the ground state). In the MRCI and DDCI treatments, the bridging O $2p$ and the Ti $3d$ electrons within the central three-octahedra unit were correlated.[4]

Considering only isotropic interaction parameters, the effective spin Hamiltonian between three TM sites reads

$$\mathcal{H}_{three} = J_1(\tilde{\mathbf{S}}_1 \cdot \tilde{\mathbf{S}}_2 + \tilde{\mathbf{S}}_2 \cdot \tilde{\mathbf{S}}_3) + J_2 \tilde{\mathbf{S}}_1 \cdot \tilde{\mathbf{S}}_3, \tag{3.2}$$

where J_1 is the NN isotropic Heisenberg interaction, J_2 is the NNN isotropic Heisenberg interaction between $\tilde{\mathbf{S}}_1$ and $\tilde{\mathbf{S}}_3$. For a spin $S=1/2$ at each site ($S_1=S_2=S_3=1/2$), J_1 and J_2 can be extracted from the differences between the energy eigenvalues of the quartet and two doublet states:

$$J_1 = \frac{2}{3}(E_Q - E_{D_u}), \qquad J_2 = J_1 + (E_{D_u} - E_{D_g}). \tag{3.3}$$

In this equation, $J > 0$ and $J < 0$ indicate antiferromagnetic and ferromagnetic interactions, respectively. A similar approach has been applied in earlier research for the cupric oxide [209].

The QC results for J_1 and J_2 at different levels of approximation [CASSCF, MRCI, CISD(Q) and DDCI] are listed in Table 3.4. The NN Heisenberg coupling parameters J_1 obtained from three-center clusters are consistent with the J_1' obtained from two-center clusters. For the latter, only the bridging O $2p$ and the Ti $3d$ electrons within the central two-octahedra unit were correlated to obtain the MRCI and DDCI results presented in Table 3.4. The NNN Heisenberg

---

[4]Due to limitations concerning the size of the active and inactive orbital spaces in the MOLPRO program, it is not possbile to correlate all the O $2p$ and Ti $3d$ electrons within the central three-octahedra unit in the MRCI treatment. A new internally contracted MRCI code [208] is now available (named as MRCIC) without the existing limitation of having a maximum of 32 correlated orbitals as compared to the earlier MRCI code, however, this method is implemented only for single-state calculations.

coupling parameter J_2 is very tiny as compared with the NN coupling J_1 at all these approximation levels listed in Table 3.4. This indicates that the dominant magnetic interaction in TiPO$_4$ is the NN Heisenberg coupling.

Table 3.4: The Heisenberg coupling parameters J_1, J_2 obtained from a three-octahedra cluster and the J_1' obtained from a two-octahedra cluster in TiPO$_4$ at different levels of approximation (all values in meV). The bridging O $2p$ and the Ti $3d$ electrons within the central two-octahedra unit were correlated in the MRCI and DDCI treatments.

		Relative energies (meV)			
		CASSCF	MRCI	CISD(Q)	DDCI
S_{tot}=1/2	E_{D_u}	0.0	0.00	0.00	0.00
	E_{D_g}	17.91	23.81	28.06	37.90
S_{tot}=1	E_Q	26.86	35.74	42.03	56.97
J_1, J_2		17.91, −0.003	23.83, 0.018	28.02, −0.04	37.98, 0.08
J_1'		18.10	26.06	30.72	37.40

3.5   Conclusions

In summary, we have employed *ab initio* QC methods to investigate the ground state, the d-level excitations and the Heisenberg magnetic interactions in the quasi one-dimensional TiPO$_4$ compound. We show that the ground state wave-function displays a highly unusual admixture of d_{xz} and d_{z^2} orbital character, which is different from earlier research indicating that the ground state wave-function implies the occupation of the d_{xy} orbital in the low temperature phase [179]. Having the d_{xz} and d_{z^2} orbitals as main contributors to the $3d^1$ ground state configuration of TiPO$_4$ is related to the large positive ionic charge at P sites in the xz plane (defining the shortest Ti-P links) and of Ti nearest-neighbours along the z axis. The energies of the Ti $3d$ levels and of the NN Heisenberg magnetic coupling constant J ($\sim$ 52 meV) obtained from QC calculations are compared with available RIXS experimental data. Good agreement is found between theory and experiment. Moreover, the calculations suggest that the intersite exchange is very sensitive to the Ti−Ti interatomic distance, a finding which is relevant in the context of the SP-transition physics. The large magnetic exchange J and the huge variation of J when varying the intra-chain Ti−Ti distances seem to be related to having the Ti d_{z^2}−O p_y−Ti d_{z^2} path available for intersite superexchange. The latter maximizes the TM $3d$− ligand $2p$ orbital overlap for edge-sharing octahedra. Further, it turns out that the energy scale of the NNN Heisenberg interaction J_2 is very tiny as compared with that of the NN J and that the dominant magnetic interaction in TiPO$_4$ is the NN Heisenberg coupling.

Chapter 4

Magnetic anisotropy of Fe ions within the Li$_3$N lattice

In this chapter, we investigate the electronic structure and magnetic anisotropy of Fe ions placed within the Li$_3$N lattice. We provide *ab initio* results of many-body quantum chemistry (QC) calculations for both Fe^{1+} d^7 and Fe^{2+} d^6 species at a Li lattice site. A remarkably large magnetic anisotropy energy of 305 K (26 meV) is computed for divalent Fe^{2+} d^6 substitutes at Li-ion sites with D_{6h} point-group symmetry. This is similar to values calculated by the same approach and confirmed experimentally for linearly coordinated monovalent Fe^{1+} d^7 species, remarkably large in the research area of single-molecule magnets.

4.1 Introduction

Single molecule magnets (SMMs), or molecular nanomagnets, are polynuclear metal complexes whose structures consist of magnetic clusters of exchange-coupled transition-metal ions surrounded by a shell of ligands. One of the most important aspects for technological applications of SMMs is the magnetic bistability. The latter refers to the existence of two stable electronic states under the same external conditions such as temperature, pressure or other external perturbations. The bistability in SMMs is related to the spin orientation of a given electronic state (M_S components). SMMs can be modeled through double-well potentials, with the levels $S_m=\pm S$ having the lowest energy and a potential barrier in between, as illustrated in Fig.4.1. Below a certain 'blocking' temperature, the system can be trapped in one of those states having spin projection $+m$ or $-m$ and exhibit magnetic hysteresis. Such effects have only been observed at rather low temperatures so far but intensive work is going on to identify systems with superior properties in this regard: higher blocking temperatures, longer relaxation times and larger coercivity fields. An impelling idea is realizing regular, stable arrays of such molecules for high-density data storage [211], provided that the associated blocking temperatures and relaxation times are appropriately optimized.

SMM physics was first pointed out by Sessoli *et al.* for a Mn$_{12}$ complex, in 1993 [212]. Since

---

Large part of this chapter is published in Nanoscale 9, 10596 (2017) [210].
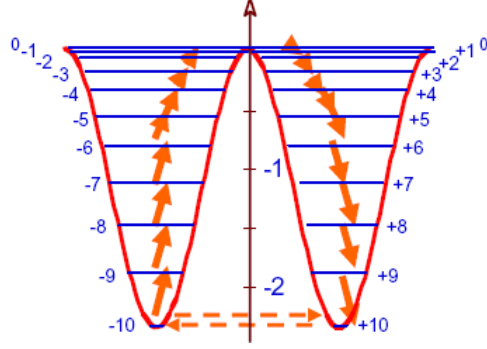
Figure 4.1: Schematic representation of the energy landscape of a SMM with a total spin S=10. Magnetization reversal can occur via quantum tunnelling between energy levels (dashed arrows) when the energy levels in the two wells are in resonance. Phonon absorption (solid arrows) can also excite the magnetic state up to the top of the potential energy barrier with the quantum number M=0 and phonon emission descends the spin to the second well [211].

then the field advanced dramatically, with dozens of new SMMs being reported, either d-metal or f-metal based. As concerns their specific magnetic properties, the most remarkable are nowadays the Tb^{3+} and Dy^{3+} SMMs with N$_2^{3-}$ ligand bridges [213, 214], some lanthanide single-ion magnets with high-symmetry environment [215], the fullerene-encapsulated f-electron SMMs [216], one-dimensional chains of the endofullerene Dy$_2$ScN@C$_{80}$ packed inside single-walled carbon nanotubes [217] and the linear Fe^{1+} complexes [218]. Interestingly, SMM-like behaviour has been also identified recently for linearly coordinated Fe-ion substitutes within the solid-state matrix of Li$_3$N [219]. The latter findings [218, 219] open new research avenues in this field because, due to the well known 'orbital quenching' issue in transition-metal (TM) compounds, mononuclear d-metal ions have been rarely considered as good candidates to achieving first rate SMM characteristics.

The electronic structure and magnetic anisotropy of Fe ions placed within the Li$_3$N lattice (the crystal structure is shown in Fig.4.2(a)) have been investigated on the theoretical side by calculations based on density functional theory (DFT) [220–223]. A Fe^{1+} d^7 valence electron configuration has been assumed in the DFT studies [221–223] but diffraction [224, 225] and X-ray absorption experiments on TM centers within the Li$_3$N matrix suggest 2+ valence states for d-metal ions in such an environment [226]. In this chapter we provide unbiased *ab initio* results of many-body QC calculations for both Fe^{1+} d^7 and Fe^{2+} d^6 species at a Li lattice site. The computed Fe^{1+} d^7 excitation spectrum indicates an axial magnetic anisotropy of 31 meV for linear N-Fe-N coordination, in agreement with experimental results for relatively large amount of Fe cation substitution [219, 227]. What is more, the calculated magnetic anisotropy reaches values of similar magnitude for Fe^{2+} d^6, 26.3 meV (i.e., 305 K), if the overall lattice symmetry is not broken by vacancies in the immediate neighborhood. This is related to an unexpected $d_{z^2}^1 d_{xy}^{1.5} d_{x^2-y^2}^{1.5} d_{yz}^1 d_{zx}^1$ ground-state configuration in which due to subtle many-body effects one electron is removed from the 'deeper' d_{z^2} level [221–223], as compared to the Fe^{1+} $d_{z^2}^2 d_{xy}^{1.5} d_{x^2-y^2}^{1.5} d_{yz}^1 d_{zx}^1$ ground state. With a vacant nearest-neighbor (NN) Li site — which ensures charge neutrality and coincides with a Li$_{3-2x}$TM$_x^{2+}$N picture [226] for the substitution process

a

b
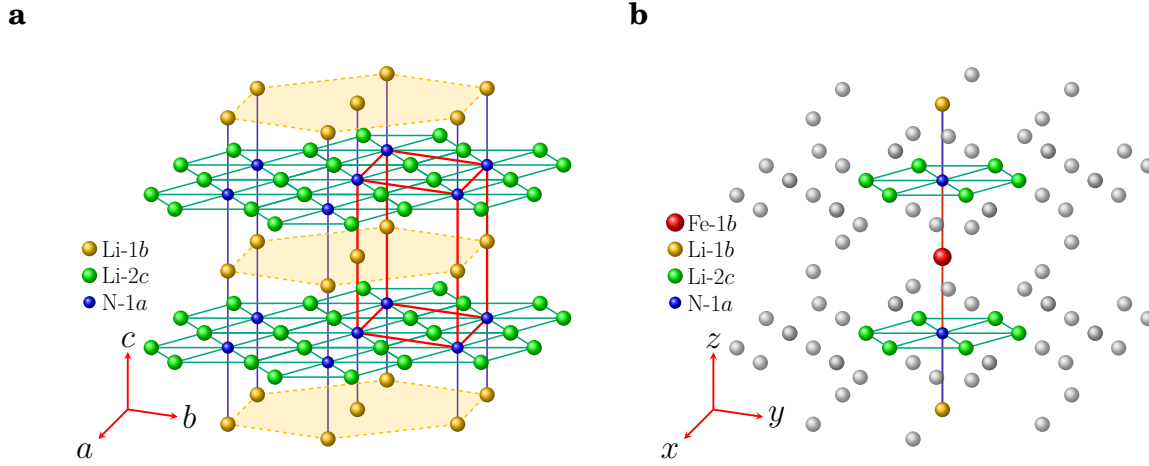
Figure 4.2: a) Crystal structure of Li$_3$N, with Li$_2$N honeycomb layers separated by Li-1b sites. The crystallographic unit cell is indicated as a red polyhedron. b) Configuration of nearby sites around a Fe cation at the 1b crystallographic position in Li$_3$N. These sites define the fragment treated at the all-electron quantum mechanical level in our calculations. The extended solid-state surroundings are modeled as a large array of point charges, depicted here as small grey spheres. A similar type of linear coordination of the Fe ion (Fe^{1+} d^7) is found in certain molecular systems [218].

— the interaction between the $d^1_{z^2}d^{1.5}_{xy}d^{1.5}_{x^2-y^2}d^1_{yz}d^1_{zx}$ and $d^2_{z^2}d^1_{xy}d^1_{x^2-y^2}d^1_{yz}d^1_{zx}$ states, arising from breaking the symmetry around the Fe^{2+} ion, reduces the magnetic anisotropy to $\approx$15 meV. The latter number provides an explanation for the strong reduction of the magnetic anisotropy observed experimentally in the very dilute system [227] and support for the Li$_{3-2x}$TM$^{2+}_x$N model [226] at very small concentrations of TM centers. Corroborated with earlier experimental results [226, 227], our computational data can therefore reconcile the Li$_{3-x}$TM$^{1+}_x$N and Li$_{3-2x}$TM$^{2+}_x$N cation-substitution models, suggesting that due to finite concentration of Li-ion vacancies the TM 2+ valence state dominates in the very dilute TM:Li$_3$N system while TM 1+ plays a dominant role at large concentrations of TM species. Most importantly, our findings draw attention to the very large magnetic anisotropy associated with the Fe^{2+} $d^1_{z^2}d^{1.5}_{xy}d^{1.5}_{x^2-y^2}d^1_{yz}d^1_{zx}$ configuration in full D_{6h} symmetry, analogous to Fe^{1+} values discussed in Refs. [218, 219].

4.2 Fe^{1+} d^7 ions at Li$_3$N lattice sites

We focus on cation substitution at linearly coordinated 1b Li sites, since that is the geometrical configuration maximizing the single-ion magnetic anisotropy [218, 221]. The many-body QC calculations were performed on [FeN$_2$Li$_{14}$]$^{9+}$ clusters as depicted in Fig.4.2(b), using the room-temperature lattice parameters reported in Ref.[228]. We utilized the quantum chemistry package MOLPRO [181]. To compute the magnetic anisotropy and the on-site d–d excitation spectrum, an embedded cluster consisting of one central Fe ion, the two NN NLi$_6$ hexagonal plaquettes and the nearby two Li sites on the z axis was considered. The solid-state surroundings were modeled as a finite array of point charges fitted [154] to reproduce the crystal Madelung field in the cluster region [229]. We applied all-electron Douglas-Kroll basis sets of triple-zeta

Table 4.1: 3d-shell energy levels for a Fe^{1+} ion at the Li 1b crystallographic position in Li$_3$N; unless otherwise specified, units of eV are used. All 3d^7 $S=3/2$ and the few lowest $S=1/2$ states are listed. The spin-orbit calculations provide three main groups of Kramers doublets: between 0 and 100 meV, at 1.1–1.2 eV and from 1.75 eV onwards.

Fe^{1+} 3d^7 splittings	CASSCF	MRCI	MRCI+SOC
$^4E_{2g}$ $(a_{1g}^2 e_{2g}^3 e_{1g}^2)$	0	0	0, 30, 62, 96 meV
$^4E_{1g}$ $(a_{1g}^2 e_{2g}^2 e_{1g}^3)$	0.91	1.09	$1.11-1.16$
$a\,^4E_{1g}$ $(a_{1g}^1 e_{2g}^3 e_{1g}^3)$	1.50	1.78	1.75
$a\,^4A_{2g}$ $(a_{1g}^1 e_{2g}^4 e_{1g}^2,\ a_{1g}^1 e_{2g}^2 e_{1g}^4)$	1.67	1.87		
$a\,^2E_{2g}$ $(a_{1g}^2 e_{2g}^3 e_{1g}^2)$	2.23	2.05		
$^2E_{1g}$ $(a_{1g}^2 e_{2g}^4 e_{1g}^1)$	2.25	2.11		
$b\,^2E_{2g}$ $(a_{1g}^2 e_{2g}^3 e_{1g}^2)$	2.29	2.11		
$^2E_{1g}$ $(a_{1g}^2 e_{2g}^3 e_{1g}^2)$	2.50	2.35	2.41
$b\,^4E_{1g}$ $(a_{1g}^1 e_{2g}^3 e_{1g}^3)$	2.69	2.70	
$b\,^4A_{2g}$ $(a_{1g}^1 e_{2g}^4 e_{1g}^2,\ a_{1g}^1 e_{2g}^2 e_{1g}^4)$	3.27	3.28	

quality for the central Fe ion [182] and all-electron triple-zeta basis sets for the two NN nitrogen ligands and the Li species [118], supplemented with polarization functions.

In a first step, the orbitals were optimized for an average of all d^7 high-spin ($S=3/2$) states using the multiconfigurational complete-active-space self-consistent-field method (CASSCF), with an active space of five 3d orbitals at the Fe site and seven electrons for the Fe^{1+} d^7 valence configuration. This ensures a balanced description of all d^7 electron configurations: $a_{1g}^2 e_{2g}^3 e_{1g}^2$, $a_{1g}^2 e_{2g}^2 e_{1g}^3$, $a_{1g}^1 e_{2g}^3 e_{1g}^3$, $a_{1g}^1 e_{2g}^4 e_{1g}^2$ and $a_{1g}^1 e_{2g}^2 e_{1g}^4$, where d_{z^2} belongs to the A_{1g} irreducible representation, $\{d_{xy}, d_{x^2-y^2}\}$ to E_{2g} and $\{d_{yz}, d_{zx}\}$ to E_{1g}, for D_{6h} point-group symmetry. Following the CASSCF calculation, multireference configuration-interaction (MRCI) computations with single and double excitations were performed [63, 230]. Spin-orbit couplings were subsequently accounted for according to the procedure described in Ref. [148]. We allowed relaxation of the N-Fe-N bonds, i.e., for the two nitrogen ions adjacent to the Fe cation we determined the z-axis positions which minimize the total energy while fixing all other lattice coordinates as in the unmingled Li$_3$N crystal. At the MRCI levels, the 'relaxed' Fe^{1+}-N bond lengths are 1.92 Å, slightly shorter than the experimental Li-N distances along the z axis [228].

Relative energies describing the excitation spectrum of the Fe^{1+} 3d^7 center are provided in Table 4.1. The a and b labels in Table 4.1 are used in order to distinguish between states implying the same electron configuration, irreducible representation and spin multiplicity. In the scalar-relativistic calculations, at both CASSCF and MRCI levels, the lowest electron configuration is $^4E_{2g}$ $(a_{1g}^2 e_{2g}^3 e_{1g}^2)$, the same as for the linear iron(I) complex reported in Ref.[218]. Comparing the CASSCF and MRCI numbers, the corrections brought by the CI treatment increase the excitation energies of the spin-quartet states by $0.01-0.3$ eV and decrease the excitation energies of the spin-doublet states by $0.14-0.18$ eV. In the MRCI + SOC computational frame,

we predict three main sets of excited states: low-lying excited states related to the magnetic anisotropy of the ($S = 3/2$, $L = 2$) $a_{1g}^2 e_{2g}^3 e_{1g}^2$ configuration in the range of $\lesssim 100$ meV, high-spin e_{2g} to e_{1g} excitations at 1.1–1.2 eV and a multitude of crystal-field excitations from 1.75 eV onwards. The spin-orbit treatment was carried out in terms of all $S = 3/2$ quartets and those doublets with MRCI relative energies of less than 2.5 eV. The lowest excited state, defining the magnetic anisotropy energy, lies in this case at 29.9 meV. If the orbitals are optimized just for the $a_{1g}^2 e_{2g}^3 e_{1g}^2$ ground-state configuration, this particular excitation energy changes to 31.1 meV.

4.3 Fe^{2+} d^6 ions at Li_3N lattice sites

The observation that a finite amount of vacant Li sites would necessarily require a higher ionized state for some of the TM centers [226, 231] makes the Fe^{2+} d^6 valence electron configuration worth investigating (according to a $Li_{3-x-2y}Fe_x^{1+}Fe_y^{2+}N$ picture). To retain overall charge neutrality of the cluster in Fig.4.2(b), we compensated the larger, 2+ valence state of the Fe ion by adding one (negative) electronic charge to the nearby crystalline surroundings. In particular, we equally distributed this elementary negative charge over the six closest Li $1b$ sites within the xy plane. This way, the D_{6h} point-group symmetry at the Fe site is preserved. The results are summarized in Table 4.2. The very surprising result for the Fe^{2+} d^6 ion is that the computed ground-state electron configuration defies a simple diagram of single-electron levels according to which, from the Fe^{1+} $a_{1g}^2 e_{2g}^3 e_{1g}^2$ 'reference', removal of one additional electron yields a $a_{1g}^2 e_{2g}^2 e_{1g}^2$ orbital occupation [222, 223]. Instead, the QC calculations indicate that $3d$-shell Coulomb interactions are such that it is energetically more favorable to remove one electron from the apical a_{1g} d_{z^2} orbital rather than further depleting the 'in-plane' e_{2g}'s, d_{xy} and $d_{x^2-y^2}$ (see Fig.4.3). An important detail here is that there are no negatively charged ions in the plane within which the lobes of the latter lie while the former points to anions with formal 3− charges. Consequently, the $3d^6$ ground-state configuration is $a_{1g}^1 e_{2g}^3 e_{1g}^2$ according to our calculations, with an occupation of the e_g levels that provides again a large angular momentum ($L = 2$) and strong axial anisotropy. Using orbitals optimized for an average of all $S = 2$ d^6 states, the magnetic anisotropy energy comes as 26.3 meV in the d^6 spin-orbit MRCI calculation (see Table 4.2); the same value, 26.3 meV, is obtained with orbitals optimized just for the lowest two quintet states.
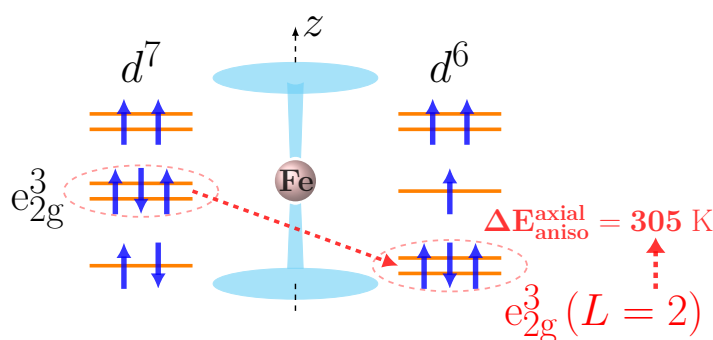
Figure 4.3: Schematic representation of an Fe centre with linear coordination for d^7 and d^6 electron configurations.

Table 4.2: $3d$-shell energy levels for a Fe^{2+} ion at the Li $1b$ crystallographic position in Li$_3$N; unless otherwise specified, units of eV are used. All $3d^6$ $S = 2$ and the lowest $S = 1$ and $S = 0$ states are listed. The spin-orbit calculations provide four main groups of excited states: up to $\approx$105 meV, 180–200 meV, 1.2–1.3 eV and from 1.8 eV onwards.

Fe^{2+} $3d^6$ splittings	CASSCF	MRCI	MRCI+SOC
$^5E_{2g}$ ($a_{1g}^1 e_{2g}^3 e_{1g}^2$)	0	0	0, 26, 52, 78, 104 meV
$^5A_{1g}$ ($a_{1g}^2 e_{2g}^2 e_{1g}^2$)	0.26	0.14	0.18 − 0.19
$^5E_{1g}$ ($a_{1g}^1 e_{2g}^2 e_{1g}^3$)	1.09	1.18	1.21 − 1.26
$a\,^3E_{1g}$ ($a_{1g}^2 e_{2g}^3 e_{1g}^1$)	2.31	1.84	1.84
$b\,^3E_{1g}$ ($a_{1g}^2 e_{2g}^3 e_{1g}^1$)	2.37	1.89	|
$a\,^3E_{2g}$ ($a_{1g}^1 e_{2g}^3 e_{1g}^2$)	2.58	2.38	|
$b\,^3E_{2g}$ ($a_{1g}^1 e_{2g}^3 e_{1g}^2$)	2.74	2.55	|
$^3A_{2g}$ ($a_{1g}^1 e_{2g}^3 e_{1g}^2$)	2.81	2.55	|
$^1A_{1g}$ ($a_{1g}^2 e_{2g}^4$)	3.34	2.77	2.83

That is 305 K, room-temperature energy scale.

Also for these computations, we considered all the high-spin ($S = 2$) states in the spin-orbit treatment but only the spin triplets and singlets with MRCI relative energies of less than 2.8 eV. As for the Fe^{1+} d^7 ion, the different m_J states associated with the ground-state configuration cover an energy window extending up to $\approx$100 meV. The first crystal-field excitation, however, implies here an energy scale of only $\approx$200 meV; that is the $^5E_{2g}$ ($a_{1g}^1 e_{2g}^3 e_{1g}^2$) to $^5A_{1g}$ ($a_{1g}^2 e_{2g}^2 e_{1g}^2$) transition. Other excited states lie in the energy range of 1.2–1.3 eV and from 1.8 eV onwards. All these results correspond to 'relaxed' Fe^{2+}-N bonds of 1.88 Å. Significant shortening of the N-TM-N bonds has been also inferred from extended x-ray absorption fine structure (EXAFS) measurements on TM ions embedded within the solid-state Li$_3$N matrix [226].

An additional set of calculations was then performed with one of the NN Li ions at a $2c$ crystallographic position explicitly removed from the cluster described by QC methods. This also preserves overall charge neutrality, according to the Li$_{3-2x}$ TM$_x^{2+}$N model of Muller-Bouvet et al. [226]. The symmetry being lower with such a Li vacant site, the $a_{1g}^1 e_{2g}^3 e_{1g}^2$ and $a_{1g}^2 e_{2g}^2 e_{1g}^2$ configurations, in particular, can interact and admix. As a result, the low-energy part of the MRCI spectrum displays now a richer structure: with orbitals optimized in the prior CASSCF step just for the $a_{1g}^1 e_{2g}^3 e_{1g}^2$ and $a_{1g}^2 e_{2g}^2 e_{1g}^2$ configurations and maximum spin multiplicity, the relative energies of the spin-orbit MRCI states are 0 (two states), 15, 17, 23, 81, 84, 86 and 94 (again as a doublet) meV. In other words, the magnetic anisotropy energy of the Fe^{2+} d^6 ion is reduced from $\Delta_{D_{6h}}^{d^6} = 26$ meV in D_{6h} symmetry to $\Delta_{C_s}^{d^6} = 15$ meV when the symmetry is broken by creating a vacancy at a NN Li site. Analysis of the spin-orbit wave-functions shows that these effects imply admixture(s) of the $a_{1g}^2 e_{2g}^2 e_{1g}^2$ components of only tenths of 1% to the low-lying $a_{1g}^1 e_{2g}^3 e_{1g}^2$ states. Obviously, the more complicated structure of the spectrum in the lower-

symmetry case is related to having slightly different degrees of $a_{1g}^1 e_{2g}^3 e_{1g}^2 - a_{1g}^2 e_{2g}^2 e_{1g}^1$ admixture for different spin-orbit eigenvectors. The relaxed Fe-N bond lengths are in both cases, without and with a Li-ion vacancy, 1.88 Å. According to experimental investigations [224, 225], the Li-ion vacancies mainly occur within the Li_2N planes.

4.4 Discussion

Our computational results for the magnetic anisotropies of Fe^{1+} d^7 and Fe^{2+} d^6 centers within the solid-state matrix of Li_3N find strong support in recent experimental data on $Li_{3-x-2y}Fe_x^{1+}Fe_y^{2+}N$, that indicate magnetic anisotropy energies $\Delta_{x\to 0} = 13$ meV in the very dilute case and $\Delta_{x\gg y} = 27$ meV for high concentration of Fe [227]. These drastic variations in the measurements can be assigned to the presence of a finite amount of Li-ion vacancies. An intrinsic load of vacant Li sites has been indeed found experimentally for Li_3N, in the range of ~1% [232], which suggests that for keeping overall charge neutrality Fe ions in the immediate neighborhood of such vacancies might adopt a Fe^{2+} d^6 configuration. The reason no connection has been made so far between these variations of the magnetic properties and the possible predominance of Fe^{2+} d^6 species in the very dilute case is the fact that the d^6 ground-state configuration is usually associated for linear coordination with a $d_{z^2}^2 d_{xy}^1 d_{x^2-y^2}^1 d_{yz}^1 d_{zx}^1$ orbital occupation [221–223] for which single-ion anisotropy can only occur through weaker, second-order SOC's. The good agreement between our MRCI value $\Delta_{C_s}^{d^6} = 15$ meV and the experimentally derived $\Delta_{x\to 0} = 13$ meV makes therefore plausible the scenario in which the magnetic properties in the dilute regime are mainly determined by Fe^{2+} d^6 ($a_{1g}^1 e_{2g}^3 e_{1g}^2$) ions with broken-symmetry nearby surroundings. Additional support is provided by the good agreement between the MRCI result $\Delta_{D_{6h}}^{d^7} = 30$ meV (see Table 4.1) and the experimental estimate $\Delta_{x\gg y} = 27$ meV at large concentrations of Fe.

Resonant inelastic x-ray scattering (RIXS) measurements on the $Fe:Li_3N$ system might throw fresh light on the problem. The high resolution achieved nowadays in RIXS should allow to directly verify our prediction of a distinct peak at 0.15–0.20 eV for the Fe^{2+} d^6 electron configuration. According to our computational results, the position of these crystal-field excited states is about the same in D_{6h} symmetry (see Table 4.2) and when the symmetry is broken by creating a Li vacancy next to the Fe^{2+} d^6 center. That post-CASSCF quantum chemistry calculations can describe the RIXS d–d excitation spectra with very good accuracy has been convincingly shown already for TM ions in a variety of environments [233–236]. Another experimental technique capable of verifying the existence of Fe^{2+} d^6 ions in $Fe:Li_3N$ is Mössbauer spectroscopy. In addition to stimulating further experimental investigations, our computational data define the frame for subsequent model-Hamiltonian constructions for addressing the magnetodynamics of this system [237]. Aspects which remain to be clarified is the role of spin-phonon couplings in under-barrier spin relaxation [237] but also the occurrence of clustering effects among the Fe-ion substitutes and of sizable magnetic exchange between proximate Fe sites.

4.5   Conclusion

To summarize, our *ab initio* data put into the spotlight the linearly coordinated Fe^{2+} d^6 ion as candidate for viable SMM behaviour. The calculated magnetic anisotropy splitting of 26.3 meV (i.e., 305 K) in D_{6h} symmetry compares favorably to values measured (28 meV [218] and 27–37 meV [219, 227]) or computed by similar theoretical methods (26 meV [218]) for Fe^{1+} d^7 species with linear coordination, remarkable large in the research area of SMMs. This substantial spin-reversal energy barrier of the Fe^{2+} ion is associated with a $a_{1g}^1 e_{2g}^3 e_{1g}^2$ ground-state electron configuration, not anticipated by earlier DFT calculations for TM species in such an environment [221–223] and made possible through a subtle interplay between ligand/crystal-field splittings and on-site Coulomb interactions. The effects we point out here warrant more detailed investigations of both iron(I) and iron(II) complexes with linear or quasilinear two-ligand coordination. For iron(II), engineering of the $^5E_{2g} - \,^5A_{1g}$ splitting towards larger values would allow large magnetic anisotropy barriers also for symmetries much lower than D_{6h}.

Chapter 5

Electronic structure and magnetic properties of $4d^1/5d^1$ double-perovskites

The electronic structure and magnetic properties of d^1 ions in molybdenum- and osmium-based double-perovskites are addressed in this chapter by *ab initio* many-body quantum chemistry (QC) calculations. Our results demonstrate the subtle interplay of spin-orbit interactions, covalency and electron-lattice couplings as the major factor in deciding the nature of the magnetic ground states of $4d$ and $5d$ quantum materials. Cation charge imbalance in the double-perovskite structure is further shown to allow a fine tuning of the gap between the t_{2g} and e_g levels, an effect of much potential in the context of orbital engineering in such systems.

5.1 Introduction

A defining feature of d-electron systems is the presence of sizable electron correlations, also referred to as Mott-Hubbard physics. The latter has been traditionally associated with first-series ($3d$) transition-metal (TM) oxides. But recently one more ingredient entered the TM-oxide 'Mottness' paradigm — large spin-orbit couplings (SOCs) in $4d$ and $5d$ quantum materials [13, 31]. It turns out that for specific t_{2g}-shell electron configurations, a strong SOC can effectively augment the effect of Hubbard correlations [13]: although the $4d$ and $5d$ orbitals are relatively extended objects and the Coulomb repulsive interactions are weakened as compared with the more compact $3d$ states, the spin-orbit-induced level splittings can become large enough to break apart the 'nonrelativistic' t_{2g} bands into sets of well-separated, significantly narrower subbands for which even a modest Hubbard U acting on the respective Wannier orbitals can then open up a finite Mott-Hubbard-like gap [13]. On top of that, SOC additionally reshuffles the intersite superexchange [15]. The surprisingly large anisotropic magnetic interactions that come into play via the strong SOCs in iridates [189, 239–243], for example, are responsible for an exotic assortment of novel magnetic ground states and excitations [31, 239, 244].

In case of large t_{2g}–e_g splittings, the spin-orbit-coupled t_{2g}^1 and t_{2g}^5 electron configurations can be in first approximation viewed as 'complementary': in the simplest picture, the d-shell

---

Large part of this chapter is published in npj Quantum Materials 1, 16029 (2016) [238].
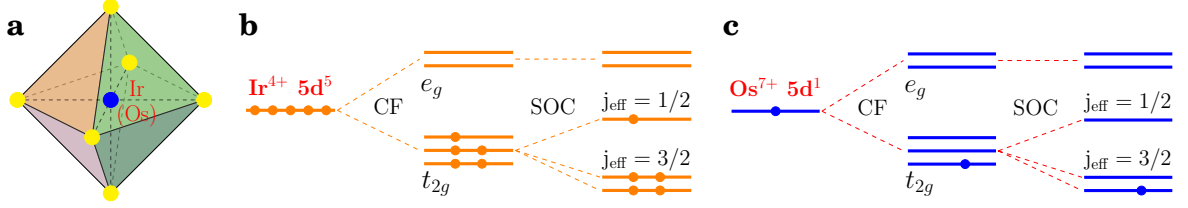
Figure 5.1: (a) Illustration of the octahedral geometry of a Ir^{4+} or Os^{7+} ion. (b) Splitting of the Ir^{4+} $5d$ levels by octahedral crystal field and SOC into $j_{eff} = 1/2$ and $j_{eff} = 3/2$ levels, with a $j_{eff} = 1/2$ ground state. (c) Splitting of the Os^{7+} $5d$ levels by octahedral crystal field and SOC into $j_{eff} = 3/2$ and $j_{eff} = 1/2$ levels, with a $j_{eff} = 3/2$ ground state.

manifold can be shrunk to the set of $j = 1/2$ and $j = 3/2$ relativistic levels, with a $j = 3/2$ ground state for the TM t_{2g}^1 configuration and a $j = 1/2$ ground state for t_{2g}^5 [245–247], as illustrated in Fig.5.1. Although strongly spin-orbit-coupled t_{2g}^5 oxides and halides — iridates, rhodates and ruthenates, in particular — have generated substantial experimental and theoretical investigations in recent years, much of the properties of $5d$ and $4d$ t_{2g}^1 systems remain to large extent unexplored.

From textbook arguments [245–247], the t_{2g}^1 $j = 3/2$ quadruplet should be characterized by a vanishing magnetic moment in cubic symmetry, due to perfect cancellation of the spin and angular momentum contributions. But this assertion leaves unexplained the wide variety of magnetic properties recently found in $4d^1$ and $5d^1$ cubic oxide compounds [19–22, 27–29, 248]. Ba_2YMoO_6, e.g., develops no magnetic order despite a Curie-Weiss temperature of $\approx$–200 K [20, 248] and features complex magnetic dynamics that persists down to the mK range, possibly due to either a valence-bond-glass [19] or spin-liquid [21] ground state. Also Ba_2NaOsO_6 displays an antiferromagnetic Curie-Weiss temperature [27, 28] but orders ferromagnetically below 7 K [29], whereas Ba_2LiOsO_6 is a spin-flop antiferromagnet [29]. A summary of some of the properties of these compounds is presented in Table 5.1.

In this chapter, we carry out a detailed *ab initio* investigation of the Mo^{5+} $4d^1$ and Os^{7+} $5d^1$ relativistic electronic structure in the double-perovskite compounds Ba_2YMoO_6, Ba_2LiOsO_6 and Ba_2NaOsO_6. In addition to providing reliable results for the energy scale of the d-level splittings, t_{2g}–e_g and induced by SOC within the t_{2g}^1 manifold, we analyse the role of TM d–O p orbital mixing plus the strength of electron-lattice couplings. It is found that strong metal d–O p hybridization generates a finite magnetic moment even for perfectly cubic environment around the TM site, providing *ab initio* support to the phenomenological covalency factor introduced in this context by Stevens [249]. The TM d^1 magnetic moment is further enhanced by tetragonal distortions, against which the octahedral oxygen cage is unstable. Although additional investigations are needed for clarifying the role of intersite cooperative couplings [250, 251], our calculations emphasize the high sensitivity of the effective magnetic moments to both metal-ligand covalency effects and local JT physics. The material dependence for the ratio among the strengths of the spin-orbit interaction, the JT coupling parameter and the effective covalency factor that we compute here provide new perspectives for future studies addressing the role of intersite interactions on the double-perovskite face centered cubic (*fcc*) lattice.

Table 5.1: Representative double-perovskites in which the magnetic ions have a d^1 electron configuration. Θ_{CW} and μ_{eff} are the Curie-Weiss temperature and effective magnetic moment, respectively. This table is reproduced from Ref. [31].

Compound	$4d^1/5d^1$	Electron configuration	Θ_{CW}(K)	$\mu_{eff}(\mu_B)$	Magnetic transition	References
Ba_2YMoO_6	Mo^{5+}	$4d^1$	$-91 \sim -219$	$1.34 \sim 1.72$	PM down to 2 K	[19–23, 248]
Ba_2NaOsO_6	Os^{7+}	$5d^1$	~ -10	~ 0.6	FM T_c= 6.8 K	[28]
Ba_2LiOsO_6	Os^{7+}	$5d^1$	-40.5	0.733	AFM $T_c \sim 8$ K	[27]

5.2 Structural details of double-perovskites

Structurally, ordered double-perovskites with chemical formula $A_2BB'O_6$ are derived from the usual perovskites ABO_3 by selectively replacing half of the B ions with another species, denoted as B' (see Fig.5.2(a)). There are many such compounds with nonmagnetic B and B' sites occupied by $4d$ and/or $5d$ TM elements with d^1 or d^2 configuration (Re^{6+}, Os^{7+} and Mo^{5+} for d^1; Re^{5+} and Os^{6+} for d^2) [19–29, 248, 252, 253]. Because of the difference in the valence charges and ionic radii between the B and B' ions, the magnetic B' ions form an *fcc* lattice structure with very little intersite disorder and a lattice constant twice that of the original cubic cell. Moreover, the large separation of the TM B' ions in this structure (see Fig.5.2(b)) suppresses electron hopping

(a)

- A
- Oxygen
- BO_6 octahedron
- $B'O_6$ octahedron

(b)

- B
- B'
- Oxygen
- d_{xy} orbitals
- p_x, p_y orbitals
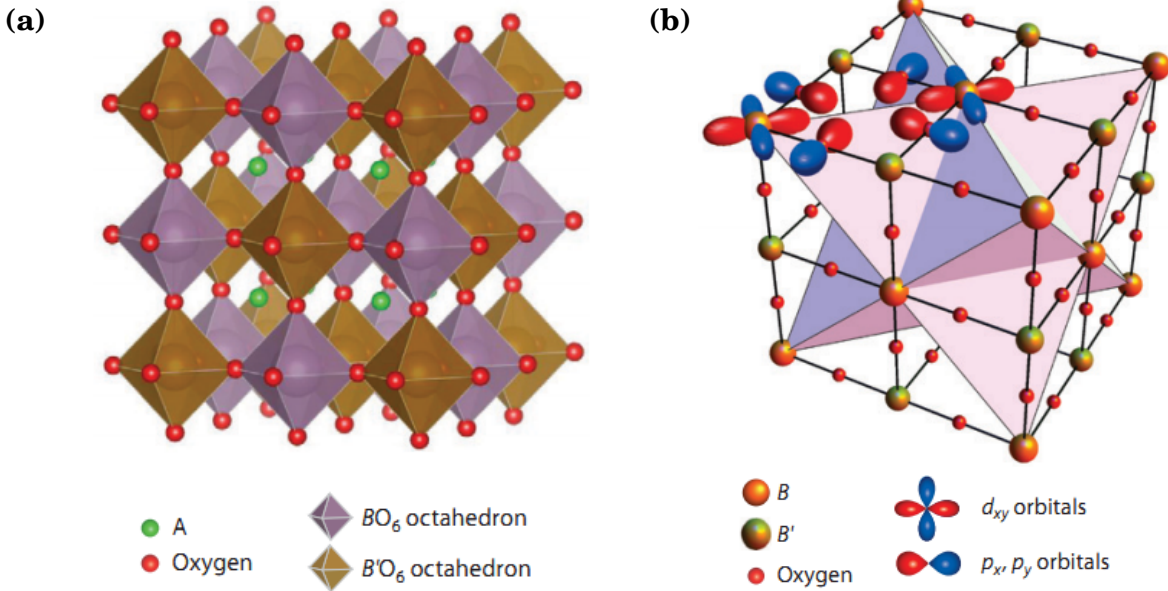
Figure 5.2: (a) The crystal structure of an ordered double-perovskite $A_2BB'O_6$. (b) The same structure, showing the geometrically frustrated *fcc* lattice of B sites as edge-sharing tetrahedra. Two d_{xy} orbitals on nearest-neighbor B sites are shown, with the intermediate p_x, p_y orbitals involved in their exchange path. A sites are not shown. Figure taken from Ref. [31].

and promotes Mott-insulating behavior.

At room temperature, Ba_2YMoO_6 and Ba_2MOsO_6 (M=Li, Na) have cubic double-perovskite structure, space group $Fm\bar{3}m$ [27]. Ba_2YMoO_6, with a lattice parameter a=8.392 Å at 297.8 K, shows no distortion from cubic symmetry even at 2.8 K [20]. At 293 K the lattice parameters for Ba_2LiOsO_6 and Ba_2NaOsO_6 are a=8.105 Å and a=8.287 Å [27], respectively.

5.3 $4d/5d$-shell excitations

QC calculations were performed on embedded clusters made of one reference MnO_6/OsO_6 octahedron. The closest Y/Li/Na and Ba cations around the reference $[MnO_6]/[OsO_6]$ fragment were also included in the actual cluster, as in the sketch shown in Fig.5.3(b). The farther solid-state surroundings were modeled as a finite array of point charges fitted to reproduce the crystal Madelung field in the cluster region [154, 229]. Crystallographic data as derived in Ref.[20] for Ba_2YMoO_6 and in Ref.[27] for Ba_2LiOsO_6 and Ba_2NaOsO_6 were employed. All *ab initio* calculations were carried out with the quantum chemistry package MOLPRO [181].

We used effective core potentials (ECP's), valence basis functions of triple-zeta quality, and two f polarization functions for the reference Mo/Os ions [149, 254] for which the d-shell excitations are explicitly computed. All-electron triple-zeta basis sets supplemented with two d polarization functions [118] were applied for each of the six adjacent O ligands. The eight Ba nearest neighbors were in each case modeled by Ba^{2+} 'total-ion' pseudopotentials (TIP's) supplemented with a single s function [255]. For Ba_2YMoO_6, the six nearby Y sites were described by ECP's and valence basis functions of double-zeta quality [254]. In Ba_2LiOsO_6 and Ba_2NaOsO_6, we employed TIP's for the six nearest Li and Na cations and sets of one s and one p functions

(a)

(b)
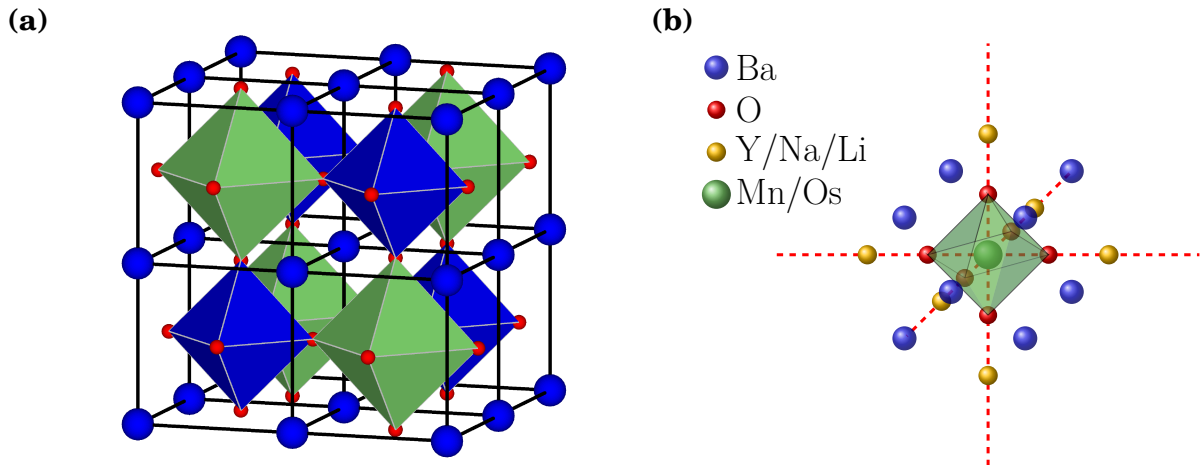
Figure 5.3: (a) Sketch of the atomic positions in a cubic double-perovskite compound, $Ba_2BB'O_6$. B stands here for either Y, Na or Li (site at the center of a dark-blue octahedron); B' is either Mo or Os (site at the center of a light-green octahedron). O ions are shown as small red spheres while the Ba sites are the larger blue spheres. (b) Sketch of the cluster used for the calculation of the d-level splittings. It consists of a central $[MnO_6]/[OsO_6]$ fragment and the closest Y/Na/Li and Ba cations.

[256].

For the CASSCF calculations of the d-shell splittings, we used active spaces of either three (t_{2g}) or five (t_{2g} plus e_g) orbitals. The CASSCF optimizations were carried out for an average of either the $^2T_{2g}(t_{2g}^1)$ or $^2T_{2g}(t_{2g}^1) + {}^2E_{2g}(e_g^1)$ eigenfunctions of the scalar relativistic Hamiltonian. The Pipek-Mezey localization module [186] available in MOLPRO was employed for separating the TM d and O $2p$ valence orbitals into different groups, i.e., centered either at sites of the central octahedron or at farther sites. All O $2p$ and Mo/Os $4d/5d$ electrons on the reference TM O$_6$ octahedron were correlated in the MRCI treatment. The latter was performed with single and double substitutions with respect to the CASSCF reference, as described in Ref. [230, 257]. The spin-orbit treatment was carried out according to the procedure described in Ref. [148].

There is no first-order SO interaction within the e_g manifold since the orbital angular momentum is completely quenched within this subspace. On the other hand, the SO interaction within the t_{2g} manifold removes the three-fold degeneracy. Provided that a large crystal field splitting separates the e_g and t_{2g} levels, one can treat the t_{2g} manifold as having an effective orbital angular momentum $\tilde{l} = 1$. These $\left|\tilde{l}, m_l\right\rangle$ states in the t_{2g}-orbital basis can be written as [246]

$$
\begin{aligned}
|1,1\rangle &= \frac{1}{\sqrt{2}}\big(-|d_{yz}\rangle + i|d_{xz}\rangle\big), \\
|1,0\rangle &= d_{xy}, \\
|1,-1\rangle &= \frac{1}{\sqrt{2}}\big(|d_{yz}\rangle + i|d_{xz}\rangle\big).
\end{aligned}
\tag{5.1}
$$

Within the LS-coupling scheme, one finds three Kramers doublets [258] with effective total angular momenta $\tilde{j} = 1/2$ ($m_j = \pm 1/2$), $\tilde{j} = 3/2$ ($m_j = \pm 1/2, \pm 3/2$). The $\tilde{j} = 1/2$ doublet is higher in energy as compared to the quartet $\tilde{j} = 3/2$ states. The energy difference between these SO $\tilde{j} = 1/2$ and $\tilde{j} = 3/2$ states is $3\lambda/2$, where λ is the SOC strength. Each $\left|\tilde{j}, m_j\right\rangle$ wave-function can be derived in the d-orbital basis using Eqs.(5.1) and the Clebsch-Gordan coefficients as

$$
\begin{aligned}
\left|\frac{1}{2}, \frac{1}{2}\right\rangle &= \frac{1}{\sqrt{3}}\left(\left|d_{yz}, -\frac{1}{2}\right\rangle + i\left|d_{zx}, -\frac{1}{2}\right\rangle + \left|d_{xy}, \frac{1}{2}\right\rangle\right), \\
\left|\frac{1}{2}, -\frac{1}{2}\right\rangle &= \frac{1}{\sqrt{3}}\left(\left|d_{yz}, \frac{1}{2}\right\rangle - i\left|d_{zx}, \frac{1}{2}\right\rangle - \left|d_{xy}, -\frac{1}{2}\right\rangle\right), \\
\left|\frac{3}{2}, \frac{1}{2}\right\rangle &= \frac{1}{\sqrt{6}}\left(\left|d_{yz}, -\frac{1}{2}\right\rangle + i\left|d_{zx}, -\frac{1}{2}\right\rangle - 2\left|d_{xy}, \frac{1}{2}\right\rangle\right), \\
\left|\frac{3}{2}, -\frac{1}{2}\right\rangle &= \frac{1}{\sqrt{6}}\left(-\left|d_{yz}, \frac{1}{2}\right\rangle + i\left|d_{zx}, \frac{1}{2}\right\rangle - 2\left|d_{xy}, -\frac{1}{2}\right\rangle\right), \\
\left|\frac{3}{2}, \frac{3}{2}\right\rangle &= \frac{1}{\sqrt{2}}\left(\left|d_{yz}, \frac{1}{2}\right\rangle + i\left|d_{zx}, \frac{1}{2}\right\rangle\right), \\
\left|\frac{3}{2}, -\frac{3}{2}\right\rangle &= \frac{1}{\sqrt{2}}\left(-\left|d_{yz}, -\frac{1}{2}\right\rangle + i\left|d_{zx}, -\frac{1}{2}\right\rangle\right).
\end{aligned}
\tag{5.2}
$$

In the following sections, we first investigate the essential features of the electronic structure of the cubic lattice configuration, without accounting for electron-lattice couplings.

5.3.1   Mo^{5+} $4d$-shell splittings in cubic Ba$_2$YMoO$_6$

Results for the Mo^{5+} $4d$-shell splittings ($\Delta_{3/2\to1/2}$ and $\Delta_{t_{2g}\to e_g}$) and 'static' $g_\parallel$ factors are listed in Table 5.2. At the CASSCF and MRCI levels, the crystal field splitting between t_{2g} and e_g ($\Delta_{t_{2g}\to e_g}$) is around ~4.6 eV. By comparing the CASSCF and MRCI results, with the inclusion of correlation effects brought by MRCI, the e_g^1 states shift to lower energy by 0.29 eV. However, with the inclusion of SO interactions, the excitation energies of the e_g^1 states increase by 0.05 eV in both CASSCF and MRCI. The strength of the SOC parameter can be derived from the splitting $\Delta_{3/2\to1/2}$ as $\lambda = \frac{2}{3}\Delta_{3/2\to1/2}^{\text{CASSCF}} = 89$ meV, which is somewhat smaller than earlier estimates of 99 meV for Mo^{5+} impurities in SrTiO$_3$ [259].

The g-factors were computed following the prescription of Bolvin [260] and Vancoillie [261]. It maps the matrix elements (ME's) of the *ab initio* Zeemen Hamiltonian

$$H_z = -\vec{\mu} \cdot \vec{h} = \mu_B \left(\vec{L} + g_e \vec{S} \right) \cdot \vec{h} \tag{5.3}$$

onto the ME's of the model pseudospin Hamiltonian

$$H_s = \mu_B \vec{h} \cdot \bar{\bar{g}} \cdot \vec{\tilde{S}}, \tag{5.4}$$

where $\vec{\mu}$, $\vec{L}$, $\vec{S}$ and $\vec{\tilde{S}}$ are magnetic moment, orbital angular-momentum, spin and pseudospin operators, respectively.

For a Kramers doublet ground state $\{\psi, \bar{\psi}\}$, the Abragam-Bleaney tensor [246] $\mathbf{G} = g g^T$ can be expressed in matrix form as

$$
\begin{aligned}
G_{kl} &= 2 \sum_{u,v=\psi,\bar{\psi}} \left\langle u | \hat{L}_k + g_e \hat{S}_k | v \right\rangle \left\langle v | \hat{L}_l + g_e \hat{S}_l | u \right\rangle \\
&= \sum_{m=x,y,z} \left(\Lambda_{km} + g_e \sum_{km} \right)\left(\Lambda_{lm} + g_e \sum_{lm} \right),
\end{aligned}
\tag{5.5}
$$

where g_e is the free-electron g factor and the $\bar{\bar{\Lambda}}$ and $\bar{\bar{\Sigma}}$ tensors are defined by

$$
\begin{aligned}
\Lambda_{kx} &= 2Re[\langle\bar{\psi}|\hat{L}_k|\psi\rangle], & \sum_{kx} &= 2Re[\langle\bar{\psi}|\hat{S}_k|\psi\rangle], \\
\Lambda_{ky} &= 2Im[\langle\bar{\psi}|\hat{L}_k|\psi\rangle], & \sum_{ky} &= 2Im[\langle\bar{\psi}|\hat{S}_k|\psi\rangle], \\
\Lambda_{kz} &= 2[\langle\psi|\hat{L}_k|\psi\rangle], & \sum_{kz} &= 2[\langle\psi|\hat{S}_k|\psi\rangle].
\end{aligned}
\tag{5.6}
$$

Table 5.2: Mo^{5+} $4d$-shell splittings ($j=3/2$ to $j=1/2$ and $t_{2g}-e_g$) and 'static' $g_\parallel$ factors in cubic Ba$_2$YMoO$_6$. Only the $4d$ t_{2g} orbitals were active in the CASSCF calculation for computing $\Delta_{3/2\to1/2}$; all five $4d$ orbitals were active in the calculations for $g_\parallel$ and $\Delta_{t_{2g}\to e_g}$. For the latter, values including SOC are provided within parentheses. All energies in eV.

Mo $4d^1$ electronic structure	CASSCF	MRCI
$\Delta_{3/2\to1/2}$	0.133	0.130
$\Delta_{t_{2g}\to e_g}$	4.75 (4.80)	4.46 (4.51)
$g_\parallel$	0.18	0.20

The ME's of $\hat{L}_k$ ($k = x, y, z$) were extracted from the MOLPRO outputs, while the ME's of $\hat{S}_k$ were derived using the conventional expressions for the generalized Pauli matrices:

$$\begin{aligned}
\left(\hat{S}_z\right)_{MM'} &= M\delta_{MM'}, \\
\left(\hat{S}_x\right)_{MM'} &= \frac{1}{2}\sqrt{(S+M)(S-M+1)}\delta_{M-1,M'} \\
&\quad + \frac{1}{2}\sqrt{(S-M)(S+M+1)}\delta_{M+1,M'}, \\
\left(\hat{S}_y\right)_{MM'} &= -\frac{i}{2}\sqrt{(S+M)(S-M+1)}\delta_{M-1,M'} \\
&\quad + \frac{i}{2}\sqrt{(S-M)(S+M+1)}\delta_{M+1,M'}.
\end{aligned} \tag{5.7}$$

$\bar{\bar{G}}$ is next diagonalized and the g-factors were calculated as the positive square roots of the three eigenvalues of $\mathbf{G}$, i.e., $g_{xx} > 0$, $g_{yy} > 0$ and $g_{zz} > 0$. The corresponding eigenvectors specify the rotation matrix to the main magnetic axes. In case of cubic double-perovskite compounds, the magnetic X, Y and Z axes are along these three C_4 axes, with $g_{zz}(g_\parallel) > g_{xx} = g_{yy} = 0$.

A most interesting finding is that despite the cubic environment the QC calculations yield a nonvanishing magnetic moment and a finite g-factor (see Table 5.2). This obviously does not fit the nonmagnetic $j = 3/2$ quartet ground state assumed to arise in standard textbooks on crystal-field theory [246, 247] from exact cancellation between the spin and the orbital moments. At a qualitative level, it has been argued by Stevens [249] that finite g-factor values can in fact occur for $j = 3/2$ ions due to TM-O covalency on the TM O_6 octahedron. For better insight into the nature of such effects, we therefore performed a simple numerical experiment in which the six ligands coordinating the reference Mo^{5+} $4d^1$ ion are replaced by -2 point charges with no atomic basis functions. In that additional set of computations the magnetic moment and the g-factor do vanish, in agreement with the purely ionic picture of Kotani, Abragam and Bleaney [245, 246]. This shows that one tuning knob for switching magnetism on is indeed the TM $4d - O$ $2p$ orbital hybridization. The latter is strong for high ionisation states such as Mo^{5+} (as the tails of the $4d$-like valence orbitals indicate in the case the nearest-neighbor ligands are provided with atomic basis sets, see Fig.5.4(a)), gives rise to partial quenching of the orbital moment and makes that the exact cancellation between the spin and the orbital moments no longer holds.

5.3.2 Os^{7+} $5d$-shell splittings in cubic Ba_2LiOsO_6 and Ba_2NaOsO_6

Results for the Os^{7+} $5d$-shell splittings ($\Delta_{3/2 \to 1/2}$ and $\Delta_{t_{2g} \to e_g}$) and 'static' $g_\parallel$ factors are listed in Table 5.3. These Os^{7+} $5d$-shell splittings show very similar features to the Mo^{5+} $4d$-shell splittings in cubic Ba_2YMoO_6. The SO wave-functions indicate that the ground state is the $\tilde{j} = 3/2$ quartet, separated from the higher-lying $\tilde{j} = 1/2$ state by at least 0.5 eV by both CASSCF+SOC and MRCI+SOC calculations.

The TM $5d - O$ $2p$ orbital hybridization effect is even stronger for the formally Os^{7+} ion in Ba_2LiOsO_6 and Ba_2NaOsO_6 as compared with that for Mo^{5+} in Ba_2YMoO_6. As shown in Table 5.3, $g_\parallel$ factors as large as 0.4 are computed in this case. The QC results also allow us to estimate the strength of the effective Os^{7+} $5d^1$ SOC constant, with $\lambda = \frac{2}{3}\Delta^{CASSCF}_{3/2 \to 1/2} = 387$ meV, lower than

Table 5.3: Os^{7+} $5d$-shell splittings ($j = 3/2$ to $j = 1/2$ and $t_{2g}-e_g$) and 'static' $g_\parallel$ factors in cubic Ba$_2$LiOsO$_6$ and Ba$_2$NaOsO$_6$. Only the $5d$ t_{2g} orbitals were active in the CASSCF calculation for computing $\Delta_{3/2\rightarrow1/2}$; all five $5d$ orbitals were active in the calculations for $g_\parallel$ and $\Delta_{t_{2g}\rightarrow e_g}$. For the latter, values including SOC are provided within parentheses. All energies in eV.

Os $5d^1$ electronic structure	CASSCF	MRCI
Ba$_2$LiOsO$_6$:		
$\Delta_{3/2\rightarrow1/2}$	0.58	0.56
$\Delta_{t_{2g}\rightarrow e_g}$	6.17 (6.44)	5.95 (6.21)
$g_\parallel$	0.39	0.40
Ba$_2$NaOsO$_6$:		
$\Delta_{3/2\rightarrow1/2}$	0.58	0.57
$\Delta_{t_{2g}\rightarrow e_g}$	6.41 (6.68)	6.19 (6.45)
$g_\parallel$	0.31	0.40

$\lambda = 468$ meV in tetravalent $5d^5$ iridates [262].

5.4 Effect of covalency and vibronic couplings on magnetic properties

As the t_{2g}^1 electron configuration is susceptible to JT effects, we carried out further investigations on the stability of an ideal TM O$_6$ octahedron against tetragonal (z-axis) distortions. In these calculations, the coordinates of the two oxygen ions on the z-axis are varied while keeping all other lattice coordinates unchanged, as illustrated in Fig.5.4(b). A total-energy profile for specified geometric configurations is provided in Fig. 5.4(c) for an embedded MoO$_6$ octahedron. It is seen that the minimum corresponds to about 3% tetragonal compression, as compared to the cubic octahedron of the $Fm3m$ crystalline structure [20]. As expected, the magnetic moment rapidly increases in the presence of distortions, as illustrated in Table 5.4 and Fig. 5.4(d).

Depending on further details related to the strength of the intersite couplings among 'JT centers', *static* deformations away from cubic symmetry may be realized in some systems, as observed for example in the Re^{6+} $5d^1$ double-perovskite Sr$_2$MgReO$_6$ [25] and rare-earth molibdates [263, 264]. If the local JT couplings and intersite interactions are relatively weak, one may be left on the other hand in a *dynamic* JT regime, as earlier pointed out for the particular t_{2g}^1 configuration by, e.g., Kahn and Kettle [265]. The relevant vibrational modes that couple to the $^2T_{2g}(t_{2g}^1)$ electronic term are those of E_g symmetry [$(3z^2-r^2)$- and (x^2-y^2)-like]. From the quantum chemistry calculations, we find that the potential-energy well is significantly shallower for these normal coordinates, as compared to z-axis-only compression. The value we computed for the Mo^{5+} ion in Ba$_2$YMoO$_6$, $\approx$40 meV, is comparable to the estimate made in the 1970's for Mo^{5+} t_{2g}^1 impurity ions within the SrTiO$_3$ matrix, $\approx$60 meV [266]. For the osmates, the depth of this
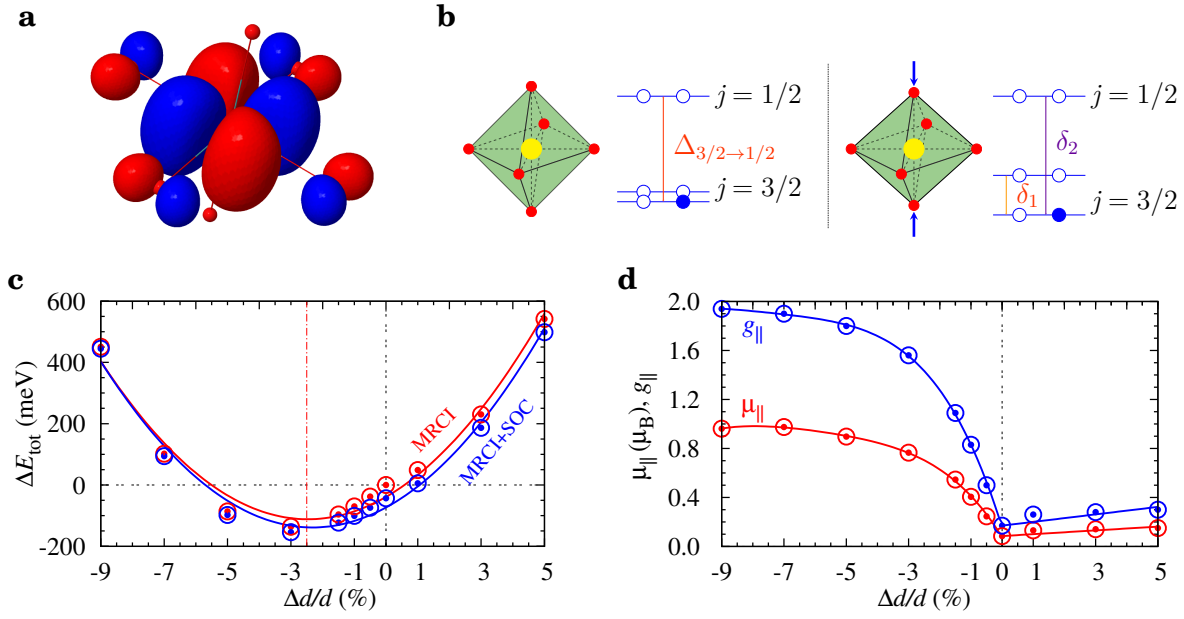
Figure 5.4: (a) Mo $4d$ t_{2g} function as obtained by CASSCF calculations. The tails at the nearest-neighbor O sites have substantial weight. (b) TM t_{2g} splittings in cubic (left) and tetragonal (right) symmetry; $\delta_1 = 0$ and $\delta_2 = \Delta_{3/2 \to 1/2}$ for cubic octahedra. (c) Ground-state energy of Ba_2YMoO_6 as function of z-axis tetragonal distortion, MRCI results both with and without spin-orbit coupling. (d) Variation of the Mo $4d^1$ magnetic moment ($\mu_\parallel$) and g factor ($g_\parallel$) with the amount of z-axis tetragonal distortion, MRCI results including spin-orbit interactions.

potential well is much reduced, with E_{JT} values in the range of 10–15 meV by spin–orbit MRCI calculations (Table 5.5).

The vibronic model of Kahn and Kettle [265] provides specific expressions for the g-factors. In particular, $g_\parallel$ can be parametrized as [265]

$$g_\parallel = 2(1 - k_{cov}k_{vib}), \tag{5.8}$$

Table 5.4: Mo^{5+} t_{2g}^1 electronic structure with 'static' tetragonal squeezing of the reference MoO_6 octahedron. Only the t_{2g}^1 configuration was considered in the reference CASSCF. $\Delta_{t_{2g}}$ is t_{2g} tetragonal splitting without SOC, δ_1 and δ_2 are excitation energies within the t_{2g}^1 manifold with SOC accounted for ($\delta_1 = 0$ and $\delta_2 = \Delta_{3/2 \to 1/2}$ for cubic octahedra). MRCI results, all energies in eV.

MoO_6 flattening	0.5%	1.5%	3%	5%
$\Delta_{t_{2g}}$	0.02	0.07	0.15	0.27
δ_1	0.02	0.05	0.12	0.24
δ_2	0.14	0.17	0.23	0.33
$\mu_\parallel$ (μ_B)	0.24	0.55	0.75	0.89
$g_\parallel$ ($k_{vib} = 1$)	0.50	1.09	1.55	1.80

Table 5.5: TM $g_\parallel$ factors using the Kahn-Kettle vibronic model [265] and *ab initio* estimates for λ, k_{cov} and E_{JT}. $x = 3E_{\text{JT}}/2\hbar\omega$, $\rho = 3\lambda/2\hbar\omega$, $\hbar\omega$ is set to 70 meV [22, 267], and $g_\parallel = 2(1 - k_{\text{cov}}k_{\text{vib}})$.

	E_{JT}	x	ρ	k_{vib}	k_{cov}	$g_\parallel$
Mo^{5+} $4d^1$, Ba$_2$YMoO$_6$	40	0.86	1.90	0.74	0.90	0.66
Os^{7+} $5d^1$, Ba$_2$LiOsO$_6$	10	0.21	8.29	0.98	0.80	0.44
Os^{7+} $5d^1$, Ba$_2$NaOsO$_6$	15	0.32	8.29	0.97	0.80	0.45

where k_{cov} is Stevens' covalency factor [249] and

$$k_{\text{vib}} = \exp[-x/(1+\rho)]. \tag{5.9}$$

The parameters x and ρ are defined as [265] $x = 3E_{\text{JT}}/2\hbar\omega$ and $\rho = 3\lambda/2\hbar\omega$, where $\hbar\omega$ is the E_g-mode vibrational energy and $g_\perp = 0$ by symmetry [246, 249, 265]. Recent infrared transmission spectra indicate that $\hbar\omega \approx 560$ cm$^{-1} \approx 70$ meV for the bond stretching phonons [22, 267]. The k_{vib} parameter can be interpreted as a factor arising from a reduction of the orbital angular momentum. The effective parameter k_{cov} we can easily evaluate from the static $g_\parallel$ values obtained in the MRCI spin-orbit treatment (see Table 5.2 and Table 5.3) if vibronic interactions are neglected ($k_{\text{vib}} = 1$ for 'frozen' cubic octahedra), with $k_{\text{cov}} \equiv 1 - g_\parallel^{\text{MRCI}}/2$. This yields covalency reduction factors of 0.90 for Ba$_2$YMoO$_6$ and 0.80 for the osmates.

Estimates for $g_\parallel$ are provided in Table 5.5, using the Kahn-Kettle vibronic model and the QC results for λ, k_{cov} and E_{JT}. It is seen that a large ρ/x ratio (i.e., large λ/E_{JT}) makes that $g_\parallel$ is generated mostly through covalency effects in the osmates, with minor contributions from vibronic couplings. On the other hand, the small ρ/x ratio in Ba$_2$YMoO$_6$ gives rise to a strong enhancement of $g_\parallel$ through vibronic effects, with a factor of nearly 4 between $(1 - k_{\text{cov}}k_{\text{vib}})$ and $(1 - k_{\text{cov}})$. In the Kahn-Kettle frame, we thus find that the TM magnetic moment is mainly due to vibronic effects in Ba$_2$YMoO$_6$ and predominantly to strong covalency in Ba$_2$LiOsO$_6$ and Ba$_2$NaOsO$_6$.

5.5 Discussion

Experimentally, the measured magnetic moments are indeed significantly smaller in Ba$_2$LiOsO$_6$ and Ba$_2$NaOsO$_6$ [28, 29] as compared to Ba$_2$YMoO$_6$ [20, 22, 248, 266]. With regard to the estimates we make here for $g_\parallel$, possible sources of errors concern the accuracy of the calculated E_{JT} when using the experimental crystal structure as reference and correlation and polarisation effects beyond a single TM O$_6$ octahedron [268, 269]. The latter effects would only increase E_{JT}. With respect to the former aspect, it was found that by advanced QC calculations the lattice constants of TM oxides can be computed with deviations of less than 0.5% from the measured values [268], which implies rather small corrections to E_{JT}. Interestingly, recent findings of additional phonon modes at low temperatures [22] indicate static distortions of the MoO$_6$ oc-

tahedra in Ba_2YMoO_6 and indeed a rather large E_{JT}. Using lattice structures optimized by density functional calculations, Iwahara *et al.* [270] found somewhat different results for the E_{JT} effective parameters. Valuable experimental data that can be directly compared to these calculations would be the results of electron spin resonance measurements of the g factor.

It is also worth pointing out that using the Kahn-Kettle model even a E_{JT} of 75 meV, five to seven times larger than the values computed by MRCI for the osmates (see Table 5.5), still yields a rather moderate $g_{\parallel}$ factor of 0.65 for the Os $5d^1$ ion. Such $g_{\parallel}$ factors of 0.4–0.6 compare quite well with the low-temperature magnetic moment derived from magnetization and muon spin relaxation measurements on Ba_2NaOsO_6, $\approx 0.2\,\mu_B$ [28, 29]. For the Mo $4d^1$ ion in Ba_2YMoO_6, the computed $g_{\parallel}$ factor is much more sensitive to variations of E_{JT} — increasing E_{JT} from, e.g., 40 to 200 meV enhances $g_{\parallel}$ of Eq.5.8 from ≈ 0.6 to ≈ 1.6.

One other remarkable prediction of Kahn and Kettle [265] is that the splitting of the $j = 3/2$ and $j = 1/2$ states is increased through vibronic couplings, by a factor

$$\gamma = 1 + x\frac{3+\rho}{3(\rho^2-1)}. \qquad (5.10)$$

This effect turns out to be small in the osmates, given the small x and large ρ in those compounds. But we compute a strong modification of the $j = 3/2$ to $j = 1/2$ excitation energy for Ba_2YMoO_6, from about 0.13 eV in the absence of vibronic interactions (see Table 5.2) to ≈ 0.20 eV with JT effects included ($E_{JT} = 40$ meV). Experimentally the situation can be clarified by direct resonant inelastic X-ray scattering (RIXS) measurements on Ba_2YMoO_6. High-resolution RIXS measurements could also address the occurrence of static distortions at low temperatures, suggested for Ba_2YMoO_6 on the basis of extra phonon modes in the low-T infrared transmission spectra [22] and for Ba_2NaOsO_6 from the integrated entropy through the magnetic phase transition at ~ 7 K [28]. According to the MRCI data in Table 5.4, a reduction by 0.5–1.5% of the interatomic distances on one set of O–Mo–O links already gives a splitting of 20–50 meV of the low-lying spin–orbit states. Splittings of this size should be accessible with last-generation RIXS apparatus.

Also of interest is an experimental confirmation of the unusually large t_{2g}–e_g gap we predict in the double-perovskite heptavalent osmates, $\gtrsim 6$ eV (see Table 5.3). According to the results of additional computations we carried out, the source of this exceptional d-level splitting is the stabilization of the Os t_{2g} states due to the large effective charge (formally 7+) at the nearest-neighbor Os sites. The latter are situated on the axes along which the lobes of the t_{2g} orbitals are oriented; in contrast, the lobes of the e_g functions point towards the monovalent species (Li^{1+} or Na^{1+}). For example, test CASSCF calculations in which the size of the point charges placed at the 12 Os and 6 alkaline-ion nearest-neighbor sites are modified from the formal ionic values 7+ and 1+ ($12 \times 7 + 6 \times 1 = 90$) to 5+ and 5+ ($12 \times 5 + 6 \times 5 = 90$) show a reduction of about 2 eV of the t_{2g}–e_g level splitting. Similar effects, with relative shifts and even inversion of the d-electron energy levels due to charge imbalance at nearby cation sites, were recently evidenced in Sr_2RhO_4 and Sr_2IrO_4 [189, 262], the rare-earth 227 iridates $R_2Ir_2O_7$ [271] and $Cd_2Os_2O_7$ [191]. The mechanism has not been thoroughly explored so far experimentally but seems to hold much potential in the context of orbital engineering in TM compounds.

5.6   Conclusions

To summarize, it is well known that nominal orbital degeneracy gives rise in $3d$ TM oxides to subtle couplings between the electronic and lattice degrees of freedom and very rich physics. Here we resolve the effect of electron-lattice interactions on the magnetic properties of heavier, $4d$ and $5d$ TM ions with a formally degenerate t_{2g}^1 electron configuration in the double-perovskite materials Ba_2YMoO_6, Ba_2LiOsO_6 and Ba_2NaOsO_6. In particular, by using advanced QC electronic-structure calculations, we reconcile the notion of a nonmagnetic spin-orbit-coupled t_{2g}^1 $j = 3/2$ ground state put forward by Kotani, Abragam, Bleaney and others [245–247] with the variety of magnetic properties recently observed in $4d^1$ and $5d^1$ double-perovskites. Our analysis shows that the sizable magnetic moments and g-factors found experimentally are due to strong TM d – ligand p hybridization and dynamic JT effects, providing new perspectives on the interplay between metal-ligand interactions and SOCs in TM oxides. It also suggests the possible theoretical frame for addressing the remarkably rich magnetic properties of d^1 double-perovskites [19, 21, 28, 29, 31] in particular. Over the last two decades, vibronic couplings have unjustifiably received low attention in the case of these intriguing materials.

Chapter 6

Magnetic interactions in the $5d^3$ perovskite NaOsO$_3$

In this chapter, using many-body quantum chemistry (QC) calculations, we address magnetic exchange interactions in the $S=3/2$ orthorhombic perovskite NaOsO$_3$, which hosts a metal-insulator transition (MIT) driven by antiferromagnetic ordering. We first investigate the on-site $d-d$ excitations in NaOsO$_3$, and further map the calculated two-site magnetic spectrum onto model Hamiltonians including both isotropic Heisenberg and anisotropic Dzyaloshinskii-Moriya (DM) interactions. We find antiferromagnetic (AFM) nearest-neighbor (NN) Heisenberg exchange interactions J_{ac} = 24.4 meV and J_b = 20.9 meV, around twice larger than the J proposed by analyzing the magnon excitation spectra of Ref. [272]. The magnitudes of the single-ion anisotropy and DM vectors are 2 meV and 2.5 meV, respectively. Our QC results provide useful information for more detailed investigations of the magnetic properties of NaOsO$_3$.

6.1   Introduction

$5d$ transition-metal oxides (TMOs), having comparable scales for the kinetic energy, on-site Coulomb repulsion and spin-orbit coupling (SOC), provide an excellent platform for the emergence of properties beyond those possible in $3d$-based materials [31, 33]. Extensive research has been focused on unconventional spin-orbit physics in various $5d$ systems. Of particular interest in this regard are the $5d^5$ iridates. In iridates, the subtle interplay between spin-orbit interactions and sizable electron correlations gives rise to large anisotropic interactions and magnetic moments [13, 15, 243, 273–277]. Due to the strong SOC, these magnetic moments are described as effective $j \approx 1/2$ entities [13, 15] and the effective anisotropic exchange parameters are orders of magnitude larger than in $3d$ TMOs [240, 243, 278–282]. For instance, in the square-lattice system Sr$_2$IrO$_4$, the prevailing anisotropy is the antisymmetric coupling, i.e., the Dzyaloshinskii-Moriya (DM) interaction, which is as large as ~15 meV [15, 189, 283, 284], while in honeycomb Na$_2$IrO$_3$ the symmetric anisotropic exchange defines the dominant contribution to the effective spin Hamiltonian [15, 242, 243]. In addition to the insulating $j_{eff} \approx 1/2$ ground state in $5d^5$ iridates, questions abound concerning the effects of SOC and the strength of magnetic interactions in other $5d$ TMOs.

The $5d^3$ osmates present a particularly intriguing puzzle. Considering a d^3 ion in an octahedral environment, the octahedral crystal field splits the d levels into a lower-lying triply degenerate t_{2g} and a higher-lying doubly degenerate e_g group of levels. The three electrons occupying the t_{2g} levels form a $S = 3/2$ state, orbital singlet, thus there is no orbital angular momentum. In such case the SOC enters only as a perturbation [285]. Yet there is clear experimental evidence that SOC has considerable influence in $5d^3$ TMOs. This has been demonstrated by the observation of large spin gaps in their magnetic excitation spectra [272, 286–288]. One of the most intensively studied materials is the perovskite NaOsO$_3$, which has been proposed to be an example of Slater insulator [17, 18, 272, 289–291]. First-principles calculations within the local density approximation with Hubbard U corrections (LDA+U method) suggest that AFM interactions are important to opening up the insulating gap [17], whilst the SOC plays a minor role. Du *et al.* [289] performed calculations within the local spin density approximation (LSDA) and also determined that the inclusion of SOC only slightly perturbed the band structure. By using neutron and X-ray scattering, it has been established that NaOsO$_3$ has G-type AFM order, with Os ions coupled antiferromagnetically with all of their nearest neighbors and spins of Os ions oriented along the c axis [18], as shown in Fig. 6.1. The MIT at T$_{MIT}$=410 K occurs concomitant with the onset of long-range commensurate 3D AFM order [17, 18, 289–291]. The magnetic exchange interactions directly probed by resonant inelastic X-ray scattering (RIXS) show a dispersive and strongly gapped (58 meV) excitation, which was modeled within a minimal effective Hamiltonian with single-ion anisotropy (SIA) and Heisenberg exchange (NN $J_{ac}=J_b$=13.9 meV) [272]. It should be noted that in NaOsO$_3$ one would expect a non-zero DM vector [292], as the oxygen anion mediating the superexchange between two Os sites does not sit at an inversion centre.

In this study we provide results of many-body QC calculations for NaOsO$_3$. We describe the local Os^{5+} $5d^3$ multiplet structure, the $5d^3$ zero-field splitting (ZFS) and also determine the parameters of the effective NN spin Hamiltonian, i.e., NN Heisenberg exchange and the DM interaction.

6.2   Os $5d$-shell excitations

The general formula of a perovskite is ABO$_3$. The most idealized structure implies cubic $Pm\bar{3}m$ symmetry. In this structure, the A cation sits on the corners of a cube, the smaller B cation sits at the centre of the cube and is octahedrally coordinated to oxygen ions located at the face centers. NaOsO$_3$ exists in the orthorhombic $Pnma$ space group [17], with lattice parameters a = 5.384 Å, b = 7.580 Å and c = 5.328 Å. The orthorhombic distortion arises as a result of a concerted rotation of the OsO$_6$ octahedra in the ac plane, coupled with a tilting about the b axis (see Fig.6.1(a)).

To determine the Os^{5+} $5d$-shell electronic structure, an embedded cluster consisting of one central OsO$_6$ octahedron, the six NN OsO$_6$ octahedra and the nearby eight Na ions was considered in our QC study. The solid-state surroundings were modeled as a large array of point charges fitted [154] to reproduce the crystal Madelung field in the cluster region. We used ef-

Table 6.1: MRCI and MRCI+SOC relative energies (eV) for the Os^{5+} $5d^3$ multiplet structure in $NaOsO_3$. Notations for O_h symmetry are used. Each MRCI+SOC value stands for a spin-orbit doublet. For the ^4T states, only the lowest and highest components are shown.

$5d^3$ splittings	MRCI	MRCI+SOC($\times 2$)	Exp. [272]
$^4A_2$ (t_{2g}^3)	0.00	0.00; 3.8×10^{-3}	
^2E (t_{2g}^3)	1.48; 1.48	1.50; 1.52	
$^2T_1$ (t_{2g}^3)	1.57; 1.58; 1.58	1.67; 1.68; 1.81	$1.0 - 1.7$
$^2T_2$ (t_{2g}^3)	2.31; 2.31; 2.32	2.66; 2.84; 2.86	
$^4T_2$ ($t_{2g}^2 e_g^1$)	5.00; 5.02; 5.04	5.11 ... 5.38	
$^4T_1$ ($t_{2g}^2 e_g^1$)	5.72; 5.76; 5.78	6.03 ... 6.33	$3.5 - 4.8$
$^4T_1$ ($t_{2g}^1 e_g^2$)	10.14; 10.15; 10.19	10.44 ... 10.91	

fective core potentials (ECP's) along with tripe-zeta valence basis sets for the central Os ion [149] and all-electron triple-zeta basis sets for the six adjacent O ligands [118], supplemented with polarization functions. For the Os NN's, we employed ECP's: each Os^{5+} ion was treated as a pseudo phosphorus (P^{5+}) ion [293]. The core potential consists of a $[Xe]4f^{14}$ closed-shell and three additional electrons occupying the $5d_{xy}$, $5d_{yz}$ and $5d_{xz}$ orbitals, while the $5d_{z^2}$ and $5d_{x^2-y^2}$ orbitals are kept empty. A $2s2p2d$ basis set was optimized for this ECP's and the MOL-PRO input is given in Table 6.5. All-electron double-zeta basis sets [118] were applied for those O ions coordinating the NN Os sites but not shared with the central octahedron. The eight nearest Na cations were modeled by total-ion potentials supplemented with one s function [256]. For the complete active space self-consistent field (CASSCF) calculations, we used an active space of five orbitals (the t_{2g} and e_g orbitals at the central Os site) and three electrons. The self-consistent-field (SCF) optimization was carried out for an average of ten quartet and eight doublet states associated with this manifold. The Pipek-Mezey localization module [186] available in MOLPRO was employed for separating the Os $5d$ and O $2p$ valence orbitals into different groups, i.e., centered either at sites of the central octahedron or at NN octahedra. In following multirefer-ence configuration-interaction (MRCI) computations [230, 294], the O $2p$ and Os $5d$ electrons at the central octahedron were correlated, with single and double substitutions with respect to the CASSCF reference. The MRCI treatment was performed for the quartet and doublet multi-plicities as ten- and eight-root calculations, respectively. All these states entered the spin-orbit treatment, in both CASSCF and MRCI. The spin-orbit treatment was carried out according to the procedure described in Ref. [148]. All QC calculations were performed with the MOLPRO package [181]. Crystallographic data as derived in Ref. [17] were employed.

From simple considerations based on ligand-field theory (LFT), the orbital ground state (GS) for a d^3 ion in octahedral coordination is a singlet. According to our QC calculations, the lowest electron configuration indeed is $^4A_2(t_{2g}^3)$ if SOC is not included; see Table 6.1. We use here the

Table 6.2: Relative energies (eV) at the MRCI and MRCI+SOC level of theory for the Os^{5+} $5d^3$ multiplet structure in NaOsO$_3$, as obtained in additional calculations where the NN Os^{5+} ions are explicitly modeled as open-shell Os^{5+} t_{2g}^3 ions. Notations for O_h symmetry are used. Each MRCI+SOC value stands for a spin-orbit doublet. For the ^4T states, only the lowest and highest components are shown.

$5d^3$ splittings	MRCI	MRCI+SOC($\times 2$)	Exp. [272]
$^4A_2$ (t_{2g}^3)	0.00	0.00; 5.5×10^{-3}	
^2E (t_{2g}^3)	1.51; 1.51	1.41; 1.52	
$^2T_1$ (t_{2g}^3)	1.63; 1.63; 1.65	1.65; 1.66; 1.78	$1.0-1.7$
$^2T_2$ (t_{2g}^3)	2.44; 2.47; 2.49	2.64; 2.76; 2.86	
$^4T_2$ $(t_{2g}^2 e_g^1)$	4.50; 4.52; 4.52	4.54 ... 4.84	
$^4T_1$ $(t_{2g}^2 e_g^1)$	5.31; 5.32; 5.40	5.41 ... 5.73	$3.5-4.8$
$^4T_1$ $(t_{2g}^1 e_g^2)$	9.23; 9.26; 9.30	9.28 ... 9.81	

more convenient notations associated to O_h symmetry, although the calculations were performed for the actual experimental geometry, with lower point-group symmetry. The components of the $^4A_2$ GS term can interact via SOC with higher-lying T_2 terms and for noncubic axial systems further split into two Kramers doublets with $m_s=\pm1/2$ and $m_s=\pm3/2$, respectively [295, 296]. The MRCI+SOC data in Table 6.1 show that the ZFS of the $^4A_2$ multiplet is 3.8 meV. A first estimate of the SIA parameter is then $|A| \approx 1.9$ meV, much larger than for $3d$ ions in similar coordination [295, 296]. The t_{2g}^3 excited states ^2E, $^2T_1$ and $^2T_2$ occur in the energy region $1.5-3.0$ eV. The $t_{2g} - e_g$ transitions associated with quartet states are located in two different energy windows, i.e., $t_{2g}^3 - t_{2g}^2 e_g^1$ transitions from 5.1 to 6.4 eV and $t_{2g}^3 - t_{2g}^1 e_g^2$ transitions from 10.4 to 11.0 eV. These $d-d$ transitions in NaOsO$_3$ are analogous to those of the $5d^3$ pyrochlore Cd$_2$Os$_2$O$_7$ [191], since both Os ions have similar octahedral environment. A better description of the states in the energy window from 1.5 to 11.0 eV is expected to be achieved by accounting for configurational mixing implying higher-lying $t_{2g}^{3-n} e_g^n$ and charge-transfer $d^4 L$ (L denotes an O $2p$ hole) states.

Modeling the NN Os ions

One additional set of calculations was carried out having all six NN Os sites modeled as Os^{5+} species with open-shell $5d^3$ configurations. In these extra calculations, ECP's along with double-zeta valence basis sets were applied for the NN Os ions [149]. The CASSCF calculations were performed in two steps. In the first step, all 21 Os t_{2g} orbitals, i.e., three t_{2g} orbitals of the central Os site plus eighteen t_{2g} orbitals of the NN Os sites, and 21 Os $5d$ electrons were considered as active (CAS[21, 21]). All these Os $5d$ orbitals and the $2p$ orbitals of oxygens belonging to the central octahedron were optimized for the high-spin $S_{tot} = 21/2$ state. Appropriate changes were further operated for the optimized orbital set to remove the NN Os t_{2g} orbitals from explicit treatment by means of a level shift in order to calculate the on-site $d-d$ excita-
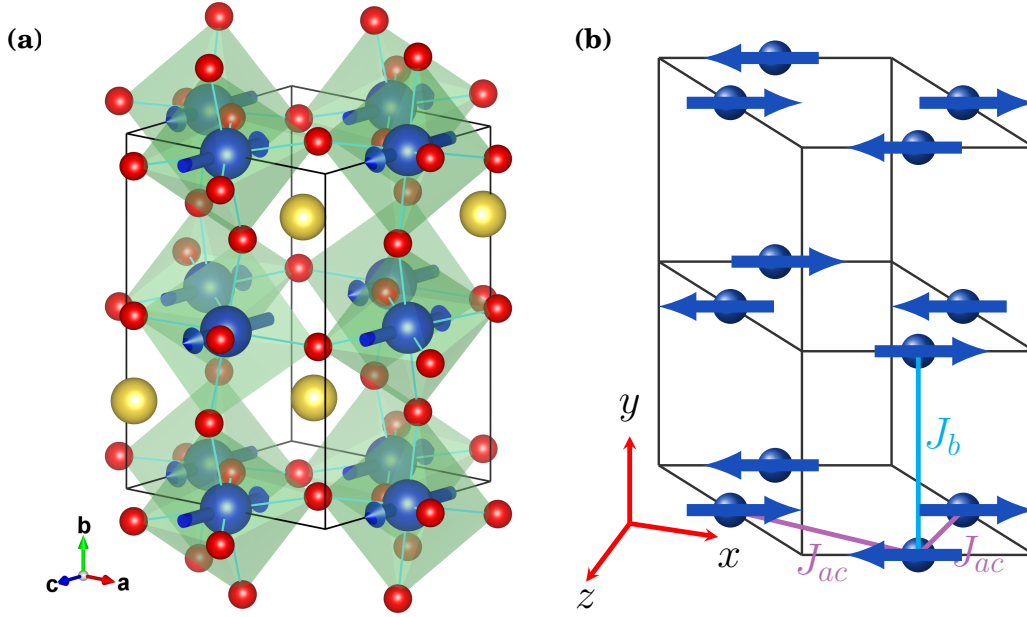
Figure 6.1: (a) Distorted crystal structure of $NaOsO_3$, space group $Pnma$. There is a doubling along the b axis due to tilting of the OsO_6 octahedra. The red and yellow spheres indicate oxygen and Na atoms, respectively. (b) The G-type AFM order is shown schematically. For clarity only the Os ions are represented. The NN exchange paths J_{ac} and J_c are shown. The choice of the local coordinate system $\{x, y, z\}$ is discussed in the text.

tions for the central Os ion in the average field of the NN Os t_{2g} orbitals. All five $5d$ orbitals and three electrons of the central Os ion were considered to be active (CAS[3,5]). The calculated Os $5d$-shell excitations are given in Table 6.2.

The Os^{5+} $5d^3$ multiplet structure computed by modeling the NN Os sites as Os^{5+} t_{2g}^3 ions (see Table 6.2) display the same sequence of electronic states as Table 6.1. The MRCI+SOC SIA parameter is 2.75 meV, about 45% larger than the SIA parameter estimated in Table 6.1. The $t_{2g}-t_{2g}$ transitions are located in the energy region $1.4-2.9$ eV, similar with the results in Table 6.1. The $t_{2g}^3 - t_{2g}^2 e_g^1$ and $t_{2g}^3 - t_{2g}^1 e_g^2$ transitions associated with quartet states occur from 4.5 to 5.7 eV and 9.3 to 9.8 eV, respectively, $0.6-1.1$ eV lower as compared to the results in Table 6.1.

6.3 Magnetic couplings and Dzyaloshinskii-Moriya interaction

To determine the NN magnetic couplings, we carried out many-body QC calculations for larger embedded clusters. To accurately describe the charge distribution in the immediate neighborhood of the two central OsO_6 octahedra, the ten adjacent octahedra and the closest 12 Na sites were also incorporated in the actual cluster. It is worth pointing out that there are two different Os-O-Os bond angles (θ_1 and θ_2) in $NaOsO_3$ [17]: $\theta_1 = 155.2°$ for the NN exchange path J_{ac} with a Os-Os bond length d_1(Os-Os) = 3.787 Å and $\theta_2 = 153.9°$ for the NN exchange path J_b with a Os-Os bond length d_2(Os-Os) = 3.790 Å, as shown in Fig. 6.1(b). Different embedded clusters were constructed for these two different bond angles. The basis functions of the central Os sites, NN Os sites and nearest Na sites used here were the same as for those used in computing the

Table 6.3: Relative energies (meV) of the singlet, triplet, quintet and septet states for two NN Os $5d^3$ sites with different Os-O-Os bond angles (θ_1 and θ_2) in NaOsO$_3$. The energy of the singlet is taken as reference for each angle.

	ROHF	MCSCF	MRCI	MRCI+SOC
θ_1=155.2°, d(Os$_1$−Os$_2$)=3.787Å:				
S_{tot}=0	0.00	0.00	0.00	0.00
S_{tot}=1	−9.28	14.23	24.41	24.4, 24.4, 24.7
S_{tot}=2	−27.84	42.76	73.39	73.6, 73.6, 73.8, 73.8, 73.9
S_{tot}=3	−55.65	85.57	146.57	147.0, 147.0, 147.2, 147.2, 147.3, 147.3, 147.4
θ_2=153.9°, d(Os$_1$−Os$_2$)=3.790Å:				
S_{tot}=0	0.00	0.00	0.00	0.00
S_{tot}=1	−8.73	11.83	20.89	20.9, 20.9, 21.2
S_{tot}=2	−26.13	35.58	62.69	62.9, 62.9, 63.1, 63.1, 63.2
S_{tot}=3	−52.09	71.32	125.41	125.8, 125.8, 126.0, 126.0, 126.2, 126.2, 126.2

Os $5d$-shell excitations presented in Table 6.1 (see Section 6.2). For the O ligand bridging the two magnetically active Os sites, we employed quintuple-zeta valence basis sets and four polarization d functions [118]. All-electron tripe-zeta basis sets [118] were used for the other O ions located at the two central OsO$_6$ octahedra. For farther ligands in our cluster, we applied minimal atomic-natural-orbital basis sets [297].

Multiconfiguration wave-functions were first generated by state-averaged MCSCF optimizations for the lowest singlet, triplet, quintet and septet states for this [Os$_2$O$_{11}$] fragment. Those configuration state functions give rise in the spin-orbit calculations to sixteen spin-orbit states. For each spin multiplicity, the MCSCF active space was defined by the set of six Os t_{2g} orbitals accommodating a total number of six electrons. We then further accounted for single and double excitations from the Os t_{2g} and bridging O $2p$ orbitals on top of the MCSCF reference wavefunctions. To derive the magnitude of direct exchange, we additionally performed restricted open-shell Hartree-Fock (ROHF) calculations [63].

Results for two NN Os $5d^3$ sites at different levels of approximation are shown in Table 6.3. We note that, without SOC, the energy splittings between the different spin states follow the sequence J, $3J$ and $6J$, which can be fitted to the Heisenberg-Dirac-van Vleck (HDVV) Hamiltonian $\hat{\mathcal{H}}=J_{ij}\tilde{\mathbf{S}}_i \cdot \tilde{\mathbf{S}}_j$ (J_{ij} is the isotropic AFM exchange constant between spins $\tilde{\mathbf{S}}_i$ and $\tilde{\mathbf{S}}_j$) [298]. A first estimate by MRCI gives $J_{ac} \approx 24$ meV and $J_b \approx 21$ meV.

Non-Heisenberg terms can be further obtained from spin-orbit calculations within the manifold defined by the lowest singlet, triplet, quintet and septet spin states for the two Os t_{2g}^3 sites.

Table 6.4: Intersite isotropic Heisenberg coupling parameters J and DM vectors extracted from the MRCI+SOC calculations for different Os-O-Os bond angles (θ_1 and θ_2) in NaOsO$_3$ (all values in meV).

$\theta_1 = 155.2°$:	J_1	24.4
	$\mathbf{D_1}$ (D_{1x}, D_{1y}, D_{1z})	(0, −1.83, 1.96)
$\theta_2 = 153.9°$:	J_2	20.9
	$\mathbf{D_2}$ (D_{2x}, D_{2y}, D_{2z})	(2.12, 0, -1.41)

Including SOCs does not bring significant corrections to the effective Heisenberg superexchange. However, the spin-orbit interactions lift the degeneracy of the initial spin multiplets and bring in antisymmetric contributions. To describe the latter, we adopt a two-site effective Hamiltonian $\mathcal{H}_{mod}$ containing, in addition to the Heisenberg term, a DM antisymmetric exchange contribution and a biquadratic term:

$$\mathcal{H}_{mod}^{ij} = J\tilde{\mathbf{S}}_i \cdot \tilde{\mathbf{S}}_j + \mathbf{D} \cdot \tilde{\mathbf{S}}_i \times \tilde{\mathbf{S}}_j + K(\tilde{\mathbf{S}}_i \cdot \tilde{\mathbf{S}}_j)^2, \tag{6.1}$$

where $\tilde{\mathbf{S}}_i$, $\tilde{\mathbf{S}}_j$ are pseudospin-3/2 operators, J is the isotropic Heisenberg coupling, $\mathbf{D}$ is the antisymmetric DM exchange vector and K is the non-Heisenberg biquadratic coupling parameter. The local coordinate system {x, y, z} is defined in Fig. 6.1(b), with the x axis along the NN J_{ac} exchange path and the y axis along the NN J_c exchange path. The $\mathcal{H}_{mod}$ Hamiltonian is then compared with the *ab initio* 16×16 effective matrix $\mathcal{H}_{eff}$ derived from the MRCI+SOC calculations (see more details in Table 6.6, Table 6.7 and Table 6.8). We found perfect one-to-one correspondence between the two sets of matrix elements and could easily extract the numerical parameters J, $\mathbf{D}$ and K. The magnitude of K is smaller than 0.01 meV, thus the biquadratic coupling can be ignored in further analysis. The corresponding parameters J and $\mathbf{D}$ are listed in Table 6.4.

In a recent study by S. Calder *et al.* [272], RIXS was used to directly probe magnetic exchange interactions: a dispersive and strongly gapped (∼58 meV) excitation was observed and described within a minimal model Hamiltonian with NN Heisenberg exchange ($J_{ac}=J_b$=13.9 meV) and a spin-orbit induced anisotropic term, i.e., either symmetric exchange anisotropy (1.4 meV) or SIA (4 meV). Interestingly, the J_{ac} and J_b computed from spin-orbit MRCI calculations are about 76% and 50% larger, respectively, as compared to the results reported from the RIXS experiment [272]. The puzzling aspect is that QC calculations based on either configuration-interaction techniques or second-order perturbation theory always underestimate the experimentally derived J coupling constants and are able to reproduce the latter with accuracy better than 20% in insulating 3d-metal oxides [82–86, 299]. It has been also shown that accurate J's [300] and $d-d$ excitation energies [240, 300–302] can indeed be computed for 5d oxides such as the iridates. The QC results we discuss here should therefore stimulate further detailed analysis in order to clarify the magnitude of the NN Heisenberg couplings in NaOsO$_3$.

6.4 Summary

In this chapter, we employ *ab initio* many-body QC methods to study the on-site $d-d$ excitations in NaOsO$_3$. We further map the calculated two-site magnetic spectrum onto model Hamiltonians including both isotropic Heisenberg and anisotropic DM interactions. We find AFM NN Heisenberg exchange interactions of $J_{ac} = 24.4$ and $J_b = 20.9$ meV, almost twice larger than the NN J derived in Ref. [272] from RIXS data. The magnitudes of the SIA and DM vectors are in the range of 2 meV and 2.5 meV, respectively. According to the QC results, the dominant magnetic interaction in NaOsO$_3$ is the AFM NN Heisenberg exchange. The magnetic couplings we compute here motivate more detailed investigations of the adiabatic magnon spectra in NaOsO$_3$.

Table 6.5: The MOLPRO input for the ECP's of the NN Os^{5+} ions used in QC calculations [293].

```
ecp,P,10,3;
1;2,1.,0.;
2;1,1.00,5.;3,1.00,5.*1.00;
2;1,0.82,5.;3,0.82,5.*0.82;
2;1,0.50,5.;3,0.50,5.*0.50;

s,P,0.610,0.180;
p,P,0.750,0.166;
d,P,0.644,0.118;
```

Table 6.6: Matrix elements of the spin Hamiltonian in the coupled basis $|S^{tot}, M_S^{tot}\rangle$ for $\mathcal{H}_{mod}^{ij} = J\tilde{\mathbf{S}}_i \cdot \tilde{\mathbf{S}}_j + \mathbf{D} \cdot \tilde{\mathbf{S}}_i \times \tilde{\mathbf{S}}_j + K(\tilde{\mathbf{S}}_i \cdot \tilde{\mathbf{S}}_j)^2$, $\tilde{S}_{i,j} = \frac{3}{2}$.

$\mathcal{H}_{mod}^{ij}$	$\lvert 3,-3\rangle$	$\lvert 3,-2\rangle$	$\lvert 3,-1\rangle$	$\lvert 3, 0\rangle$	$\lvert 3, 1\rangle$	$\lvert 3, 2\rangle$	$\lvert 3, 3\rangle$
$\langle 3, -3\rvert$	$\frac{9}{4}J + \frac{81}{16}K$	0	0	0	0	0	0
$\langle 3, -2\rvert$	0	$\frac{9}{4}J + \frac{81}{16}K$	0	0	0	0	0
$\langle 3, -1\rvert$	0	0	$\frac{9}{4}J + \frac{81}{16}K$	0	0	0	0
$\langle 3, 0\rvert$	0	0	0	$\frac{9}{4}J + \frac{81}{16}K$	0	0	0
$\langle 3, 1\rvert$	0	0	0	0	$\frac{9}{4}J + \frac{81}{16}K$	0	0
$\langle 3, 2\rvert$	0	0	0	0	0	$\frac{9}{4}J + \frac{81}{16}K$	0
$\langle 3, 3\rvert$	0	0	0	0	0	0	$\frac{9}{4}J + \frac{81}{16}K$
$\langle 2, -2\rvert$	$\frac{3}{2}\sqrt{\frac{3}{2}}(d_y + id_x)$	$i\frac{3}{2}d_z$	$\frac{3}{2\sqrt{10}}(d_y - id_x)$	0	0	0	0
$\langle 2, -1\rvert$	0	$\frac{3}{2}(d_y + id_x)$	$i3\sqrt{\frac{2}{5}}d_z$	$\frac{3}{2}\sqrt{\frac{3}{10}}(d_y - id_x)$	0	0	0
$\langle 2, 0\rvert$	0	0	$\frac{3}{2}\sqrt{\frac{3}{5}}(d_y + id_x)$	$i\frac{9}{2\sqrt{5}}d_z$	$\frac{3}{2}\sqrt{\frac{3}{5}}(d_y - id_x)$	0	0
$\langle 2, 1\rvert$	0	0	0	$\frac{3}{2}\sqrt{\frac{3}{10}}(d_y + id_x)$	$i3\sqrt{\frac{2}{5}}d_z$	$\frac{3}{2}(d_y - id_x)$	0
$\langle 2, 2\rvert$	0	0	0	0	$\frac{3}{2\sqrt{10}}(d_y + id_x)$	$i\frac{3}{2}d_z$	$\frac{3}{2}\sqrt{\frac{3}{2}}(d_y - id_x)$
$\langle 1, -1\rvert$	0	0	0	0	0	0	0
$\langle 1, 0\rvert$	0	0	0	0	0	0	0
$\langle 1, 1\rvert$	0	0	0	0	0	0	0
$\langle 0, 0\rvert$	0	0	0	0	0	0	0

$\mathcal{H}_{mod}^{ij}$	$\lvert 2,-2\rangle$	$\lvert 2,-1\rangle$	$\lvert 2,0\rangle$	$\lvert 2,1\rangle$	$\lvert 2,2\rangle$	$\lvert 1,-1\rangle$	$\lvert 1,0\rangle$	$\lvert 1,1\rangle$	$\lvert 0,0\rangle$
$\langle 3, -3\rvert$	$\frac{3}{2}\sqrt{\frac{3}{2}}(d_y - id_x)$	0	0	0	0	0	0	0	0
$\langle 3, -2\rvert$	$-\frac{3}{2}id_z$	$\frac{3}{2}(d_y - id_x)$	0	0	0	0	0	0	0
$\langle 3, -1\rvert$	$\frac{3}{2\sqrt{10}}(d_y + id_x)$	$-i3\sqrt{\frac{2}{5}}d_z$	$\frac{3}{2}\sqrt{\frac{3}{5}}(d_y - id_x)$	0	0	0	0	0	0
$\langle 3, 0\rvert$	0	$\frac{3}{2}\sqrt{\frac{3}{10}}(d_y + id_x)$	$-i\frac{9}{2\sqrt{5}}d_z$	$\frac{3}{2}\sqrt{\frac{3}{10}}(d_y - id_x)$	0	0	0	0	0
$\langle 3, 1\rvert$	0	0	$\frac{3}{2}\sqrt{\frac{3}{5}}(d_y + id_x)$	$-i3\sqrt{\frac{2}{5}}d_z$	$\frac{3}{2\sqrt{10}}(d_y - id_x)$	0	0	0	0
$\langle 3, 2\rvert$	0	0	0	$\frac{3}{2}(d_y + id_x)$	$-i\frac{3}{2}d_z$	0	0	0	0
$\langle 3, 3\rvert$	0	0	0	0	$\frac{3}{2}\sqrt{\frac{3}{2}}(d_y + id_x)$	0	0	0	0
$\langle 2, -2\rvert$	$-\frac{3}{4}J + \frac{9}{16}K$	0	0	0	0	$2\sqrt{\frac{3}{5}}(d_y - id_x)$	0	0	0
$\langle 2, -1\rvert$	0	$-\frac{3}{4}J + \frac{9}{16}K$	0	0	0	$-i2\sqrt{\frac{3}{5}}d_z$	$\sqrt{\frac{6}{5}}(d_y - id_x)$	0	0
$\langle 2, 0\rvert$	0	0	$-\frac{3}{4}J + \frac{9}{16}K$	0	0	$\sqrt{\frac{2}{5}}(d_y + id_x)$	$-i\frac{4}{\sqrt{5}}d_z$	$\sqrt{\frac{2}{5}}(d_y - id_x)$	0
$\langle 2, 1\rvert$	0	0	0	$-\frac{3}{4}J + \frac{9}{16}K$	0	0	$\sqrt{\frac{6}{5}}(d_y + id_x)$	$-i2\sqrt{\frac{3}{5}}d_z$	0
$\langle 2, 2\rvert$	0	0	0	0	$-\frac{3}{4}J + \frac{9}{16}K$	0	0	$2\sqrt{\frac{3}{5}}(d_y + id_x)$	0
$\langle 1, -1\rvert$	$2\sqrt{\frac{3}{5}}(d_y + id_x)$	$i2\sqrt{\frac{3}{5}}d_z$	$\sqrt{\frac{2}{5}}(d_y - id_x)$	0	0	$-\frac{11}{4}J + \frac{121}{16}K$	0	0	$\frac{1}{2}\sqrt{\frac{5}{2}}(d_y - id_x)$
$\langle 1, 0\rvert$	0	$\sqrt{\frac{6}{5}}(d_y + id_x)$	$i\frac{4}{\sqrt{5}}d_z$	$\sqrt{\frac{6}{5}}(d_y - id_x)$	0	0	$-\frac{11}{4}J + \frac{121}{16}K$	0	$-i\frac{1}{2}\sqrt{5}d_z$
$\langle 1, 1\rvert$	0	0	$\sqrt{\frac{2}{5}}(d_y + id_x)$	$i2\sqrt{\frac{3}{5}}d_z$	$2\sqrt{\frac{3}{5}}(d_y - id_x)$	0	0	$-\frac{11}{4}J + \frac{121}{16}K$	$\frac{1}{2}\sqrt{\frac{5}{2}}(d_y + id_x)$
$\langle 0, 0\rvert$	0	0	0	0	0	$\frac{1}{2}\sqrt{\frac{5}{2}}(d_y + id_x)$	$i\frac{1}{2}\sqrt{5}d_z$	$\frac{1}{2}\sqrt{\frac{5}{2}}(d_y - id_x)$	$-\frac{15}{4}J + \frac{225}{16}K$

Table 6.7: Effective interaction matrix in the coupled basis $|S^{\text{tot}}, M_S^{\text{tot}}\rangle$, obtained from two-site MRCI+SOC calculations for an Os-O-Os bond angle $\theta_1 = 155.2°$ (all values in meV).

$\mathcal{H}_{eff}^{ij}$	$|3,-3\rangle$	$|3,-2\rangle$	$|3,-1\rangle$	$|3, 0\rangle$	$|3, 1\rangle$	$|3, 2\rangle$	$|3, 3\rangle$
$\langle 3, -3|$	146.953	0	0	0	0	0	0
$\langle 3, -2|$	0	146.953	0	0	0	0	0
$\langle 3, -1|$	0	0	146.953	0	0	0	0
$\langle 3, 0|$	0	0	0	146.953	0	0	0
$\langle 3, 1|$	0	0	0	0	146.953	0	0
$\langle 3, 2|$	0	0	0	0	0	146.953	0
$\langle 3, 3|$	0	0	0	0	0	0	146.953
$\langle 2, -2|$	−3.362	2.947i	−0.868	0	0	0	0
$\langle 2, -1|$	0	−2.745	3.728i	−1.503	0	0	0
$\langle 2, 0|$	0	0	−2.126	3.954i	−2.126	0	0
$\langle 2, 1|$	0	0	0	−1.503	3.728i	−2.745	0
$\langle 2, 2|$	0	0	0	0	−0.868	2.947i	−3.362
$\langle 1, -1|$	0	0	0	0	0	0	0
$\langle 1, 0|$	0	0	0	0	0	0	0
$\langle 1, 1|$	0	0	0	0	0	0	0
$\langle 0, 0|$	0	0	0	0	0	0	0

$\mathcal{H}_{eff}^{ij}$	$|2,-2\rangle$	$|2,-1\rangle$	$|2,0\rangle$	$|2,1\rangle$	$|2,2\rangle$	$|1,-1\rangle$	$|1,0\rangle$	$|1,1\rangle$	$|0,0\rangle$
$\langle 3, -3|$	−3.362	0	0	0	0	0	0	0	0
$\langle 3, -2|$	−2.947i	−2.745	0	0	0	0	0	0	0
$\langle 3, -1|$	−0.868	−3.728i	−2.126	0	0	0	0	0	0
$\langle 3, 0|$	0	−1.503	−3.954i	−1.503	0	0	0	0	0
$\langle 3, 1|$	0	0	−2.126	−3.728i	−0.868	0	0	0	0
$\langle 3, 2|$	0	0	0	−2.745	−2.947i	0	0	0	0
$\langle 3, 3|$	0	0	0	0	−3.362	0	0	0	0
$\langle 2, -2|$	73.774	0	0	0	0	−2.877	0	0	0
$\langle 2, -1|$	0	73.774	0	0	0	−3.078i	−2.034	0	0
$\langle 2, 0|$	0	0	73.775	0	0	−1.175	−3.553i	−1.175	0
$\langle 2, 1|$	0	0	0	73.774	0	0	−2.034	−3.078i	0
$\langle 2, 2|$	0	0	0	0	73.774	0	0	−2.877	0
$\langle 1, -1|$	−2.877	3.078i	−1.175	0	0	24.789	0	0	−1.477
$\langle 1, 0|$	0	−2.034	3.554i	−2.034	0	0	24.789	0	−2.230i
$\langle 1, 1|$	0	0	−1.175	3.078i	−2.877	0	0	24.789	−1.477
$\langle 0, 0|$	0	0	0	0	0	−1.477	2.230i	−1.477	0.382

Table 6.8: Effective interaction matrix in the coupled basis $|S^{tot}, M_S^{tot}\rangle$, obtained from two-site MRCI+SOC calculations for an Os-O-Os bond angle θ_2=153.9° (all values in meV).

$\mathcal{H}_{eff}^{ij}$	$|3,-3\rangle$	$|3,-2\rangle$	$|3,-1\rangle$	$|3, 0\rangle$	$|3, 1\rangle$	$|3, 2\rangle$	$|3, 3\rangle$
$\langle 3, -3|$	125.808	0	0	0	0	0	0
$\langle 3, -2|$	0	125.808	0	0	0	0	0
$\langle 3, -1|$	0	0	125.808	0	0	0	0
$\langle 3, 0|$	0	0	0	125.808	0	0	0
$\langle 3, 1|$	0	0	0	0	125.808	0	0
$\langle 3, 2|$	0	0	0	0	0	125 .808	0
$\langle 3, 3|$	0	0	0	0	0	0	125.808
$\langle 2, -2|$	3.895i	−2.117i	−1.006i	0	0	0	0
$\langle 2, -1|$	0	3.180i	−2.677i	−1.742i	0	0	0
$\langle 2, 0|$	0	0	2.463i	−2.840i	−2.463i	0	0
$\langle 2, 1|$	0	0	0	1.742i	−2.677i	−3.181i	0
$\langle 2, 2|$	0	0	0	0	1.006i	−2.117i	−3.895i
$\langle 1, -1|$	0	0	0	0	0	0	0
$\langle 1, 0|$	0	0	0	0	0	0	0
$\langle 1, 1|$	0	0	0	0	0	0	0
$\langle 0, 0|$	0	0	0	0	0	0	0

$\mathcal{H}_{eff}^{ij}$	$|2,-2\rangle$	$|2,-1\rangle$	$|2,0\rangle$	$|2,1\rangle$	$|2,2\rangle$	$|1,-1\rangle$	$|1,0\rangle$	$|1,1\rangle$	$|0,0\rangle$
$\langle 3, -3|$	−3.895i	0	0	0	0	0	0	0	0
$\langle 3, -2|$	2.117i	−3.180i	0	0	0	0	0	0	0
$\langle 3, -1|$	1.006i	2.677i	−2.464i	0	0	0	0	0	0
$\langle 3, 0|$	0	1.742i	2.840i	−1.742i	0	0	0	0	0
$\langle 3, 1|$	0	0	2.464i	2.678i	−1.006i	0	0	0	0
$\langle 3, 2|$	0	0	0	3.180i	2.118i	0	0	0	0
$\langle 3, 3|$	0	0	0	0	3.895i	0	0	0	0
$\langle 2, -2|$	63.094	0	0	0	0	3.330i	0	0	0
$\langle 2, -1|$	0	63.094	0	0	0	−2.222i	2.355i	0	0
$\langle 2, 0|$	0	0	63.094	0	0	−1.360i	−2.566i	1.360i	0
$\langle 2, 1|$	0	0	0	63.094	0	0	−2.355i	−2.222i	0
$\langle 2, 2|$	0	0	0	0	63.094	0	0	−3.330i	0
$\langle 1, -1|$	−3.330i	2.222i	1.360i	0	0	21.303	0	0	1.707i
$\langle 1, 0|$	0	−2.355i	2.566i	2.355i	0	0	21.300	0	−1.614i
$\langle 1, 1|$	0	0	−1.360i	2.222i	3.330i	0	0	21.300	−1.707i
$\langle 0, 0|$	0	0	0	0	0	−1.707i	1.614i	1.707i	0.403

Chapter 7

Superexchange interactions between spin-orbit-coupled $j \simeq 1/2$ ions in oxides with face-sharing ligand octahedra

In this chapter, using *ab initio* wave-function-based calculations, we provide valuable insights with regard to the magnetic exchange in $5d$ and $4d$ oxides with face-sharing ligand octahedra, $BaIrO_3$ and $BaRhO_3$. Surprisingly strong antiferromagnetic Heisenberg interactions as large as 400 meV are computed for idealized iridate structures with 90° Ir-O-Ir bond angles and in the range of 125 meV for angles of 80° as measured experimentally in $BaIrO_3$. These estimates exceed the values derived so far for corner-sharing and edge-sharing systems and motivate more detailed experimental investigations of quantum magnets with extended $5d/4d$ orbitals and networks of face-sharing ligand cages. The strong electron-lattice couplings evidenced by our calculations suggest rich phase diagrams as function of strain and pressure, a research direction with much potential for materials of this type.

7.1   Introduction

The interest in the preparation and characterization of $5d$ oxides and halides goes back to the 1950's but some of the major implications of having a strong spin-orbit coupling (SOC), at least for certain $5d^n$ electron configurations, have been only recently realized. The work of Kim *et al.* on the square-lattice $5d^5$ iridate Sr_2IrO_4 [13, 273], for example, led to the concept of a spin-orbit driven (Mott-like) insulator while Jackeli and Khaliullin [239] brought to the forefront of oxide research the honeycomb $5d^5$ iridates, as possible hosts for Kitaev physics [303] and novel magnetic ground states and excitations [304]. Both types of these iridate structures – square and honeycomb lattices – have been the topic of extensive investigations in recent years. The honeycomb compounds display edge-sharing ligand octahedra and advanced electronic-structure calculations indicate that the Kitaev exchange is indeed the largest intersite magnetic coupling [242, 243]. Remarkably large anisotropic interactions were also found for corner-sharing ligand cages in Sr_2IrO_4, in that case of Dzyaloshinskii-Moriya type, with strengths in the range of 10–15 meV [189, 239].

7. Superexchange interactions between spin-orbit-coupled $j \simeq 1/2$ ions in oxides with
face-sharing ligand octahedra

70

In contrast to the cases of corner- and edge-sharing coordination, little is known with respect to the magnitude of the effective coupling constants for adjacent octahedra connected through a O_3 facet. Representative materials of the latter type are the canted antiferromagnet $BaIrO_3$ [305–310], the putative spin-liquid $Ba_3InIr_2O_9$ [311], the spin-gapped system $Ba_3BiIr_2O_9$ [312], $BaRhO_3$ [313] and $BaCoO_3$ [314]. Here we provide *ab initio* results with regard to the strength of facet-mediated superexchange for IrO_6 (RhO_6) octahedra as found in the $5d$ ($4d$) t_{2g}^5 system $BaIrO_3$ ($BaRhO_3$). We predict remarkably large antiferromagnetic (AFM) Heisenberg interactions in the range of 100 meV for Ir-O-Ir angles of about 80° as found experimentally in $BaIrO_3$ [313]. Moreover, for bond angles $\gtrsim 85°$ the Heisenberg J even exceeds 200 meV in our simulations. So strong AFM superexchange has been found so far only in one-dimensional corner-sharing cuprates [315, 316]. Our findings point to a picture of unusually large, AFM couplings within the face-sharing octahedral units of $BaIrO_3$. The strong dependence on bond angles of the effective magnetic interactions further resonates with available experimental data on $BaIrO_3$ [306, 309, 317–319] and $Ba_3BiIr_2O_3$ [312], that indicate subtle interplay between the electronic and lattice degrees of freedom in these compounds.

7.2 Material model

$BaIrO_3$ features a distorted hexagonal structure with both face-sharing and corner-sharing IrO_6 octahedra [320]. Those connected by one single ligand form honeycomb-like planes; the linkage of adjacent honeycomb layers is ensured by inter-layer Ir ions, located such that blocks of three face-sharing octahedra are formed along the c axis, see Fig. 7.1(a). Since for any pair of nearest-neighbor (NN) octahedra the actual point-group symmetry is very low, we focus in our study on an idealized material model displaying D_{3h} symmetry: $[Ir_2O_9]^{10-}$ units as depicted in Fig. 7.1(b) around which we additionally considered, for keeping overall charge neutrality, three Ba sites within the plane of the median O_3 facet and two extra Ba ions along the z axis. Although this material model is somewhat oversimplified, it should rather well describe the essential short-range electron interactions, as confirmed by similar investigations of edge-sharing $5d^5$ compounds [243].

One feature of $5d$ transition-metal (TM) ions is that their valence orbitals are much more diffuse as compared to first-series TM species. The ligand field is therefore more effectively felt and for instance the Ir^{4+} ions tend to adopt low-spin t_{2g}^5 configurations. The more extended nature of the $5d$ functions further gives rise to large intersite hoppings and large superexchange, as in e.g. Sr_2IrO_4 [189, 239] and $CaIrO_3$ [321]. Under strong octahedral crystal fields (CFs) and spin-orbit interactions, with one single unpaired electron ($S=1/2$) in the t_{2g} manifold (orbital angular momentum $L=1$), the $5d^5$ ($4d^5$) valence electron configuration of Ir^{4+} (Rh^{4+}) in $BaIrO_3$ ($BaRhO_3$) yields an effective $j=1/2$ Kramers-doublet ground state [239, 246]. Deviations from a perfect cubic environment may lead to some degree of admixture between the $j=1/2$ and lower-lying $j=3/2$ spin-orbit states [246].

To estimate the strengths of the exchange interactions in $BaIrO_3$ and $BaRhO_3$, both isotropic and anisotropic, we here employ many-body *ab initio* techniques from wave-function-based quan-

(a)

(b)
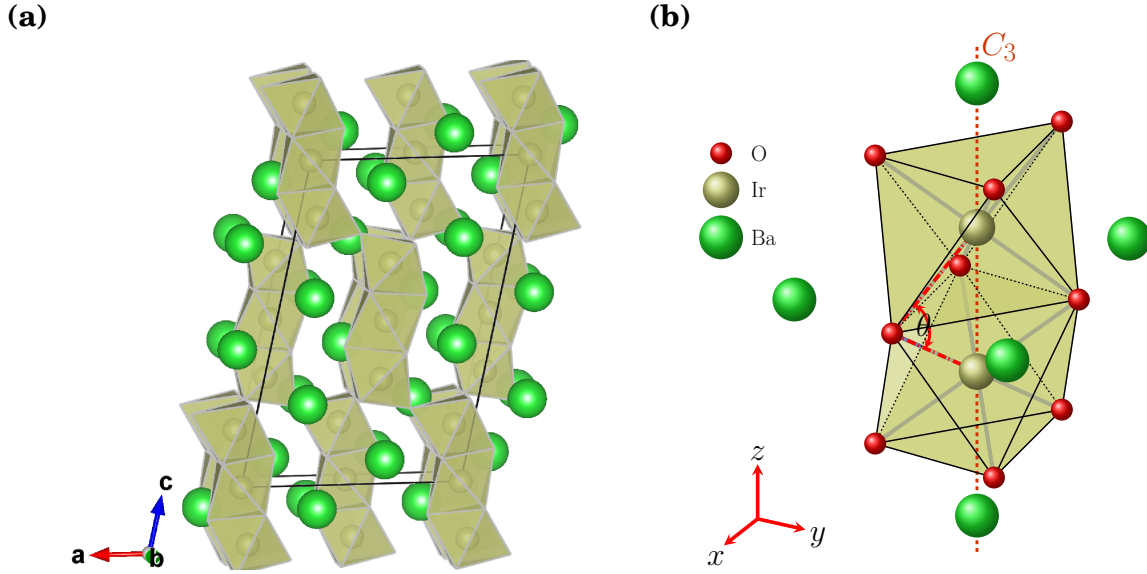
Figure 7.1: (a) Crystal structure of $BaIrO_3$, with both face-sharing and corner-sharing IrO_6 octahedra. Ba atoms are shown as large green spheres. (b) Material model used for the calculation of magnetic interactions between two NN TM sites with face-sharing connectivity of the O octahedra. The point-group symmetry is D_{3h}.

tum chemistry (QC), then map the magnetic spectrum obtained in the QC calculations onto an appropriate effective spin Hamiltonian. The form of the latter is dictated by the symmetry of the material model employed in the QC simulations.

7.3 Magnetic interactions

For the idealized M_2O_9 cluster (M=Ir, Rh) of face-sharing octahedra (Fig. 7.1(b)) the overall symmetry is D_{3h}. Each particular superexchange path M_i-O_n-M_j ($n = 1, 2, 3$) implies a finite Dzyaloshinskii-Moriya (DM) vector $\mathbf{D}_{ij}^n$, since there is no inversion center for the M_2O_9 unit. However, given the D_{3h} symmetry, these DM vectors lie within the plane of the O_3-facet and are related to each other through rotations around the C_3 axis. This yields a vanishing DM coupling $\mathbf{D}_{ij} = \sum_n \mathbf{D}_{ij}^n = 0$. For a pair of NN 1/2 pseudospins $\tilde{\mathbf{S}}_i$ and $\tilde{\mathbf{S}}_j$ with this type of linkage, the most general bilinear spin Hamiltonian can be then cast in the form

$$\mathcal{H}_{ij} = J_{ij}\tilde{\mathbf{S}}_i \cdot \tilde{\mathbf{S}}_j + \tilde{\mathbf{S}}_i \cdot \Gamma_{ij} \cdot \tilde{\mathbf{S}}_j, \tag{7.1}$$

where J_{ij} is the isotropic Heisenberg exchange and Γ_{ij} is a symmetric traceless second-rank tensor that describes the symmetric exchange anisotropy. Considering the three-fold rotational symmetry around the M-M link, it is convenient to have one of the coordinates along the line defined by the two M sites. We therefore use the local frame indicated in Fig. 7.1(b), with both Ir ions on the z axis. In this coordinate system the $\bar{\bar{\Gamma}}$ tensor is diagonal and, for symmetry reasons,

72

7. Superexchange interactions between spin-orbit-coupled $j \simeq 1/2$ ions in oxides with
face-sharing ligand octahedra

can be written as

$$\bar{\bar{\Gamma}} = \begin{pmatrix} \Gamma & 0 & 0 \\ 0 & \Gamma & 0 \\ 0 & 0 & -2\Gamma \end{pmatrix}. \tag{7.2}$$

The eigenstates of such a two-site $\tilde{S}=1/2$ system are the singlet $|\Psi_S\rangle = (|\uparrow\downarrow\rangle - |\downarrow\uparrow\rangle)/\sqrt{2}$ and the three triplet components $|\Psi_1\rangle = (|\uparrow\downarrow\rangle + |\downarrow\uparrow\rangle)/\sqrt{2}$, $|\Psi_2\rangle = (|\uparrow\uparrow\rangle + |\downarrow\downarrow\rangle)/\sqrt{2}$, $|\Psi_3\rangle = (|\uparrow\uparrow\rangle - |\downarrow\downarrow\rangle)/\sqrt{2}$. The corresponding eigenvalues are

$$
\begin{aligned}
E_S &= -\frac{3}{4}J, & E_1 &= \frac{1}{4}J - \frac{1}{2}\Gamma, \\
E_2 &= \frac{1}{4}J + \Gamma, & E_3 &= \frac{1}{4}J - \frac{1}{2}\Gamma.
\end{aligned}
\tag{7.3}
$$

Expression (7.1) can be then simplified to

$$\mathcal{H}_{ij} = \bar{J}\tilde{\mathbf{S}}_i \cdot \tilde{\mathbf{S}}_j + \bar{\Gamma}\tilde{S}_i^z \tilde{S}_j^z, \tag{7.4}$$

where $\bar{J} \equiv J + \Gamma$ and $\bar{\Gamma} \equiv -3\Gamma$.

Energy-consistent relativistic pseudopotentials were used for the Ir [149] and Rh [254] ions. For the Ir/Rh sites, the valence orbitals were described by basis sets of tripe-zeta quality supplemented with two f polarization functions [149, 254]. For the ligand O's bridging the two magnetically active Ir (Rh) ions, quintuple-zeta valence basis sets and four d polarization functions were applied [118]. The other O's were modeled by triple-zeta valence basis sets [118]. The five Ba ions were modeled by Ba^{2+} 'total-ion' pseudopotentials (TIP's) supplemented with a single s function [255]. We used interatomic distances as derived by E. Stitzer *et al.* [313]. All computations were performed with the MOLPRO quantum chemistry package [181].

The first step in the actual QC calculations is defining a relevant set of Slater determinants in the prior complete-active-space self-consistent-field (CASSCF) treatment [63]. For two IrO_6 (RhO_6) octahedra, an optimal choice is having five electrons and three (t_{2g}) orbitals at each of the two magnetically active Ir (Rh) sites. The self-consistent-field optimization was carried out for an average of the lowest nine singlet and lowest nine triplet states associated with this manifold. Subsequent multireference configuration-interaction (MRCI) computations were performed for each spin multiplicity, either singlet or triplet, as nine-root calculations. All these states entered the spin-orbit treatment [148], in both CASSCF and MRCI. Within the group of 36 spin-orbit eigenvectors associated with the $t_{2g}^5 - t_{2g}^5$ manifold, the lowest-lying four "magnetic" states are separated by a significant energy gap from the other 32 states. The latter correspond to on-site $j \approx 3/2$ to $j \approx 1/2$ transition and are therefore left aside in the actual mapping procedure. In other words, given the strong SOC and large $j \approx 3/2$ to $j \approx 1/2$ excitation energies, the initial 36×36 problem can be smoothly mapped onto a 4×4 construction as defined by the effective Hamiltonian (7.1).

In the MRCI treatment, single and double excitations from the six Ir (Rh) t_{2g} orbitals and from the $2p$ shells of the bridging O ligand sites were taken into account. The Pipek-Mezey localization module [186] available in MOLPRO was employed for separating the metal $5d$ ($4d$) and

O $2p$ valence orbitals into different groups. To derive the magnitude of the direct exchange, we additionally performed calculations in which the active space is again defined by ten electrons and six orbitals but intersite $t_{2g}-t_{2g}$ excitations are forbidden by restricting to maximum five the number of electrons per TM site. We refer to these results as rAS (restricted active space, maximum one hole per site).

The mapping of the *ab initio* QC data onto the effective spin model defined by Eq. (7.1) implies the lowest four spin-orbit states associated with the different possible couplings of two NN pseudospins-1/2. In order to safely identify the singlet and triplet components, we also consider the Zeeman coupling

$$\hat{\mathcal{H}}^Z = \sum_{l=A,B} \mu_B (\mathbf{L}_l + g_e \mathbf{S}_l) \cdot \mathbf{H}, \tag{7.5}$$

where $\mathbf{L}_l$ and $\mathbf{S}_l$ are angular-momentum and spin operators at a given Ir/Rh site, while g_e and μ_B stand for the free-electron Landé factor and Bohr magneton, respectively. Each of the resulting matrix element computed at the QC level is assimilated to the corresponding matrix element of the effective spin Hamiltonian. This one-to-one correspondence between *ab initio* and effective-model matrix elements enables a clear assignment of each magnetically active spin-orbit CASSCF/MRCI state and determination of all couplings constants.

[Ir$_2$O$_9$] unit

Effective magnetic couplings for Ir$_2$O$_9$ fragments of two face-sharing IrO$_6$ octahedra are listed in Table 7.1, for an Ir-Ir interatomic distance $d_0 = 2.63$ Å and ligand coordinates that provide Ir-O-Ir angles $\theta_0 = 80°$. These structural parameters, obtained by averaging the bond lengths and bond angles in the experimentally determined lattice configuration of BaIrO$_3$ [313] correspond to slightly elongated octahedra. For cubic (undistorted) octahedra, $\theta_c = 70.52°$. Results at three different levels of approximation are shown: spin-orbit rAS (rAS+SOC), CASSCF (CAS+SOC) and MRCI (CI+SOC). The rAS data account for only direct $d-d$ exchange. For $d_0 = 2.63$ Å and $\theta_0 = 80°$, the rAS $\bar{J}$ is -14.9 meV while the anisotropic $\bar{\Gamma}$ is -0.7 meV when including SOC. The magnitude of the ferromagnetic (FM) rAS $\bar{J}$ is similar to that computed

Table 7.1: Energy splittings for the lowest four spin-orbit states of two face-sharing NN IrO$_6$ octahedra and the corresponding effective coupling constants at different levels of approximation, for $d_0 = 2.63$ Å and $\theta_0 = 80°$ (all values in meV). The J values without SOC by rAS, CAS and CI are -1.2, 27.4 and 35.4 meV, respectively.

	rAS+SOC	CAS+SOC	CI+SOC
$\Psi_S = (\lvert\uparrow\downarrow\rangle - \lvert\downarrow\uparrow\rangle)/\sqrt{2}$	15.2	0.0	0.0
$\Psi_2 = (\lvert\uparrow\uparrow\rangle + \lvert\downarrow\downarrow\rangle)/\sqrt{2}$	0.4	72.0	123.3
$\Psi_3 = (\lvert\uparrow\uparrow\rangle - \lvert\downarrow\downarrow\rangle)/\sqrt{2}$	0.0	74.0	126.5
$\Psi_1 = (\lvert\uparrow\downarrow\rangle + \lvert\downarrow\uparrow\rangle)/\sqrt{2}$	0.0	74.0	126.5
$\bar{J}, \bar{\Gamma}$	$-14.9, -0.7$	$72.0, 4.1$	$123.3, 6.3$

74

7. Superexchange interactions between spin-orbit-coupled $j \simeq 1/2$ ions in oxides with face-sharing ligand octahedra

in square-lattice $3d^9$ Cu oxides [205, 206, 322, 323] and in the corner-sharing iridate Ba_2IrO_4 [324]. The anisotropic $\bar{\Gamma}$ is also FM at the rAS level and its magnitude is slightly larger as compared with the AFM rAS $\bar{\Gamma}$ of the corner-sharing iridate Ba_2IrO_4 [324]. By CASSCF and MRCI, the singlet Ψ_S becomes the ground state, well below the "triplet" components Ψ_1, Ψ_2 and Ψ_3. This indicates that the AF Heisenberg exchange $\bar{J}$ ($\bar{J} > 0$) defines now the largest energy scale. In the CASSCF approximation, only $t_{2g}-t_{2g}$ intersite excitations are accounted for, i.e., $t_{2g}^6-t_{2g}^4$ configurations. The $\bar{J}$ value extracted by CAS+SOC, 72 meV, is twice as large as compared, e.g., to the CASSCF J's in layered $3d^9$ cuprates [205, 206, 322, 323] and in the corner-sharing iridate Ba_2IrO_4 [324]. In the configuration-interaction treatment, which includes TM t_{2g} to e_g and charge-transfer O $2p$ to Ir $5d$ excitations as well, $\bar{J}$ is 123.3 meV, about 70% larger as compared to the CAS+SOC result. By accounting for correlation effects, the symmetric anisotropic coupling $\bar{\Gamma}$ is also significantly enlarged, from -0.7 meV by rAS+SOC to 6.3 meV by spin-orbit MRCI.

In the case of face-sharing ligand octahedra, the TM ions often form dimers, trimers or chains [313]. This type of low-dimensional packing usually results in sizable distortions of the ligand cages. It is known that the effective spin interactions are strongly dependent on structural details such as bond angles [325–328] and bond lengths [329]. For better insight into the dependence of the NN magnetic couplings on such structural parameters, we performed addi-
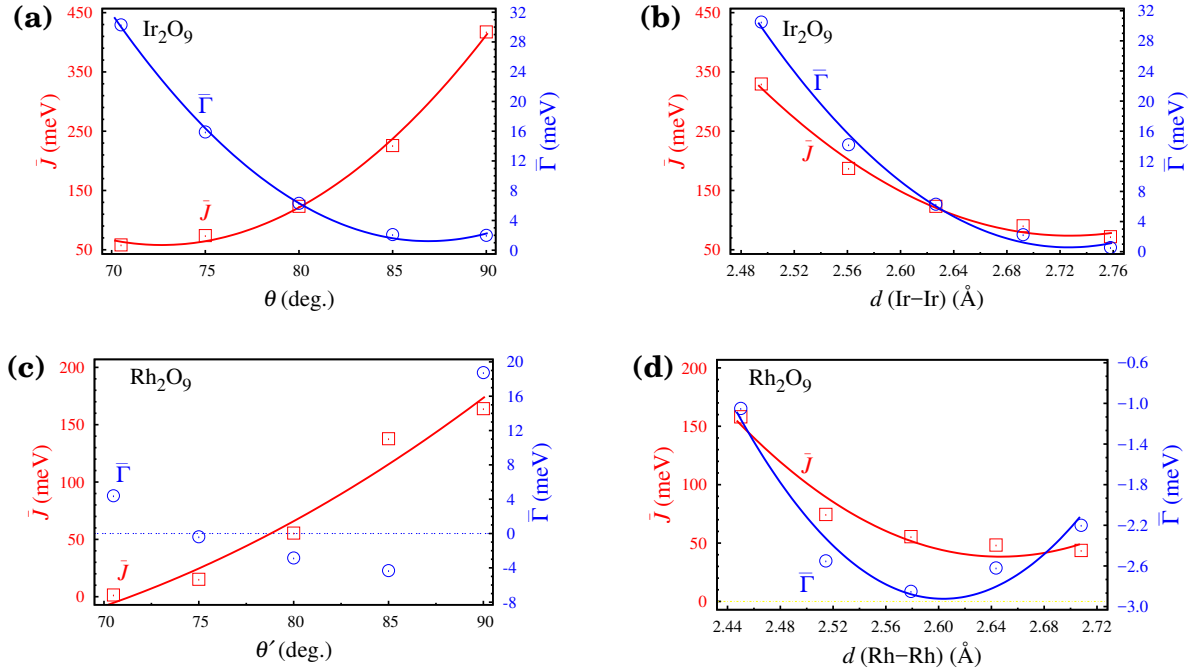
Figure 7.2: Dependence on structural details of the NN effective magnetic couplings for Ir_2O_9 and Rh_2O_9 fragments of face-sharing octahedra, spin-orbit MRCI results. (a, c) Variations as function of the Ir-O-Ir bond angle θ and Rh-O-Rh bond angle θ' when fixing the Ir-Ir distance to $d_0 = 2.63$ Å and the Rh-Rh distance to $d_0' = 2.58$ Å. Ligands are radially displaced in planes perpendicular to the z axis. Curves were drawn as a guide to the eye; a simple fit is not possible for $\bar{\Gamma}$ in the case of $4d$ magnetic sites. (b, d) Variations as function of the TM-TM interatomic distance when keeping unchanged the positions of the ligands. The latter are at distances of $r_0 = 1.57$ Å (Ir_2O_9) and $r_0' = 1.54$ Å (Rh_2O_9) from the z axis.

Table 7.2: Energy splittings for the lowest four spin-orbit states and the corresponding effective coupling constants for variable Ir-O-Ir angle, MRCI+SOC results (meV). The NN Ir-Ir distance is d_0=2.63 Å. The Ir-O-Ir angle θ is listed for each geometry; distances between Ir and the bridging O's, d(Ir-O), are provided within brackets.

	70.5°(2.27Å)	75°(2.16Å)	80°(2.04Å)	85°(1.94Å)	90°(1.86Å)
Ψ_S	0.0	0.0	0.0	0.0	0.0
Ψ_2	58.2	73.9	123.3	225.8	417.5
Ψ_1	73.4	81.8	126.5	226.9	418.5
Ψ_3	73.4	81.8	126.5	226.9	418.5
$\bar{J}, \bar{\Gamma}$	58.2, 30.3	73.9, 15.9	123.3, 6.3	225.8, 2.1	417.5, 2.0

tional calculations for distorted geometries with all ligands pushed closer to (or farther from) the Ir-Ir axis, which therefore yields larger (or smaller) Ir-O-Ir bond angles while keeping the overall D_{3h} point-group symmetry. The resulting MRCI+SOC data are provided in Table 7.2. The overall trends for the magnetic couplings $\bar{J}$ and $\bar{\Gamma}$ are illustrated graphically in Fig. 7.2(a). It is seen that the angle dependence for both $\bar{J}$ and $\bar{\Gamma}$ can be rather well reproduced with parabolic curves (one exception is the $\bar{\Gamma}$'s presented in Fig.7.2(c) for Rh$_2$O$_9$ fragments). The Heisenberg $\bar{J}$ displays a steep increase with larger angle, i.e., from 58 meV at 70.5° to 417 meV at 90°. On the other hand, the anisotropic coupling $\bar{\Gamma}$ shows a rapid decrease, from a remarkably large value of 30 meV at 70.5° to 2 meV at 90°.

We further analyzed the dependence on the Ir-Ir interatomic distance d(Ir-Ir) of the magnetic interactions. In this set of calculations, the distance between the O ligands and the z axis (along the Ir-Ir bond) was fixed to 1.57 Å, while d(Ir-Ir) was either increased or reduced by up to 5% with respect to the reference Ir-Ir separation $d=d_0$=2.63 Å. As shown in Fig. 7.2(b) (see also
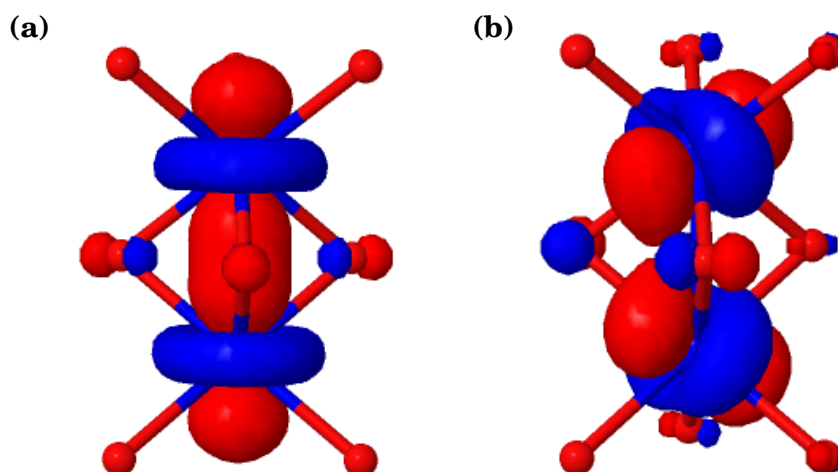
Figure 7.3: Natural orbitals of a_{1g} (a) and e_g^{π} (b) type for a Ir$_2$O$_9$ fragment of face-sharing octahedra, as obtained by CASSCF calculations. The former have strong σ-type overlap.

Table 7.7), both $\bar{J}$ and $\bar{\Gamma}$ have again pronounced parabolic dependence on d(Ir-Ir). In contrast to the variations as function of angle displayed in Fig. 7.2(a), here $\bar{J}$ and $\bar{\Gamma}$ follow the same trend. More specifically, both $\bar{J}$ and $\bar{\Gamma}$ rapidly increase with decreasing d(Ir-Ir).

We also performed calculations in which the six O ligands not shared by the Ir ions were displaced as well along the z axis, such that each Ir site remains in the center of the octahedron. We found that the differences between the $\bar{J}$ values obtained from these computations and the corresponding $\bar{J}$'s in Fig. 7.2(b) are rather small, not more than 15%.

The face-sharing linkage and additional distortions applied to the two-octahedra clusters split the t_{2g} levels into a_{1g} and e_g^π components. For all Ir_2O_9 units considered here, we find that the a_{1g} sublevels lie at lower energy and that the t_{2g} hole has e_g^π character without SOC. The a_{1g} orbitals belonging to NN sites have substantial direct overlap [see Fig 7.3(a)], much larger than in the case of e_g^π orbitals [see Fig 7.3(b)]. The rather small AFM Heisenberg J derived from the calculations without SOC (see caption of Table 7.1) is therefore the result of (relatively) weak direct exchange involving the higher-lying e_g^π states. By accounting for spin-orbit interactions, however, the Heisenberg J is enhanced to impressive values that are up to three times larger than the results obtained without SOC (72 vs 27 meV at the CASSCF level, 123 vs 35 meV by MRCI, see Table 7.1). This strong increase of the Heisenberg J is the consequence of mixing a_{1g} character to the spin-orbit ground-state wave-function.

$[Rh_2O_9]$ unit

In order to make an informative comparison between $5d$ and $4d$ oxides, we also performed calculations for the effective magnetic couplings on $[Rh_2O_9]$ fragments consisting of two face-sharing RhO_6 octahedra, with a Rh-Rh interatomic distance $d_0' = 2.58$ Å and Rh-O-Rh bond angles $\theta_0' = 80°$. As for the material model of face-sharing $5d^5$ octahedra, the structural parameters of the Rh_2O_9 cluster were chosen according to the average bond lengths and bond angles of the $BaRhO_3$ compound. We used in this regard the crystallographic data reported in Ref. [313]. QC results are presented in Table 7.3. Interestingly, the $\bar{J}$ value obtained by spin-orbit rAS is the same as for the Ir_2O_9 cluster (Table 7.1). However, the $\bar{J}$'s obtained by CAS+SOC and

Table 7.3: Energy splittings for the lowest four spin-orbit states of two face-sharing NN RhO_6 octahedra and the corresponding effective coupling constants at different levels of approximation, for $d_0' = 2.58$ Å and $\theta_0' = 80°$ (all in meV). The J values without SOC by rAS, CAS and CI are -0.9, 19.0 and 29.4 meV, respectively.

	rAS+SOC	CAS+SOC	CI+SOC
$\Psi_S = (|\uparrow\downarrow\rangle - |\downarrow\uparrow\rangle)/\sqrt{2}$	16.0	0.0	0.0
$\Psi_3 = (|\uparrow\uparrow\rangle - |\downarrow\downarrow\rangle)/\sqrt{2}$	0.0	25.4	54.0
$\Psi_1 = (|\uparrow\downarrow\rangle + |\downarrow\uparrow\rangle)/\sqrt{2}$	0.0	25.4	54.0
$\Psi_2 = (|\uparrow\uparrow\rangle + |\downarrow\downarrow\rangle)/\sqrt{2}$	1.1	26.5	55.5
$\bar{J}, \bar{\Gamma}$	$-14.9, -2.3$	$26.5, -2.2$	$55.5, -2.8$

Table 7.4: Energy splittings and the corresponding effective coupling constants for variable Rh-O-Rh angle, MRCI+SOC results (meV). The NN Rh-Rh distance is 2.58 Å. The Rh-O-Rh angle θ' is listed for each geometry; distances between Rh and the bridging O's, d(Rh-O), are provided within brackets.

	70.5°(2.23Å)	75°(2.12Å)	80°(2.04Å)	85°(1.91Å)	90°(1.82Å)
Ψ_S	0.0	0.0	0.0	0.0	0.0
Ψ_3	3.7	15.0	54.0	135.7	173.4
Ψ_1	3.7	15.0	54.0	135.7	173.4
Ψ_2	1.5	15.2	55.5	137.8	164.0
$\bar{J}, \bar{\Gamma}$	1.5, 4.4	15.2, −0.4	55.5, −2.8	137.8, −4.3	164.0, 18.8

CI+SOC are significantly smaller as compared with those in Table 7.1. Still, $\bar{J}$ remains much larger than the magnetic couplings in the edge-sharing $4d^5$ compounds Li_2RhO_3 and α-$RuCl_3$ [326, 327].

Energy splittings within the group of the four low-lying $d^5 - d^5$ states and the resulting effective coupling constants for different Rh-O-Rh angles are listed in Table 7.4. Furthermore, the dependence of $\bar{J}$ and $\bar{\Gamma}$ on the Rh-O-Rh bond angles and on the Rh-Rh interatomic distances are illustrated in Fig. 7.2(c) and Fig. 7.2(d), respectively (for more details, see Table 7.8 and Table 7.9). As indicated in Fig. 7.2(c), $\bar{J}$ displays nearly linear behavior with variable angle, increasing from 1.5 meV at 70.5° to 164 meV at 90°. $\bar{\Gamma}$ changes sign from AFM to FM coupling close to 75°, with a minimum of −6 meV at 85°, and then changes back to AFM values for larger angles. On the other hand, with variable d(Rh-Rh) [Fig. 7.2(d)], $\bar{\Gamma}$ is always FM, with a minimum of −2.8 meV at 2.56 Å, and $\bar{J}$ features a similar trend as for Ir sites in Fig. 7.2(b).

7.4 Discussion

We analyze in more detail in this section the relative values of the different contributions to intersite exchange, i.e., direct $t_{2g}-t_{2g}$ exchange, $t_{2g}-t_{2g}$ electron/hole hopping and indirect hopping via the bridging oxygens. In first place, it is clear that a systematically small portion of FM potential exchange to the overall $\bar{J}$ is here of secondary importance. The contribution coming from direct hopping can be straightforwardly estimated from the CASSCF J since only intersite $M(t_{2g})$–$M(t_{2g})$ excitation processes (t_{2g}^6–t_{2g}^4 polar configurations) are taken into account at the CASSCF level. In the CI treatment, superexchange paths including the bridging-ligand $2p$ and TM e_g orbitals are also added on top of direct hopping, providing a more comprising description of intersite exchange mechanisms. In the case of $BaIrO_3$, for instance, when the Ir-O-Ir bond angle is 80°, the exchange calculated at the CASSCF level (without SOC), $J = 27.4$ meV, is already 77% of the CI result, 35.4 meV (see Table 7.1). While this fraction is significantly reduced if the Ir-O-Ir bond angle is modified towards 90° (see Table 7.6), indicating that the $d - p - d$ superexchange contribution starts to rise as a result of shorter Ir-O bonds, the data computed for 80° bond angles show that, given the large direct-hopping integrals, the direct AFM $d-d$

78

7. Superexchange interactions between spin-orbit-coupled $j \simeq 1/2$ ions in oxides with face-sharing ligand octahedra

Table 7.5: Angle dependence of the trigonal CF splitting Δ_t (eV) obtained from MRCI calculations for Ir_2O_9 and Rh_2O_9 fragments of face-sharing octahedra. The a_{1g} level is for all angles the lowest in energy.

θ/θ'	Δ_t^{Ir}	Δ_t^{Rh}
70.5	-0.86	-0.69
75	-0.89	-0.67
80	-0.71	-0.53
85	-0.43	-0.29
90	-0.20	-0.10

superexchange may surpass the $d-p-d$ superexchange. The two mechanisms should be considered in any case on equal footing for high-quality estimates. In the context of recent discussions on the role of the various types of intersite exchange [330, 331], our QC data provide a more quantitative picture on the different contributions.

Given the facet-sharing geometry, the direct $d-d$ electron/hole hopping between a_{1g} orbitals is considerable. This hopping interferes with the indirect hopping via the bridging-oxygen O_3 group, providing a total transfer integral t. Since the exchange coupling J is mainly controlled by the square of t ($J \sim t^2/U$, where U is the on-site Coulomb repulsion), a large $\bar{J}$ value of up to ≈ 400 meV (see Table 7.6 and 7.7) is not surprising. Both the direct ($\sim t^{dd}$) and indirect ($\sim t^{dpd}$) transfer processes can occur trough the e_g^π and a_{1g} channels independently. The transfer integrals of the e_g^π and a_{1g} channels, t_e and t_a, contribute to the total transfer integral t with different weights. The corresponding channel weights are controlled by the ratio Δ_t/λ, with λ being the spin-orbit coupling, 0.47 eV for Ir and 0.15 eV for Rh [262]; the dependence of the trigonal splitting Δ_t on bond angles is illustrated in Table 7.5.

The different terms entering the total transfer integral t are expected to behave differently when varying the geometry of the M-O_3-M structure. The large direct overlap between two NN a_{1g} orbitals suggests that the direct hopping t_a^{dd} contributes significantly to t_a, as evidenced in Fig. 7.3. In contrast, the e_g^π orbitals are tilted with respect to the z axis, thus giving rise to weaker direct overlap and more significant $d-p-d$ couplings (see Fig.7.3(b)), i.e., a more important role of t_e^{dpd} in t_e. It is the interplay between these processes, $d-d$ and $d-p-d$ superexchange, that is mainly responsible for the strong variations as function of bond angles and bond lengths. From a wider perspective, it is clear that the equilibrium geometrical configuration and the associated J value depend on interactions and degrees of freedom that also involve the extended crystalline surroundings. An interesting aspect to be considered is inter-site couplings within the entire M_3O_{12} block of three face-sharing octahedra along the c axis (see Fig.7.1(a)). One question concerns the possibility of cooperative M$-$M dimerization as driving force for the charge density wave observed in $BaIrO_3$ [306]. Two-site bond formation on three-center units with a spin 1/2 at each magnetic site and long-range ordering of these 'dimers' has been earlier

proposed in, e.g., the quasi-1D system NaV_2O_5 [85, 195].

7.5 Conclusions

To summarize, we employ QC methods to provide valuable insights on the effective magnetic interactions in $5d$ and $4d$ oxides with face-sharing oxygen octahedra, $BaIrO_3$ and $BaRhO_3$. The same methodology has previously been used to derive magnetic coupling constants in good agreement with experimental estimates in the perovskite iridate $CaIrO_3$ [321, 332], in square-lattice Ba_2IrO_4 [277] and Sr_2IrO_4 [189], and in pyrochlore iridates [328]. The large AFM Heisenberg interactions computed here for face-sharing octahedra are remarkable since they exceed the values computed so far for corner-sharing [277, 321, 322, 333] and edge-sharing systems [325]. One peculiar exception with regard to edge-sharing $4d^5$ NN ligand cages is $RuCl_3$ under high pressure [334], where a strong stabilization of the singlet state is also found for certain $Ru-Ru$ bonds. The present findings on face-sharing octahedra as encountered in $BaIrO_3$ and $BaRhO_3$ and recent results on $RuCl_3$ [334] only provide additional motivation for even more detailed electronic-structure calculations on both edge- and face-sharing compounds, with main focus on the subtle interplay among strong spin-orbit interactions, direct $d-d$ orbital overlap and bonding, and couplings to the lattice degrees of freedom.

Table 7.6: Energy splittings for the lowest four spin-orbit states of two face-sharing NN IrO$_6$ octahedra and the corresponding effective coupling constants obtained from rAS+SOC, CAS+SOC and MRCI+SOC calculations. For each geometry the Ir-Ir distance was fixed to 2.63Å. For θ=90°, for instance, the J values without SOC by rAS, CAS and CI are 0.04, 64.7 and 116.4 meV, respectively. Distances between Ir sites and the bridging O's, d(Ir-O), are provided within brackets. The data are presented as complementary to those in Table 7.2 (all values in meV).

θ, d(Ir-O)	rAS+SOC	CASSCF+SOC	MRCI+SOC
70.5° (2.27Å):			
Ψ_S	9.9	0.0	0.0
Ψ_2	0.0	24.8	58.2
Ψ_1	0.5	34.9	73.4
Ψ_3	0.5	34.9	73.4
$\bar{J}, \bar{\Gamma}$	−9.9, 1.1	24.8, 20.3	58.2, 30.3
75° (2.16Å):			
Ψ_S	12.8	0.0	0.0
Ψ_2	0.0	36.3	73.9
Ψ_1	0.0	41.6	81.8
Ψ_3	0.0	41.6	81.8
$\bar{J}, \bar{\Gamma}$	−12.8, 0.0	36.3, 10.5	73.9, 15.9
80° (2.04Å):			
Ψ_S	15.2	0.0	0.0
Ψ_2	0.4	72.0	123.3
Ψ_1	0.0	74.0	126.5
Ψ_3	0.0	74.0	126.5
$\bar{J}, \bar{\Gamma}$	−14.9, −0.7	72.0, 4.1	123.3, 6.3
85° (1.94Å):			
Ψ_S	16.2	0.0	0.0
Ψ_2	0.3	149.4	225.8
Ψ_1	0.0	150.1	226.9
Ψ_3	0.0	150.1	226.9
$\bar{J}, \bar{\Gamma}$	−15.9, −0.6	149.4, 1.3	225.8, 2.1
90° (1.86Å):			
Ψ_S	17.0	0.0	0.0
Ψ_2	0.0	293.6	417.5
Ψ_1	0.3	294.2	418.5
Ψ_3	0.3	294.2	418.5
$\bar{J}, \bar{\Gamma}$	−17.0, 0.7	293.6, 1.2	417.5, 2.0

Table 7.7: Energy splittings for the lowest four spin-orbit states of two face-sharing NN IrO_6 octahedra and the corresponding effective coupling constants obtained from rAS+SOC, CAS+SOC and MRCI+SOC calculations. The relative distances from the O ligands to the z axis were fixed to 1.57 Å. The data are presented as complementary to those in Fig. 7.2(b) (all values in meV).

d(Ir-Ir)	rAS+SOC	CASSCF+SOC	MRCI+SOC
2.50Å:			
Ψ_S	22.0	0.0	0.0
Ψ_2	0.5	188.6	329.7
Ψ_1	0.0	198.1	345.0
Ψ_3	0.0	198.1	345.0
$\bar{J},\bar{\Gamma}$	-21.5 -0.93	188.6, 18.9	329.7, 30.5
2.56Å:			
Ψ_S	18.3	0.0	0.0
Ψ_2	0.4	106.7	187.2
Ψ_1	0.0	111.2	194.3
Ψ_3	0.0	111.2	194.3
$\bar{J},\bar{\Gamma}$	-17.9, -0.8	106.7, 8.9	187.2, 14.2
2.63Å:			
Ψ_S	15.2	0.0	0.0
Ψ_2	0.4	72.0	123.3
Ψ_1	0.0	74.0	126.5
Ψ_3	0.0	74.0	126.5
$\bar{J},\bar{\Gamma}$	-14.9, -0.7	72.0, 4.1	123.3, 6.3
2.69Å:			
Ψ_S	12.6	0.0	0.0
Ψ_2	0.3	54.7	90.5
Ψ_1	0.0	55.5	91.7
Ψ_3	0.0	55.5	91.7
$\bar{J},\bar{\Gamma}$	-12.4, -0.54	54.7, 1.7	90.5, 2.2
2.76Å:			
Ψ_S	10.4	0.0	0.0
Ψ_2	0.2	44.5	72.1
Ψ_1	0.0	44.8	72.4
Ψ_3	0.0	44.8	72.4
$\bar{J},\bar{\Gamma}$	-10.3, -0.4	44.5, 0.6	72.1, 0.5

Table 7.8: Energy splittings for the lowest four spin-orbit states of two face-sharing NN RhO$_6$ octahedra and the corresponding effective coupling constants obtained from rAS+SOC, CAS+SOC and MRCI+SOC calculations. For each geometry the Rh-Rh distance was fixed to 2.58 Å . Distances between Rh sites and the bridging O's, d(Rh-O), are provided within brackets. The data are presented as complementary to those in Table 7.4 (all values in meV).

θ, d(Rh-O)	rAS+SOC	CASSCF+SOC	MRCI+SOC
70.5° (2.23Å):			
Ψ_S	10.4	6.5	0.0
Ψ_3	0.0	1.0	3.7
Ψ_1	0.0	1.0	3.7
Ψ_2	0.6	0.0	1.5
$\bar{J}, \bar{\Gamma}$	−9.9 −1.1	−6.5, 2.0	1.5, 4.4
75° (2.12Å):			
Ψ_S	13.3	0.0	0.0
Ψ_3	0.0	0.1	15.0
Ψ_1	0.0	0.1	15.0
Ψ_2	0.8	0.4	15.2
$\bar{J}, \bar{\Gamma}$	−12.5, −1.7	0.4, −0.6	15.2, −0.4
80° (2.06Å):			
Ψ_S	16.0	0.0	0.0
Ψ_3	0.0	25.4	54.0
Ψ_1	0.0	25.4	54.0
Ψ_2	1.1	26.5	55.5
$\bar{J}, \bar{\Gamma}$	−14.9, −2.3	26.5, −2.2	55.5, −2.8
85° (1.91Å):			
Ψ_S	17.7	0.0	0.0
Ψ_3	0.0	82.4	135.7
Ψ_1	0.0	82.4	135.7
Ψ_2	1.3	84.0	137.8
$\bar{J}, \bar{\Gamma}$	−16.4, −2.6	84.0, −3.2	137.8, −4.3
90° (1.82Å):			
Ψ_S	16.5	0.0	0.0
Ψ_3	0.0	165.4	173.4
Ψ_1	0.0	165.4	173.4
Ψ_2	0.9	190.5	164.0
$\bar{J}, \bar{\Gamma}$	−15.6, −1.8	190.5, −50.2	164.0, 18.8

Table 7.9: Energy splittings for the lowest four spin-orbit states of two face-sharing NN RhO$_6$ octahedra and the corresponding effective coupling constants obtained from rAS+SOC, CAS+SOC and MRCI+SOC calculations. The relative distances from the O ligands to the z axis are fixed to 1.54 Å. The data are presented as complementary to those in Fig. 7.2(d) (all values in meV).

d(Rh-Rh)	rAS+SOC	CASSCF+SOC	MRCI+SOC
2.45Å:			
Ψ_S	22.0	0.0	0.0
Ψ_3	0.0	49.5	157.6
Ψ_1	0.0	49.5	157.6
Ψ_2	1.6	50.0	158.1
$\bar{J},\bar{\Gamma}$	-20.4 -3.2	50.0, -1.1	158.1, -1.1
2.51Å:			
Ψ_S	18.8	0.0	0.0
Ψ_3	0.0	30.1	73.2
Ψ_1	0.0	30.1	73.2
Ψ_2	1.4	31.1	74.5
$\bar{J},\bar{\Gamma}$	-17.5, -2.7	31.1, -2.1	74.5, -2.5
2.58Å:			
Ψ_S	16.0	0.0	0.0
Ψ_3	0.0	25.4	54.0
Ψ_1	0.0	25.4	54.0
Ψ_2	1.1	26.5	55.5
$\bar{J},\bar{\Gamma}$	-14.9, -2.3	26.5, -2.2	55.5, -2.8
2.64Å:			
Ψ_S	13.6	0.0	0.0
Ψ_3	0.0	23.8	47.0
Ψ_1	0.0	23.8	47.0
Ψ_2	1.0	24.7	48.3
$\bar{J},\bar{\Gamma}$	-12.6, -1.9	24.7, -2.0	48.3, -2.6
2.71Å:			
Ψ_S	11.5	0.0	0.0
Ψ_3	0.0	22.6	42.6
Ψ_1	0.0	22.6	42.6
Ψ_2	0.8	23.5	43.7
$\bar{J},\bar{\Gamma}$	-10.7, -1.6	23.5, -1.7	43.7, -2.2

Chapter 8

Ab initio computation of resonant inelastic X-ray scattering spectra for d-ions in solids

In this chapter, we discuss ways to describe the readjustment of the charge distribution in the 'vicinity' of an excited electron for the modeling of resonant inelastic X-ray scattering (RIXS). We test to this end a nonorthogonal configuration-interaction type of approach, based on performing separate self-consistent field (SCF) optimizations for different electron configurations. We apply this methodology to the computation of X-ray absorption (XA) and RIXS excitations and cross sections of Cu^{2+} $3d^9$ ions in $KCuF_3$ and Ni^{2+} $3d^8$ ions in La_2NiO_4. We discuss in this context ways to consider orbital ordering effects (alternately occupied $d_{x^2-z^2}$ and $d_{y^2-z^2}$ orbitals) in $KCuF_3$. For the more complex Ni^{2+} $3d^8$ configuration in the nickelate La_2NiO_4, trends found experimentally for the incoming-photon incident-angle and polarization dependence are well reproduced.

8.1   Introduction

RIXS is a fast developing experimental technique in which X-ray photons are scattered inelastically off matter. It is a second order photon-in-photon-out process, in which the incoming photon excites a core electron that consequently decays by the emission of an outgoing photon. "Inelastic" means here that the energy of the outgoing photon is lower than the energy of the incoming photon. The energy loss is transferred to intrinsic excitations of the material under study. RIXS can measure a diversity of different elementary excitations in correlated electron systems [335, 336], for example, dispersive magnetic modes [337, 338], orbital excitations [11, 339, 340] and phonons [341, 342]. Photon sources deliver many orders of magnitude more particles per second in a much smaller spot than, for instance, neutron sources [335] and the interaction between photons and matter is relatively strong compared to the neutron-matter interaction. These features make RIXS possible on very small volume samples, thin films, surfaces and nano-objects, in addition to bulk single crystal or powder samples [335].

There has been a large number of RIXS-related publications on strongly correlated materi-

als. It has been proved that RIXS is a powerful tool to probe the interplay between charge, spin, orbital and lattice degrees of freedom. In the RIXS process, the system absorbs a high-energy X-ray photon, leading to a creation of an excited intermediate state that has a core-hole, from which the system relaxes radiatively. These intermediate states are transient and strongly perturbed with respect to the ground state of the system. The presence of short-lived intermediate states in the resonant process is one significant complication as concerns the theoretical modeling of RIXS. Another aspect is that the intermediate electron configuration determines all the transition probabilities from the initial to the final state. Therefore considering all intermediate states in theoretical modeling is of crucial importance for computing the scattering cross sections of the different excitations and for the interpretation of RIXS spectra.

In previous theoretical RIXS studies, methods based on model-Hamiltonian [335, 336, 343–350] and *ab initio* wave-function-based quantum chemistry (QC) [235, 351–354] have been used to compute full RIXS spectra for correlated *d*-electron open-shell systems, in order to address either the *d*-shell multiplet structure [235, 348–352] or Mott-Hubbard physics [343–347]. However, in these earlier theoretical studies the valence-shell charge relaxation in response to the creation of a core-hole in the intermediate RIXS states is either missing or described just phenomenologically. Recently, Maganas *et al.* [355] developed a protocol for the calculation of valence-to-core (VtC) RIXS [alternatively referred to as VtC resonant X-ray emission scattering (RXES)] spectra based on restricted open-shell configuration interaction with singles (ROCIS) and its parameterized version based on a density functional theory (DFT) ground-state determinant ROCIS/DFT [356, 357]. A recent work by Bogdanov *et al.* [236] proposed a multireference configuration-interaction-type of methodology for the *ab initio* calculation of transition-metal (TM) *L*-edge excitations in solids and tested this computational scheme for the more convenient case of a Cu^{2+} $3d^9$ ion in Li_2CuO_2. The idea is to carry out nonorthogonal configuration-interaction calculations based on independent SCF optimizations for the many-body wave-functions describing the reference d^n and core-hole $2p^5 d^{n+1}$ configurations. In this chapter, using the same methodology discussed in Ref. [236], we perform calculations on $KCuF_3$, a strongly correlated *d*-electron system with cooperative Jahn-Teller (JT) distortions, commenting on orbital ordering effects in computing RIXS spectra. Afterwards, we carry out computations on La_2NiO_4 (Ni^{2+} d^8), having more than one single hole in the initial configuration of the valence $3d$ shell, and further compare the calculated RIXS cross section with experimental RIXS spectra.

8.2   Resonant inelastic X-ray scattering (RIXS)

8.2.1   RIXS process

In a typical RIXS experiment, an incident photon beam is shone on the sample and the scattered radiation is collected. The scattering process is illustrated in Fig.8.1. The incident X-ray energy is chosen to resonate with one of the absorption edges of the system, i.e., the energy required to scatter off a core electron to an excited state above the Fermi level. The incident and scattered
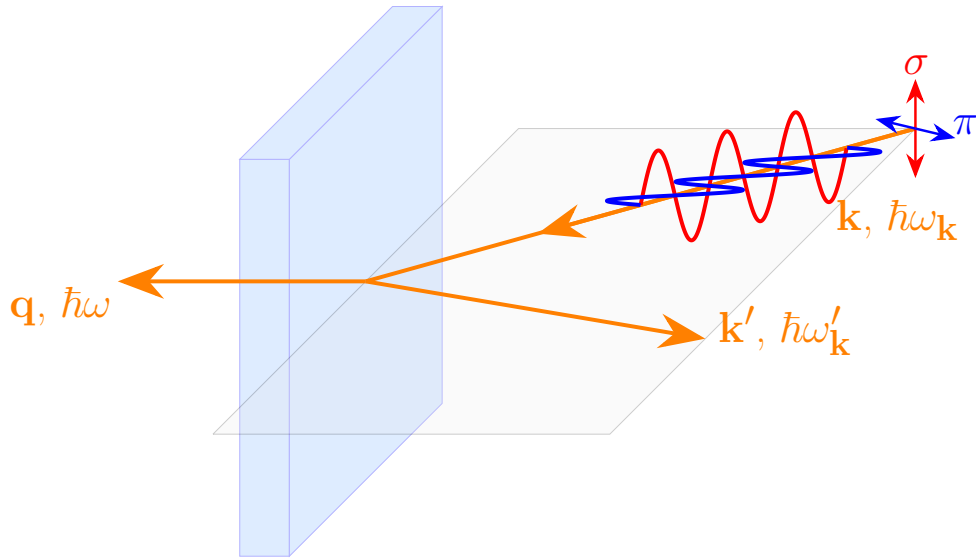
Figure 8.1: Simple illustration of a RIXS experiment. An incident photon beam with energy $\hbar\omega_{\mathbf{k}}$, momentum $\mathbf{k}$ and polarization ϵ is shone on the sample and the scattered photons are collected under a fixed direction. The RIXS cross section is measured as a function of the scattered photon energy $\hbar\omega_{\mathbf{k}'}$, momentum $\mathbf{k}'$ and polarization ϵ'. A finite energy $\hbar\omega = \hbar\omega_{\mathbf{k}} - \hbar\omega_{\mathbf{k}'}$ and momentum $\mathbf{q} = \mathbf{k} - \mathbf{k}'$ are transferred to the system.

radiation momenta are different, thus a finite momentum $\vec{q} = \vec{k} - \vec{k}'$ is transferred to the system. The photon momentum is comparable with the crystal momentum of solid state electrons for typical X-ray energies used in RIXS, therefore the transferred momentum $\vec{q}$ can be mapped into the Brillouin zone of the system. For this reason, RIXS can also probe the momentum dispersion of elementary excitations.

To illustrate the essential processes in a RIXS experiment, we choose a copper-oxide material ($Cu^{2+}\ 3d^9$) as a typical example. The electronic configuration of Cu^{2+} is $1s^22s^22p^63s^23p^63d^9$, with a partially filled $3d$ valence shell. One can tune the incident photon energy to resonate with the copper K, L or M absorption edge, and in each case the incident photon promotes a different type of core electron into an empty valence orbital. The copper K-edge transition $1s \rightarrow 4p$ is around 9000 eV, in the hard X-ray regime. The $L_{2,3}$ edge $2p \rightarrow 3d$ (~ 900 eV) and $M_{2,3}$ edge $3p \rightarrow 3d$ (~ 80 eV) transitions are in soft X-ray regime [335]. After absorbing a X-ray photon, the system is in a highly unstable state, with a hole deep in the electronic core. It therefore quickly decays from such an intermediate state, for instance, via an Auger process, in which an electron of the Cu^{2+} ion fills the core-hole while another electron is simultaneously emitted [335].

8.2.2 Direct and indirect RIXS

In the RIXS process, the transition to the final state can be either direct or indirect [358, 359]. For direct RIXS, the incident photon promotes a core electron into an unoccupied state slightly above the Fermi level. Subsequently an electron from an occupied valence state slightly below the Fermi level decays and annihilates the core-hole, as indicated in Fig.8.2(a). In this case, the system is left into an excited state induced by the electron-photon interaction. One example
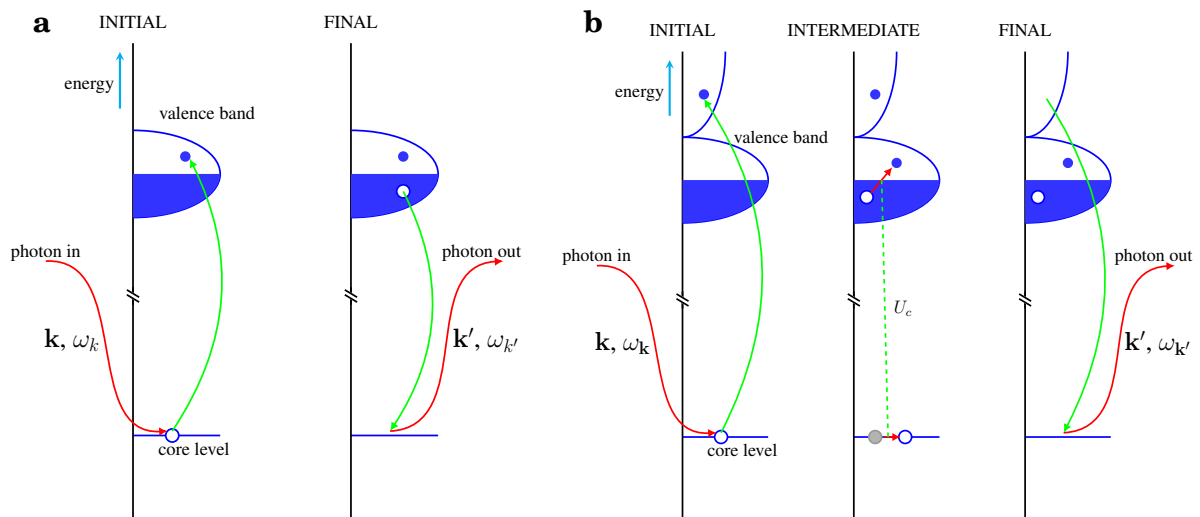
Figure 8.2: In both direct and indirect scattering processes, a valence excitation with momentum $\hbar\mathbf{k}' - \hbar\mathbf{k}$ and energy $\hbar\omega_{\mathbf{k}} - \hbar\omega_{\mathbf{k}'}$ is created. (a) In the direct scattering process, the incident photon excites a core electron into a low-lying unoccupied state of the valence band. Afterwards, the empty core state is filled by an electron from the occupied states with the emission of a photon. (b) In an indirect scattering process, the incident photon excites an electron from a deep-lying core level into an unoccupied state far above the Fermi level. The photoelectron subsequently decays leaving behind an excitation in the valence band. This figure is reproduced from Ref. [335].

for such transitions is the TM *L*-edge, i.e., an initial dipole transition $2p \rightarrow 3d$ and subsequent $3d \rightarrow 2p$ decay.

In an indirect RIXS process, the incident photon promotes a core electron into an unoccupied state several electron volts above the Fermi level. After that, this excited electron decays to fill the core-hole. If there is no any additional interaction, inelastic scattering process cannot occur since the the final state coincides with the initial state of the system. But in the intermediate state a core-hole is present: the core-hole and the excited electron are strongly interacting with each other and with the valence electrons of the system. In particular, the core-hole Coulomb interaction, usually described as a core-hole potential U_c, dominates the intermediate state dynamics and can produce an excitation in the valence band of the system. In this way, the system is left into an excited sate, which is not induced by the electron-photon interaction, but is indirectly produced by the core-hole potential, as indicated in Fig.8.2(b). One such example is RIXS at the TM *K*-edge ($1s \rightarrow 4p \rightarrow 1s$ transitions).

8.3   Interaction of light and matter

To develop the theory of RIXS, we need to derive the Hamiltonian that describes the interaction of the incident X-ray beam with the electrons in a system. Assuming a system with fixed nuclei, the total Hamiltonian can be written as:

$$H = H_{field} + H_{el} + H',\tag{8.1}$$

where H_{field} describes the quantized electromagnetic field, H_{el} is the electronic part and H' represents the interaction between electromagnetic and electronic fields. The general form of the latter term H' [360] can be written as:

$$
\begin{aligned}
H' &= \frac{e^2}{2m_e c^2} \sum_j \left[\mathbf{A}(\vec{r}_j) \right]^2 - \frac{e}{m_e c} \sum_j \mathbf{A}(\vec{r}_j) \cdot \vec{p}_j \\
&\quad - \frac{e\hbar}{m_e c} \sum_j \vec{\sigma}_j \cdot \left[\vec{\nabla} \times \mathbf{A}(\vec{r}_j) \right] - \frac{e\hbar}{2(m_e c)^2} \frac{e^2}{c^2} \sum_j \vec{\sigma}_j \cdot \left[\dot{\mathbf{A}}(\vec{r}_j) \times \mathbf{A}(\vec{r}_j) \right],
\end{aligned}
\tag{8.2}
$$

where $\mathbf{A}(\vec{r}_j)$ is the vector potential at position $\vec{r}_j$, $\vec{p}_j$ and $\vec{\sigma}_j$ are the momentum and spin operators acting on an electron, respectively, while e, m_e, c, $\hbar$ are fundamental constants. The vector potential $\mathbf{A}(\vec{r}_j)$ can be expanded in a set of plane waves:

$$
\mathbf{A}(\vec{r}_j) = \sum_{\vec{k}\epsilon} \sqrt{\frac{2\pi\hbar c^2}{\omega_{\vec{k}} v}} \left(\vec{\epsilon}_{\vec{k}\epsilon} a_{\vec{k}\epsilon} e^{i\vec{k}\cdot\vec{r}_j} + \vec{\epsilon}_{\vec{k}\epsilon}^* a_{\vec{k}\epsilon}^\dagger e^{-i\vec{k}\cdot\vec{r}_j} \right),
\tag{8.3}
$$

where v is the volume of system and $a_{\vec{k}\epsilon}$ ($a_{\vec{k}\epsilon}^\dagger$) is the annihilation (creation) operator of a photon with wave vector $\vec{k}$, energy $\hbar\omega_{\vec{k}}$ and polarization $\epsilon = \{\sigma, \pi\}$ with the corresponding unit polarization vector $\vec{\epsilon}_{\vec{k}\epsilon}$ ($\vec{\epsilon}_{\vec{k}\epsilon}^*$). The operator for $\mathbf{A}(\vec{r}_j)$ is linear in the annihilation operator $a_{\vec{k}\epsilon}$ and creation operator $a_{\vec{k}\epsilon}^\dagger$. When it acts on a state $|n_k\rangle$, it can either destroy or create a photon in that state. Absorption corresponds to the former. Scattering involves the destruction of a photon in one state $|n_k\rangle$ and the creation of a new photon in a state $|n_{k'}\rangle$.

In Eq.(8.2), the two terms of H' that contribute to the first order amplitude are the ones proportional to $\left[\mathbf{A}(\vec{r}_j) \right]^2$ and $\vec{\sigma}_j \cdot \left[\dot{\mathbf{A}}(\vec{r}_j) \times \mathbf{A}(\vec{r}_j) \right]$. The latter is smaller than the former by a factor $\hbar\omega_{\vec{k}}/m_e c^2 \ll 1$ ($m_e c^2 \sim 0.511$ MeV, so $\hbar\omega_{\vec{k}}/m_e c^2 \sim 0.02$ for 10 keV X-rays) [335]. The term $\left[\mathbf{A}(\vec{r}_j) \right]^2$ in fact contributes to the Bragg peaks and non-resonant scattering processes [335, 360]. The magnetic term with $\vec{\sigma}_j \cdot \left[\vec{\nabla} \times \mathbf{A}(\vec{r}_j) \right]$ and the nonmagnetic term with $\mathbf{A}(\vec{r}_j) \cdot \vec{p}_j$ in Eq.(8.2) contribute to the second order amplitude, which becomes large when $\hbar\omega_{\vec{k}}$ matches a resonance energy of the system. The magnetic term gives a dipole transition of order $(\vec{k}\cdot\vec{r})\hbar|\vec{k}|$, and the nonmagnetic term can induce a dipole transition of the order $|\vec{p}| = \hbar|\vec{k}|$, thus the ratio between these two terms can be estimated as $|\vec{k}||\vec{r}|$ [335]. Assuming $|\vec{r}| \sim na_0/Z$, with the principal quantum number n, the Bohr radius a_0 and atomic number Z, such ratios for e.g. the Cu-L edge and Ni-L edge are estimated to be 2.8×10^{-3} and 2.6×10^{-3}, respectively. In the RIXS process, it is the second order amplitude that dominates the scattering [335]. Thus the dominant contribution to resonant absorption and scattering is given by the nonmagnetic (optical transition) part of H', i.e., $\mathbf{A}(\vec{r}_j) \cdot \vec{p}_j$. Therefore we continue by keeping only the nonmagnetic terms in the following.

Using the expansion in Eq.(8.3), the nonmagnetic terms of $\mathbf{A}(\vec{r}_j) \cdot \vec{p}_j$ can be rewritten as:

$$
H'_{op} = \sum_{j,\vec{k}\epsilon} \frac{e}{m_e} \sqrt{\frac{2\pi\hbar}{\omega_{\vec{k}} v}} \left(\vec{\epsilon}_{\vec{k}\epsilon} a_{\vec{k}\epsilon} e^{i\vec{k}\cdot\vec{r}_j} + \vec{\epsilon}_{\vec{k}\epsilon}^* a_{\vec{k}\epsilon}^\dagger e^{-i\vec{k}\cdot\vec{r}_j} \right) \cdot \vec{p}_j.
\tag{8.4}
$$

The matrix elements (MEs) for the absorption of one photon characterized by $\vec{k}$ and ϵ, which would decrease the number of such photons $n_{\vec{k}\epsilon}$ by one $\left(n_{\vec{k}\epsilon} - 1 \right)$ and excite the electronic system

from state $|a\rangle$ to state $|b\rangle$, can be expressed as:

$$
\begin{aligned}
\left\langle b;n_{\vec{k}\epsilon}-1\left|H'_{op}\right|a;n_{\vec{k}\epsilon}\right\rangle &= \sum_{j=1}^{N}\frac{e}{m_e}\sqrt{\frac{2\pi\hbar}{\omega_{\vec{k}}v}}\left\langle b;n_{\vec{k}\epsilon}-1\left|\left(\vec{\epsilon}_{\vec{k}\epsilon}\cdot\vec{p}_j\right)a_{\vec{k}\epsilon}e^{i\vec{k}\cdot\vec{r}_j}\right|a;n_{\vec{k}\epsilon}\right\rangle \\
&= \sum_{j=1}^{N}\frac{e}{m_e}\sqrt{\frac{2\pi\hbar}{\omega_{\vec{k}}v}}\left\langle b\left|\left(\vec{\epsilon}_{\vec{k}\epsilon}\cdot\vec{p}_j\right)e^{i\vec{k}\cdot\vec{r}_j}\right|a\right\rangle\cdot\left\langle n_{\vec{k}\epsilon}-1\left|a_{\vec{k}\epsilon}\right|n_{\vec{k}\epsilon}\right\rangle. \quad (8.5)
\end{aligned}
$$

With the electric dipole approximation, we have:

$$
e^{i\vec{k}\cdot\vec{r}_j}=1+i\vec{k}\cdot\vec{r}_j+\cdots\approx 1. \tag{8.6}
$$

The annihilation and creation operators have the properties:

$$
a_{\vec{k}\epsilon}|n\rangle=\sqrt{n}\,|n-1\rangle,\qquad a^{\dagger}_{\vec{k}\epsilon}|n\rangle=\sqrt{n+1}\,|n+1\rangle. \tag{8.7}
$$

The Fourier transform of the momentum in quantum mechanics is the position operator:

$$
\left\langle b_{\vec{k}\epsilon}\left|\vec{p}_j\right|a_{\vec{k}\epsilon}\right\rangle=im_e\omega_{\vec{k}}\left\langle b_{\vec{k}\epsilon}\left|\vec{r}_j\right|a_{\vec{k}\epsilon}\right\rangle. \tag{8.8}
$$

Using Eq.(8.6), Eq.(8.7) and Eq.(8.8), the Eq.(8.5) reduces to:

$$
\begin{aligned}
\left\langle b;n_{\vec{k}\epsilon}-1\left|H'_{op}\right|a;n_{\vec{k}\epsilon}\right\rangle &= \sum_{j=1}^{N}ie\sqrt{\frac{2\pi\hbar\omega_{\vec{k}}}{v}}\left\langle b\left|\left(\vec{\epsilon}_{\vec{k}\epsilon}\cdot\vec{r}_j\right)\right|a\right\rangle\cdot\left\langle 0\left|a_{\vec{k}\epsilon}\right|1\right\rangle \\
&= ie\sqrt{\frac{2\pi\hbar\omega_{\vec{k}}}{v}}\left\langle b\left|\left(\vec{\epsilon}_{\vec{k}\epsilon}\cdot\vec{R}\right)\right|a\right\rangle, \quad (8.9)
\end{aligned}
$$

where we introduced the total position operator $\vec{R}=\sum_j\vec{r}_j$ and assumed that the radiation is incoherent, i.e., every photon can be dealt with individually, with the number of photons in a mode $n_{\vec{k}\epsilon}=1$.

8.4   Absorption and scattering cross-sections

8.4.1   X-ray absorption cross section

We consider here the case of resonance, when an electron is excited from a core level but does not leave the solid. The interaction between sample and the incident radiation is given by the Hamiltonian H'_{op} in Eq.8.4, which defines transitions between the initial $|i\rangle$ and final $|f\rangle$ states. The transition probability per unit time, W, between $|i\rangle$ and $|f\rangle$ is given in first-order perturbation theory by Fermi's golden rule as:

$$
W=\frac{2\pi}{\hbar}\left|\left\langle f\left|H'_{op}\right|i\right\rangle\right|^2\rho(E_f), \tag{8.10}
$$

where the initial $|i\rangle$ and final $|f\rangle$ states are eigenfunctions of the total Hamiltonian in Eq.(8.1), with the total energy conserved $E_i-E_f=0$, and $\rho(E_f)$ is the density of states, defined such that $\rho(E_f)dE_f$ is the number of final states with energy in the interval dE_f centered around E_f.

When a photon $\vec{k}_\epsilon$ is absorbed, the electronic system is excited from the ground state $|gs\rangle$ to a core-hole state $|ch\rangle$ with the density of states defined by the delta function $\delta(E_{gs} + \hbar\omega_{\vec{k}} - E_{ch})$. Substituting the MEs of absorption [Eq.(8.9)] into Eq.(8.10), we have

$$
\begin{aligned}
W_{\vec{k}\epsilon} &= \frac{2\pi}{\hbar}\left|\langle ch|H'_{op}|gs\rangle\right|^2 \times \delta(E_{gs} + \hbar\omega_{\vec{k}} - E_{ch}) \\
&= \frac{4\pi^2 \alpha c \hbar\omega_{\vec{k}}}{v}\left|\langle ch|\vec{\epsilon}_{\vec{k}\epsilon}\cdot\vec{R}|gs\rangle\right|^2 \times \delta(E_{gs} + \hbar\omega_{\vec{k}} - E_{ch}),
\end{aligned}
\tag{8.11}
$$

where $\alpha = e^2/(\hbar c) \approx 1/137$ is the fine structure constant. Considering the ratio between the transition probability per unit time given by Eq.(8.11) and the incident flux Φ_0 (the number of photons per second per unit area, $\Phi_0 = c/v$), we get the expression for the absorption cross section:

$$
\sigma_{\vec{k}\epsilon} = \frac{W_{\vec{k}\epsilon}}{\Phi_0} = 4\pi^2 \alpha\hbar\omega_{\vec{k}}\left|\langle ch|\vec{\epsilon}_{\vec{k}\epsilon}\cdot\vec{R}|gs\rangle\right|^2 \times \delta(E_{gs} + \hbar\omega_{\vec{k}} - E_{ch}).
\tag{8.12}
$$

The next question is how to define the $\delta(E_{gs} + \hbar\omega_{\vec{k}} - E_{ch})$ function in Eq.(8.12) explicitly. The excited state $|ch\rangle$ is a short-lived state and tends to decay via various channels. The possible decay channels are: (1) direct X-ray emission; (2) fluorescent X-ray emission when an electron from the outer shell fills the core-hole level creating an outgoing photon; (3) the two-electron Auger process where one electron fills the core-hole while another electron is simultaneously emitted [335]. These decay processes give rise to a finite lifetime broadening of the core-hole state, which is approximated by introducing a damping force in time-dependent perturbation theory [361, 362]. We can therefore replace the δ-function in Eq.(8.12) by a Lorentzian [362] of full width at half maximum (FWHM) Γ_{ch}[1], in order to account for the finite lifetime of the final states. Thus, the expression of XA cross section, involving summation over all possible initial and core-hole states, is

$$
\begin{aligned}
\sigma^{XA}_{\vec{k},\epsilon} = 4\pi^2 \alpha\hbar\omega_\epsilon \sum_j \frac{1}{g_{gs}} \sum_l &\left|\left\langle \Psi^l_{c^\star}\left|\vec{\epsilon}_{\vec{k}\epsilon}\cdot\vec{R}\right|\Psi^j_{gs}\right\rangle\right|^2 \\
&\times \frac{\Gamma_{c^\star}/2\pi}{(E_{gs} + \hbar\omega - E^l_{c^\star})^2 + (\Gamma_{c^\star})^2/4},
\end{aligned}
\tag{8.13}
$$

where $\hbar\omega$ is the energy of the incoming photons, $\Gamma_{c^\star}$ is the lifetime for the core-hole state and g_{gs} indicates the degeneracy of the ground state.

From Eq.(8.13), we can see that $\sigma^{XA}_{\vec{k},\epsilon}$ depends on energy, polarization, the propagation direction of the incoming X-rays and also on the nature of the ground state and excited states.

8.4.2 RIXS double differential cross section

The dominant part of the electron-radiation interaction Hamiltonian H'_{op} in Eq.8.4 includes only terms that create or annihilate a single photon. To obtain resonant scattering terms, one has to take the expansion at least to the second-order. The scattering transition probability in second-

---

[1] $\Gamma_{ch} = \hbar W^{tot}_{|ch\rangle}$ is a parameter related to the total transition probability per unit time from the $|ch\rangle$ state and usually is estimated from experiment [363, 364].
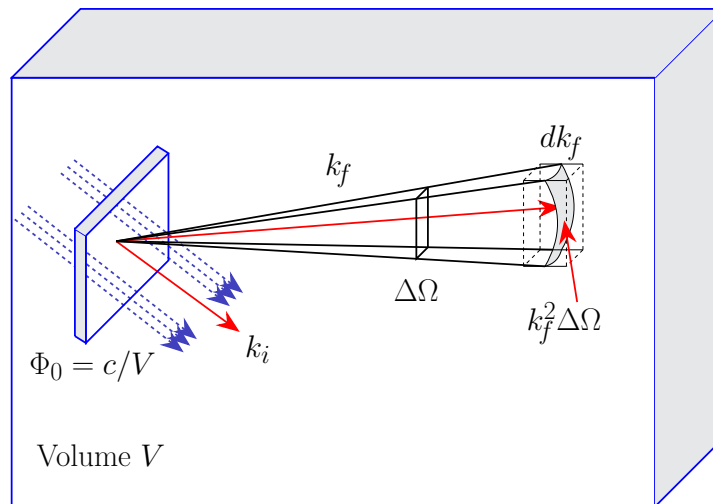
Figure 8.3: Illustration of the differential scattering cross-section. The integration is over the values of k_f accessible within the solid angle element $\Delta\Omega$. Figure is reproduced from Ref. [365].

order perturbation theory is given by

$$
W = \frac{2\pi}{\hbar} \left| \langle f | H'_{op} | i \rangle + \sum_N \frac{\langle f | H'_{op} | n \rangle \langle n | H'_{op} | i \rangle}{E_i - E_n} \right|^2 \rho(E_f),
\tag{8.14}
$$

where $|i\rangle$, $|n\rangle$ and $|f\rangle$ are initial, intermediate and final states, respectively. $\rho(E_f)$ is the density of final states. The sum is over all possible intermediate states. The first-order term $\langle f | H'_{op} | i \rangle$ vanishes within the dipole approximation, according to the form of Eq.(8.4). Therefore, we ignore this term in the following.

Here we use the standard method to derive the density of states $\rho(E_f)$, where it is assumed that the X-rays and sample occupy a box of volume V. The scattering process involves absorption of a single photon with known energy, momentum and polarization $\{\hbar\omega,\ \vec{k},\ \epsilon\}$ and emission of another photon characterized by the parameters $\{\hbar\omega',\ \vec{k}',\epsilon'\}$. We apply periodic boundary conditions to the X-ray wave-functions and the uniform density of states is $V/(2\pi)^3$. The density of states with energy E_f is equal to the number of states with wave vectors between k_f and $k_f + dk_f$. Therefore we have

$$
\rho(E_f) = \left(\frac{V}{8\pi^3}\right) k_f^2 dk_f \Delta\Omega,
\tag{8.15}
$$

where k_f and the solid angle element $\Delta\Omega$ are indicated in Fig.8.3. Since $E_f = \hbar k_f c = \hbar\omega'$, it follows that

$$
k_f^2 dk_f = \frac{1}{\hbar^2 c^2} E_f^2 dk_f = \frac{\omega'^2}{\hbar c^3} d\hbar\omega'.
\tag{8.16}
$$

$$
\rho(E_f) = \left(\frac{V}{8\pi^3}\right) \frac{\omega'^2}{\hbar c^3} d\hbar\omega' \Delta\Omega.
\tag{8.17}
$$

The double differential cross section is obtained by substituting the MEs (8.9) and the density of states (8.17) into the expression of the transition rate (8.14), and further dividing the transition rate by the incident flux ($\Phi_0 = c/V$). The restriction on resonant inelastic scattering

events is introduced by including a delta function $\delta(E_{gs} + \hbar\omega - E_{fs} - \hbar\omega')$ in Eq.(8.14). Thus the form of the Kramers-Heisenberg dispersion formula [366] is:

$$\frac{d^2\sigma_{\vec{k},\epsilon}}{d\Omega d\hbar\omega'} = \frac{\alpha^2\hbar^2}{c^2}\omega\omega'^3 \left| \sum_{ch} \frac{\langle fs|\vec{\epsilon}'\cdot\vec{R}|ch\rangle\langle ch|\vec{\epsilon}\cdot\vec{R}|gs\rangle}{E_{gs} + \hbar\omega - E_{ch}} \right|^2 \times \delta(E_{gs} + \hbar\omega - E_{fs} - \hbar\omega'). \qquad (8.18)$$

Finite lifetimes for the excited core-hole states and final states are further introduced and they are characterized by natural breadths Γ_{ch} and Γ_{fs}, respectively. The summation should be made over all available final states and the possible degeneracy of the ground state. The expression for the RIXS double differential cross section that we used in our calculations is:

$$\frac{d^2\sigma_{\vec{k},\epsilon}}{d\Omega d\hbar\omega'} = \frac{\alpha^2\hbar^2}{c^2}\omega\omega'^3 \times \sum_{gs} \frac{1}{g_{gs}} \sum_{fs} \left| \sum_{ch} \frac{\langle fs|\vec{\epsilon}'\cdot\vec{R}|ch\rangle\langle ch|\vec{\epsilon}\cdot\vec{R}|gs\rangle}{E_{gs} + \hbar\omega - E_{ch} + i\Gamma_{ch}/2} \right|^2$$
$$\times \frac{\Gamma_{\text{fs}}/2\pi}{(E_{\text{gs}} + \hbar\omega - E_{\text{fs}} - \hbar\omega')^2 + \Gamma_{\text{fs}}^2/4}, \qquad (8.19)$$

where the imaginary component $i\Gamma_{ch}$ is added to account for the lifetime of the intermediate state.

8.5 Cu^{2+} d^9 L_3-edge RIXS spectra

The perovskite KCuF$_3$ has attracted significant theoretical and experimental interest since the 1960s, given the strong coupling among the charge, orbital and spin degrees of freedom [367, 368] and effectively one-dimensional magnetic properties [369]. The crystal structure of KCuF$_3$ is made up of distorted CuF$_6$ octahedra, arranged in such a way as to give an almost equal Cu-Cu distance along the three principal axes of the pseudocubic perovskite cell with lattice parameters $a = b = 8.28$ Å and $c = 7.85$ Å [370]. The octahedral symmetry is broken well above room temperature by JT cooperative distortions [368, 371]: CuF$_6$ octahedra that are adjacent in the ab-plane are alternately elongated along either the a- or b-axis. The degeneracy of the Cu e_g levels in an ideal perovskite lattice is therefore lifted, the ground state implying alternate hole occupation of the $3d_{x^2-z^2}$ and $3d_{y^2-z^2}$ orbitals (orbital ordering effect), as shown in Fig.8.4(a).

In this section, we compute the Cu^{2+} d^9 L_3-edge RIXS spectra in KCuF$_3$ using QC methods and discuss the way to consider orbital ordering effects.

8.5.1 Computational scheme for Cu^{2+} d^9 L-edge excitations

QC calculations were performed on an embedded cluster made of one CuF$_6$ octahedron. Crystallographic data as reported in Ref. [370] were employed to construct the cluster and the embedding potential. The latter corresponds to a finite array of point charges fitted to reproduce the crystal Madelung field in the cluster region [152]. For the Cu ion, we used all-electron triple-zeta Douglas-Kroll basis sets with diffuse functions and weighted core-valence sets (aug-cc-pwCVTZ-DK [372]) to capture core-valence correlation effects. For the six F ligands, all-electron double-zeta Douglas-Kroll basis sets with diffuse functions (aug-cc-pVDZ-DK) [373] were used.

Cu^{2+} $3d^9$ valence-excited states. To access the on-site Cu^{2+} $3d^9$ valence-excited states, we used an active space of five $3d$ orbitals (t_{2g} and e_g) and nine electrons in the complete active space self-consistent field (CASSCF) [63] calculations. The SCF optimization was carried out for an average of all five doublet states associated with this manifold. The Pipek-Mezey localization module[186] available in MOLPRO was employed for localizing the Cu and F orbitals. On top of the CASSCF reference, the multireference configuration-interaction (MRCI) [230, 257] expansion additionally includes single and double excitations from the Cu $2s, 2p, 3s, 3p, 3d$ shells and the $2p$ orbitals of the F ligands. All five valence-excited doublet states entered the spin-orbit calculations, both at the CASSCF and MRCI levels. Spin-orbit (SO) effects were accounted for by diagonalizing the Breit-Pauli SO matrix in the basis of correlated scalar-relativistic states [148]. Corresponding *d*-*d* excitation energies at different levels of approximation are presented in Table 8.1.

Cu^{2+} $2p^5 3d^{10}$ core-hole states. For the intermediate $2p^5 3d^{10}$ core-hole states, the CASSCF treatment was performed in terms of fifteen electrons and five Cu $3d$ orbitals plus three Cu $2p$ orbitals while freezing these Cu $2p$ orbitals (with the occupation restriction of having maximum five electrons) in the active space. The SCF optimization was carried out for an average of three doublet states associated with the $2p^5 3d^{10}$ configuration. Appropriate changes were operated in the subsequent MRCI treatment such that the Cu $2p$ orbitals have at most five $2p$ electrons for internal and semi-internal substitutions. The Cu $2s, 2p, 3s, 3p, 3d$ shells and F $2p$ shells were correlated. The MRCI was performed as three-root calculation; these three core-hole states further entered the spin-orbit calculations. Computed $2p^6 3d^9 \rightarrow 2p^5 3d^{10}$ excitation energies at different levels of approximation are listed in Table 8.1.

Dipole transition matrix elements. The individual SCF optimizations of the valence-excited and core-hole states leads to sets of nonorthogonal orbitals. The MRCI dipole transition matrix elements between wave-functions expressed in terms of such nonorthogonal orbitals for the $3d^9$ and $2p^5 d^{10}$ groups of states (i.e., five valence-excited and three core-hole states) were derived according to the procedure described in Ref. [374].

The scattering geometry used in our computation is shown in Fig.8.4(c). The beam hits the sample surface at an incident angle θ and the outgoing beam is collected at an angle Ω. The scattering angle $180° - \Omega$ is fixed at $146°$. The momentum $\boldsymbol{q}$ transferred to the sample due to the scattering process and its projection onto the sample ab-plane $\boldsymbol{q_a}$ and c axis $\boldsymbol{q_c}$ are also shown. It should be noted that, for a fixed Ω, $\boldsymbol{q}$ is fixed, but $\boldsymbol{q_a}$ and $\boldsymbol{q_c}$ can be easily changed in both magnitude and direction in reciprocal space by rotating the sample around an axis perpendicular or parallel to the scattering plane (SP). According to the scattering geometry in Fig.8.4(c), we define here the SP as parallel to the c axis and achieve different values of $\boldsymbol{q_c}$ by changing the incident angle θ. With such notations,

$$|\boldsymbol{q}| = \left|\vec{k}_{in} - \vec{k}_{out}\right| = 2 \times \left|\vec{k}_{in}\right| \times \cos\left(\frac{\Omega}{2}\right), \tag{8.20}$$

$$|\boldsymbol{q_c}| = |\boldsymbol{q}| \times \sin\left(\theta + \frac{\Omega}{2}\right), \qquad |\boldsymbol{q_a}| = |\boldsymbol{q}| \times \cos\left(\theta + \frac{\Omega}{2}\right), \tag{8.21}$$

where $\vec{k}_{in}$ ($\vec{k}_{out}$) is the momentum carried by ingoing (outgoing) photons and we assume $\left|\vec{k}_{in}\right| \approx$

$\left|\vec{k}_{out}\right|$. The incoming light is linearly polarized, either perpendicular to the SP (σ polarization) or within the SP (π polarization). For the outgoing radiation, we carry out a summation over the two independent polarization directions.

For the analysis of the QC wave-functions, we use a local coordinate frame {x,y,z} with x, y and z axes as indicated in Fig.8.4(b), which is the same with the frame defined in Fig.8.4(c). The rotation of the σ, π and π' (introduced as outgoing π polarization) vectors as function of the angle θ is described by the following geometrical relations:

$$
\begin{aligned}
\vec{D}_\sigma &= \vec{D}_y, \\
\vec{D}_\pi &= \vec{D}_x \sin\theta + \vec{D}_z \cos\theta, \\
\vec{D}_{\pi'} &= \vec{D}_x \sin(\theta + \Omega) + \vec{D}_z \cos(\theta + \Omega),
\end{aligned}
\tag{8.22}
$$

where $\vec{D}_\epsilon^{kl} = \left\langle \Psi_{fs}^k \left| e \cdot \vec{R} \right| \Psi_{c^\star}^l \right\rangle$ stands for dipole transition matrix elements. The expression for the XA cross section in Eq.(8.13) changes then to

$$
\begin{aligned}
I^{XAS}(\hbar\omega,\epsilon,\theta) = 4\pi^2 \alpha\hbar\omega \sum_j \frac{1}{g_{gs}} \sum_l &\left| \left\langle \Psi_{c^\star}^l \left| \vec{D}_\epsilon \right| \Psi_{gs}^j \right\rangle \right|^2 \\
&\times \frac{\Gamma_{c^\star}/2\pi}{(E_{gs}^j + \hbar\omega - E_{c^\star}^l)^2 + (\Gamma_{c^\star})^2/4}.
\end{aligned}
\tag{8.23}
$$

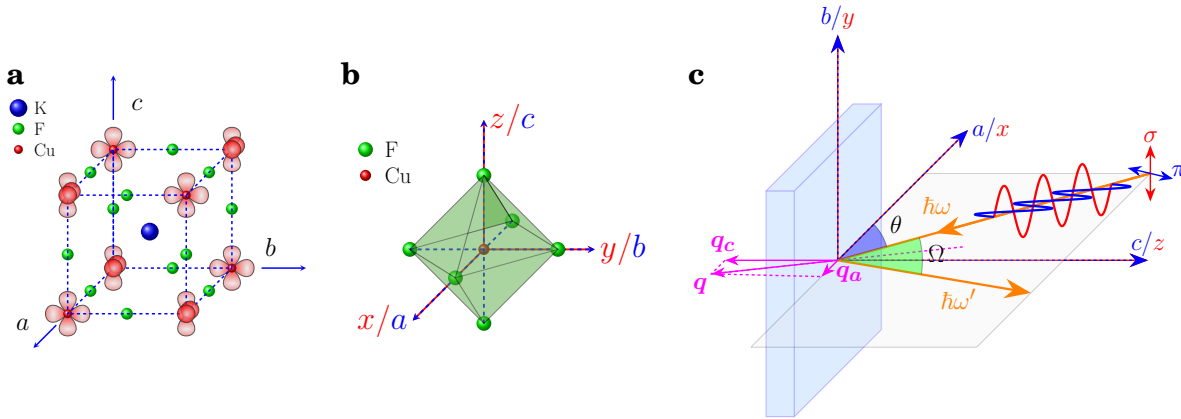The RIXS double differential cross section can be computed according to Eq.(8.19) by summing

Figure 8.4: (a): Crystal structure and a possible orbital pattern in KCuF$_3$. The hole in the Cu 3d shell alternately occupies $d_{x^2-z^2}$ and $d_{y^2-z^2}$ orbitals. (b): The [CuF$_6$] cluster used in the QC calculations. (c): The RIXS scattering geometry used in our computation. Linearly polarized X-rays with energy $\hbar\omega$ hit the surface (assumed to be parallel to the ab-plane) of the sample at an incident angle θ and the outgoing beam with energy $\hbar'\omega$ is collected at the angle Ω. The SP is here the crystallographic (010) plane (and can be adjusted by rotating the cluster around the z axis). The incident angle θ can be changed whereas the angle Ω is fixed as 34°. The projection of the transferred momentum $\boldsymbol{q}$ onto the ab-plane $\boldsymbol{q_a}$ and on the c axis $\boldsymbol{q_c}$ are also shown.

Table 8.1: Relative energies for Cu^{2+} $3d^9$ and $2p^5 3d^{10}$ states in KCuF$_3$; units of eV are used. The Jahn-Teller distortions occur within the xy plane. Each MRCI+SOC value stands for a spin-orbit Kramers doublet.

Hole orbital	CASSCF	MRCI	MRCI+SOC	Exp.[a]
$d_{x^2-z^2}$	0.00	0.00	0.00	0.00
d_{y^2}	0.76	0.82	0.79	0.71–1.02
d_{xz}	0.82	0.89	0.88	1.05–1.15
d_{xy}	0.98	1.05	1.09	1.21–1.37
d_{yz}	1.08	1.16	1.23	1.34–1.46
$p_{3/2}$	940.50; 940.54	939.18; 939.21	932.46; 932.52	–
$p_{1/2}$	940.60	939.28	952.74	–

[a] Optical absorption results reported in Ref. [375]. The two numbers correspond to the onsets and the maxima of the absorption bands, respectively.

over the outgoing polarization directions:

$$
I^{RIXS}(\hbar\omega, \hbar\omega', \epsilon, \theta) = \frac{d^2\sigma^{RIXS}_{\vec{k},\epsilon}}{d\Omega' d\hbar\omega'} =
$$

$$
\frac{\alpha^2\hbar^2}{e^4 c^2}\omega\omega'^3 \sum_{\epsilon'}\sum_{j}\frac{1}{g_{gs}}\sum_{k}\left|\sum_{l}\frac{\left\langle\Psi^k_{fs}\left|\vec{D}_{\epsilon'}\right|\Psi^l_{c\star}\right\rangle\left\langle\Psi^l_{c\star}\left|\vec{D}_\epsilon\right|\Psi^j_{gs}\right\rangle}{E^j_{gs} + \hbar\omega - E^l_{c\star} + (i\Gamma_{c\star}/2)}\right|^2
$$

$$
\times \frac{\Gamma_{fs}/2\pi}{(E^j_{gs} + \hbar\omega - E^k_{fs} - \hbar\omega')^2 + (\Gamma_{fs})^2/4}. \tag{8.24}
$$

The natural widths $\Gamma_{c\star}$ and Γ_{fs} are here set to 1 eV and 0.16 eV, respectively, typical values for Cu *L*-edge RIXS [335, 339].

8.5.2   Results and discussion

The *d-d* excitation energies from optical spectra of KCuF$_3$ [375] are compared with QC calculations in Table 8.1. The CASSCF and MRCI *d*-level splittings are very similar with those obtained by using a more elaborated Hartree-Fock (HF) embedding [79]. In Table 8.1, the MRCI treatment brings corrections of $0.06-0.08$ eV to the CASSCF splittings, somewhat smaller than for other cuprates discussed in Ref. [79]. This is related to the more ionic character of the Cu-F bond in KCuF$_3$ and smaller degree of Cu $3d$ and F $2p$ orbital mixing [79]. The MRCI results tend to slightly underestimate the values corresponding to the maxima of the experimental absorption peaks [375], by $0.23-0.28$ eV.

According to the relative energies of Cu^{2+} core-hole $2p^5 3d^{10}$ states obtained from MRCI+SOC calculations in Table 8.1, the $2p^5$ $j = 3/2$ quartet and $j = 1/2$ doublet are separated by ~20 eV. The Cu L_3- and L_2-edges are at ~932.5 and ~952.7 eV, respectively.
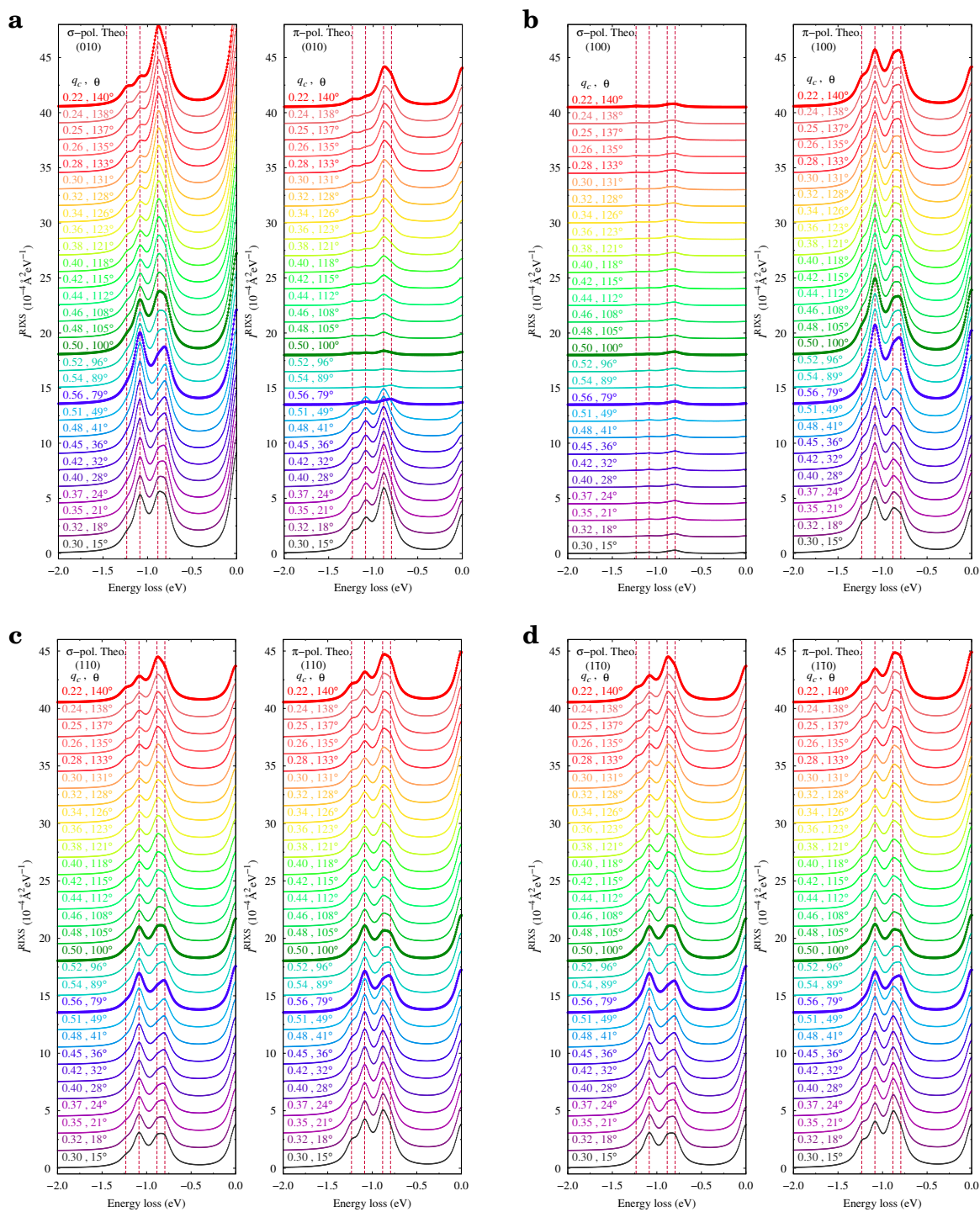
Figure 8.5: Calculated (MRCI+SOC) RIXS double differential cross sections with σ- and π-polarizations at different transferred momenta $\boldsymbol{q_c}$ (incident angle θ) for Cu^{2+} d^9 ions in KCuF$_3$. (a,b,c,d): RIXS spectra computed by defining the SP as (010), (100), (110) and (1$\bar{1}$0), respectively.

By setting the energy of the incident photons at the Cu L_3-edge (932.5 eV), the RIXS intensities for σ- and π-polarizations at different transferred momenta $\boldsymbol{q_c}$ (incident angle θ) can be computed. We use the scattering geometry shown in Fig.8.4(c) but adjust the SP as being

either the crystallographic (010) or (110) plane by rotating the cluster around the z axis [see Fig. 8.4(b)]. In order to account for the different orientation of the $3d$ hole orbitals on adjacent Cu sites [$3d_{y^2-z^2}$ and $3d_{z^2-x^2}$, see Fig. 8.4(a)], we rotate the cluster around the z axis by 90°. In our case, after 90° rotation around the z axis, the SP's (010) and (110) change to (100) and (1$\bar{1}$0), respectively. The computed RIXS spectra for such different SP's are presented in Fig. 8.5. These spectra [Fig. 8.5(a) and Fig. 8.5(b)], obtained by defining the SP's either as (010) and (100), reveal significantly different features. In particular, the intensities for σ-polarization computed for the (100) plane are weaker as compared to those for the (010) plane. Differences are also obvious between the intensities for π-polarization, i.e., the intensity of the excitation peak at ~1.1 eV for the (100) plane is much stronger than that for the (010) plane and with θ changing from 79° to ~121° the intensities for all excitation peaks when having a (010) SP are much weaker as compared to those for a (100) SP. On the other hand, with the same θ for either σ- or π-polarization, the intensities computed for the (110) and (1$\bar{1}$0) SP's are identical.

8.6   Ni^{2+} d^8 L_3-edge RIXS spectra

In recent years, La$_2$NiO$_4$ has been extensively investigated because of its structural similarity with the high-T_c superconductor La$_2$CuO$_4$. In both systems, the transition-metal-oxide planes, NiO$_2$ or CuO$_2$, can be doped with hole-like charge carriers resulting in a large number of different structural and electronic phases, in particular the superconducting phase in the case of the cuprate [376–380]. For RIXS processes, the Ni^{2+} d^8 configuration, with more than one single hole in the initial configuration of the valence $3d$ shell, also involves more intermediate (thirty core-hole states) and final states (twenty-five valence states), as compared to the case of the Cu^{2+} d^9 configuration (three core-hole states, five valence states). We apply here the methodology described in Section 8.5 to address the Ni^{2+} L-edge $2p \rightarrow 3d$ excitations in La$_2$NiO$_4$ and compute the Ni^{2+} d^8 L_3-edge RIXS spectra.
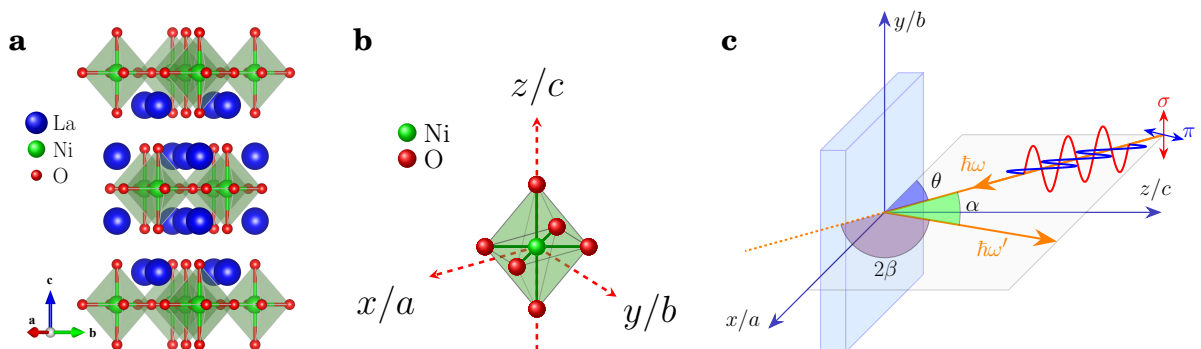

Figure 8.6: (a): Schematic representation of the orthorhombic La$_2$NiO$_4$ structure. (b): The [NiO$_6$] cluster used in QC calculations. (c): RIXS experimental scattering geometry. Linearly polarized X-rays with energy $\hbar\omega$ are incident upon the sample. The scattered photons ($\hbar\omega'$) are collected at 2β=130° and measured as a function of final energy.

Table 8.2: $3d$-shell energy levels for a Ni^{2+} $3d^8$ ion in La$_2$NiO$_4$; unless otherwise specified, units of eV are used. All $3d^8$ valence-excited states are listed. Notations corresponding to D_{4h} point-group symmetry are used to label the various states. For brevity, notations as in O_h symmetry are used for the $3d$ orbitals. Energies relative to the $^3B_{1g}$ ground state are given. For all the high-spin states, only the lowest and highest SO components are given. The RIXS experimental data are taken from Ref. [338].

Ni^{2+} $3d^8$ splittings	CASSCF	MRCI	MRCI+SOC	Exp.
$^3B_{1g}$ ($t_{2g}^6 e_g^2$)	0.00	0.00	$0.00-0.00$	0.00
^3E_g ($t_{2g}^5 e_g^3$)	0.72	0.77	$0.72-0.84$	1.06
$^3B_{2g}$ ($t_{2g}^5 e_g^3$)	1.18	1.30	$1.28-1.30$	
$^3A_{2g}$ ($t_{2g}^5 e_g^3, t_{2g}^4 e_g^4$)	1.40	1.47	$1.44-1.48$	1.61
$^1A_{1g}$ ($t_{2g}^6 e_g^2$)	1.88	1.70	1.70	
^3E_g ($t_{2g}^4 e_g^4, t_{2g}^5 e_g^3$)	1.64	1.79	$1.78-1.85$	2.29
$^1B_{1g}$ ($t_{2g}^6 e_g^2$)	2.08	1.98	2.04	
^1E_g ($t_{2g}^5 e_g^3$)	2.71	2.67	2.67; 2.67	2.93
$^1B_{2g}$ ($t_{2g}^5 e_g^3$)	3.08	3.11	3.08	
$^3A_{2g}$ ($t_{2g}^4 e_g^4, t_{2g}^5 e_g^3$)	3.09	3.11	$3.12-3.14$	3.35
$^1A_{2g}$ ($t_{2g}^5 e_g^3$)	3.49	3.30	3.32	
^3E_g ($t_{2g}^5 e_g^3, t_{2g}^4 e_g^4$)	3.42	3.43	$3.42-3.49$	3.80
$^1A_{1g}$ ($t_{2g}^6 e_g^2, t_{2g}^4 e_g^4$)	3.66	3.52	3.57	–
^1E_g ($t_{2g}^5 e_g^3, t_{2g}^4 e_g^4$)	4.14	4.05	4.07; 4.07	–
$^1A_{1g}$ ($t_{2g}^4 e_g^4, t_{2g}^6 e_g^2$)	4.43	4.38	4.40	–
^1E_g ($t_{2g}^4 e_g^4, t_{2g}^5 e_g^3$)	4.54	4.49	4.50; 4.50	–
$^1B_{1g}$ ($t_{2g}^4 e_g^4$)	4.55	4.52	4.54	–
$^1B_{2g}$ ($t_{2g}^4 e_g^4$)	4.69	4.65	4.66	–
$^1A_{1g}$ ($t_{2g}^4 e_g^4, t_{2g}^6 e_g^2$)	7.76	7.63	7.65	–

8.6.1 Computational scheme for Ni^{2+} d^8 L-edge excitations

QC calculations were carried out on one NiO$_6$ octahedron as depicted in Fig.8.6(b), using the crystal structure data reported in Ref. [381]. The farther solid-state surroundings were modeled as a finite array of point charges fitted to reproduce the crystal Madelung field in the cluster region [152]. For the Ni ion, we used all-electron triple-zeta Douglas-Kroll basis sets with diffuse functions and weighted core-valence sets aug-cc-pwCVTZ-DK [372] to capture core-valence correlation effects. For the six O ligands, all-electron double-zeta Douglas-Kroll basis sets with diffuse functions aug-cc-pVDZ-DK [373] were used. All *ab initio* calculations were carried out with the QC package MOLPRO [181].

$3d^8$ **valence-excited states.** To access the Ni^{2+} $3d^8$ on-site valence-excited states, we

Table 8.3: $3d$-shell energy levels for a Ni^{2+} $3d^8$ ion in La_2NiO_4, obtained from QC calculations in which the SCF optimization was performed for an average of the lowest one triplet and two singlet $t_{2g}^6 e_g^2$ states (all values in eV). The RIXS experimental data are taken from Ref. [338].

Ni^{2+} $3d^8$ splittings	CASSCF	MRCI	MRCI+SOC	Exp.
$^3B_{1g}$ $(t_{2g}^6 e_g^2)$	0.00	0.00	$0.00 - 0.00$	0.00
^3E_g $(t_{2g}^5 e_g^3)$	1.06	1.01	$0.96 - 1.07$	1.06
$^3B_{2g}$ $(t_{2g}^5 e_g^3)$	1.63	1.61	$1.60 - 1.62$	1.61
$^3A_{2g}$ $(t_{2g}^5 e_g^3, t_{2g}^4 e_g^4)$	1.96	1.85	$1.86 - 1.91$	
$^1A_{1g}$ $(t_{2g}^6 e_g^2)$	2.07	1.77	1.72	
^3E_g $(t_{2g}^4 e_g^4, t_{2g}^5 e_g^3)$	2.28	2.22	$2.21 - 2.32$	2.29
$^1B_{1g}$ $(t_{2g}^6 e_g^2)$	2.29	2.06	2. 06	
^1E_g $(t_{2g}^5 e_g^3)$	3.30	3.01	3.02; 3.02	2.93
$^1B_{2g}$ $(t_{2g}^5 e_g^3)$	3.79	3.55	3.57	3.35
$^3A_{2g}$ $(t_{2g}^4 e_g^4, t_{2g}^5 e_g^3)$	3.90	3.61	$3.63 - 3.64$	
$^1A_{2g}$ $(t_{2g}^5 e_g^3)$	3.91	3.64	3.65	3.80
$^1A_{1g}$ $(t_{2g}^6 e_g^2, t_{2g}^4 e_g^4)$	4.01	3.74	3.76	

used an active space of five $3d$ orbitals (t_{2g} and e_g) and eight electrons in the CASSCF [63] calculations. The SCF optimization was carried out for an average of ten triplet and fifteen singlet states associated with this manifold. The Pipek-Mezey localization module [186] available in MOLPRO was employed for localizing the Ni and O orbitals. On top of the CASSCF reference, the MRCI [230, 257] expansion additionally includes single and double excitations from the Ni $2s, 2p, 3s, 3p, 3d$ shells and the $2p$ shells of the O ligands. All these valence-excited states entered the spin-orbit calculations, both at the CASSCF and MRCI levels. SO effects were accounted for by diagonalizing the Breit-Pauli SO matrix in the basis of correlated scalar-relativistic states [148]. Corresponding d-d excitation energies at different levels of approximation are presented in Table 8.2.

We also carried out a set of calculations in which the SCF optimization of the valence-excited states was performed for an average of the lowest one triplet and two singlet $t_{2g}^6 e_g^2$ states. The MRCI treatment was performed for both spin multiplicities, triplet and singlet, as eight- and seven-root calculations, respectively; these MRCI states were further considered in the spin-orbit calculations. Computed on-site $d-d$ excitation energies at different levels of approximation are provided in Table 8.3. More discussion and comparison with experimental data are provided in section 8.6.2.

$2p^5 3d^9$ **core-hole states.** For the intermediate $2p^5 3d^9$ core-hole states, the CASSCF treatment was performed in terms of fourteen electrons and five Ni $3d$ orbitals plus three Ni $2p$ orbitals while freezing these Ni $2p$ orbitals (with the occupation restriction of having maximum

Table 8.4: Relative energies (eV) for Ni^{2+} $2p^5 3d^9$ states in La$_2$NiO$_4$. The numbers of states included in the spin-orbit treatments, i.e., singlet (S) and triplet (T), for $2p^6 3d^8$ and $2p^5 3d^9$ configurations are given in the first column.

States considered	CAS+SOC[a]	MRCI+SOC[a]	Experiment
$2p^6 3d^8$(10T, 15S)	856.2	855.0	
$2p^5 3d^9$(15T, 15S)			854.0[b]
$2p^6 t_{2g}^6 e_g^2$(1T)	855.0	853.6	
$2p^5 t_{2g}^6 e_g^3$(6T)			

[a] The relative energy is the energy difference between the lowest energies of the SO components associated with the $2p^6 3d^8$ and $2p^5 3d^9$ configurations.

[b] This energy was measured as the maximum intensity of the L_3-edge XAS [338].

five electrons) in the active space. The SCF optimization was carried out for an average of fifteen triplet states associated with the $2p^5 3d^9$ configurations. On top of the CASSCF reference, in order to exclude the $2p^6 3d^8$ valence-excited states, appropriate changes were further operated in the subsequent MRCI treatment such that the Ni $2p$ orbitals have at most five $2p$ electrons for internal and semi-internal substitutions in the case of the Ni $2p^5 3d^9$ configuration. The electrons of the Ni $2s, 2p, 3s, 3p, 3d$ shells and of the O $2p$ shells were correlated. The MRCI was performed for each spin multiplicity, triplet or singlet, as fifteen-root calculation. All these core-hole states entered the spin-orbit calculations.

Here we also performed additional calculations in which the SCF optimization of the valence-excited $2p^6 3d^8$ and core-hole $2p^5 3d^9$ configurations were carried out for the triplet $^3B_{1g}$ ($t_{2g}^6 e_g^2$) state and six triplet states associated with the $2p^5 t_{2g}^6 e_g^3$ configuration, respectively. In such calculations, the MRCI treatment was performed for both spin multiplicities, triplet and singlet, as one- and six-root calculations, respectively; all these states further entered the spin-orbit calculations. Computed $p_{3/2} p^6 d^9 \rightarrow p^5 d^{10}$ excitation energies at different levels of approximation are listed in Table 8.4.

Dipole transition matrix elements. The dipole transition matrix elements between wavefunctions expressed in terms of such nonorthogonal orbitals were derived according to the procedure described in Ref. [374].

The Ni L_3-edge RIXS measurements of La$_2$NiO$_4$ were performed by Fabbris *et al.* [338] in Brookhaven National Laboratory. The experimental scattering geometry and the polarizations are specified in Fig.8.6(c). Linearly polarized X-rays were incident at an angle (θ) with the sample plane. The latter has a c axis surface normal. The scattering angle between the incoming and outgoing light beams was fixed to α=180°-2β=50°, while the incident angle θ was varied from 20° to 120°. The incoming light was linearly polarized, either perpendicular to the scattering plane (σ polarization) or within the scattering plane (π polarization). For the outgoing radiation, we carried out a summation over the two independent polarization directions.

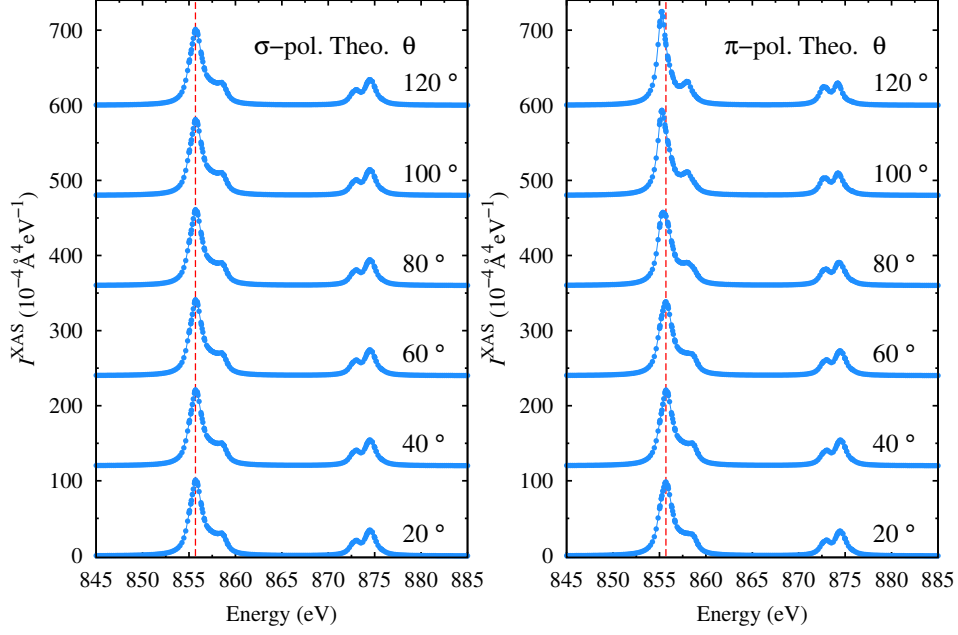For the analysis of the QC wave-functions, we use a local coordinate frame {x,y,z} with x, y

Figure 8.7: Calculated (MRCI+SOC) XA spectra for σ- and π-polarizations with different incident angles θ for a Ni^{2+} d^8 ion in La$_2$NiO$_4$. The L_3-edge incident energy for RIXS is chosen as the maximum XAS intensity, as shown by the red dashed line (~855.5 eV).

and z along the a, b and c axes of the La$_2$NiO$_4$ unit cell, respectively. The rotation of the σ, π and π' (introduced as outgoing π polarization) vectors as function of the angle θ is described by the following geometrical relations:

$$
\begin{aligned}
\vec{D}_\sigma &= \vec{D}_y, \\
\vec{D}_\pi &= \vec{D}_x \sin\theta + \vec{D}_z \cos\theta, \\
\vec{D}_{\pi'} &= \vec{D}_x \sin(\theta + \alpha) + \vec{D}_z \cos(\theta + \alpha),
\end{aligned}
\tag{8.25}
$$

where $\vec{D}_\epsilon^{kl} = \left\langle \Psi_{\text{fs}}^k \left| e \cdot \vec{R} \right| \Psi_{c^\star}^l \right\rangle$ stands for dipole transition matrix elements.

The expressions for the XA cross section and the RIXS double differential cross section are the same as Eq.8.23 and Eq.8.24. The natural widths $\Gamma_{c^\star}$ and Γ_{fs} are here set as 0.4 eV and 0.15 eV, respectively, typical values for Ni L-edge RIXS [382, 383].

8.6.2   Results and discussion

In Table 8.4, with all $3d^8$ valence-excited and $2p^63d^9$ core-hole states considered, the $p_{3/2}$ $2p^63d^9 \rightarrow 2p^53d^{10}$ excitation energy as computed at the CAS+SOC level overestimates by about 2.2 eV the experimental result. The MRCI+SOC treatment yields corrections of ~1.2 eV, which brings the *ab initio* value within 1.0 eV of the measured $p_{3/2}$ XA edge. For the results in which the $^3B_{1g}$ ($t_{2g}^6 e_g^2$) ground state and the six triplet states associated with the $2p^5 t_{2g}^6 e_g^3$ configuration were explicitly optimized, the $p_{3/2}$ excitation energies decrease by 1.2 eV and 1.4 eV in CAS+SOC and MRCI+SOC, respectively, as compared to these of the former set of calculations.

The calculated XA spectrum is presented in Fig.8.7. Inelastic scattering features are at incident photon energies of $854 - 860$ and $872 - 877$ eV, which are the Ni L_3- and L_2-edges,
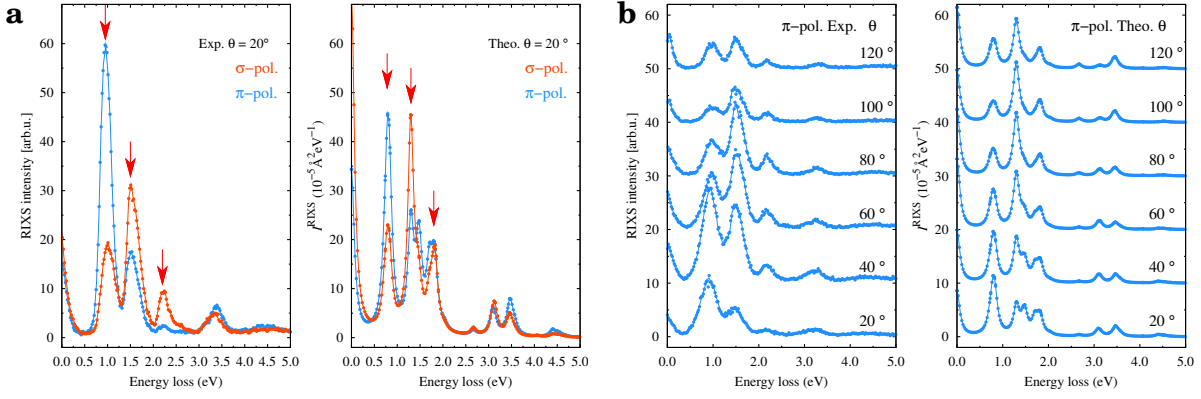
Figure 8.8: Ni d^8 L_3-edge RIXS spectra in La$_2$NiO$_4$. (a): Experimental data and QC results compared for σ- and π-polarizations at an incident angle $\theta=20°$. (b): The experimental data and QC results compared for π-polarization at incident angles $\theta=20°$, $40°$, $60°$, $80°$, $100°$, $120°$.

respectively. The $2p$ core-hole states in La$_2$NiO$_4$ are split by approximately 18 eV due to SOC. The effect of SOC is on the other hand fairly small for the Ni $3d^8$ valence states and brings only tiny corrections to those relative energies. Experimentally, the L_3-edge energy was set to the maximum intensity of the L_3 XAS [338]. Similarly, we set the L_3-edge incident energy (~855.5 eV) at the maximum XA intensity, as shown in Fig.8.7.

By setting the incident photon energy at the Ni L_3-edge (855.5 eV), the RIXS intensities
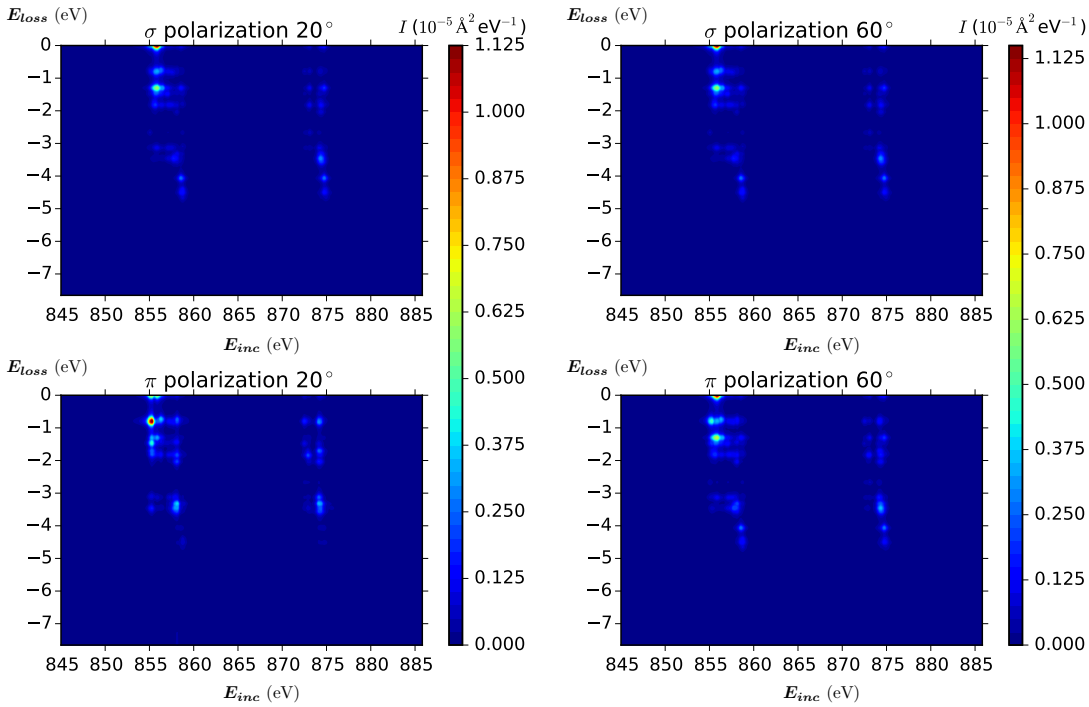

Figure 8.9: Theoretical $I(E_{inc}, E_{loss})$ RIXS plots for La$_2$NiO$_4$ using the geometrical setup employed in the measurements.

for σ- and π-polarizations at different incident angles θ were computed. Fig.8.8 shows the *ab initio* results for full Ni L_3-edge RIXS spectra along with experimental data. When changing the incident angle θ, the evolution of the RIXS intensities is different for each of the main peaks, which is also apparent from the $I(E_{inc}, E_{loss})$ plots in Fig.8.9. Regarding the RIXS intensities for π-polarization at different incident angles θ, the QC data agree well with the experiment, with all major trends well reproduced. The intensities of the two peaks in the range of $0.5 - 1.5$ eV, in particular, clearly display distinct behavior with increasing angle θ – while the excitation peak at about 0.8 eV first loses spectral weight then slightly increases (for the experimental spectra the intensity of this excitation peak first increases with θ changing from $20°$ to $40°$), the one at about 1.3 eV acquires more intensity then slightly decreases. With regard to peak positions, the agreement with the experimental data is within 0.3 eV for the first excitation peak $(^3E_g, t_{2g}^5 e_g^3)$. The second excitation peak has to do with the $^3B_{2g}(t_{2g}^5 e_g^3)$, $^3A_{2g}(t_{2g}^4 e_g^4, t_{2g}^5 e_g^3)$ and $^1A_{1g}$ $(t_{2g}^6 e_g^2)$ states. On the computational side, this excitation peak is slightly split apart at low incident angles $(\theta = 20°, 40°)$ but not strongly enough to be resolved as two individual peaks in experiment. For the third excitation peak around 2.2 eV in experiment, the MRCI calculations underestimate the relative energy by 0.4 eV. It should be noted that Ni $3d$ to O $2p$ charge-transfer (CT) states are not included explicitly in these calculations, since it is computationally more demanding to accurately model both the valence-excited and CT than only the valence-excited states, and accordingly RIXS features from CT states are absent in the calculated RIXS maps in Fig.8.9.

For the results of on-site $d - d$ excitations presented in Table 8.3, in which the one triplet and two singlet states associated with the $t_{2g}^6 e_g^2$ configuration were explicitly optimized, the agreement of MRCI with the RIXS experimental results is within ~ 0.2 eV. In particular, within the energy region up to 2.3 eV, the agreement between MRCI and experimental results is significantly improved as compared to the results presented in Table 8.2. At first sight, it may be surprising that the better agreement with experiment is obtained for optimizing the states associated with the ground state $(t_{2g}^6 e_g^2)$ configuration. The use of the state-average SCF optimization only for the low excited states associated with the ground state $(t_{2g}^6 e_g^2)$ configuration (with large weight for ground state configuration), yields more suitable orbitals to represent ground state, leading to a stabilization of energy of ground state and large $d - d$ excitation energies.

It is seen that at $20°$ incident angle, for the third excitation peak in Fig.8.8(a), the intensities with σ-polarization have predominant spectral weight in the RIXS experiment. However, the σ- and π-polarization intensities are similar for the *ab initio* results. In order to address these different dichroism features between the RIXS experiment and *ab initio* results, we computed L_3-edge RIXS spectra of each spin-orbit coupled component associated with the $^3B_{1g}$ $(t_{2g}^6 e_g^2)$ ground state. The compositions of the spin-orbit eigenvectors for these three components on the
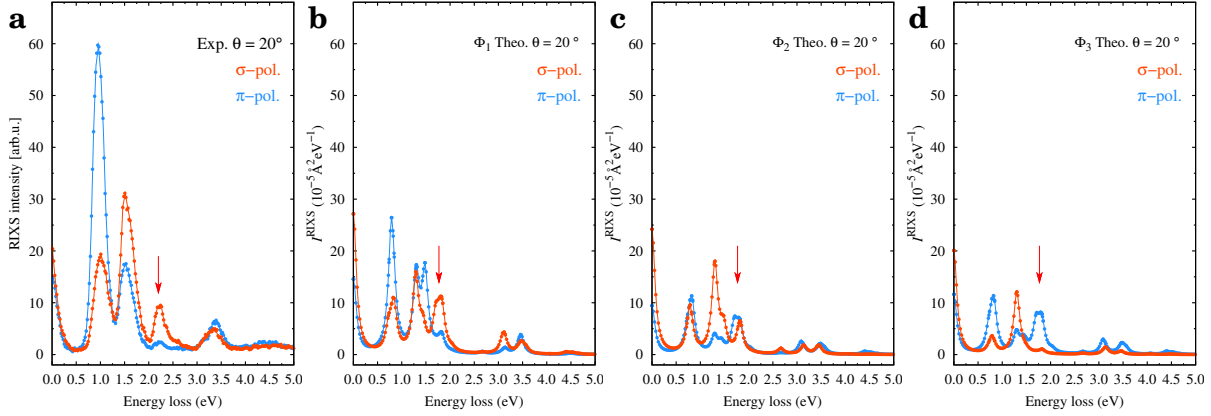
Figure 8.10: (a) The experimental RIXS spectra for σ- and π-polarizations at the incident angle $\theta=20°$. (b), (c) and (d): Calculated (MRCI+SOC) RIXS spectra for σ- and π-polarization at the incident angle $\theta=20°$ for each spin-orbit coupled $^3B_{1g}$ component, ϕ_1, ϕ_2 and ϕ_3 (see text).

basis of spin z-projection (s_z) obtained from the MRCI+SOC calculations are:

$$\phi_1 \approx 98.25\%\left|^3B_{1g}, s_z = 0\right\rangle + \quad 0.84\%\left|^3E_g, s_z = 1\right\rangle \quad + 0.84\%\left|^3E_g, s_z = -1\right\rangle,$$
$$\phi_2 \approx 31.48\%\left|^3B_{1g}, s_z = 1\right\rangle + 67.19\%\left|^3B_{1g}, s_z = -1\right\rangle + 0.89\%\left|^3E_g, s_z = 0\right\rangle, \tag{8.26}$$
$$\phi_3 \approx 67.19\%\left|^3B_{1g}, s_z = 1\right\rangle + 31.48\%\left|^3B_{1g}, s_z = -1\right\rangle + 0.89\%\left|^3E_g, s_z = 0\right\rangle,$$

where ϕ_2 and ϕ_3 have the same energy and the energy difference between ϕ_1 and ϕ_2 (ϕ_3) is $E_{\phi_2,\phi_3} - E_{\phi_1} = 2.1$ meV. The disentangled L_3-edge RIXS spectra for each spin-orbit coupled component ϕ_1, ϕ_2 and ϕ_3 with σ- and π-polarizations at the incident angle $\theta=20°$ are shown in Fig.8.10. It is apparent that, for the third excitation peak, the computed RIXS spectrum for component ϕ_1 has a very similar dichroism feature with that of experiment, i.e., the intensities of σ-polarization are predominant. Therefore, we argue that this dichroism feature revealed from the RIXS experiment provides information on the spin orientation in the actual material.

In our *ab initio* calculations, the dipole transition matrix elements are absolute values, not just relative estimates as in semi-empirical schemes. The theoretical plots presented in Fig.8.5, Fig.8.8 and Fig.8.9 are based on such absolute values. With the absolute cross section, one can quantify specific 'scattering properties' of the material, e.g. how many photons of particular energy and polarization will be scattered by a given atomic site in a given direction [236].

8.7 Conclusions

In $3d$ TM compounds, the on-site $d-d$ transitions and L-edge $2p \rightarrow 3d$ transitions are relatively localized excitations, for which the number of electrons in the system is conserved and the longer-range polarization effects are not very important. In such case, many-body schemes based on relatively small clusters are able to describe the 'local' multiplet structure and reproduce the major features of RIXS spectra. We use a multireference configuration-interaction-type

of methodology for the *ab initio* calculation of TM *L*-edge excitations of Cu^{2+} $3d^9$ ions in $KCuF_3$ and Ni^{2+} $3d^8$ ions in La_2NiO_4. For the more convenient case of Cu^{2+} $3d^9$ ions in $KCuF_3$, we discuss the way to consider orbital ordering effects (alternately occupied $3d_{x^2-z^2}$ and $3d_{y^2-z^2}$ orbitals) in computing RIXS spectra. For the case of Ni^{2+} $3d^8$ ions in La_2NiO_4, which has more than one single hole in the initial configuration of the valence $3d$ shell and also has more intermediate $2p^5 3d^9$ and final $2p^6 3d^8$ states in the RIXS process as compared with the Cu^{2+} $3d^9$ ion, the RIXS spectra obtained with our computational scheme show good agreement with experimental data, for both excitation energies and polarization- and angle- dependent intensities.

Chapter 9

Summary and outlook

This thesis focuses on the theoretical investigation of the electronic structure and magnetic interactions present in $3d$ and $4d/5d$ transition metal (TM) compounds. We use many-body quantum chemistry (QC) methods that provide a theoretical frame for the rigorous construction and systematic improvement of correlated N-electron wave-functions. A summary of the results discussed in this thesis and an outlook for future work are provided in the following.

In Chapter 3 we compute $d - d$ transitions fully *ab initio* and assign excitation peaks of experimental spectra measured in spin-Peierls (SP) TiPO$_4$ compound. In this material we find that the d^1 ground state is composed of an admixture of d_{z^2} and d_{xz} orbital character, which is related to the large positive ionic charge at P sites in the xz plane (defining the shortest Ti-P links) and of Ti nearest-neighbors (NN) along the z axis, see also Fig. 3.1. Such results on TiPO$_4$ confirm for the 1D case cation charge-imbalance effects earlier evidenced in 2D [189, 262] and 3D [191, 271] systems. In addition, the magnitude of the NN Heisenberg magnetic coupling calculated by QC methods compares well with resonant inelastic X-ray scattering (RIXS) experimental data. We further demonstrate that the intersite exchange is very sensitive to the Ti-Ti interatomic distance, which is relevant in the context of SP physics in TiPO$_4$. In our *ab initio* calculations, due to the limitations of currently available computational resources, we only computed the NN and next-nearest-neighbor (NNN) intrachain superexchange interaction (the chain is defined by TiO$_6$ octahedra along the c axis, see Fig. 3.1), while another puzzling aspect is the strength and type of the interchain superexchange interaction.

In Chapter 4, we have studied the magnetic anisotropy of Fe ions within the Li$_3$N lattice. The calculated magnetic anisotropy splitting of 26.3 meV for Fe^{2+} d^6 ions in D_{6h} symmetry compares favorably to values measured or computed by similar theoretical methods for Fe^{1+} d^7 species with linear coordination. This substantial spin-reversal energy barrier of the Fe^{2+} ion is associated with a $a_{1g}^1 e_{2g}^3 e_{1g}^2$ ground-state electron configuration. Our study therefore puts into the spotlight the linearly coordinated Fe^{2+} d^6 ion as candidate for viable SMM behavior. One interesting aspect of future work on Fe ions within the Li$_3$N lattice is superexchange interactions between individual Fe ions that substitute the Li-1b sites. In particular, how large and which sign are the Fe-Fe magnetic couplings for different types of units, for instance, the magnetic couplings between the Fe ions bridged by one N ion along the c axis or between the NN Fe ions in the ab plane (see Fig. 4.2(a)). Another interesting aspect is to substitute the Li-1b sites in the Li$_3$N matrix by other TM species, such as Mn, Co and Ni [219] or even $4d/5d$ TM elements.

Of particular interests in this aspect are to investigate variations of the magnitude of magnetic anisotropy and the $d-d$ excitation energies, the effect of having a vacancy at the Li site nearby the TM ion, as caused by different substituted TM species.

In Chapter 5 we address the effect of electron-lattice interactions on the magnetic properties of $4d$ and $5d$ TM ions with a formally degenerate t_{2g}^1 electron configuration in the double-perovskite (DP) materials Ba_2YMoO_6, Ba_2LiOsO_6 and Ba_2NaOsO_6. Our analysis indicates that the sizable magnetic moments and g-factors found experimentally are due to both strong TM d − ligand p hybridization and dynamic Jahn-Teller effects. Our results also point out that cation charge imbalance in the DP structure allows a fine tuning of the gap between the t_{2g} and e_g levels. The mechanism has not been explored so far experimentally but seems to hold much potential in the context of orbital engineering in TM compounds.

In Chapter 6 we report a study of magnetic exchange interactions in the S=3/2 orthorhombic perovskite $NaOsO_3$. We mapped the *ab initio* QC results onto model Hamiltonians including both isotropic Heisenberg interactions and anisotropic Dzyaloshinskii- Moriya (DM) exchange. We found antiferromagnetic (AFM) NN Heisenberg exchange interactions of J_{ac}=24.4 meV and J_b=20.9 meV, twice larger than the J extracted from the magnon excitation spectra reported in Ref. [272]. The QC results motivate further experimental measurements or theoretical analysis to clarify the magnitude of the NN Heisenberg couplings and more detailed investigations of the adiabatic magnon spectra in $NaOsO_3$.

In Chapter 7 we provide valuable insights on the effective magnetic interactions in $5d$ and $4d$ oxides with face-sharing oxygen octahedra, $BaIrO_3$ and $BaRhO_3$, for different bond-angles and bond-lengths. The large AFM Heisenberg interactions computed here emphasize the subtle interplay among strong spin-orbit interactions, direct intersite orbital overlap and orbital bonding, and couplings to the lattice degrees of freedom in face-sharing compounds. For future work, one interesting question is what if there are unpaired electrons localized on dimers of the Ir/Rh atoms. One example is $Ba_3InIr_2O_9$, where mixed-valence Ir_2O_9 with $Ir^{4.5+}$ are formed, sharing one unpaired electron per dimer [311]. Such mixed-valence dimers with an unpaired electron delocalized between the two $Ir^{4.5+}$ ions are very different from the conventional dimers formed by two magnetic ions holding one unpaired electron each. More recently, the mixed-valence iridates have attracted much attention since they are proposed as a promising playground for unexplored electronic states and new regimes of anisotropic exchange interactions [311].

In Chapter 8 we apply a computational scheme for computing intensities as measured in X-ray absorption and RIXS experiments. We take into account the readjustment of the charge distribution in the 'vicinity' of an excited electron for the modeling of RIXS. For L_3-edge spectra of Cu^{2+} $3d^9$ ions in $KCuF_3$, we discuss the way to consider orbital ordering effects (alternately occupied $d_{x^2-z^2}$ and $d_{y^2-z^2}$ orbitals). For L_3-edge spectra of Ni^{2+} $3d^8$ ions in La_2NiO_4, the computed spectra reproduce trends found experimentally for the incoming-photon incident-angle and polarization dependence. For future studies, one aspect is to carry out more involved calculations using the same computational scheme for arbitrary electron configuration of the valence $3d$-shell (d^n) in TM compounds. Another aspect is to perform investigations with the similar

computational procedure on $5d$ TM materials.

Publication list

1. *Covalency and vibronic couplings make a nonmagnetic $j=3/2$ ion magnetic*
   L. Xu, N.A. Bogdanov, A. Princep, P. Fulde, J. van den Brink, L. Hozoi
   npj Quantum Materials 1 (2016),16029/1-6

2. *Spin-reversal energy barriers of 305 K for Fe^{2+} d^6 ions with linear ligand coordination*
   L. Xu, Z. Zangeneh, R. Yadav, S. Avdoshenko, J. van den Brink, A. Jesche, L. Hozoi
   Nanoscale 9 (2017), Issue 30, 10596–10600

3. *Doping dependence of collective spin and orbital excitations in the spin-1 quantum antiferromagnet $La_{2-x}Sr_xNiO_4$ observed by X rays*
   G. Fabbris, D. Meyers, **L. Xu**, V.M. Katukuri, L. Hozoi, X. Liu, Z.-Y. Chen, J. Okamoto, T. Schmitt, A. Uldry, B. Delley, G.D. Gu, D. Prabhakaran, A.T. Boothroyd, J. van den Brink, D.J. Huang, M.P.M. Dean
   Physical Review Letters 118 (2017), Issue 15, 156402/1-8

4. *Superexchange interactions between spin-orbit-coupled $j \simeq 1/2$ ions in oxides with face-sharing octahedra*
   L. Xu, R. Yadav, V. Yushankhai, L. Siurakshina, J. van den Brink, L. Hozoi
   Physical Review B 99 (2019), Issue 11, 115119/1-11

5. *Disentangling orbital and magnetic contributions to the exotic spin Peierls transition in $TiPO_4$*
   M. Dantz, **L. Xu**, C. Wagner, J. Pelliciari, J. Trinckauf, Y. Huang, X. Lu, Y. H. Cho, V. N. Strokov, A. O. Mitrushchenkov, S.-W. Cheong, L. Hozoi, J. van den Brink, J. Geck, T. Schmitt (Submitted)

Bibliography

[1] M. Imada, A. Fujimori, and Y. Tokura, "Metal-insulator transitions," Rev. Mod. Phys. **70**, 1039–1263 (1998).

[2] A. P. Ramirez, "Colossal magnetoresistance," J. Phys. Condens. Matter **9**, 8171 (1997).

[3] B. J. Sternlieb, J. P. Hill, U. C. Wildgruber, G. M. Luke, B. Nachumi, Y. Moritomo, and Y. Tokura, "Charge and Magnetic Order in $La_{0.5}Sr_{1.5}MnO_4$," Phys. Rev. Lett. **76**, 2169–2172 (1996).

[4] M. L. Medarde, "Structural, magnetic and electronic properties of RNO_3 perovskites (R = rare earth)," J. Phys. Condens. Matter **9**, 1679 (1997).

[5] J. van den Brink, G. Khaliullin, and D. Khomskii, "Charge and Orbital Order in Half-Doped Manganites," Phys. Rev. Lett. **83**, 5118–5121 (1999).

[6] J. G. Bednorz and K. A. Müller, "Possible high-T_c superconductivity in the Ba-La-Cu-O system," Z. Phys. B **64**, 189–193 (1986).

[7] B. Keimer, S. A. Kivelson, M. R. Norman, S. Uchida, and J. Zaanen, "From quantum matter to high-temperature superconductivity in copper oxides," Nature **518**, 179–186 (2015).

[8] S. Maekawa, T. Tohyama, S. E. Barnes, S. Ishihara, W. Koshibae, and G. Khaliullin, *Physics of Transition Metal Oxides* (Springer, Berlin, 2004).

[9] D. Khomskii, *Transition Metal Compounds* (Cambridge University Press, 2014).

[10] C. Kim, Z.-X. Shen, N. Motoyama, H. Eisaki, S. Uchida, T. Tohyama, and S. Maekawa, "Separation of spin and charge excitations in one-dimensional $SrCuO_2$," Phys. Rev. B **56**, 15589–15595 (1997).

[11] J. Schlappa, K. Wohlfeld, K. J. Zhou, M. Mourigal, M. W. Haverkort, V. N. Strocov, L. Hozoi, C. Monney, S. Nishimoto, S. Singh, A. Revcolevschi, J.-S. Caux, L. Patthey, H. M. Rønnow, J. van den Brink, and T. Schmitt, "Spin-orbital separation in the quasi-one-dimensional Mott insulator Sr_2CuO_3," Nature **485**, 82–85 (2012).

[12] J. M. Law, C. Hoch, R. Glaum, I. Heinmaa, R. Stern, J. Kang, C. Lee, M.-H. Whangbo, and R. K. Kremer, "Spin-Peierls transition in the $S = \frac{1}{2}$ compound $TiPO_4$ featuring large intrachain coupling," Phys. Rev. B **83**, 180414 (2011).

[13] B. J. Kim, H. Jin, S. J. Moon, J.-Y. Kim, B.-G. Park, C. S. Leem, J. Yu, T. W. Noh, C. Kim, S.-J. Oh, J.-H. Park, V. Durairaj, G. Cao, and E. Rotenberg, "Novel J_{eff}=1/2 mott state induced by relativistic spin-orbit coupling in Sr_2IrO_4," Phys. Rev. Lett. **101**, 076402 (2008).

[14] S. J. Moon, H. Jin, K. W. Kim, W. S. Choi, Y. S. Lee, J. Yu, G. Cao, A. Sumi, H. Funakubo, C. Bernhard, and T. W. Noh, "Dimensionality-Controlled Insulator-Metal Transition and Correlated Metallic State in $5d$ Transition Metal Oxides $Sr_{n+1}Ir_nO_{3n+1}$ ($n = 1, 2,$ and ∞)," Phys. Rev. Lett. **101**, 226402 (2008).

[15] G. Jackeli and G. Khaliullin, "Mott insulators in the strong spin-orbit coupling limit: From Heisenberg to a quantum compass and Kitaev models," Phys. Rev. Lett. **102**, 017205 (2009).

[16] A. Shitade, H. Katsura, J. Kuneš, X.-L. Qi, S.-C. Zhang, and N. Nagaosa, "Quantum Spin Hall Effect in a Transition Metal Oxide Na_2IrO_3," Phys. Rev. Lett. **102**, 256403 (2009).

[17] Y. G. Shi, Y. F. Guo, S. Yu, M. Arai, A. A. Belik, A. Sato, K. Yamaura, E. Takayama-Muromachi, H. F. Tian, H. X. Yang, J. Q. Li, T. Varga, J. F. Mitchell, and S. Okamoto, "Continuous metal-insulator transition of the antiferromagnetic perovskite $NaOsO_3$," Phys. Rev. B **80**, 161104 (2009).

[18] S. Calder, V. O. Garlea, D. F. McMorrow, M. D. Lumsden, M. B. Stone, J. C. Lang, J.-W. Kim, J. A. Schlueter, Y. G. Shi, K. Yamaura, Y. S. Sun, Y. Tsujimoto, and A. D. Christianson, "Magnetically driven metal-insulator transition in $NaOsO_3$," Phys. Rev. Lett. **108**, 257209 (2012).

[19] M. A. de Vries, A. C. Mclaughlin, and J.-W. G. Bos, "Valence Bond Glass on an fcc Lattice in the Double Perovskite Ba_2YMoO_6," Phys. Rev. Lett. **104**, 177202 (2010).

[20] T. Aharen, J. E. Greedan, C. A. Bridges, A. A. Aczel, J. Rodriguez, G. MacDougall, G. M. Luke, T. Imai, V. K. Michaelis, S. Kroeker, H. Zhou, C. R. Wiebe, and L. M. D. Cranswick, "Magnetic properties of the geometrically frustrated S=1/2 antiferromagnets, La_2LiMoO_6 and Ba_2YMoO_6, with the B-site ordered double perovskite structure: Evidence for a collective spin-singlet ground state," Phys. Rev. B **81**, 224409 (2010).

[21] J. P. Carlo, J. P. Clancy, T. Aharen, Z. Yamani, J. P. C. Ruff, J. J. Wagman, G. J. Van Gastel, H. M. L. Noad, G. E. Granroth, J. E. Greedan, H. A. Dabkowska, and B. D. Gaulin, "Triplet and in-gap magnetic states in the ground state of the quantum frustrated fcc antiferromagnet Ba_2YMoO_6," Phys. Rev. B **84**, 100404 (2011).

[22] Z. Qu, Y. Zou, S. Zhang, L. Ling, L. Zhang, and Y. Zhang, "Spin-phonon coupling probed by infrared transmission spectroscopy in the double perovskite Ba_2YMoO_6," J. Appl. Phys. **113**, 17E137 (2013).

[23] M. A. de Vries, J. O. Piatek, M. Misek, J. S. Lord, H. M. Rønnow, and J.-W. G. Bos, "Low-temperature spin dynamics of a valence bond glass in Ba_2YMoO_6," New J. Phys. **15**, 043024 (2013).

[24] T. Aharen, J. E. Greedan, C. A. Bridges, A. A. Aczel, J. Rodriguez, G. MacDougall, G. M. Luke, V. K. Michaelis, S. Kroeker, C. R. Wiebe, H. Zhou, and L. M. D. Cranswick, "Structure and magnetic properties of the $S = 1$ geometrically frustrated double perovskites La_2LiReO_6 and Ba_2YReO_6," Phys. Rev. B **81**, 064436 (2010).

[25] C. R. Wiebe, J. E. Greedan, P. P. Kyriakou, G. M. Luke, J. S. Gardner, A. Fukaya, I. M. Gat-Malureanu, P. L. Russo, A. T. Savici, and Y. J. Uemura, "Frustration-driven spin freezing in the $S = \frac{1}{2}$ fcc perovskite Sr_2MgReO_6," Phys. Rev. B **68**, 134410 (2003).

[26] C. R. Wiebe, J. E. Greedan, G. M. Luke, and J. S. Gardner, "Spin-glass behavior in the $S = 1/2$ fcc ordered perovskite Sr_2CaReO_6," Phys. Rev. B **65**, 144413 (2002).

[27] K. E. Stitzer, M. D. Smith, and H.-C. zur Loye, "Crystal growth of $Ba_2MOsO_6(M=Li,Na)$ from reactive hydroxide fluxes," Solid State Sci. **4**, 311–316 (2002).

[28] A. S. Erickson, S. Misra, G. J. Miller, R. R. Gupta, Z. Schlesinger, W. A. Harrison, J. M. Kim, and I. R. Fisher, "Ferromagnetism in the Mott Insulator Ba_2NaOsO_6," Phys. Rev. Lett. **99**, 016404 (2007).

[29] A. J. Steele, P. J. Baker, T. Lancaster, F. L. Pratt, I. Franke, S. Ghannadzadeh, P. A. Goddard, W. Hayes, D. Prabhakaran, and S. J. Blundell, "Low-moment magnetism in the double perovskites $Ba_2MOsO_6(M=Li,Na)$," Phys. Rev. B **84**, 144416 (2011).

[30] T. Aharen, J. E. Greedan, F. Ning, T. Imai, V. Michaelis, S. Kroeker, H. Zhou, C. R. Wiebe, and L. M. D. Cranswick, "Magnetic properties of the $S = \frac{3}{2}$ geometrically frustrated double perovskites La_2LiRuO_6 and Ba_2YRuO_6," Phys. Rev. B **80**, 134423 (2009).

[31] W. Witczak-Krempa, G. Chen, Y. B. Kim, and L. Balents, "Correlated quantum phenomena in the strong spin-orbit regime," Annu. Rev. Condens. Matter Phys. **5**, 57–82 (2014).

[32] M. Z. Hasan and C. L. Kane, "Colloquium: Topological insulators," Rev. Mod. Phys. **82**, 3045–3067 (2010).

[33] D. Pesin and L. Balents, "Mott physics and band topology in materials with strong spin-orbit interaction," Nat. Phys. **6**, 376–381 (2010).

[34] X.-L. Qi and S.-C. Zhang, "Topological insulators and superconductors," Rev. Mod. Phys. **83**, 1057–1110 (2011).

[35] A. Bansil, H. Lin, and T. Das, "Colloquium: Topological band theory," Rev. Mod. Phys. **88**, 021004 (2016).

[36] M. Mogi, M. Kawamura, R. Yoshimi, A. Tsukazaki, Y. Kozuka, N. Shirakawa, K. S. Takahashi, M. Kawasaki, and Y. Tokura, "A magnetic heterostructure of topological insulators as a candidate for an axion insulator," Nat. Mater. **16**, 516–521 (2017).

[37] D. Xiao, J. Jiang, J.-H. Shin, W. Wang, F. Wang, Y.-F. Zhao, C. Liu, W. Wu, M. H. W. Chan, N. Samarth, and C.-Z. Chang, "Realization of the Axion Insulator State in Quantum Anomalous Hall Sandwich Heterostructures," Phys. Rev. Lett. **120**, 056801 (2018).

[38] H. Weyl, "Elektron und Gravitation. I," Zeitschrift für Physik **56**, 330–352 (1929).

[39] X. Wan, A. M. Turner, A. Vishwanath, and S. Y. Savrasov, "Topological semimetal and Fermi-arc surface states in the electronic structure of pyrochlore iridates," Phys. Rev. B **83**, 205101 (2011).

[40] A. A. Burkov and L. Balents, "Weyl Semimetal in a Topological Insulator Multilayer," Phys. Rev. Lett. **107**, 127205 (2011).

[41] B. Q. Lv, H. M. Weng, B. B. Fu, X. P. Wang, H. Miao, J. Ma, P. Richard, X. C. Huang, L. X. Zhao, G. F. Chen, Z. Fang, X. Dai, T. Qian, and H. Ding, "Experimental Discovery of Weyl Semimetal TaAs," Phys. Rev. X **5**, 031013 (2015).

[42] S.-Y. Xu, I. Belopolski, N. Alidoust, M. Neupane, G. Bian, C. Zhang, R. Sankar, G. Chang, Z. Yuan, C.-C. Lee, S.-M. Huang, H. Zheng, J. Ma, D. S. Sanchez, B. Wang, A. Bansil, F. Chou, P. P. Shibayev, H. Lin, S. Jia, and M. Z. Hasan, "Discovery of a Weyl fermion semimetal and topological Fermi arcs," Science **349**, 613–617 (2015).

[43] B. Canals and C. Lacroix, "Pyrochlore antiferromagnet: A three-dimensional quantum spin liquid," Phys. Rev. Lett. **80**, 2933–2936 (1998).

[44] B. Canals and C. Lacroix, "Quantum spin liquid: The Heisenberg antiferromagnet on the three-dimensional pyrochlore lattice," Phys. Rev. B **61**, 1149–1159 (2000).

[45] Z. Y. Meng, T. C. Lang, S. Wessel, F. F. Assaad, and A. Muramatsu, "Quantum spin liquid emerging in two-dimensional correlated Dirac fermions," Nature **464**, 847–851 (2010).

[46] L. Savary and L. Balents, "Quantum spin liquids: a review," Rep. Prog. Phys. **80**, 016502 (2017).

[47] F. Wilczek, "Two applications of axion electrodynamics," Phys. Rev. Lett. **58**, 1799–1802 (1987).

[48] A. M. Essin, J. E. Moore, and D. Vanderbilt, "Magnetoelectric Polarizability and Axion Electrodynamics in Crystalline Insulators," Phys. Rev. Lett. **102**, 146805 (2009).

[49] K. Nomura and N. Nagaosa, "Surface-Quantized Anomalous Hall Current and the Magnetoelectric Effect in Magnetically Disordered Topological Insulators," Phys. Rev. Lett. **106**, 166802 (2011).

[50] C. Shekhar, A. K. Nayak, Y. Sun, M. Schmidt, M. Nicklas, I. Leermakers, U. Zeitler, Y. Skourski, J. Wosnitza, Z. Liu, Y. Chen, W. Schnelle, H. Borrmann, Y. Grin, C. Felser, and B. Yan, "Extremely large magnetoresistance and ultrahigh mobility in the topological Weyl semimetal candidate NbP," Nat. Phys. **11**, 645–649 (2015).

[51] B. Yan and C. Felser, "Topological Materials: Weyl Semimetals," Annu. Rev. Condens. Matter Phys. **8**, 337–354 (2017).

[52] L. Balents, "Spin liquids in frustrated magnets," Nature **464**, 199–208 (2010).

[53] F. L. Pratt, P. J. Baker, S. J. Blundell, T. Lancaster, S. Ohira-Kawamura, C. Baines, Y. Shimizu, K. Kanoda, I. Watanabe, and G. Saito, "Magnetic and non-magnetic phases of a quantum spin liquid," Nature **471**, 612–616 (2011).

[54] H. Watanabe, T. Shirakawa, and S. Yunoki, "Microscopic Study of a Spin-Orbit-Induced Mott Insulator in Ir Oxides," Phys. Rev. Lett. **105**, 216410 (2010).

[55] R. O. Jones, "Density functional theory: Its origins, rise to prominence, and future," Rev. Mod. Phys. **87**, 897–923 (2015).

[56] G. Graziano, "Quantum chemistry: DFT's midlife crisis," Nat. Rev. Chem. **1**, 0019 (2017).

[57] R. O. Jones and O. Gunnarsson, "The density functional formalism, its applications and prospects," Rev. Mod. Phys. **61**, 689–746 (1989).

[58] K.H.J. Buschow, *Handbook of Magnetic Materials*, Vol. 13 (Elsevier, 2001) pp. 87–228.

[59] G. Kotliar, S. Y. Savrasov, K. Haule, V. S. Oudovenko, O. Parcollet, and C. A. Marianetti, "Electronic structure calculations with dynamical mean-field theory," Rev. Mod. Phys. **78**, 865–951 (2006).

[60] T. Maier, M. Jarrell, T. Pruschke, and M. H. Hettler, "Quantum cluster theories," Rev. Mod. Phys. **77**, 1027–1080 (2005).

[61] V. I. Anisimov, J. Zaanen, and O. K. Andersen, "Band theory and Mott insulators: Hubbard U instead of Stoner I," Phys. Rev. B **44**, 943–954 (1991).

[62] L. Vaugier, H. Jiang, and S. Biermann, "Hubbard U and Hund exchange J in transition metal oxides: Screening versus localization trends from constrained random phase approximation," Phys. Rev. B **86**, 165105 (2012).

[63] T. Helgaker, P. Jørgensen, and J. Olsen, *Molecular Electronic-Structure Theory* (Wiley, Chichester, 2000).

[64] J.-Q. Sun and R. J. Bartlett, "Second-order many-body perturbation-theory calculations in extended systems," J. Chem. Phys. **104**, 8553–8565 (1996).

[65] B. O. Roos, K. Andersson, M. P. Fülscher, P.-â. Malmqvist, L. Serrano-Andrés, K. Pierloot, and M. Merchán, "Multiconfigurational Perturbation Theory: Applications in Electronic Spectroscopy," Adv. Chem. Phys. , 219–331 (1996).

[66] J. Finley and P.-Å. Malmqvist and B. O. Roos and L. Serrano-Andrés, "The multi-state CASPT2 method," Chem. Phys. Lett. **288**, 299–306 (1998).

[67] P. Y. Ayala, K. N. Kudin, and G. E. Scuseria, "Atomic orbital Laplace-transformed second-order Møller–Plesset theory for periodic systems," J. Chem. Phys. **115**, 9698–9707 (2001).

[68] L. Maschio, D. Usvyat, F. R. Manby, S. Casassa, C. Pisani, and M. Schütz, "Fast local-MP2 method with density-fitting for crystals. I. Theory and algorithms," Phys. Rev. B **76**, 075101 (2007).

[69] C. Pisani, L. Maschio, S. Casassa, M. Halo, M. Schütz, and D. Usvyat, "Periodic local MP2 method for the study of electronic correlation in crystals: Theory and preliminary applications," J. Comput. Chem. **29**, 2113–2124 (2008).

[70] M. Marsman, A. Grüneis, J. Paier, and G. Kresse, "Second-order Møller–Plesset perturbation theory applied to extended systems. I. Within the projector-augmented-wave formalism using a plane wave basis set," J. Chem. Phys. **130**, 184103 (2009).

[71] L. Hozoi, U. Birkenheuer, P. Fulde, A. Mitrushchenkov, and H. Stoll, "*Ab initio* wave function-based methods for excited states in solids: Correlation corrections to the band structure of ionic oxides," Phys. Rev. B **76**, 085109 (2007).

[72] A. Shukla, M. Dolg, P. Fulde, and H. Stoll, "Wave-function-based correlated *ab initio* calculations on crystalline solids," Phys. Rev. B **60**, 5211–5216 (1999).

[73] G. H. Booth, A. Grüneis, G. Kresse, and A. Alavi, "Towards an exact description of electronic wavefunctions in real solids," Nature **493**, 365–370 (2012).

[74] A. S. P. Gomes and C. R. Jacob, "Quantum-chemical embedding methods for treating local electronic excitations in complex chemical systems," Annu. Rep. Prog. Chem., Sect. C: Phys. Chem. **108**, 222–277 (2012).

[75] T. A. Wesolowski, S. Shedge, and X. Zhou, "Frozen-Density Embedding Strategy for Multilevel Simulations of Electronic Structure," Chem. Rev. **115**, 5891–5928 (2015).

[76] P. Fulde, *Correlated Electrons in Quantum Matter* (World Scientific, Singapore, 2012).

[77] L. Hozoi, L. Siurakshina, P. Fulde, and J. van den Brink, " *Ab initio* determination of Cu $3d$ orbital energies in layered copper oxides ," Sci. Rep. **1** (2011).

[78] A. Stoyanova, L. Hozoi, P. Fulde, and H. Stoll, "Wave-function-based approach to quasiparticle bands: Insight into the electronic structure of *c*-ZnS," Phys. Rev. B **83**, 205119 (2011).

[79] H.-Y. Huang, N. A. Bogdanov, L. Siurakshina, P. Fulde, J. van den Brink, and L. Hozoi, "*Ab initio* calculation of d-d excitations in quasi-one-dimensional Cu d^9 correlated materials," Phys. Rev. B **84**, 235125 (2011).

[80] L. Hozoi, A.H. de Vries, and R. Broer, "X-ray spectroscopy at the Mn K-edge in $LaMnO_3$: An ab initio study," Phys. Rev. B **64**, 165104 (2001).

[81] A. H. de Vries, L. Hozoi, R. Broer, and P. S. Bagus, "Importance of interatomic hole screening in core-level spectroscopy of transition metal oxides: Mn 3s hole states in MnO," Phys. Rev. B **66**, 035108 (2002).

[82] K. Fink, R. Fink, and V. Staemmler, "*Ab initio* Calculation of the Magnetic Exchange Coupling in Linear Oxo-Bridged Binuclear Complexes of Titanium(III), Vanadium(III), and Chromium(III)," Inorg. Chem. **33**, 6219–6229 (1994).

[83] C. de Graaf, R. Broer, and W.C. Nieuwpoort, "Comparison of the superexchange interaction in NiO and in a NiO[100] surface," Chem. Phys. Lett. **271**, 372–376 (1997).

[84] D. Muñoz, I. de P. R. Moreira, and F. Illas, "Effective *t-J* model Hamiltonian parameters of monolayered cuprate superconductors from *ab initio* electronic structure calculations," Phys. Rev. B **65**, 224521 (2002).

[85] L. Hozoi, C. Presura, C. de Graaf, and R. Broer, "Electronic structure $\alpha^{'} - NaV_2O_5$: Wave-function-based embedded-cluster calculations," Phys. Rev. B **67**, 035117 (2003).

[86] C. J. Calzado, S. Evangelisti, and D. Maynau, "Local Orbitals for the Truncation of Inactive Space: Application to Magnetic Systems," J. Phys. Chem. A **107**, 7581–7588 (2003).

[87] U. Birkenheuer, P. Fulde, and H. Stoll, "A simplified method for the computation of correlation effects on the band structure of semiconductors," Theor. Chem. Acc. **116**, 398–403 (2006).

[88] A. Stoyanova, L. Hozoi, P. Fulde, and H. Stoll, "Correlation-induced corrections to the band structure of boron nitride: A wave-function-based approach," J. Chem. Phys. **131**, 044119 (2009).

[89] M. P. de Lara-Castells and A. O. Mitrushchenkov, "A finite cluster approach to an extended transition metal oxide: A wave function based study," J. Phys. Chem. C **115**, 17540–17557 (2011).

[90] N. Govind, Y. A. Wang, and E. A. Carter, "Electronic-structure calculations by first-principles density-based embedding of explicitly correlated systems," J. Chem. Phys. **110**, 7677–7688 (1999).

[91] P. Huang and E. A. Carter, "Self-consistent embedding theory for locally correlated configuration interaction wave functions in condensed matter," J. Chem. Phys. **125**, 084102 (2006).

[92] A. S. P. Gomes, C. R. Jacob, and L. Visscher, "Calculation of local excitations in large systems by embedding wave-function theory in density-functional theory," Phys. Chem. Chem. Phys. **10**, 5353–5362 (2008).

[93] W. M. Haynes, *Handbook of Chemistry and Physics* (CRC Press, 2011).

[94] W. Kohn and L. J. Sham, "Self-consistent equations including exchange and correlation effects," Phys. Rev. **140**, A1133–A1138 (1965).

[95] A. Georges, G. Kotliar, W. Krauth, and M. J. Rozenberg, "Dynamical mean-field theory of strongly correlated fermion systems and the limit of infinite dimensions," Rev. Mod. Phys. **68**, 13–125 (1996).

[96] A. I. Liechtenstein, V. I. Anisimov, and J. Zaanen, "Density-functional theory and strong interactions: Orbital ordering in Mott-Hubbard insulators," Phys. Rev. B **52**, R5467–R5470 (1995).

[97] B. Himmetoglu, A. Floris, S. de Gironcoli, and M. Cococcioni, "Hubbard-corrected DFT energy functionals: The LDA+U description of correlated systems," Int. J. Quantum Chem. **114**, 14–49 (2014).

[98] S. Katsura, T. Morita, S. Inawashiro, T. Horiguchi, and Y. Abe, "Lattice Green's Function. Introduction," J. Math. Phys. **12**, 892–895 (1971).

[99] O. Gunnarsson, O. K. Andersen, O. Jepsen, and J. Zaanen, "Density-functional calculation of the parameters in the Anderson model: Application to Mn in CdTe," Phys. Rev. B **39**, 1708–1722 (1989).

[100] M. Cococcioni and S. de Gironcoli, "Linear response approach to the calculation of the effective interaction parameters in the LDA + U method," Phys. Rev. B **71**, 035105 (2005).

[101] F. Aryasetiawan, M. Imada, A. Georges, G. Kotliar, S. Biermann, and A. I. Lichtenstein, "Frequency-dependent local interactions and low-energy effective models from electronic structure calculations," Phys. Rev. B **70**, 195104 (2004).

[102] H. T. Dang, X. Ai, A. J. Millis, and C. A. Marianetti, "Density functional plus dynamical mean-field theory of the metal-insulator transition in early transition-metal oxides," Phys. Rev. B **90**, 125114 (2014).

[103] P. Fulde, *Electron Correlations in Molecules and Solids* (Springer, Berlin, 1993).

[104] P. Fulde, *Correlated Electrons in Quantum Matter* (World Scientific, Singapore, 2012).

[105] D. Munõz, C. De Graaf, and F. Illas, "Putting error bars on the *ab initio* theoretical estimates of the magnetic coupling constants: The parent compounds of superconducting cuprates as a case study," J. Comput. Chem. **25**, 1234–1241 (2004).

[106] M. Born and R. Oppenheimer, "Zur Quantentheorie der Molekeln," Ann. Phys. **389**, 457–484 (1927).

[107] C. Eckart, "The kinetic energy of polyatomic molecules," Phys. Rev. **46**, 383–387 (1934).

[108] J. C. Slater, "A simplification of the Hartree-Fock method," Phys. Rev. **81**, 385–390 (1951).

[109] J. L. Lagrange, *Analytical Mechanics [Mécanique Analytique], translated and edited by A. Boissonnade and V. N. Vagliente* (Kluwer Academic, Imprint Dordrecht, Boston, Massachusetts, 1997).

[110] J. C. Slater, "Atomic shielding constants," Phys. Rev. **36**, 57–64 (1930).

[111] S. F. Boys, "Electronic wave functions - I. A general method of calculation for the stationary states of any molecular system," Proc. R. Soc. A **200**, 542–554 (1950).

[112] F. Jensen, *Introduction to Computational Chemistry* (John Wiley & Sons Ltd, 2007).

[113] R. Ditchfield, W. J. Hehre, and J. A. Pople, "Self-Consistent Molecular-Orbital Methods. IX. An Extended Gaussian-Type Basis for Molecular-Orbital Studies of Organic Molecules," J. Chem. Phys. **54**, 724–728 (1971).

[114] R. Krishnan, J. S. Binkley, R. Seeger, and J. A. Pople, "Self-consistent molecular orbital methods. XX. A basis set for correlated wave functions," J. Chem. Phys. **72**, 650–654 (1980).

[115] A. Schäfer, H. Horn, and R. Ahlrichs, "Fully optimized contracted Gaussian basis sets for atoms Li to Kr," J. Chem. Phys. **97**, 2571–2577 (1992).

[116] A. Schäfer, C. Huber, and R. Ahlrichs, "Fully optimized contracted Gaussian basis sets of triple zeta valence quality for atoms Li to Kr," J. Chem. Phys. **100**, 5829–5835 (1994).

[117] K. Pierloot, B. Dumez, P.-O. Widmark, and B. Roos, "Density matrix averaged atomic natural orbital (ANO) basis sets for correlated molecular wave functions," Theor. chim. Acta **90**, 87–114 (1995).

[118] T. H. Dunning Jr., "Gaussian basis sets for use in correlated molecular calculations. I. The atoms boron through neon and hydrogen," J. Chem. Phys. **90**, 1007–1023 (1989).

[119] Z.-H. Li and M. W. Wong, "Scaling of correlation basis set extension energies," Chem. Phys. Lett. **337**, 209–216 (2001).

[120] David Feller, "Application of systematic sequences of wave functions to the water dimer," J. Chem. Phys. **96**, 6104–6114 (1992).

[121] P.-O. Löwdin, "Quantum Theory of Many-Particle Systems. III. Extension of the Hartree-Fock Scheme to Include Degenerate Systems and Correlation Effects," Phys. Rev. **97**, 1509–1520 (1955).

[122] R.J. Harrison and N.C. Handy, " Full CI calculations on BH, H_2O, NH_3, and HF," Chem. Phys. Lett. **95**, 386–391 (1983).

[123] S. R. Langhoff and E. R. Davidson, "Configuration interaction calculations on the nitrogen molecule," Int. J. Quantum Chem. **8**, 61–72 (1974).

[124] K. Andersson, P. A. Malmqvist, B.O. Roos, A. J. Sadlej, and K. Wolinski, "Second-order perturbation theory with a CASSCF reference function," J. Phys. Chem. **94**, 5483–5488 (1990).

[125] C. Møller and M. S. Plesset, "Note on an approximation treatment for many-electron systems," Phys. Rev. **46**, 618–622 (1934).

[126] P. Celani and H.-J. Werner, "Analytical energy gradients for internally contracted second-order multireference perturbation theory," J. Chem. Phys. **119**, 5044–5057 (2003).

[127] L. Gagliardi and B. O. Roos, "Multiconfigurational quantum chemical methods for molecular systems containing actinides," Chem. Soc. Rev. **36**, 893–903 (2007).

[128] C. Angeli, R. Cimiraglia, and J.-P. Malrieu, "N-electron valence state perturbation theory: a fast implementation of the strongly contracted variant," Chem. Phys. Lett. **350**, 297–305 (2001).

[129] C. Angeli, R. Cimiraglia, and J.-P. Malrieu, "*N*-electron valence state perturbation theory: A spinless formulation and an efficient implementation of the strongly contracted and of the partially contracted variants," J. Chem. Phys. **117**, 9138–9153 (2002).

[130] de Graaf, C. and Sousa, C. and de P. R. Moreira, I. and Illas, F., "Multiconfigurational perturbation theory: An efficient tool to predict magnetic coupling parameters in biradicals, molecular complexes, and ionic insulators," J. Phys. Chem. A **105**, 11371–11378 (2001).

[131] C. Angeli and C. J. Calzado, "The role of the magnetic orbitals in the calculation of the magnetic coupling constants from multireference perturbation theory methods," J. Chem. Phys. **137**, 034104 (2012).

[132] P. Pyykkö, "Relativistic effects in structural chemistry," Chem. Rev. **88**, 563–594 (1988).

[133] J. Autschbach, "Perspective: Relativistic effects," J. Chem. Phys. **136**, 150902 (2012).

[134] M. Reiher and A. Wolf, *Relativistic Quantum Chemistry: The Fundamental Theory of Molecular Science* (WILEY-VCH & Co. KGaA, Weinheim, 2009).

[135] W. H. E. Schwarz, A. Rutkowski, and S. G. Wang, "Understanding relativistic effects of chemical bonding," Int. J. Quantum Chem. **57**, 641–653 (1996).

[136] P. A. M. Dirac, "The quantum theory of the electron," Roy. Soc. Proc. A **117**, 610–624 (1928).

[137] P. A. M. Dirac, "The quantum theory of the Electron. Part II," Roy. Soc. Proc. A **118**, 351–361 (1928).

[138] O. Klein, "Quantentheorie und fünfdimensionale relativitätstheorie," Z. Phys. **37**, 895–906 (1926).

[139] W. Gordon, "Der comptoneffekt nach der schrödingerschen theorie," Z. Phys. **40**, 117–133 (1926).

[140] E. E. Salpeter and H. A. Bethe, "A relativistic equation for bound-state problems," Phys. Rev. **84**, 1232–1242 (1951).

[141] E. E. Salpeter, "Mass corrections to the fine structure of hydrogen-like atoms," Phys. Rev. **87**, 328–343 (1952).

[142] G. Breit, "The effect of retardation on the interaction of two electrons," Phys. Rev. **34**, 553–573 (1929).

[143] L. L. Foldy and S. A. Wouthuysen, "On the dirac theory of spin 1/2 particles and its non-relativistic limit," Phys. Rev. **78**, 29–36 (1950).

[144] Pauli W., *Handbuch der Physik*, Vol. 5 (Springer, Berlin,1958).

[145] R. McWeeny, *Methods of Molecular Quantum Mechanics* (Academic Press, London, 1992).

[146] H. Bethe and E. Salpeter, *Quantum Mechanics of One- and Two-Electron Atoms* (Springer, Berlin, 1957).

[147] B. A. Heß, C. M. Marian, U. Wahlgren, and O. Gropen, "A mean-field spin-orbit method applicable to correlated wavefunctions," Chem. Phys. Lett. **251**, 365–371 (1996).

[148] A. Berning, M. Schweizer, H.-J. Werner, P. J. Knowles, and P. Palmieri, "Spin-orbit matrix elements for internally contracted multireference configuration interaction wavefunctions," Mol. Phys. **98**, 1823–1833 (2000).

[149] D. Figgen, K. A. Peterson, M. Dolg, and H. Stoll, "Energy-consistent pseudopotentials and correlation consistent basis sets for the 5d elements Hf–Pt," J. Chem. Phys. **130**, 164108 (2009).

[150] M. Dolg and X. Cao, "Relativistic Pseudopotentials: Their Development and Scope of Applications," Chem. Rev. **112**, 403–480 (2012).

[151] P. Horsch and P. Fulde, "On the theory of electronic correlations in solids," Z. Phys. B **36**, 23–35 (1979).

[152] M. Klintenberg, S.E. Derenzo, and M.J. Weber, "Accurate crystal fields for embedded cluster calculations," J. Comput. Phys. Commun. **131**, 120–128 (2000).

[153] S. E. Derenzo, M. K. Klintenberg, and M. J. Weber, "Determining point charge arrays that produce accurate ionic crystal fields for atomic cluster calculations," J. Chem. Phys. **112**, 2074–2081 (2000).

[154] M. Klintenberg, S.E. Derenzo, and M.J. Weber, "Accurate crystal fields for embedded cluster calculations," J. Comput. Phys. Commun. **131**, 120–128 (2000).

[155] P. P. Ewald, "Die Berechnung optischer und elektrostatischer Gitterpotentiale," Ann. Phys. **369**, 253–287 (1921).

[156] F. R. Manby, M. Stella, J. D. Goodpaster, and T. F. Miller, "A Simple, Exact Density-Functional-Theory Embedding Scheme," J. Chem. Theory Comput. **8**, 2564–2568 (2012).

[157] M. von Arnim W. Alsheimer U. Birkenheuer, C. Willnauer and D. Izotov, "Wavefunction-based correlation calculations for hole and electron attachment states in solids and polymers," Annual report (Max Planck Institute for the Physics of Complex Systems, Dresden, Germany, 2000–2002), https://www.pks.mpg.de/pdf/institutsbericht00_01_short.pdf.

[158] L. Hozoi, U. Birkenheuer, H. Stoll, and P. Fulde, "Spin-state transition and spin-polaron physics in cobalt oxide perovskites: *ab initio* approach based on quantum chemical methods," New J. Phys. **11**, 023023 (2009).

[159] H. Park, S. Chang, J. Jean, J. J. Cheng, P. T. Araujo, M. Wang, M. G. Bawendi, M. S. Dresselhaus, V. Bulović, J. Kong, and S. Gradečak, "Graphene Cathode-Based ZnO Nanowire Hybrid Solar Cells," Nano Lett. **13**, 233–239 (2013).

[160] V. Bisogni, K. Wohlfeld, S. Nishimoto, C. Monney, J. Trinckauf, K. Zhou, R. Kraus, K. Koepernik, C. Sekar, V. Strocov, B. Büchner, T. Schmitt, J. van den Brink, and J. Geck, "Orbital Control of Effective Dimensionality: From Spin-Orbital Fractionalization to Confinement in the Anisotropic Ladder System $CaCu_2O_3$," Phys. Rev. Lett. **114**, 096402 (2015).

[161] B. J. Kim, H. Koh, E. Rotenberg, S.-J. Oh, H. Eisaki, N. Motoyama, S. Uchida, T. Tohyama, S. Maekawa, Z.-X. Shen, and C. Kim, "Distinct spinon and holon dispersions in photoemission spectral functions from one-dimensional $SrCuO_2$," Nat. Phys. **2**, 397–401 (2006).

[162] S. Glawion, J. Heidler, M. W. Haverkort, L. C. Duda, T. Schmitt, V. N. Strocov, C. Monney, K. J. Zhou, A. Ruff, M. Sing, and R. Claessen, "Two-Spinon and Orbital Excitations of the Spin-Peierls System TiOCl," Phys. Rev. Lett. **107**, 107402 (2011).

[163] A. I. Buzdin and L. N. Bulaevskii, "Spin-Peierls transition in quasi-one-dimensional crystals," Sov. Phys. Usp. **23**, 409 (1980).

[164] M. Hase, I. Terasaki, and K. Uchinokura, "Observation of the spin-Peierls transition in linear Cu^{2+} (spin-1/2) chains in an inorganic compound $CuGeO_3$," Phys. Rev. Lett. **70**, 3651–3654 (1993).

[165] L. P. Regnault, M. Aïn, B. Hennion, G. Dhalenne, and A. Revcolevschi, "Inelastic-neutron-scattering investigation of the spin-Peierls system $CuGeO_3$," Phys. Rev. B **53**, 5579–5597 (1996).

[166] M. Enderle, C. Mukherjee, B. Fåk, R. K. Kremer, J.-M. Broto, H. Rosner, S.-L. Drechsler, J. Richter, J. Malek, A. Prokofiev, W. Assmus, S. Pujol, J.-L. Raggazzoni, H. Rakoto,

M. Rheinstädter, and H. M. Rønnow, "Quantum helimagnetism of the frustrated spin-1/2 chain LiCuVO$_4$," Europhys. Lett. **70**, 237 (2005).

[167] M. G. Banks, R. K. Kremer, C. Hoch, A. Simon, B. Ouladdiaf, J.-M. Broto, H. Rakoto, C. Lee, and M.-H. Whangbo, "Magnetic ordering in the frustrated Heisenberg chain system cupric chloride CuCl$_2$," Phys. Rev. B **80**, 024404 (2009).

[168] Law J. M., Hoch C., Whangbo M.-H., and Kremer R. K., "Description of Anhydrous (Black) Dioptase as a S=1/2 Uniform Antiferromagnetic Chain System," Z. Anorg. Allg. Chem. **636**, 54–61 (2010).

[169] G. Khaliullin and S. Maekawa, "Orbital Liquid in Three-Dimensional Mott Insulator: LaTiO$_3$," Phys. Rev. Lett. **85**, 3950–3953 (2000).

[170] G. Khaliullin, P. Horsch, and A. M. Oleś, "Spin Order due to Orbital Fluctuations: Cubic Vanadates," Phys. Rev. Lett. **86**, 3879–3882 (2001).

[171] R. J. Beynon and J. A. Wilson, "TiOCl, TiOBr-are these RVB d^1, S=1/2 materials? The results of scandium substitution set in the context of other S=1/2 systems of current interest for high-temperature superconductivity and the metal-insulator transition," J. Phys.: Condens. Matter **5**, 1983 (1993).

[172] A. Krimmel, J. Strempfer, B. Bohnenbuck, B. Keimer, M. Hoinkis, M. Klemm, S. Horn, A. Loidl, M. Sing, R. Claessen, and M. v. Zimmermann, "Incommensurate structure of the spin-Peierls compound TiOCl in zero and finite magnetic fields," Phys. Rev. B **73**, 172413 (2006).

[173] V. Kataev, J. Baier, A. Möller, L. Jongen, G. Meyer, and A. Freimuth, "Orbital order in the low-dimensional quantum spin system TiOCl probed by ESR," Phys. Rev. B **68**, 140405 (2003).

[174] R. Rückamp, J. Baier, M. Kriener, M. W. Haverkort, T. Lorenz, G. S. Uhrig, L. Jongen, A. Möller, G. Meyer, and M. Grüninger, "Zero-Field Incommensurate Spin-Peierls Phase with Interchain Frustration in TiOCl," Phys. Rev. Lett. **95**, 097203 (2005).

[175] A. Seidel, C. A. Marianetti, F. C. Chou, G. Ceder, and P. A. Lee, "$S = \frac{1}{2}$ chains and spin-Peierls transition in TiOCl," Phys. Rev. B **67**, 020405 (2003).

[176] G. Caimi, L. Degiorgi, N. N. Kovaleva, P. Lemmens, and F. C. Chou, "Infrared optical properties of the spin-$\frac{1}{2}$ quantum magnet TiOCl," Phys. Rev. B **69**, 125108 (2004).

[177] M. Shaz, S. van Smaalen, L. Palatinus, M. Hoinkis, M. Klemm, S. Horn, and R. Claessen, "Spin-Peierls transition in TiOCl," Phys. Rev. B **71**, 100405 (2005).

[178] R. Glaum, M. Reehuis, N. Stüßer, U. Kaiser, and F. Reinauer, "Neutron Diffraction Study of the Nuclear and Magnetic Structure of the CrVO$_4$ Type Phosphates TiPO$_4$ and VPO$_4$," J. Solid State Chem. **126**, 15–21 (1996).

[179] D. Wulferding, A. Möller, K.-Y. Choi, Y. G. Pashkevich, R. Y. Babkin, K. V. Lamonova, P. Lemmens, J. M. Law, R. K. Kremer, and R. Glaum, "Lattice and orbital fluctuations in TiPO$_4$," Phys. Rev. B **88**, 205136 (2013).

[180] M. Bykov, J. Zhang, A. Schönleber, A. Wölfel, S. I. Ali, S. van Smaalen, R. Glaum, H.-J. Koo, M.-H. Whangbo, P. G. Reuvekamp, J. M. Law, C. Hoch, and R. K. Kremer, "Spin-Peierls distortions in TiPO$_4$," Phys. Rev. B **88**, 184420 (2013).

[181] H. J. Werner, P. J. Knowles, G. Knizia, F. R. Manby, and M. Schütz, "Molpro: a general-purpose quantum chemistry program package," Wiley Rev: Comp. Mol. Sci. **2**, 242–253 (2012).

[182] N. B. Balabanov and K. A. Peterson, "Systematically convergent basis sets for transition metals. I. All-electron correlation consistent basis sets for the 3d elements Sc–Zn," J. Chem. Phys. **123**, 064107 (2005).

[183] M. Dolg, U. Wedig, H. Stoll, and H. Preuss, "Energy-adjusted ab initio pseudopotentials for the first row transition elements," J. Chem. Phys. **86**, 866–872 (1987).

[184] J. M. L. Martin and A. Sundermann, "Correlation consistent valence basis sets for use with the Stuttgart–Dresden–Bonn relativistic effective core potentials: The atoms Ga–Kr and In–Xe," J. Chem. Phys. **114**, 3408–3420 (2001).

[185] A. Bergner, M. Dolg, W. Küchle, H. Stoll, and H. Preuss, "*Ab initio* energy-adjusted pseudopotentials for elements of groups 13–17," Mol. Phys. **80**, 1431–1441 (1993).

[186] J. Pipek and P. G. Mezey, "A fast intrinsic localization procedure applicable for *ab initio* and semiempirical linear combination of atomic orbital wave functions," J. Chem. Phys. **90**, 4916–4926 (1989).

[187] "Jmol: an open-source Java viewer for chemical structures in 3D," http://www.jmol.org/.

[188] L. Hozoi, H. Gretarsson, J. P. Clancy, B.-G. Jeon, B. Lee, K. H. Kim, V. Yushankhai, P. Fulde, D. Casa, T. Gog, J. Kim, A. H. Said, M. H. Upton, Y.-J. Kim, and J. van den Brink, "Longer-range lattice anisotropy strongly competing with spin-orbit interactions in pyrochlore iridates," Phys. Rev. B **89**, 115111 (2014).

[189] N. A. Bogdanov, V. M. Katukuri, J. Romh·nyi, V. Yushankhai, V. Kataev, B. Büchner, J. van den Brink, and L. Hozoi, "Orbital reconstruction in nonpolar tetravalent transition-metal oxide layers," Nat. Commun. **6**, 7306 (2015).

[190] M. Dantz, L. Xu, C. Wagner, J. Pelliciari, J. Trinckauf, Y. Huang, X. Lu, Y. H. Cho, V. N. Strokov, A. O. Mitrushchenkov, S.-W. Cheong, L. Hozoi, J. van den Brink, J. Geck, and T. Schmitt, "Disentangling orbital and magnetic contributions to the exotic spin Peierls transition in TiPO$_4$," (unpublished).

[191] N. A. Bogdanov, R. Maurice, I. Rousochatzakis, J. van den Brink, and L. Hozoi, "Magnetic state of pyrochlore $Cd_2Os_2O_7$ emerging from strong competition of ligand distortions and longer-range crystalline anisotropy," Phys. Rev. Lett. **110**, 127206 (2013).

[192] A. Lupascu, J. P. Clancy, H. Gretarsson, Zixin Nie, J. Nichols, J. Terzic, G. Cao, S. S. A. Seo, Z. Islam, M. H. Upton, Jungho Kim, D. Casa, T. Gog, A. H. Said, V. M. Katukuri, H. Stoll, L. Hozoi, J. van den Brink, and Young-June Kim, "Tuning Magnetic Coupling in Sr_2IrO_4 Thin Films with Epitaxial Strain," Phys. Rev. Lett. **112**, 147201 (2014).

[193] C. de Graaf, C. Sousa, and R. Broer, "Ionization and excitation energies in CuCl and NiO within different embedding schemes," J. Mol. Struct. (Theochem) **458**, 53–60 (1998).

[194] R. Maurice, P. Verma, J. M. Zadrozny, S. Luo, J. Borycz, J. R. Long, D. G. Truhlar, and L. Gagliardi, "Single-Ion Magnetic Anisotropy and Isotropic Magnetic Couplings in the Metal–Organic Framework Fe2(dobdc)," Inorg. Chem. **52**, 9379–9389 (2013).

[195] L. Hozoi, A. H. de Vries, A. B. van Oosten, R. Broer, J. Cabrero, and C. de Graaf, "Theoretical Characterization of the Ground and Optically Excited States of $\alpha^{'}-NaV_2O_5$," Phys. Rev. Lett. **89**, 076407 (2002).

[196] N. W. Winter, R. M. Pitzer, and D. K. Temple, "Theoretical study of a Cu^+ ion impurity in a NaF host," J. Chem. Phys. **86**, 3549–3556 (1987).

[197] J. Miralles, O. Castell, R. Caballol, and J.-P. Malrieu, " Specific CI calculation of energy differences: Transition energies and bond energies ," Chem. Phys. **172**, 33–43 (1993).

[198] J. Miralles, J.-P. Daudey, and R. Caballol, " Variational calculation of small energy differences. The singlet-triplet gap in $[Cu_2Cl_6]^{2-}$," Chem. Phys. Lett. **198**, 555–562 (1992).

[199] D. Muñoz, F. Illas, and I. de P. R. Moreira, " Accurate Prediction of Large Antiferromagnetic Interactions in High- T_c $HgBa_2Ca_{n-1}Cu_nO_{2n+2+\delta}$ ($n = 2, 3$) Superconductor Parent Compounds ," Phys. Rev. Lett. **84**, 1579–1582 (2000).

[200] C. J. Calzado, J. F. Sanz, and J. P. Malrieu, " Accurate *ab initio* determination of magnetic interactions and hopping integrals in $La_{2-x}Sr_xCuO_4$ systems ," J. Chem. Phys. **112**, 5158–5167 (2000).

[201] J. Cabrero, N. Ben Amor, C. de Graaf, F. Illas, and R. Caballol, " *Ab initio* Study of the Exchange Coupling in Oxalato-Bridged Cu(II) Dinuclear Complexes ," J. Phys. Chem. A **104**, 9983–9989 (2000).

[202] C. J. Calzado, J. Cabrero, J. P. Malrieu, and R. Caballol, " Analysis of the magnetic coupling in binuclear complexes. I. Physics of the coupling ," J. Chem. Phys. **116**, 2728–2747 (2002).

[203] P. Löwdin, "Exchange, Correlation, and Spin Effects in Molecular and Solid-State Theory," Rev. Mod. Phys. **34**, 80–87 (1962).

[204] A.B. van Oosten, R. Broer, and W.C. Nieuwpoort, "Heisenberg exchange enhancement by orbital relaxation in cuprate compounds," Chem. Phys. Lett. **257**, 207–212 (1996).

[205] Y. Guo, J. Langlois, and W. A. Goddard, "Electronic structure and valence-bond band structure of cuprate superconducting materials," Science **239**, 896–899 (1988).

[206] R. L. Martin and P. W. Saxe, "*Ab initio* electronic structure theory for a cluster model of $La_{2-x}Sr_xCuO_4$," Int. J. Quantum Chem. **34**, 237–244 (1988).

[207] C. J. Calzado, J. Cabrero, J. P. Malrieu, and R. Caballol, "Analysis of the magnetic coupling in binuclear complexes. I. Physics of the coupling," J. Chem. Phys. **116**, 2728–2747 (2002).

[208] K. R. Shamasundar, G. Knizia, and H.-J. Werner, "A new internally contracted multi-reference configuration interaction method," J. Chem. Phys. **135**, 054101 (2011).

[209] A.-M. Pradipto, R. Maurice, N. Guihéry, C. de Graaf, and R. Broer, "First-principles study of magnetic interactions in cupric oxide," Phys. Rev. B **85**, 014409 (2012).

[210] L. Xu, Z. Zangeneh, R. Yadav, S. Avdoshenko, J. van den Brink, A. Jesche, and L. Hozoi, "Spin-reversal energy barriers of 305 K for Fe^{2+} d^6 ions with linear ligand coordination," Nanoscale **9**, 10596–10600 (2017).

[211] L. Bogani and W. Wernsdorfer, "Molecular spintronics using single-molecule magnets," Nat. Mater. **7**, 179–186 (2008).

[212] R. Sessoli, D. Gatteschi, A. Caneschi, and M. A. Novak, "Magnetic bistability in a metal-ion cluster," Nature **365**, 141–143 (1993).

[213] J. D. Rinehart, M. Fang, W. J. Evans, and J. R. Long, "Strong exchange and magnetic blocking in N_2^{3-}- radical-bridged lanthanide complexes," Nat. Chem. **3**, 538—542 (2011).

[214] J. D. Rinehart, M. Fang, W. J. Evans, and J. R. Long, "A N_2^{3-}-radical-bridged terbium complex exhibiting magnetic hysteresis at 14 K," J. Am. Chem. Soc. **133**, 14236–14239 (2011).

[215] S. K. Gupta, T. Rajeshkumar, G. Rajaraman, and R. Murugavel, "An air-stable Dy(III) single-ion with high anisotropy barrier and blocking temperature," Chem. Sci. **7**, 5181–5191 (2016).

[216] A. L. Svitova, K. B. Ghiassi, C. Schlesier, K. Junghans, Y. Zhang, M. M. Olmstead, A. L. Balch, L. Dunsch, and A. A. Popov, "Endohedral fullerene with μ_3-carbido ligand and titanium-carbon double bond stabilized inside a carbon cage," Nat. Commun. **5**, 3568 (2014).

[217] S. M. Avdoshenko, F. Fritz, C. Schlesier, A. Kostanyan, J. Dreiser, M. Luysberg, A. A. Popov, C. Meyer, and R. Westerström, "Partial magnetic ordering in one-dimensional arrays of endofullerene single-molecule magnet peapods," Nanoscale **10**, 18153–18160 (2018).

[218] J. M. Zadrozny, D. J. Xiao, M. Atanasov, G. J. Long, F. Grandjean, F. Neese, and J. R. Long, "Magnetic blocking in a linear iron(I) complex," Nat. Chem. **5**, 577–581 (2013).

[219] A. Jesche, R. W. McCallumm, S. Thimmaiah, J. L. Jacobs, V. Taufour, A. Kreyssig, R. S. Houk, S. L.Bud'ko, and P. C. Canfield, "Giant magnetic anisotropy and tunneling of the magnetization in $Li_2(Li_{1-x}Fe_x)N$," Nat. Commun. **5**, 3333 (2014).

[220] J. Klatyk, W. Schnelle, F. R. Wagner, R. Niewa, P. Novák, R. Kniep, M. Waldeck, V. Ksenofontov, and P. Gütlich, "Large orbital moments and internal magnetic fields in lithium nitridoferrate(I)," Phys. Rev. Lett. **88**, 207202 (2002).

[221] P. Novak and F. R. Wagner, "Electronic structure of Li nitridoferrate: effects of correlation and spin-orbit coupling," Phys. Rev. B **66**, 184434 (2002).

[222] V. P. Antropov and V. N. Antonov, "Colossal anisotropy of the magnetic properties of doped Li nitrodometalates," Phys. Rev. B **90**, 094406 (2014).

[223] L. Ke and M. van Schilfgaarde, "Band-filling effect on magnetic anisotropy using a Green's function method," Phys. Rev. B **92**, 014423 (2015).

[224] D. H. Gregory, P. M. O'Meara, A. G. Gordon, J. P. Hodges, S. Short, and J. D. Jorgensen, "Structure of Lithium Nitride and Transition-Metal-Doped Derivatives, $Li_{3-x-y}M_xN$ (M=Ni, Cu): A Powder Neutron Diffraction Study," Chem. Mater. **14**, 2063–2070 (2002).

[225] A. G. Gordon, R. I. Smith, C. Wilson, Z. Stoeva, and D. H. Gregory, "Crystal growth, defect structure and magnetism of new Li_3N−derived lithium nitridocobaltates," Chem. Commun. **24**, 2812–2813 (2004).

[226] D. Muller-Bouvet, J.-P. Pereira-Ramos, S. Bach, P. Willmann, and A. Michalowicz, "Effect of Cobalt Substitution on $Li_{3-2x}Co_xN$ Local Structure: A XAS Investigation," Inorg. Chem. **53**, 6127–6131 (2014).

[227] A. Jesche, L. Ke, J. L. Jacobs, B. Harmon, R. S. Houk, and P. C. Canfield, "Alternating magnetic anisotropy of $Li_2(Li_{1-x}T_x)N$ (T=Mn, Fe, Co, and Ni)," Phys. Rev. B **91**, 180403 (2015).

[228] A. Huq, J. W. Richardson, E. R. Maxey, D. Chandra, and W.-M. Chien, "Structural studies of Li_3N using neutron powder diffraction ," J. Alloys & Compounds **436**, 256–260 (2007).

[229] B. Roos and U. Wahlgren, MADPOT and MADFIT programs (1969).

[230] H.-J. Werner and P. J. Knowles, "An efficient internally contracted multiconfiguration-reference configuration interaction method," J. Chem. Phys. **89**, 5803–5814 (1988).

[231] J.B. Ducros, S. Bach, J.P. Pereira-Ramos, and P. Willmann, "Layered lithium cobalt nitrides: A new class of lithium intercalation compounds," J. Power Sources **175**, 517–525 (2008).

[232] H. Schulz and K. H. Thiemann, "Defect structure of the ionic conductor lithium nitride Li$_3$N," Acta Cryst. A **35**, 309–314 (1979).

[233] M. Minola, L. Hozoi, D. Di Castro, R. Felici, M. Moretti Sala, A. Tebano, G. Balestrino, G. Ghiringhelli, J. van den Brink, and L. Braicovich, "Measurement of the effect of lattice strain on magnetic interactions and orbital splitting in CaCuO$_2$ using resonant inelastic x-ray scattering," Phys. Rev. B **87**, 085124 (2013).

[234] M. Guo, E. Kallman, L. K. Sørensen, M. G. Delcey, R. V. Pinjari, and M. Lundberg, "Molecular Orbital Simulations of Metal 1s2p Resonant Inelastic X-ray Scattering," J. Phys. Chem. A **120**, 5848–5855 (2016).

[235] K. Kunnus, W. Zhang, M. G. Delcey, R. V. Pinjari, P. S. Miedema, S. Schreck, W. Quevedo, H. Schröder, A. Föhlisch, K. J. Gaffney, M. Lundberg, M. Odelius, and P. Wernet, "Viewing the Valence Electronic Structure of Ferric and Ferrous Hexacyanide in Solution from the Fe and Cyanide Perspectives," J. Phys. Chem. B **120**, 7182–7194 (2016).

[236] N. A. Bogdanov, V. Bisogni, R. Kraus, C. Monney, K. Zhou, T. Schmitt, J. Geck, A. O. Mitrushchenkov, H. Stoll, J. van den Brink, and L. Hozoi, "Orbital breathing effects in the computation of X-ray d-ion spectra in solids by ab initio wave-function-based methods," J. Phys. Condens. Matter **29**, 035502 (2017).

[237] A. Lunghi, F. Totti, R. Sessoli, and S. Sanvito, "The role of anharmonic phonons in under-barrier spin relaxation of single molecule magnets," Nat. Commun. **8**, 14620 (2017).

[238] L. Xu, N. A. Bogdanov, A. Princep, P. Fulde, J. van den Brink, and L. Hozoi, "Covalency and vibronic couplings make a nonmagnetic $j = 3/2$ ion magnetic," Npj Quantum Materials **1**, 16029 (2016).

[239] G. Jackeli and G. Khaliullin, "Mott insulators in the strong spin-orbit coupling limit: From Heisenberg to a quantum compass and Kitaev models," Phys. Rev. Lett. **102**, 017205 (2009).

[240] H. Gretarsson, J. P. Clancy, Y. Singh, P. Gegenwart, J. P. Hill, J. Kim, M. H. Upton, A. H. Said, D. Casa, T. Gog, and Y.-J. Kim, "Magnetic excitation spectrum of Na$_2$IrO$_3$ probed with resonant inelastic x-ray scattering," Phys. Rev. B **87**, 220407 (2013).

[241] Sae H.-C., J.-W. Kim, J. Kim, H. Zheng, C. C. Stoumpos, C. D. Malliakas, J. F. Mitchell, K. Mehlawat, Y. Singh, Y. Choi, T. Gog, A. Al-Zein, M. M. Sala, M. Krisch, J. Chaloupka, G. Jackeli, G. Khaliullin, and B. J. Kim, "Direct evidence for dominant bond-directional interactions in a honeycomb lattice iridate Na$_2$IrO$_3$," Nat. Phys. **11**, 462–466 (2015).

[242] Y. Yamaji, Y. Nomura, M. Kurita, R. Arita, and M. Imada, "First-Principles study of the honeycomb-lattice iridates Na$_2$IrO$_3$ in the presence of strong spin-orbit interaction and electron correlations," Phys. Rev. Lett. **113**, 107201 (2014).

[243] V. M. Katukuri, S. Nishimoto, V. Yushankhai, A. Stoyanova, H. Kandpal, S. Choi, R. Coldea, I. Rousochatzakis, L. Hozoi, and J. van den Brink, "Kitaev interactions between j=1/2 moments in honeycomb Na_2IrO_3 are large and ferromagnetic: insights from *ab initio* quantum chemistry calculations," New J. Phys. **16**, 013056 (2014).

[244] J. Chaloupka, G. Jackeli, and G. Khaliullin, "Kitaev-Heisenberg Model on a Honeycomb Lattice: Possible Exotic Phases in Iridium Oxides A_2IrO_3," Phys. Rev. Lett. **105**, 027204 (2010).

[245] M. Kotani, "On the magnetic moment of complex ions. (I)," J. Phys. Soc. Jap. **4**, 293–297 (1949).

[246] A. Abragam and B. Bleaney, *Electron Paramagnetic Resonance of Transition Ions* (Clarendon Press, Oxford, 1970) pp. 417–426.

[247] F. E. Mabbs and D. J. Machin, *Magnetism and Transition Metal Complexes* (Chapman and Hall, London, 1973) pp. 68–84.

[248] E. J. Cussen, D. R. Lynham, and J. Rogers, "Magnetic Order Arising from Structural Distortion: Structure and Magnetic Properties of Ba_2LnMoO_6," Chem. Mater. **18**, 2855–2866 (2006).

[249] K. W. H. Stevens, "On the Magnetic Properties of Covalent XY_6 Complexes," Proc. Roy. Soc. (London) **A219**, 542 (1953).

[250] G. Chen, R. Pereira, and L. Balents, "Exotic phases induced by strong spin-orbit coupling in ordered double perovskites," Phys. Rev. B **82**, 174440 (2010).

[251] S. Gangopadhyay and W. E. Pickett, "Spin-orbit coupling, strong correlation, and insulator-metal transitions: The J_{eff}=3/2 ferromagnetic Dirac-Mott insulator Ba_2NaOsO_6," Phys. Rev. B **91**, 045133 (2015).

[252] W. M. H. Natori, E. C. Andrade, E. Miranda, and R. G. Pereira, "Chiral Spin-Orbital Liquids with Nodal Lines," Phys. Rev. Lett. **117**, 017204 (2016).

[253] J. Romhányi, L. Balents, and G. Jackeli, "Spin-Orbit Dimers and Noncollinear Phases in d^1 Cubic Double Perovskites," Phys. Rev. Lett. **118**, 217202 (2017).

[254] K. A. Peterson, D. Figgen, M. Dolg, and H. Stoll, "Energy-consistent relativistic pseudopotentials and correlation consistent basis sets for the $4d$ elements Y-Pd," J. Chem. Phys. **126**, 124101 (2007).

[255] I. S. Lim, H. Stoll, and P. Schwerdtfeger, "Relativistic small-core energy-consistent pseudopotentials for the alkaline-earth elements from Ca to Ra," J. Chem. Phys. **124**, 034107 (2006).

[256] P. Fuentealba, H. Preuss, H. Stoll, and L. von Szentpaly, "A proper account of core-polarization with pseudopotentials: single valence-electron alkali compounds," Chem. Phys. Lett. **89**, 418 (1982).

[257] P. J. Knowles and H.-J. Werner, "Internally contracted multiconfiguration-reference configuration interaction calculations for excited states," Theor. Chim. Acta **84**, 95–103 (1992).

[258] J. S. Griffith, *The Theory of Transition-Metal Ions* (Cambridge University Press, Cambridge, 2009, 5th ed.) pp. 226–264.

[259] B. W. Faughnan, "Electron-Paramagnetic-Resonance Spectrum of Mo^{5+} in $SrTiO_3$-An Example of the Dynamic Jahn-Teller Effect," Phys. Rev. B **5**, 4925–4931 (1972).

[260] H. Bolvin, "An alternative approach to the g-matrix: Theory and applications," ChemPhysChem **7**, 1575–1589 (2006).

[261] S. Vancoillie, P.-A. Malmqvist, and K. Pierloot, "Calculation of EPR g tensors for transition-metal complexes based on multiconfigurational perturbation theory (CASPT2)," ChemPhysChem **8**, 1803–1815 (2007).

[262] V. M. Katukuri, K. Roszeitis, V. Yushankhai, A. Mitrushchenkov, H. Stoll, M. van Veenendaal, P. Fulde, J. van den Brink, and L. Hozoi, "Electronic Structure of Low-Dimensional $4d^5$ Oxides: Interplay of Ligand Distortions, Overall Lattice Anisotropy, and Spin–Orbit Interactions," Inorg. Chem. **53**, 4833–4839 (2014).

[263] A C Mclaughlin, "Simultaneous Jahn-Teller distortion and magnetic order in the double perovskite $Ba_2^{154}SmMoO_6$," Phys. Rev. B **78**, 132404 (2008).

[264] T. K. Wallace, R. H. Colman, and A. C. Mclaughlin, "A variable temperature synchrotron x-ray diffraction study of the ferroelastic double perovskite Ba_2GdMoO_6," Phys. Chem. Chem. Phys **15**, 8672 (2013).

[265] O. Kahn and S. F. A. Kettle, "Vibronic coupling in cubic complexes," Mol. Phys. **29**, 61–79 (1975).

[266] B. W. Faughnan, "Electron-Paramagnetic-Resonance Spectrum of Mo^{5+} in $SrTiO_3$—An Example of the Dynamic Jahn-Teller Effect," Phys. Rev. B **5**, 4925–4931 (1972).

[267] S. A. Prosandeev, U. Waghmare, I. Levin, and J. Maslar, "First-order Raman spectra of $AB'_{1/2}B''_{1/2}O_3$ double perovskites," Phys. Rev. B **71**, 214307 (2005).

[268] K. Doll, M. Dolg, P. Fulde, and H. Stoll, "Quantum chemical approach to cohesive properties of NiO," Phys. Rev. B **55**, 10282 (1997).

[269] J. Yang, W. Hu, D. Usvyat, D. Matthews, M. Schütz, and G. K.-L. Chan, "*Ab initio* determination of the crystalline benzene lattice energy to sub-kilojoule/mole accuracy," Science **345**, 640 (2014).

[270] N. Iwahara, V. Vieru, and L. F. Chibotaru, "Spin-orbital-lattice entangled states in cubic d^1 double perovskites," Phys. Rev. B **98**, 075138 (2018).

[271] L. Hozoi, H. Gretarsson, J. P. Clancy, B.-G. Jeon, B. Lee, K. H. Kim, V. Yushankhai, P. Fulde, D. Casa, T. Gog, J. Kim, A. H. Said, M. H. Upton, Y.-J. Kim, and J. van den Brink, "Longer-range lattice anisotropy strongly competing with spin-orbit interactions in pyrochlore iridates," Phys. Rev. B **89**, 115111 (2014).

[272] S. Calder, J. G. Vale, N. Bogdanov, C. Donnerer, D. Pincini, M. Moretti Sala, X. Liu, M. H. Upton, D. Casa, Y. G. Shi, Y. Tsujimoto, K. Yamaura, J. P. Hill, J. van den Brink, D. F. Mc-Morrow, and A. D. Christianson, "Strongly gapped spin-wave excitation in the insulating phase of $NaOsO_3$," Phys. Rev. B **95**, 020413 (2017).

[273] B. J. Kim, H. Ohsumi, T. Komesu, S. Sakai, T. Morita, H. Takagi, and T. Arima, "Phase-sensitive observation of a spin-orbital mott state in Sr_2IrO_4," Science **323**, 1329–1332 (2009).

[274] J. W. Kim, Y. Choi, J. Kim, J. F. Mitchell, G. Jackeli, M. Daghofer, J. van den Brink, G. Khaliullin, and B. J. Kim, "Dimensionality driven spin-flop transition in layered iridates," Phys. Rev. Lett. **109**, 037204 (2012).

[275] S. K. Choi, R. Coldea, A. N. Kolmogorov, T. Lancaster, I. I. Mazin, S. J. Blundell, P. G. Radaelli, Yogesh Singh, P. Gegenwart, K. R. Choi, S.-W. Cheong, P. J. Baker, C. Stock, and J. Taylor, "Spin waves and revised crystal structure of honeycomb iridate Na_2IrO_3," Phys. Rev. Lett. **108**, 127204 (2012).

[276] S. Boseggia, R. Springell, H. C. Walker, H. M. Rønnow, Ch. Rüegg, H. Okabe, M. Isobe, R. S. Perry, S. P. Collins, and D. F. McMorrow, "Robustness of basal-plane antiferromagnetic order and the $J_{eff}=1/2$ state in single-layer iridate spin-orbit mott insulators," Phys. Rev. Lett. **110**, 117207 (2013).

[277] V. M. Katukuri, V. Yushankhai, L. Siurakshina, J. van den Brink, L. Hozoi, and I. Rousochatzakis, "Mechanism of basal-plane antiferromagnetism in the spin-orbit driven iridate Ba_2IrO_4," Phys. Rev. X **4**, 021051 (2014).

[278] D. Coffey, T. M. Rice, and F. C. Zhang, "Dzyaloshinskii-Moriya interaction in the cuprates," Phys. Rev. B **44**, 10112–10116 (1991).

[279] T. Yildirim, A. B. Harris, A. Aharony, and O. Entin-Wohlman, "Anisotropic spin Hamiltonians due to spin-orbit and coulomb exchange interactions," Phys. Rev. B **52**, 10239–10267 (1995).

[280] L. Shekhtman, O. Entin-Wohlman, and A. Aharony, "Moriya's anisotropic superexchange interaction, frustration, and dzyaloshinsky's weak ferromagnetism," Phys. Rev. Lett. **69**, 836–839 (1992).

[281] J. Chaloupka, G. Jackeli, and G. Khaliullin, "Zigzag magnetic order in the iridium oxide Na_2IrO_3," Phys. Rev. Lett. **110**, 097204 (2013).

[282] K. Foyevtsova, H. O. Jeschke, I. I. Mazin, D. I. Khomskii, and R. Valentí, "*Ab initio* analysis of the tight-binding parameters and magnetic interactions in Na_2IrO_3," Phys. Rev. B **88**, 035107 (2013).

[283] B. H. Kim, G. Khaliullin, and B. I. Min, "Magnetic couplings, optical spectra, and spin-orbit exciton in $5d$ electron mott insulator Sr_2IrO_4," Phys. Rev. Lett. **109**, 167205 (2012).

[284] N. B. Perkins, Y. Sizyuk, and P. Wölfle, "Interplay of many-body and single-particle interactions in iridates and rhodates," Phys. Rev. B **89**, 035143 (2014).

[285] S. Sugano, Y. Tanabe, and H. Kamimura, *Multiplets of Transition-Metal Ions in Crystals* (Academic Press, New York, 1970).

[286] E. Kermarrec, C. A. Marjerrison, C. M. Thompson, D. D. Maharaj, K. Levin, S. Kroeker, G. E. Granroth, R. Flacau, Z. Yamani, J. E. Greedan, and B. D. Gaulin, "Frustrated fcc antiferromagnet Ba_2YOsO_6: Structural characterization, magnetic properties, and neutron scattering studies," Phys. Rev. B **91**, 075133 (2015).

[287] A. E. Taylor, R. Morrow, R. S. Fishman, S. Calder, A. I. Kolesnikov, M. D. Lumsden, P. M. Woodward, and A. D. Christianson, "Spin-orbit coupling controlled ground state in Sr_2ScOsO_6," Phys. Rev. B **93**, 220408 (2016).

[288] S. Calder, J. G. Vale, N. A. Bogdanov, X. Liu, C. Donnerer, M. H. Upton, D. Casa, A. H. Said, M. D. Lumsden, Z. Zhao, J.-Q. Yan, D. Mandrus, S. Nishimoto, J. van den Brink, J. P. Hill, D. F. McMorrow, and A. D. Christianson, "Spin-orbit-driven magnetic structure and excitation in the $5d$ pyrochlore $Cd_2Os_2O_7$," Nat. Commun. **7**, 11651 (2016).

[289] Y. Du, X. Wan, L. Sheng, J. Dong, and S. Y. Savrasov, "Electronic structure and magnetic properties of $NaOsO_3$," Phys. Rev. B **85**, 174424 (2012).

[290] M.-C. Jung, Y.-J. Song, K.-W. Lee, and W. E. Pickett, "Structural and correlation effects in the itinerant insulating antiferromagnetic perovskite $NaOsO_3$," Phys. Rev. B **87**, 115119 (2013).

[291] I. L. Vecchio, A. Perucchi, P. Di Pietro, O. Limaj, U. Schade, Y. Sun, M. Arai, K. Yamaura, and S. Lupi, "Infrared evidence of a slater metal-insulator transition in $NaOsO_3$," Sci. Rep. **3** (2013).

[292] T. Moriya, "Anisotropic superexchange interaction and weak ferromagnetism," Phys. Rev. **120**, 91–98 (1960).

[293] H. Stoll, unpublished .

[294] P. J. Knowles and H.-J. Werner, "Internally contracted multiconfiguration-reference con-figuration interaction calculations for excited states," Theor. Chim. Acta **84**, 95–103 (1992).

[295] R. Boča, "Zero-field splitting in metal complexes," Coord. Chem. Rev. **248**, 757–815 (2004).

[296] R. M. Macfarlane, "Zero field splittings of t_2^3 cubic terms," J. Chem. Phys. **47**, 2066–2073 (1967).

[297] K. Pierloot, B. Dumez, P.-O. Widmark, and B. O. Roos, "Density matrix averaged atomic natural orbital (ANO) basis sets for correlated molecular wave functions," Theor. Chimi. Acta **90**, 87–114 (1995).

[298] J. R. Gispert, *Coordination Chemistry* (Wiley, 2008) pp. 313–314.

[299] R. Broer, L. Hozoi, and W. C. Nieuwpoort, "Non-orthogonal approaches to the study of magnetic interactions," Mol. Phys. **101**, 233–240 (2003).

[300] V. M. Katukuri, H. Stoll, J. van den Brink, and L. Hozoi, "*Ab initio* determination of excitation energies and magnetic couplings in correlated quasi-two-dimensional iridates," Phys. Rev. B **85**, 220402 (2012).

[301] X. Liu, V. M. Katukuri, L. Hozoi, W.-G. Yin, M. P. M. Dean, M. H. Upton, J. Kim, D. Casa, A. Said, T. Gog, T. F. Qi, G. Cao, A. M. Tsvelik, J. van den Brink, and J. P. Hill, "Testing the Validity of the Strong Spin-Orbit-Coupling Limit for Octahedrally Coordinated Iridate Compounds in a Model System Sr_3CuIrO_6," Phys. Rev. Lett. **109**, 157401 (2012).

[302] L. Hozoi, H. Gretarsson, J. P. Clancy, B.-G. Jeon, B. Lee, K. H. Kim, V. Yushankhai, P. Fulde, D. Casa, T. Gog, J. Kim, A. H. Said, M. H. Upton, Y.-J. Kim, and J. van den Brink, "Longer-range lattice anisotropy strongly competing with spin-orbit interactions in pyrochlore iridates," Phys. Rev. B **89**, 115111 (2014).

[303] A. Kitaev, "Anyons in an exactly solved model and beyond," Ann. Phys. **321**, 2–111 (2006).

[304] Z. Nussinov and J. van den Brink, "Compass models: Theory and physical motivations," Rev. Mod. Phys. **87**, 1–59 (2015).

[305] R. Lindsay, W. Strange, B.L. Chamberland, and R.O. Moyer, "Weak ferromagnetism in $BaIrO_3$," Solid State Commun. **86**, 759–763 (1993).

[306] G. Cao, J.E. Crow, R.P. Guertin, P.F. Henning, C.C. Homes, M. Strongin, D.N. Basov, and E. Lochner, "Charge density wave formation accompanying ferromagnetic ordering in quasi-one-dimensional $BaIrO_3$," Solid State Commun. **113**, 657–662 (2000).

[307] M. L. Brooks, S. J. Blundell, T. Lancaster, W. Hayes, F. L. Pratt, P. P. C. Frampton, and P. D. Battle, "Unconventional magnetic properties of the weakly ferromagnetic metal $BaIrO_3$," Phys. Rev. B **71**, 220411 (2005).

[308] T. Nakano and I. Terasaki, "Giant nonlinear conduction and thyristor-like negative differential resistance in $BaIrO_3$ single crystals," Phys. Rev. B **73**, 195106 (2006).

[309] J.-G. Cheng, J.-S. Zhou, J. A. Alonso, J. B. Goodenough, Y. Sui, K. Matsubayashi, and Y. Uwatoko, "Transition from a weak ferromagnetic insulator to an exchange-enhanced paramagnetic metal in the $BaIrO_3$ polytypes," Phys. Rev. B **80**, 104430 (2009).

[310] M. A. Laguna-Marco, D. Haskel, N. Souza-Neto, J. C. Lang, V. V. Krishnamurthy, S. Chikara, G. Cao, and M. van Veenendaal, "Orbital magnetism and spin-orbit effects in the electronic structure of $BaIrO_3$," Phys. Rev. Lett. **105**, 216407 (2010).

[311] T. Dey, M. Majumder, J. C. Orain, A. Senyshyn, M. Prinz-Zwick, S. Bachus, Y. Tokiwa, F. Bert, P. Khuntia, N. Büttgen, A. A. Tsirlin, and P. Gegenwart, "Persistent low-temperature spin dynamics in the mixed-valence iridate $Ba_3InIr_2O_9$," Phys. Rev. B **96**, 174411 (2017).

[312] W. Miiller, M. Avdeev, Q. Zhou, B. J. Kennedy, N. Sharma, R. Kutteh, G.J. Kearley, S. Schmid, K. S. Knight, P. E. R. Blanchard, and C. D. Ling, "Giant magnetoelastic effect at the opening of a spin-gap in $Ba_3BiIr_2O_9$," J. Am. Chem. Soc. **134**, 3265–3270 (2012).

[313] K. E. Stitzer, A. E. Abed, J. Darriet, and H. Z. Loye, "Crystal growth and structure determination of barium rhodates: Stepping stones toward $2H$-$BaRhO_3$," J. Am. Chem. Soc. **126**, 856–864 (2004).

[314] J. Sugiyama, H. Nozaki, Y. Ikedo, K. Mukai, D. Andreica, A. Amato, J. H. Brewer, E. J. Ansaldo, G. D. Morris, T. Takami, and H. Ikuta, "Evidence of two dimensionality in quasi-one-dimensional cobalt oxides," Phys. Rev. Lett. **96**, 197206 (2006).

[315] H. Suzuura, H. Yasuhara, A. Furusaki, N. Nagaosa, and Y. Tokura, "Singularities in Optical Spectra of Quantum Spin Chains," Phys. Rev. Lett. **76**, 2579–2582 (1996).

[316] N. Motoyama, H. Eisaki, and S. Uchida, "Magnetic Susceptibility of Ideal Spin 1/2 Heisenberg Antiferromagnetic Chain Systems, Sr_2CuO_3 and $SrCuO_2$," Phys. Rev. Lett. **76**, 3212–3215 (1996).

[317] G. Cao, X. N. Lin, S. Chikara, V. Durairaj, and E. Elhami, "High-temperature weak ferromagnetism on the verge of a metallic state: Impact of dilute Sr doping on $BaIrO_3$," Phys. Rev. B **69**, 174418 (2004).

[318] O. B. Korneta, S. Chikara, S. Parkin, L. E. DeLong, P. Schlottmann, and G. Cao, "Pressure-induced insulating state in $Ba_{1-x}R_xIrO_3$ (R = Gd, Eu) single crystals," Phys. Rev. B **81**, 045101 (2010).

[319] M. A. Laguna-Marco, G. Fabbris, N. M. Souza-Neto, S. Chikara, J. S. Schilling, G. Cao, and D. Haskel, "Different response of transport and magnetic properties of $BaIrO_3$ to chemical and physical pressure," Phys. Rev. B **90**, 014419 (2014).

[320] S. J. Yuan, K. Butrouna, J. Terzic, H. Zheng, S. Aswartham, L. E. DeLong, F. Ye, P. Schlottmann, and G. Cao, "Ground-state tuning of metal-insulator transition by compositional variations in $BaIr_{1-x}Ru_xO_3$ ($0 \leq x \leq 1$)," Phys. Rev. B **93**, 165136 (2016).

[321] N. A. Bogdanov, V. M. Katukuri, H. Stoll, J. van den Brink, and L. Hozoi, "Post-perovskite $CaIrO_3$: A $j=1/2$ quasi-one-dimensional antiferromagnet," Phys. Rev. B **85**, 235147 (2012).

[322] A.B. van Oosten, R. Broer, and W.C. Nieuwpoort, "Heisenberg exchange enhancement by orbital relaxation in cuprate compounds," Chem. Phys. Lett. **257**, 207—-212 (1996).

[323] C. J. Calzado, J. Cabrero, J. P. Malrieu, and R. Caballol, "Analysis of the magnetic coupling in binuclear complexes. II. Derivation of valence effective Hamiltonians from *ab initio* CI and DFT calculations," J. Chem. Phys. **116**, 3985–4000 (2002).

[324] V. M. Katukuri, V. Yushankhai, L. Siurakshina, J. van den Brink, L. Hozoi, and I. Rousochatzakis, "Mechanism of basal-plane antiferromagnetism in the spin-orbit driven iridate Ba_2IrO_4," Phys. Rev. X **4**, 021051 (2014).

[325] S. Nishimoto, V.M. Katukuri, V. Yushankhai, H. Stoll, U. K. Roessler, L. Hozoi, I. Rousochatzakis, and J. van den Brink, "Strongly frustrated triangular spin lattice emerging from triplet dimer formation in honeycomb Li_2IrO_3," Nat. Commun. **7**, 10273 (2016).

[326] V. M. Katukuri, S. Nishimoto, I. Rousochatzakis, H. Stoll, J. van den Brink, and L. Hozoi, "Strong magnetic frustration and anti-site disorder causing spin-glass behavior in honeycomb Li_2RhO_3," Sci. Rep. **5**, 14718 (2015).

[327] R. Yadav, N. A. Bogdanov, V. M. Katukuri, S. Nishimoto, J. van den Brink, and L. Hozoi, "Kitaev exchange and field-induced quantum spin-liquid states in honeycomb α-$RuCl_3$," Sci. Rep. **6**, 37925 (2016).

[328] R. Yadav, M. Pereiro, N. A. Bogdanov, S. Nishimoto, A. Bergman, O. Eriksson, J. van den Brink, and L. Hozoi, "Heavy-mass magnetic modes in pyrochlore iridates due to dominant Dzyaloshinskii-Moriya interaction," Phys. Rev. Materials **2**, 074408 (2018).

[329] R. Yadav, S. Rachel, L. Hozoi, J. van den Brink, and G. Jackeli, "Strain- and pressure-tuned magnetic interactions in honeycomb Kitaev materials," Phys. Rev. B **98**, 121107 (2018).

[330] K. I. Kugel, D. I. Khomskii, A. O. Sboychakov, and S. V. Streltsov, "Spin-orbital interaction for face-sharing octahedra: Realization of a highly symmetric SU(4) model," Phys. Rev. B **91**, 155125 (2015).

[331] D. I. Khomskii, K. I. Kugel, A. O. Sboychakov, and S. V. Streltsov, "Role of local geometry in the spin and orbital structure of transition metal compounds," J. Exp. Theor. Phys. **122**, 484–498 (2016).

[332] M. Moretti Sala, M. Rossi, S. Boseggia, J. Akimitsu, N. B. Brookes, M. Isobe, M. Minola, H. Okabe, H. M. Rønnow, L. Simonelli, D. F. McMorrow, and G. Monaco, "Orbital occupancies and the putative $j_{\text{eff}} = \frac{1}{2}$ ground state in Ba_2IrO_4: A combined oxygen K-edge XAS and RIXS study," Phys. Rev. B **89**, 121101.

[333] R. R. P. Singh, P. A. Fleury, K. B. Lyons, and P. E. Sulewski, "Quantitative determination of quantum fluctuations in the spin-1/2 planar antiferromagnet," Phys. Rev. Lett. **62**, 2736–2739 (1989).

[334] G. Bastien, G. Garbarino, R. Yadav, F. J. Martinez-Casado, R. Beltrán Rodríguez, Q. Stahl, M. Kusch, S. P. Limandri, R. Ray, P. Lampen-Kelley, D. G. Mandrus, S. E. Nagler, M. Roslova, A. Isaeva, T. Doert, L. Hozoi, A. U. B. Wolter, B. Büchner, J. Geck, and J. van den Brink, "Pressure-induced dimerization and valence bond crystal formation in the Kitaev-Heisenberg magnet $\alpha-RuCl_3$," Phys. Rev. B **97**, 241108 (2018).

[335] L. J. P. Ament, M. van Veenendaal, T. P. Devereaux, J. P. Hill, and J. van den Brink, "Resonant inelastic x-ray scattering studies of elementary excitations," Rev. Mod. Phys. **83**, 705–767 (2011).

[336] M. van Veenendaal, *Theory of Inelastic Scattering and Absorption of X-rays* (Cambridge University Press, 2015).

[337] L. Braicovich, L. J. P. Ament, V. Bisogni, F. Forte, C. Aruta, G. Balestrino, N. B. Brookes, G. M. De Luca, P. G. Medaglia, F. Miletto Granozio, M. Radovic, M. Salluzzo, J. van den Brink, and G. Ghiringhelli, "Dispersion of Magnetic Excitations in the Cuprate La_2CuO_4 and $CaCuO_2$ Compounds Measured Using Resonant X-Ray Scattering," Phys. Rev. Lett. **102**, 167401 (2009).

[338] G. Fabbris, D. Meyers, L. Xu, V. M. Katukuri, L. Hozoi, X. Liu, Z.-Y. Chen, J. Okamoto, T. Schmitt, A. Uldry, B. Delley, G. D. Gu, D. Prabhakaran, A. T. Boothroyd, J. van den Brink, D. J. Huang, and M. P. M. Dean, "Doping Dependence of Collective Spin and Orbital Excitations in the Spin-1 Quantum Antiferromagnet $La_{2-x}Sr_xNiO_4$ Observed by X Rays," Phys. Rev. Lett. **118**, 156402 (2017).

[339] M. M. Sala, V. Bisogni, C. Aruta, G. Balestrino, H. Berger, N. B. Brookes, G. M. de Luca, D. Di. Castro, M. Grioni, M. Guarise, P. G. Medaglia, F. Miletto Granozio, M. Minola, P. Perna, M. Radovic, M. Salluzzo, T. Schmitt, K. J. Zhou, L. Braicovich, and G. Ghiringhelli, "Energy and symmetry of dd excitations in undoped layered cuprates measured by Cu L_3 resonant inelastic x-ray scattering," New J. Phys. **13**, 043026 (2011).

[340] C. Ulrich, L. J. P. Ament, G. Ghiringhelli, L. Braicovich, M. Moretti Sala, N. Pezzotta, T. Schmitt, G. Khaliullin, J. van den Brink, H. Roth, T. Lorenz, and B. Keimer, "Momentum Dependence of Orbital Excitations in Mott-Insulating Titanates," Phys. Rev. Lett. **103**, 107205 (2009).

[341] W. S. Lee, S. Johnston, B. Moritz, J. Lee, M. Yi, K. J. Zhou, T. Schmitt, L. Patthey, V. Strocov, K. Kudo, Y. Koike, J. van den Brink, T. P. Devereaux, and Z. X. Shen, "Role of Lattice Coupling in Establishing Electronic and Magnetic Properties in Quasi-One-Dimensional Cuprates," Phys. Rev. Lett. **110**, 265502 (2013).

[342] S. Johnston, C. Monney, V. Bisogni, K.-J. Zhou, R. Kraus, G. Behr, V. N. Strocov, J. Málek, S.-L. Drechsler, J. Geck, T. Schmitt, and J. van den Brink, "Electron-lattice interactions strongly renormalize the charge-transfer energy in the spin-chain cuprate Li_2CuO_2," Nat. Commun. **7**, 10563 (2016).

[343] L. J. P. Ament, F. Forte, and J. van den Brink, "Ultrashort lifetime expansion for indirect resonant inelastic x-ray scattering," Phys. Rev. B **75**, 115118 (2007).

[344] N. Pakhira, J. K. Freericks, and A. M. Shvaika, "Resonant inelastic x-ray scattering in a Mott insulator," Phys. Rev. B **86**, 125103 (2012).

[345] J.-I. Igarashi and T. Nagao, "Elementary excitations probed by L-edge resonant inelastic x-ray scattering in systems with weak and intermediate electron correlations," Phys. Rev. B **88**, 014407 (2013).

[346] T. Tohyama, K. Tsutsui, M. Mori, S. Sota, and S. Yunoki, "Enhanced charge excitations in electron-doped cuprates by resonant inelastic x-ray scattering," Phys. Rev. B **92**, 014515 (2015).

[347] D. Benjamin, I. Klich, and E. Demler, "Probing competing and intertwined orders with resonant inelastic x-ray scattering in the hole-doped cuprates," Phys. Rev. B **92**, 035151 (2015).

[348] L. A. Wray, W. Yang, H. Eisaki, Z. Hussain, and Y.-D. Chuang, "Multiplet resonance lifetimes in resonant inelastic x-ray scattering involving shallow core levels," Phys. Rev. B **86**, 195130 (2012).

[349] H. Ikeno, T. Mizoguchi, and I. Tanaka, " *Ab initio* charge transfer multiplet calculations on the $L_{2,3}$ XANES and ELNES of $3d$ transition metal oxides," Phys. Rev. B **83**, 155107 (2011).

[350] M. W. Haverkort, M. Zwierzycki, and O. K. Andersen, "Multiplet ligand-field theory using Wannier orbitals," Phys. Rev. B **85**, 165113 (2012).

[351] M. Guo, E. Källman, L. K. Sørensen, M. G. Delcey, R. V. Pinjari, and M. Lundberg, "Molecular Orbital Simulations of Metal $1s2p$ Resonant Inelastic X-ray Scattering," J. Phys. Chem. A **120**, 5848–5855 (2016).

[352] I. Josefsson, K. Kunnus, S. Schreck, A. Föhlisch, F. de Groot, P. Wernet, and M. Odelius, "*Ab initio* Calculations of X-ray Spectra: Atomic Multiplet and Molecular Orbital Effects in a Multiconfigurational SCF Approach to the L-edge Spectra of Transition Metal Complexes," J. Phys. Chem. Lett. **3**, 3565–3570 (2012).

[353] K. Kunnus, I. Josefsson, S. Schreck, W. Quevedo, P. S. Miedema, S. Techert, F. M. F. de Groot, M. Odelius, P. Wernet, and A. Föhlisch, "From Ligand Fields to Molecular Orbitals: Probing the Local Valence Electronic Structure of Ni^{2+} in Aqueous Solution with Resonant Inelastic X-ray Scattering," J. Phys. Chem. B **117**, 16512–16521 (2013).

[354] D. Maganas, P. Kristiansen, L.-C. Duda, A. Knop-Gericke, S. DeBeer, R. Schlögl, and F. Neese, "Combined Experimental and *Ab Initio* Multireference Configuration Interaction Study of the Resonant Inelastic X-ray Scattering Spectrum of CO_2," J. Phys. Chem. C **118**, 20163–20175 (2014).

[355] D. Maganas, S. DeBeer, and F. Neese, "A Restricted Open Configuration Interaction with Singles Method To Calculate Valence-to-Core Resonant X-ray Emission Spectra: A Case Study," Inorg. Chem. **56**, 11819–11836 (2017).

[356] A. Kubas, M. Verkamp, J. Vura-Weis, F. Neese, and D. Maganas, "Restricted Open-Shell Configuration Interaction Singles Study on M- and L-edge X-ray Absorption Spectroscopy of Solid Chemical Systems," J. Chem. Theory Comput. **14**, 4320–4334 (2018).

[357] D. Maganas, S. DeBeer, and F. Neese, "Pair Natural Orbital Restricted Open-Shell Configuration Interaction (PNO-ROCIS) Approach for Calculating X-ray Absorption Spectra of Large Chemical Systems," J. Phys. Chem. A **122**, 1215–1227 (2018).

[358] J. van den Brink and M. van Veenendaal, "Theory of indirect resonant inelastic X-ray scattering," J. Phys. Chem. Solids **66**, 2145–2149 (2005).

[359] J. van den Brink and M. van Veenendaal, "Correlation functions measured by indirect resonant inelastic X-ray scattering," EPL **73**, 121 (2006).

[360] M. Blume, "Magnetic scattering of X-rays (invited)," J. Appl. Phys. **57**, 3615–3618 (1985).

[361] V. Weisskopf and E. Wigner, "Berechnung der natürlichen Linienbreite auf Grund der Diracschen Lichttheorie," Zeitschrift für Physik **63**, 54–73 (1930).

[362] W. Heitler, *Quantum theory of radiation* (3rd ed., Oxford University Press, 1954).

[363] K. Hamalainen, S. Manninen, P. Suortti, S. P. Collins, M. J. Cooper, and D. Laundy, "Resonant Raman scattering and inner-shell hole widths in Cu, Zn and Ho," J. Phys.: Condens. Matter **1**, 5955 (1989).

[364] W. Schülke, *Electron dynamics by inelastic X-Ray scattering* (Oxford University Press, 2007).

[365] J. Als-Nielsen and D. McMorrow, *Elements of Modern X-ray Physics* (John Wiley & Sons Ltd, 2011).

[366] H. A. Kramers and W. Heisenberg, "Über die Streuung von Strahlung durch Atome," Z. Phys. **31**, 681–708 (1925).

[367] S. Kadota, I. Yamada, S. Yoneyama, and K. Hirakawa, "Formation of One-Dimensional Antiferromagnet in $KCuF_3$ with the Perovskite Structure," J. Phys. Soc. Jpn **23**, 751–756 (1967).

[368] D.I. Khomskii K.I. Kugel, "The Jahn-Teller effect and magnetism: transition metal compounds," Sov. Phys. Usp. **25**, 231 (1982).

[369] M. D. Towler, R. Dovesi, and V. R. Saunders, "Magnetic interactions and the cooperative Jahn-Teller effect in $KCuF_3$," Phys. Rev. B **52**, 10150–10159 (1995).

[370] R. H. Buttner, E. N. Maslen, and N. Spadaccini, "Structure, electron density and thermal motion of $KCuF_3$," Acta Cryst. **B46**, 131–138 (1990).

[371] L. F. Feiner, A. M. Oleś, and J. Zaanen, "Quantum Melting of Magnetic Order due to Orbital Fluctuations," Phys. Rev. Lett. **78**, 2799–2802 (1997).

[372] N. B. Balabanov and K. A. Peterson, " Systematically convergent basis sets for transition metals. I. All-electron correlation consistent basis sets for the $3d$ elements Sc—Zn," J. Chem. Phys. **123**, 064107 (2005).

[373] T. H. Dunning Jr., " Gaussian basis sets for use in correlated molecular calculations. I. The atoms boron through neon and hydrogen," J. Chem. Phys. **90**, 1007–1023 (1989).

[374] A. Mitrushchenkov and H.-J. Werner, "Calculation of transition moments between internally contracted MRCI wave functions with non-orthogonal orbitals," Mol. Phys. **105**, 1239–1249 (2007).

[375] J. Deisenhofer, I. Leonov, M. V. Eremin, Ch. Kant, P. Ghigna, F. Mayr, V. V. Iglamov, V. I. Anisimov, and D. van der Marel, "Optical Evidence for Symmetry Changes above the Néel Temperature of $KCuF_3$," Phys. Rev. Lett. **101**, 157406 (2008).

[376] Anderson, P. W., "The Resonating Valence Bond State in La_2CuO_4 and Superconductivity," Science **235**, 1196–1198 (1987).

[377] P. W. Anderson, G. Baskaran, Z. Zou, and T. Hsu, "Resonating-valence-bond theory of phase transitions and superconductivity in La_2CuO_4-based compounds," Phys. Rev. Lett. **58**, 2790–2793 (1987).

[378] A. Aharony, R. J. Birgeneau, A. Coniglio, M. A. Kastner, and H. E. Stanley, "Magnetic phase diagram and magnetic pairing in doped La_2CuO_4," Phys. Rev. Lett. **60**, 1330–1333 (1988).

[379] K. Yamada, C. H. Lee, K. Kurahashi, J. Wada, S. Wakimoto, S. Ueki, H. Kimura, Y. Endoh, S. Hosoya, G. Shirane, R. J. Birgeneau, M. Greven, M. A. Kastner, and Y. J. Kim, "Doping dependence of the spatially modulated dynamical spin correlations and the superconducting-transition temperature in $La_{2-x}Sr_xCuO_4$," Phys. Rev. B **57**, 6165–6172 (1998).

[380] Y. S. Lee, R. J. Birgeneau, M. A. Kastner, Y. Endoh, S. Wakimoto, K. Yamada, R. W. Erwin, S.-H. Lee, and G. Shirane, "Neutron-scattering study of spin-density wave order in the superconducting state of excess-oxygen-doped La_2CuO_{4+y}," Phys. Rev. B **60**, 3643–3654 (1999).

[381] J. D. Jorgensen, B. Dabrowski, Shiyou Pei, D. R. Richards, and D. G. Hinks, " Structure of the interstitial oxygen defect in $La_2NiO_{4+\delta}$," Phys. Rev. B **40**, 2187–2199 (1989).

[382] P. Kuiper, J. van Elp, D. E. Rice, D. J. Buttrey, H.-J. Lin, and C. T. Chen, "Polarization-dependent nickel $2p$ x-ray-absorption spectra of $La_2NiO_{4+\delta}$," Phys. Rev. B **57**, 1552–1557 (1998).

[383] E. Pellegrin, J. Zaanen, H.-J. Lin, G. Meigs, C. T. Chen, G. H. Ho, H. Eisaki, and S. Uchida, "O $1s$ near-edge x-ray absorption of $La_{2-x}Sr_xNiO_{4+\delta}$: Holes, polarons, and excitons," Phys. Rev. B **53**, 10667–10679 (1996).

Eidesstattliche Erklärung

Hiermit versichere ich, dass ich die vorliegende Arbeit ohne unzulässige Hilfe Dritter und ohne Benutzung anderer als der angegebenen Hilfsmittel angefertigt habe; die aus fremden Quellen direkt oder indirekt übernommenen Gedanken sind als solche kenntlich gemacht. Die Arbeit wurde bisher weder im Inland noch im Ausland in gleicher oder ähnlicher Form einer anderen Prüfungsbehörde vorgelegt.

Die vorliegende Dissertation wurde vom 01.12.2014 bis 31.01.2019 am Leibniz-Institut für Festkörper- und Werkstoffforschung Dresden (IFW Dresden), Institut für theoretische Festkörperphysik (ITF) unter der Betreuung von Prof. Dr. Jeroen van den Brink angefertigt.

Es haben keine erfolglosen Promotionsverfahren in der Vergangenheit stattgefunden. Die aktuelle Promotionsordnung der Fakultät Mathematik und Naturwissenschaften der Technischen Universität Dresden wird anerkannt.

Lei Xu
Dresden
11. March 2019